



Forschungszentrum Karlsruhe
in der Helmholtz-Gemeinschaft

Wissenschaftliche Berichte

FZKA 7515

**Colloid/Nanoparticle
formation and mobility in the
context of deep geological
nuclear waste disposal
(Project KOLLORADO-1;
Final report)**

Thorsten Schäfer¹ & Ulrich Noseck² (Eds.)

Authors:

**M. Bouby¹, A. Filby¹, H. Geckeis¹,
F. Geyer¹, R. Götz¹, W. Hauser¹, F. Huber¹,
S. Keesmann², B. Kienzler¹, P. Kunze¹,
M. Küntzel², J. Lützenkirchen¹, U. Noseck²,
P. Panak¹, M. Plaschke¹, A. Pudewills¹,
T. Schäfer¹, H. Seher¹, C. Walther¹**

¹Institut für Nukleare Entsorgung

²Gesellschaft für Anlagen- und Reaktorsicherheit
(GRS) mbH

Oktober 2010

Anmerkung:

Die diesem Bericht zugrundeliegenden Arbeiten wurden mit Mitteln des Bundesministeriums für Wirtschaft und Technologie BMWi unter dem Förderkennzeichen 02 E 10096 gefördert.

Die Verantwortung für den Inhalt dieser Veröffentlichung liegt alleine bei den Autoren.

Forschungszentrum Karlsruhe

in der Helmholtz-Gemeinschaft

Wissenschaftliche Berichte

FZKA 7515

Colloid/ Nanoparticle formation and mobility in the context of deep geological nuclear waste disposal (Project KOLLORADO-1; Final report)

Thorsten Schäfer¹ & Ulrich Noseck² (Eds.)

Authors:

M. Bouby¹, A. Filby¹, H. Geckeis¹, F. Geyer¹, R. Götz¹,
W. Hauser¹, F. Huber¹, S. Keesmann², B. Kienzler, P. Kunze¹, M.
Küntzel², J. Lützenkirchen, U. Noseck², P. Panak¹, M. Plaschke¹, A.
Pudewills¹, T. Schäfer¹, H. Seher¹, C. Walther¹

¹Institut für Nukleare Entsorgung

²Gesellschaft für Anlagen- und Reaktorsicherheit (GRS) mbH

Für diesen Bericht behalten wir uns alle Rechte vor

Forschungszentrum Karlsruhe GmbH
Postfach 3640, 76021 Karlsruhe

Mitglied der Hermann von Helmholtz-Gemeinschaft
Deutscher Forschungszentren (HGF)

ISSN 0947-8620

urn:nbn:de:0005-075156

List of content

List of figures	5
List of tables	11
1 Introduction	13
1.1 Scope of this Work	13
1.2 State of the art	13
1.3 Aims and Approach	16
2 Experimental Program	18
2.1 Laboratory program	18
2.1.1 Radionuclide Speciation in the groundwater porewater mixing zone.....	18
2.1.2 Sorption reversibility studies: Comparison of fracture filling material (FFM) from Grimsel (Switzerland) and Äspö (Sweden)	23
2.1.3 Colloid stability.....	34
2.1.4 Colloid generation at the compacted bentonite water interface	48
2.1.5 Colloid – Mineral surface interactions (microscopic approach).....	52
2.1.6 Core migration studies.....	69
2.2 Field experiments (AP 1.2) (Homologue test Run 08-01)	79
3 Modeling	82
3.1 CFM hydraulics and transport modeling (AP 2.5)	82
3.1.1 Numerical modelling of the field tracer tests	83
3.2 Finite element modelling (ADINA-F) of flow and transport in a single fracture from the Äspö HRL (Sweden)	89
3.3 1D and 2D flow and colloid facilitated transport modelling including kinetically controlled sorption processes	94
3.3.1 Experimental basis	94
3.3.1.1 Laboratory data input.....	94
3.3.2 Field experiments	95
3.3.2.1 Colloid and radionuclide retention (CRR).....	95
3.3.2.2 Colloid formation and migration (CFM).....	96
3.3.3 Modelling of sorption processes	97
3.3.4 Modelling of filtration processes	102
3.3.5 Simulations	104
3.3.5.1 1D	105
3.3.5.2 2D	110
3.3.5.3 Repository conditions	115
4 Conclusions and outlook	121
4.1 Understanding of colloidal/nanoparticle processes	121
4.2 Future directions	126
5 References	128
6 Appendix	138
6.1 Development of r³t-col	138
6.1.1 Overview.....	138
6.1.2 Mapping colloid-facilitated-transport phases on phases in r ³ t.....	139
6.1.3 Implementation of the velocity coefficient.....	139
6.1.4 Consequences of the component mapping	140
6.1.5 Extension of the r ³ t-source code	140

6.1.5.1	The source code of appl2d/cproblem_lgm.c	140
6.1.5.2	The source code in pclub/.....	142
6.1.5.3	The source code in config/	143
6.1.6	Extension of the interface	144
6.1.6.1	The file config/geometry	144
6.1.6.2	The file config/pollutant.....	145
6.1.6.3	The file config/retention	145
6.2	Verification of r³t-col.....	147
6.2.1	General test setup	147
6.2.2	Results.....	149
6.2.3	TC1: sorption process Q_1 , variation of the sorption rate k_1	149
6.2.4	TC2: Sorption process Q_7 and Q_3 :	150
6.2.5	TC3: All sorption processes. Variation of the sorption factor K_2	152
6.3	Laboratory study on colloid stability and radionuclide – colloid interaction under Äspö groundwater conditions.	154
6.3.1	Material & Methods.....	154
6.3.1.1	Äspö Ground Water (ÄGW).....	154
6.3.1.2	MX80-bentonite colloids	158
6.3.1.3	Fracture filling material (FFM)	159
6.3.1.4	Fulvic acid (FA).....	160
6.3.1.5	Stability measurements	160
6.3.1.6	Batch sorption experiments	162
6.3.2	Results and discussion.....	163
6.3.2.1	Characterisation of ÄGW.....	163
6.3.2.1.1	Storage in barrel	163
6.3.2.1.2	Influence of oxygen contact.....	164
6.3.2.1.3	Storage under anoxic conditions (glove box, Ar/1%CO ₂).....	164
6.3.2.1.4	Storage in contact with fracture filling material (FFM) under anoxic conditions (glove box, Ar/1%CO ₂).....	166
6.3.2.2	MX80 bentonite colloid stability	166
6.3.2.2.1	Stability ratio as a function of ionic strength (IS) and pH	166
6.3.2.2.2	Is the stability enhanced by the presence of organic matter?	170
6.3.2.3	Radionuclide behavior in Äspö groundwater in presence of bentonite colloids, fracture filling material and fulvic acid.	171

List of figures

Figure 2-1: Time dependent evolution of colloid concentration and average colloid size as measured by laser-induced breakdown detection (LIBD). The dashed line indicates the detection limit of LIBD.....	20
Figure 2-2: Comparison of TRLFS emission spectra taken of the end members Grimsel groundwater and synth. Febex pore water at pH 8 and 8.5 with spectra taken in mixed solutions at the same pH value. Percentage of Febex pore water admixture is 30 % (left) and 15 % (right), respectively.	22
Figure 2-3: SEM pictures of the Äspö FFM [a.) and b.)] and of the Grimsel FFM [c.) and d.)]. The sizes fraction of the material is between 0.5 and 1 mm.	24
Figure 2-4: AFM picture of Febex bentonite colloids. The line in (a) represents the height profile shown in (b).....	25
Figure 2-5: (left) Measured final pH and Eh for the RN batch-type studies as a function of contact time. (right) Eh measurement for a single point showing the response time of the redox electrode reaching a constant plateau value after several hours.	28
Figure 2-6: Time dependent evolution of radionuclide concentration for the Äspö (black symbols) and Grimsel FFM (red symbols) experiments. a.) Tc b.) U c.) Np d.) Th e.) Pu and f.) Am. Values are given both for ultracentrifugated (UC) samples and for not ultracentrifugated (not UC) samples.....	29
Figure 2-7: (a) predominance diagram for U; b.) speciation plot for U and c.) pre-dominance diagram for Tc under the given experimental conditions.....	30
Figure 2-8: Pourbaix (pe/pH) diagram for the batch experiments showing the experimental pe/pH range and the pe borderline for 50% Np reduction. (orange: Grimsel FFM; grey: Äspö FFM).....	31
Figure 2-9: Comparison of the Al concentration in the ultracentrifuged and not ultracentrifuged samples for the Äspö FFM and Grimsel FFM system.	32
Figure 2-10: Surface area normalized log (Kd) values for Np (left), Pu (middle) and Am (right) in comparison to data from [64]. Data of this study are shown as filled symbols. The N ₂ BET surface area taken for the calculation is: Äspö FFM: 0.2m ² ·g ⁻¹ , Grimsel FFM (1-2mm): 0.15m ² ·g ⁻¹ ; Grimsel FFM (0.5-1mm): 0.19m ² ·g ⁻¹ ; Grimsel FFM (0.25-0.5mm): 0.24m ² ·g ⁻¹ , respectively.	33
Figure 2-11: Time dependent hydrodynamic radius r _H increase for Febex bentonite colloids as a function of CaCl ₂ background electrolyte concentration at pH 8.	37
Figure 2-12: Stability ratio W of Febex bentonite colloids is plotted against the electrolyte concentration a) for CaCl ₂ , b) for NaCl. The critical coagulation concentration (CCC) is the intersection of W = 1 with the x-axis. The addition of 1mg·L ⁻¹ DOC (GoHy-573 FA) increases W for all measured concentrations as can be depicted from graph c).	38
Figure 2-13: Critical coagulation concentration (CCC) plotted against pH for CaCl ₂ a) and NaCl b). The Ca- CCC does not change within the analytical uncertainty for the investigated pH range. For comparison, the data from Hetzel & Doner [74] for montmorillonite (SWy-1) and beidelite is inserted. The Na- CCC values for pH 6 and 7 is within the range found in the literature, whereas for pH 8 to 10 a considerable variation is found. Possible explanations are given in the text.....	39
Figure 2-14: (a) XANES spectra of GoHy-573FA starting solution prior to Febex bentonite sorption (blue) and spectra of organics associated to Febex bentonite colloids at pH 6 and pH 8, respectively. The solid line represents a best fit of the fulvic acid spectra taking the de-convolution procedure as described in Schäfer et al. [93]. (b) Ratio image (-log (I[285.3eV to 295.0eV]/ I ₀ [283eV])) of organics associated with Febex bentonite colloids at pH 6. Brighter gray values indicate a higher concentration of organic material. (c) STXM image taken at 283eV below the	

carbon K-edge showing absorption of bentonite colloids and aggregates. Scale bar represents 2 μ m.....	41
Figure 2-15: a) Febex bentonite colloid ζ -potential in CaCl ₂ background electrolyte solution. Data points represent the measured ζ -potentials at 0.33 mmol·L ⁻¹ (filled squares) and 33 mmol·L ⁻¹ (open squares) as a function of pH. The solid lines represent the best fit for the surface potential to reproduce the measured stability ratio as given in Table 2-3. b) Silica (triangles) and α -alumina (diamonds) ζ -potential in CaCl ₂ background electrolyte solution. Data points represent the measured ζ -potentials at 0.33 mmol·L ⁻¹ (diamonds) and 33 mmol·L ⁻¹ (triangles) as a function of pH. The lines indicate the estimated edge charge for the two electrolyte concentrations using equation (5).	42
Figure 2-16: Febex bentonite colloid ζ -potential in NaCl electrolyte solution a). The lines in a) represent the best fit for the surface potential to recalculate the observed stability ratio (see Tab. 2). Measured silica and α -alumina ζ -potentials are plotted in b). The lines indicate the estimated edge charge for the two electrolyte concentrations. The edge charge is also estimated using γ -alumina ζ -potential taken from de Lint et al. [95]. The data and the estimated edge charge are given in c).	44
Figure 2-17: Interaction energy calculated for edge-edge (a,b), edge-face (c,d), face-face (e,f) and total (g,h) interaction for Febex bentonite colloids and 1 mmol·L ⁻¹ NaCl electrolyte solution as a function of pH (left) and different concentrations at pH 10 (right) for the best fit surface potentials (solid line in Fig. 6a).	47
Figure 2-18: Interaction energy calculated for the edge-face (EF) mode of interaction for pH 10 under variation of the concentration variation (zeta- potential of platelet edge and face charge for 1 mmol·L ⁻¹ NaCl inserted) (a). The energy barrier is decreasing with increasing electrolyte concentration. (b) Correlation between the measured Na-CCC values (Figure 2-13b) and the CCC derived from DLVO calculations (EF-CCC). The solid line (slope= 1) indicate perfect agreement between model and experiment (Na-CCC = EF-CCC). The shaded area in (b) shows the region of deviation and effect of edge charge shielding due to EDL spill-over.....	47
Figure 2-19: (left) Reactor of the CIEMAT setup in different assembly stages. The bentonite pellet is squeezed into a stainless-steel cylinder by two filter plates. (right) Stainless steel reactor version of the KIT-INE experimental setup. Two bentonite pellets with the PEEK spacer and the filter plates are inserted.....	49
Figure 2-20: Time dependent evolution of the LIBD determined colloid concentration and number-weighted average colloid diameter. The electrolyte concentrations are given as ionic strength.	51
Figure 2-21: Speciation of UO ₂ ²⁺ in aqueous solution, in absence of CO ₂ . [UO ₂ ²⁺] = 10 ⁻⁶ M, I = 10 ⁻² NaCl. [108] (see text) [109].....	54
Figure 2-22: AFM image of muscovite surface with adsorbed latex colloids (pH = 4, I = 10 ⁻² M NaCl, C _{colloids} = 2 g/l, Eu(III) = 10 ⁻⁵ M) (see text).....	57
Figure 2-23: Fluorescence-optical image of muscovite (a) after adsorption of fluorescent colloids (pH = 4, I = 10 ⁻² M NaCl, C _{colloids} = 0.05 g/l) and (b) in the presence of Eu(III) (pH = 4, I = 10 ⁻² M NaCl, C _{colloids} = 0.05 g/l, Eu(III) = 10 ⁻⁵ M) (see text)	58
Figure 2-24: Fluorescence intensity/surface coverage vs. pH for muscovite in the presence and absence of Eu(III). All measurements were undertaken at pH 2, 4, 6, 8, 10.....	59
Figure 2-25: Fluorescence intensity/surface coverage vs. pH of biotite in the presence and absence of Eu(III). All measurements were undertaken at pH 2, 4, 6, 8, 10 (see text)	59
Figure 2-26: Experimental snap-in forces on muscovite (see text).....	60
Figure 2-27: Experimental adhesion forces on muscovite (see text).....	61
Figure 2-28: Experimental snap-in forces on biotite (see text).....	61
Figure 2-29: Experimental adhesion forces on biotite (see text).....	62

Figure 2-30: Preparation of the core from the Grimsel test site, Switzerland, for the transport experiments. At the surface of the core epoxy resin is used as sealing material (a). Afterwards both ends were cut plane and a borehole was drilled in the middle of the core with a 90° angle to the fracture zone (b). The packer system and drilled core from the location where the packer system is placed into the Grimsel core (c).	70
Figure 2-31: Core with installed packer system (a). At the end all PEEK pipes are closed with a check valve. Final experimental setup in the laboratory (b). A peristaltic pump is used to pump the water from the bottom of the core through the fracture. Another pump is injecting the tracer cocktail and GW through the packer system. For details see text.	70
Figure 2-32: Breakthrough curves of Febex bentonite colloids and NaBr in experiment Tr1(a), Tr2(b) and Tr3(c). For NaBr the C_0 concentration in all experiments is $1 \cdot 10^{-2} \text{ mol} \cdot \text{L}^{-1}$. The C_0 concentration measured with the mobile LIBD varies for the bentonite colloids between $69.9 \text{ mg} \cdot \text{L}^{-1}$ (Tr1), $34.3 \text{ mg} \cdot \text{L}^{-1}$ (Tr2) and $57.0 \text{ mg} \cdot \text{L}^{-1}$ (Tr3), respectively. The C_0 concentration determined via acoustic LIBD in Tr3 is $62.9 \text{ mg} \cdot \text{L}^{-1}$	72
Figure 2-33: Breakthrough curves of Aluminum (a), Eu(III), Tb(III), Th(IV) and U(VI) (b) and the colloid diameter (c) in experiment Tr1. The colloid size was divided by the colloid size measured in the tracer cocktail.	74
Figure 2-34: Breakthrough curves of Aluminum (a), Eu(III), Tb(III), Th(IV) and U(VI) (b) and the colloid diameter (c) in experiment Tr2 with a flow velocity of 99.7 m a^{-1} and an injection volume of 2 mL. The C_0 concentrations are the measured concentrations in the tracer cocktail (Table 2-11). The colloid size was divided by the colloid size measured in the tracer cocktail.	74
Figure 2-35: Breakthrough curves of Aluminum (a), Eu(III), Tb(III), Th(IV) and U(VI) (b) in experiment Tr3 with a flow velocity of 42.5 m a^{-1} and an injection volume of 2 mL.	75
Figure 2-36: Colloid size distribution measured by s-curve analysis (a). Colloid size determined by mobile LIBD divided by the colloid size measured in the tracer cocktail (b).	75
Figure 2-37: Recovery vs. residence time for bentonite colloids and metal ions used in the experiments. To compare the measured values in this work, literature data is also given Hauser et al. [149], Möri et al. [139], Geckeis et al. [15], Missana et al. 2003 [150], Schäfer et al. [32] and Missana et al. 2008 [143].	77
Figure 2-38: Breakthrough curves of the homologues Hf, Tb and Th in Run 08-01 in comparison to the conservative tracer uranine of Run 08-02 under the same hydraulic conditions, but using recirculation in the packer interval. The peak maximum for the homologues is after 239 min, whereas the peak maximum of the uranine peak is delayed through the recirculation used to 544.5 min.	80
Figure 2-39: (top) Comparison of colloid breakthrough curves detected by LIBD and different channels of the single particle counting SPC (data C. Degueldre; PSI-LES). (bottom) Colloid breakthrough curve plotted as contour plot of colloid concentration (ppt) against the experimental time (x-axis) and colloid size (y-axis) taken from LIBD s-curve analysis.	81
Figure 3-1: Definition of the model boundary condition for simulation of tracer tests	84
Figure 3-2: Finite element model used for calculation of tracer tests and detail of the mesh near the boreholes; dimensions of the model plane: $20 \text{ m} \times 12 \text{ m}$	85
Figure 3-3: (a) Uranine concentration at the injection borehole (BOMI 87.010), (b) Calculated and measured break through curves at the extraction side, (c) Uranine concentration at the injection borehole (BOMI 87.010) for tracer test 07-02 and (d) Calculated and measured breakthrough curves at the extraction well (tracer mass recovery about 86%)	86
Figure 3-4: Distribution of the uranine concentration after different times.	87

Figure 3-5: (a) Uranine injection functions of two different tests, (b) Comparison of measured and calculated break-through curves for two tracer tests	87
Figure 3-6: Distribution of piezometric head and uranine concentration 10 and 54 hours after injection.....	88
Figure 3-7: Rendered 3D image of fracture in Core#8 on the basis of the μ XCT data set which shows the complex overall geometry and surface morphology. Notice the very irregular boundary on one side of the fracture.....	90
Figure 3-8: View of the semi-2D finite element mesh with the applied boundary and load conditions. Note that the aperture is shown as 30 times exaggerated for displaying reasons b.) 3D model with the inlet and outlet velocity boundary condition. The detailed view of a part of the 3D mesh shows an area inside the model where the fracture is closed.	91
Figure 3-9: Results of the semi-2D model. a.) velocity distribution in the fracture. b.) detailed view of a part of the model showing velocity vectors. c.) calculated pressure distribution. c.) snapshot of the migrating tracer at time 2250 sec.	92
Figure 3-10: Normalized experimental HTO (open symbols) and calculated (line) BTC as function of time.....	93
Figure 3-11: Breakthrough curves of Am, Pu, Np and U (top) and the respective recoveries for Am and Pu (bottom) in the CRR experiment #32 [15].....	96
Figure 3-12: Transmissivity field and location of boreholes in the shear zone (after [171]). The dipole between borehole CFM 06.002 and Pinkel for the CFM homologue experiment is shown by the red arrow.	97
Figure 3-13: Nomenclature chosen for the concentrations of the pollutant and the colloid as well as for the sorption paths.	98
Figure 3-14: Case A: Distribution coefficients for plutonium as function of time. Data from experiments (dots) and model curves on linear and logarithmic time scales. Model parameters see Table 3-4.....	100
Figure 3-15: Case A: Distribution coefficients for americium as a function of time. Data from experiments (dots) and model curves on linear and logarithmic time scales. Model parameters see Table 3-4.....	101
Figure 3-16: Case B: Distribution coefficients for plutonium and americium as function of time assuming 20% of Pu and 30% of Am not being initially sorbed to colloids. $k_1 = 0.05 \text{ h}^{-1}$. Other model parameters see Table 3-4	101
Figure 3-17: Collector efficiency vs. particle diameter for conditions listed in Table 3-5. Shaded area marks the range of colloid diameters observed under Grimsel groundwater conditions.....	104
Figure 3-18: Breakthrough curve of the I ⁻ tracer: dots = experiment, line = calculated (right side scaled).....	106
Figure 3-19: Breakthrough curves (top) and recoveries (bottom) for Pu in CRR experiment #32. Results from experiment and simulations.....	107
Figure 3-20: Concentration of Pu [mol/l] at the peak maximum of the breakthrough curve vs. groundwater travel time for different filtration rates. $k_3 = 0.005 \text{ h}^{-1}$: linear scale (left) and logarithmic scale (right).....	109
Figure 3-21: Recoveries vs. groundwater travel time for four different filtration rates: logarithmic (left) and linear (right) scale. $k_3 = 0.005 \text{ h}^{-1}$. The shaded area indicates the range of travel times applied so far in the CRR and CFM experiments.....	109
Figure 3-22: Recoveries vs. groundwater travel time for four different filtration rates: logarithmic (left) and linear (right) scale. $k_3 = 0.01 \text{ h}^{-1}$. The shaded area indicates the range of travel times applied so far in the CRR and CFM experiments.....	110

Figure 3-23: Geometry and hydrogeological/transport-related boundary conditions of 2D the computer model. Green: inflow, red outflow, blue: sealed tunnel wall and symmetry axis, black: permeable virtual boundaries within the shear zone. Notation: c = concentration; p = pressure; v = fluid velocity; f = pollutant mass flux; n is used either as a subscript to denote the normal component or in fractions in which symbolises the normal derivative of the respective variable.....	111
Figure 3-24: Determination of effective hydrogeological parameters by matching the outcome of the simulations to the experimental break through curve of the tracer.....	112
Figure 3-25: Time-dependent recovery of the injected pollutant mass. The dotted black line indicates the totally injected amount.....	112
Figure 3-26: Stationary velocity direction field at outflow rates of 165ml/min (top) and 50ml/min (bottom). For illustration purposes, the length of the arrows is not scaled with the magnitude of the velocity.	113
Figure 3-27: Snapshot of a tracer simulation with an outflow rate of 50ml/min illustrating problems with mass loss at permeable boundaries (right and top) due to the inadequate size of the model area for slow transport conditions.....	113
Figure 3-28: 2D logarithmic concentration profile of a simulation at $t = 32500$ s with active sorption processes but in the absence of colloids (top) compared with the equivalent image of the pure tracer experiment (bottom). The outflow rate is 165 ml/min and the snapshot time corresponds to the peak of the experimental tracer break through curve.....	114
Figure 3-29: Input function: experimental concentration measured at the injection area. The samples were taken from annulus.	115
Figure 3-30: Two-dimensional colour-coded display of the concentration (kg/m^3) in the tracer simulation with an outflow rate of 165ml/min at the peak (top) and the tail (bottom) of the break through curve.	115
Figure 3-31: Breakthrough curves of Pu-242 for the different cases	118
Figure 3-32: Breakthrough curves of Am-243 for the different cases	118
Figure 3-33: Breakthrough curves of U-236 for different calculation cases	119
Figure 3-34: Breakthrough curves of Th-232 for different calculation cases	120
Figure 4-1: Comparison of experimental data with model calculations; only colloid filtration ($K_2 = 0.02 \text{ h}^{-1}$ yellow dots) and colloid filtration with radionuclide desorption ($k_3 = 0.01 \text{ h}^{-1}$ green dots).....	124
Figure 4-2: Impact of the desorption rate k_3 on the breakthrough curve of Pu-242. No colloid filtration assumed.....	125
Figure 6-1: Software layers of r^3t	138
Figure 6-2: <i>Test case setup for the comparison with TRAPIC1D</i>	147
Figure 6-3: <i>Breakthrough curves from calculations with TRAPIC1D and r^3t-col for TC1</i>	150
Figure 6-4: <i>Breakthrough curves from calculations with TRAPIC1D and r^3t-col for TC2 (1)</i>	151
Figure 6-5: <i>Breakthrough curves from calculations with TRAPIC1D and r^3t-col for TC2 (2)</i>	151
Figure 6-6: <i>Breakthrough curves from calculations with TRAPIC1D and r^3t-col for TC3 (1)</i>	152
Figure 6-7: <i>Breakthrough curves from calculations with TRAPIC1D and r^3t-col for TC3 (2)</i>	153
Figure 6-8: Tapping mode AFM of a dry MX80-bentonite colloidal solution sample.....	159
Figure 6-9: Effective focal length ($L_z(P)$) determined by analyzing the position of 5000 single plasma events in the laser beam axis using a microscope CCD camera. Commercial polystyrene reference colloid dispersions (DUKE Scientific) with different colloid diameters (21, 50, 73, 102, 199, 300, 404 nm) are diluted with ultrapure water to the required colloid concentration.....	161
Figure 6-10: SEM pictures of “white” visible precipitates developing with time in the water samples kept in the glove box.....	165

Figure 6-11: Variation of the hydrodynamic diameter as a function of time for standard carboxylated latex particles (105 nm diameter, Magsphere, USA) in 0.1 M ionic strength medium (CaCl ₂) at pH > pH _{pzc} .	167
Figure 6-12: Stability ratio of the MX80-bentonite colloids (1.2 mg.L ⁻¹) as a function of pH and ionic strength induced by addition of NaCl or CaCl ₂ . The presence of natural dissolved organic matter is simulated by addition of FA.	167
Figure 6-13: a) Example of colloidal flocculate present in all solutions; b-c-d) SEM pictures of the colloidal precipitates seen in solution A (IS=0.01M); e) and f) extracted from solution B (IS=0.1 M), g) extracted from solution E (IS=0.2 M)	168
Figure 6-14: a) Supernatant BDP evolution for solution A, B, C, D, E, F (see Table 6-7 for details)	169
Figure 6-15: b) Effect of mechanical shaking after coagulation, d _{Lz(P)} is the diameter value determined directly from the calibration (see Figure 6-9) when d _{corr} is the corrected diameter value obtained after taking into account the material dependence for LIBD measurement (see text and [51]).	169
Figure 6-16: Influence of organic matter (FA-573) on the MX80-bentonite colloids stability and sedimentation kinetics. c) and d) zooms of a) and b) over the first days.	171
Figure 6-17: SEM-EDX analysis of the visible precipitates formed in batch 2 and 5, Al:Si ratio ~ 0.34	172
Figure 6-18: Additional SEM-EDX analysis on residual particles formed in batch 2, 4 and 5.	172
Figure 6-19: Evolution of the fulvic acid (FA-573, 10 mg.L ⁻¹) UV-Visible spectra in Äspö groundwater in presence of MX-80 colloids, fracture filling material, radionuclides or mixture of both.	174
Figure 6-20: a) b) c): Behavior of a) Sr ⁹⁰ (2.2 10 ⁻⁹ M), b) Cs ¹³⁷ (2.3 10 ⁻⁹ M), and c) U ²³³ (2.3 10 ⁻⁸ M) spiked to ÄGW (TRUE1-site, Feature A, KXTT4) in presence of added MX80-bentonite colloids (2.4 mg.L ⁻¹), fracture filling material (FFM) (1g : 4 mL water) and fulvic acid (FA-573, 10 mg.L ⁻¹ ~ 5 mg.L ⁻¹ DOC). The open symbols represent the behavior of the naturally occurring element measured in the batch supernatants, namely Cs ¹³³ and U ²³⁸ . Error : ± 5 %.	178

List of tables

Table 2-1: Chemical composition of the original Grimsel groundwater (GGW) and after different contact time with Grimsel/Äspö FFM in the batch-type experiments.	26
Table 2-2: Characterization of the radionuclide cocktail including concentration, initial association to bentonite colloids determined by ultracentrifugation and the analytical method used in this study.	27
Table 2-3: Stability ratio W measured with and without addition of 1 mg-L ⁻¹ DOC (GoHy-573 fulvic acid), calculated and fitted for CaCl ₂ electrolyte solution.	44
Table 2-4: Stability ratio W measured, calculated and fitted for NaCl electrolyte.	45
Table 2-5: Experimental conditions for bentonite erosion experiment.....	48
Table 2-6: Element concentration of Grimsel groundwater.....	54
Table 2-7: EDX data for the single minerals used in the sorption experiments (elemental composition in atom %, values < 1 % not included)	55
Table 2-8: Mineral surface roughness determined by AFM.....	56
Table 2-9: EDX data for the single minerals (elemental composition in atom %, values < 1 % not included) used in the force-spectroscopy experiments	56
Table 2-10: ICP-MS analysis of the tracer cocktail of experiment Tr1.....	70
Table 2-11: ICP-MS analysis of the tracer cocktail of experiment Tr2.....	71
Table 2-12: ICP-MS analysis of the tracer cocktail of experiment Tr3.....	71
Table 2-13: BTC parameters determined for the migration experiments.....	73
Table 2-14: Calculated retardation factors (R _f) for Febex bentonite colloids and Th(IV).	76
Table 2-15: Recoveries for bentonite colloids and different metal ions. The recovery of a species was calculated with the respective concentration measured in the injection cocktail of this experiment.	77
Table 3-1: Summary of tracer tests used for model calibration.....	84
Table 3-2: Comparison of hydraulic and transport parameters used to model the tracer tests.....	88
Table 3-3: Time dependence of the distribution coefficients [m ³ /kg] of selected elements for the fracture infill material Grimsel [170]. The data have been determined for three size fractions of the infill material and are listed in this order: 1-2 mm, 0.5-1 mm, and 0.25-0.5 mm).....	95
Table 3-4: Parameters used for the best simulation of the Batch experiments for Pu and for Am (in brackets, when different from Pu)	100
Table 3-5: Parameters used for the deep bed filtration approach	103
Table 3-6: Geometrical and hydraulic data for CRR migration experiment #32	106
Table 3-7: Geometrical and hydraulic data for parameter variations.....	108
Table 3-8: Radionuclides and their half-lives considered in the calculations.....	116
Table 3-9: Radionuclide inflow for the six cases.....	116
Table 3-10: Parameters for Cm, Am, Pu and Th for the six calculation cases for repository conditions.....	117
Table 6-1: Constant test case parameters.....	147
Table 6-2: Variable test case parameters	149
Table 6-3: Evolution of ÄGW (TRUE-1 site, Feature A, KXTT4) element composition during storage in barrel.	155
Table 6-4: Evolution of ÄGW (TRUE-1 site, Feature A, KXTT4) element composition during storage in glove box under anoxic conditions (Ar/1%CO ₂).....	156
Table 6-5: Evolution of ÄGW (TRUE-1 site, Feature A, KXTT4) element composition during storage in glove box under anoxic conditions (Ar/1%CO ₂) contacting with fracture filling material (FFM) ^{a)} , CT:contact time.	157

Table 6-6: Al, Mg, Si, Fe, Ca contents of the MX80-colloid stock solution as determined from 15 ICP-MS measurements.....	158
Table 6-7: Solutions preparation for LIBD analysis, a) IS: ionic strength , b) CT: contact time between MX80 bentonite colloids and FA.	162
Table 6-8: Effect of air contact and pressure release on the element composition evolution of ÄGW (TRUE-1 site, Feature A, KXTT4). The supernatant is analyzed directly or after additional 100 nm filtration. Only iron and lanthanides concentration are significantly affected (La represents hereafter the lanthanides); n.d.: no more measurable/detectable.....	164

1 Introduction

1.1 Scope of this Work

In order to assess the relevance of colloidal influences on radionuclide transport for the long-term safety of a radioactive waste repository, the KOLLORADO project integrates the results of in-vitro (geochemical), in-situ and in-silico (hydrogeological) studies. From the commonly considered set of necessary conditions (colloid presence/generation, their mobility and stability as well as the uptake of radionuclides and the irreversibility of this sorption process) required for a non-negligible impact of colloids on the pollutant propagation [1] the project focuses on the questions of

- (a) colloid generation from compacted bentonite under low saline groundwater conditions (reference repository evolution in [2, 3]),
- (b) nanoparticle mobility and
- (c) Radionuclide uptake/sorption mechanisms and the appropriate implementation of relevant data into a transport code.

Our results provide feedback for the design of future experiments. In particular the Grimsel Test Site Phase VI Project CFM (Colloid Formation and Migration) (<http://www.Grimsel.com/gts-phase-vi/cfm-section/cfm-introduction>) aims towards lower flow rates in order to capture the slow desorption dynamics of tri- and tetravalent actinides from bentonite colloids and to better simulate repository relevant conditions. The concomitant extended durations and the higher overhead in general necessitate a careful choice of parameters. Reactive transport modelling allows to assess the impact of various scenarios which are difficult or too expensive to realise under in-situ conditions. Last but not least our results may serve as a basis for an appraisal of the implications of colloid presence in the vicinity of radioactive waste repositories in different deep geological host-rock formations. To evaluate the variance of groundwaters found in geological host rock formations on the significance of colloid/nanoparticle mobility studies conducted within the SKB/KTH “Colloid project” are also documented in this report as Annex. These particular studies are financed by the Swedish Nuclear Fuel and Waste Management Company (SKB).

1.2 State of the art

Generation of energy by nuclear fission leads to the production of spent fuel elements which contain uranium, plutonium, fission products and the so-called “minor actinides” such as neptunium, americium and curium. The safe disposal of this highly toxic and radioactive waste demands its isolation from the biosphere for several hundred thousand years. Thus, the immobilization of long-lived radionuclides (actinides and fission products) over a geological timescale is the primary aim of nuclear waste disposal. Storage in deep geological formations using a multi-barrier system is currently considered as the most feasible repository concept for high-level radioactive waste in the majority of nations worldwide [4, 5]. The multi-barrier system is composed of the following:

- the waste matrix itself consisting of the spent fuel and its container (technical barrier)
- the geotechnical barrier consisting of the backfill material; this report focuses solely on compacted bentonite, and
- the geological barrier (e.g., salt, granite, clay).

For each of these barriers those processes have to be examined and described which potentially lead to the mobilisation or immobilisation of radionuclides. A variety of processes can take place in the vicinity of the individual barriers (e.g., redox reactions, hydrolysis, sorption/desorption, dissolution/precipitation, colloid formation) and each has to be evaluated. The aim is to determine rates for the immobilisation and/or mobilisation of the radionuclides at the individual barriers and from this it is possible to derive source terms for radionuclide release at the barriers considering various scenarios. The combined source terms allow quantification of the potential release of long-lived radionuclides into the biosphere and hence provide a basis for a geochemically well-founded long-term safety analysis.

The engineered barrier system (EBS) of a deep geological repository for high-level nuclear waste foresees in most concepts [6, 7] the use of bentonite as buffer and backfill material. Bentonite clay has been found to be an appropriate material for the geotechnical barrier of the multi-barrier system due to its swelling properties [8, 9] inhibiting ground water access to the waste canister and retarding radionuclide transport in form of dissolved and colloidal phases (safety functions “sorption” and “colloid filter”) away from the repository near field [10]. However, depending on the physico-chemical conditions (e.g., gas and water pressure, ground water flow velocity) the bentonite barrier may also be eroded by colloid formation [4, 5, 11]. Bentonite colloid erosion has been reported to take place at the interface between the compacted bentonite buffer and granite [12, 13]. These results as well as laboratory bentonite erosion experiments [14] show a dependence of the colloid source term on ionic strength, pH, bentonite compaction and flow velocity. Under certain conditions, as e.g. imperfect backfilling and defects in plugs or fracturing radionuclide transport through the bentonite barrier may be rather quick. Speciation of radionuclides in the groundwater/pore water mixing zone might control in such worst case scenarios the radionuclide mobility in the far-field. The lately heavily discussed scenario of glacial water intrusion [10] estimates a high erosion of bentonite buffer due to the contact with glacial water of high pH and low salinity favoring the release of bentonite colloids/particles. In the framework of the Grimsel Test Site (GTS) Phase VI the international Colloid Formation and Migration (CFM) project with partners from Japan (JAEA, AIST and CRIEPI), Switzerland (NAGRA), Sweden (SKB), Finland (POSIVA), South Korea (KAERI) and Germany (KIT-INE) investigates processes related to this bentonite erosion and the possible formation of colloids. The migration of bentonite colloids and associated radionuclides in the shearzone under investigation in CFM has been demonstrated in earlier studies [15, 16].

Beside the formation/erosion of colloidal material of smectite origin also the neo-formation of colloids due to the geochemical gradients and oversaturation of mixing waters has to be considered. Colloid formation in chemically disturbed environments has been documented in a couple of cases. Acid mine drainage waters show the formation of colloids and the mobility of heavy metals is strongly associated with this colloidal phases [17, 18]. Studies with simulated tank waste solution (TWS) from the U.S. Department of Energy (DOE) Hanford Site (Washington State) showed that the maximum formation of mobile colloids occurred at the plume fronts with calcium carbonate as one of the dominant phases of the plume front colloids [19]. The authors identified the cation exchange process during infiltration of the high- Na^+ TWS solution, with complete replacement of exchangeable $\text{Ca}^{2+}/\text{Mg}^{2+}$ from the sediment caused accumulation of these divalent cations at the moving plume front. Precipitation of supersaturated $\text{Ca}^{2+}/\text{Mg}^{2+}$ - bearing minerals caused dramatic pH reduction at the plume front which triggered, in turn, precipitation of other minerals. Concerning the formation of aluminosilicate colloids laboratory studies have already demonstrated that these newly formed phases can have a significantly influence on the speciation of trivalent actinides [20].

Colloids are known to be ubiquitous in natural ground waters and have been frequently discussed as potential carriers for radionuclides. Colloids show, in comparison with ionic

species, a different migration behaviour: due to their comparatively larger size, charge and low diffusion coefficient the probability to penetrate into matrix pores of the host rock is lower and therefore they may be transported unretarded or in the fastest streamlines of the laminar flow field being faster than the average groundwater velocity monitored by dissolved conservative tracers. Thus, colloid bound contaminants such as radionuclides may interact to a lesser degree with the surface of the host rock minerals and can be transported over considerable distances. Transport of man-made nanoparticles as well as natural occurring radionuclides by colloids has been reported e.g. for the Nevada Test Site, USA [21, 22] and the Whiteshell Research Area, Canada [23].

However, colloids can also be retained by interaction with mineral surfaces or by **agglomeration, sedimentation and filtration**. All processes strongly depend on geochemical parameters, e.g., pH, ionic strength or colloid concentration. Therefore, the colloid stability is a key parameter for colloid facilitated transport. Dynamic light scattering (photon correlation spectroscopy; PCS) is frequently used to determine the coagulation rate and critical coagulation concentration (CCC, for details on the definition see chapter 2.1.3) of various clay colloid suspensions [24-26]. Montmorillonite platelets are the major colloidal particles found to be mobilized from Febex bentonite. Due to their permanent negative face charge originating from isomorphous substitution and their pH dependent edge charge caused by broken tetrahedral and octahedral sheets exposing silanol and aluminol groups [27, 28] three different modes of interactions can be distinguished: edge-face (EF), edge-edge (EE) and face-face (FF). In order to be able to predict montmorillonite colloid stability based on extended DLVO-theory [29, 30] the overall surface potential has to be separated into potentials and interaction modes associated with the edge and face geometry of the montmorillonite platelets and summing up hydration forces, born repulsion, electric double layer repulsion and London - van der Waals attraction. One suitable approach is the geometrical assumption made by Mahmood et al. [31] to calculate the total interaction energy by using a half-cylinder with the radius equal to half the thickness of the montmorillonite platelet (see chapter 2.1.3).

In the **Colloid and Radionuclide Retardation (CRR)** experiment carried out at the Grimsel Test Site (GTS) the in situ migration behaviour of selected radionuclides and chemical radionuclide homologues in the presence and absence of bentonite colloids in a water-conducting shear zone was studied [15, 16]. Under fast flow conditions (~36 m/d) recovery of injected bentonite colloids was in the range of 50-100 %. Related laboratory experiments in granodiorite bore cores from the same site using carboxylated polystyrene (latex) colloids showed colloid recoveries ranging from 10 to nearly 50 % [32] under longer fracture residence times. Similarly low colloid recoveries with increasing residence time were found by other investigators [33]. The authors conclude that even under geochemical conditions where colloids are highly stabilized (low salinity, high pH) adsorption/filtration onto mineral surfaces may occur.

The extent of colloid adsorption on natural mineral surfaces may be influenced by, e.g., the chemical heterogeneity of the mineral surfaces, surface roughness, surface coatings, discrete surface charges (mineral edges and planes), mineral dissolution, the presence of dissolved ions or by matrix diffusion [34-39]. Degueldre et al. [40] carried out sorption experiments at pH 8 ($I = 10^{-2}$ M NaClO₄) with clay colloids and several single minerals (muscovite, biotite, quartz, feldspar) comprising the Grimsel granodiorite and observed considerable colloid adsorption. Alonso et al. [41] studied the interactions between gold colloids and a granite surface by μ -Particle Induced X-Ray Emission (μ PIXE) to determine the amount of adsorbed colloids on different minerals under varying chemical conditions. These authors concluded that adsorption of colloids on rock surfaces is generally determined by electrostatic interactions. However, colloid adsorption was also detected under unfavourable (repulsive) colloid-fracture surface attachment conditions (e.g., alkaline pH). It was suggested that chemical effects may enhance colloid/rock interaction when favourable

(attractive) electrostatic interaction does not exist. Furthermore, theoretical studies have been performed to calculate surface charge heterogeneity effects (e.g., [42]). These effects have also been experimentally evaluated, e.g. for Cu ion adsorption onto silica [43].

1.3 Aims and Approach

Laboratory program. The laboratory program conducted within the project KOLLORADO aimed on deriving data on **(a) colloidal stability, (b) potential sources of colloid formation, (c) colloid- radionuclide interaction and (d) colloid attachment/retention mechanism.** This will be elaborated in detail below:

To a): The work on colloid stability focused on:

- ⇒ Febex bentonite derived montmorillonite colloid stability determined by means of PCS under variation of pH, ionic strength, contact water cation composition (Na^+ , Ca^{2+}) and dissolved organic matter (fulvic acid).
- ⇒ The montmorillonite pH dependent edge-charge estimation by zeta-potential measurements using the recalculation method proposed by Williams and Williams [44] for different ionic strengths and
- ⇒ Comparison of experimental determined stability ratio W to model predictions using the DLVO approach published by Mahmood et al. [31].

To b): Concerning the formation of colloids at the interface between the bentonite buffer/backfill and the host rock formation two aspects are investigated in detail within the KOLLORADO project:

- ⇒ The potential formation of colloidal phases in the mixing zone between bentonite porewater and the host rock groundwater as a function of admixture of Febex bentonite pore water. Characterization of these colloidal phases by laser-induced breakdown detection (LIBD), ultrafiltration, ICP-MS, SEM-EDX and speciation of radionuclides by time resolved laser fluorescence spectroscopy (TRLFS).
- ⇒ Colloid formation through colloidal release from the compacted bentonite as a function of contact water geochemistry, confining plate pore size, and saturation state. The results are discussed in the light of the contact water composition changes and compared to the bentonite critical coagulation concentration (CCC) determined previously in batch-type coagulation studies (see chapter 2.1.3).

To c): Data sets of radionuclide desorption from montmorillonite colloids performed within the CRR project focused on short time scales capturing the fracture residence times of the in situ experiments. To gain knowledge about the long-term radionuclide-colloid-rock interaction the experimental program within KOLLORADO focused on considerable longer time-scales (weeks to months) with two different approaches:

- ⇒ Batch-type studies in the ternary system bentonite colloids – fracture filling material (FFM) and radionuclides (Am(III) , Np(V) , Pu(IV) , U(VI) , Tc(VII) , Cs(I)). Within this experimental program the FFM size fraction was varied. The results of the Grimsel groundwater/FFM system are compared to results with fracture filling material and groundwater (KXTT) from the Äspö HRL.
- ⇒ Indirect evidence of bentonite colloid metal sorption reversibility is also obtained from migration experiments and desorption rates are compared.

To d): From the present status of knowledge as given in chapter 1.2, binding mechanisms of negatively charged colloids on natural mineral surfaces are not sufficiently understood. It can be expected that electrostatic interaction will dominate colloid adsorption. However, it is not clear if additional binding mechanisms are present, especially under unfavourable (repulsive) electrostatic conditions. The work conducted within KOLLORADO intended to answer this open question based on the following approach (see chapter 2.1.5):

- ⇒ Adsorption experiments with carboxylated (negatively charged) fluorescent polystyrene colloids on natural Grimsel granodiorite fracture filling material and its single component minerals by fluorescence microscopy and mineral phase characterization by SEM/EDX.
- ⇒ Atomic Force Microscopy (AFM) force spectroscopy measurements under varied geochemical conditions to measure interaction forces between model colloid and mineral surfaces.
- ⇒ Comparison of experimental results with theoretically calculated force curves based on DLVO theory in order to develop an approach to predict colloid-surface interaction.
- ⇒ Upscaling of colloid-fracture surface interaction via macroscopic data derived from migration experiments in laboratory bore cores and in situ migration tests under variation of tracer residence times in a natural water conducting fracture.

Modeling. One goal is to shed light on the multitude of different interaction forms and paths between radionuclides, colloids and the sediment matrix. Special interest was on the consequences of kinetically controlled adsorption and desorption processes. To this end, laboratory geochemical data as measured by KIT-INE were interpreted in terms of known theories assessing thereby the contribution of the processes involved.

The sorption and filtration parameters extracted in the analysis provide necessary input for transport calculations. Having calibrated the hydrogeological parameters with tracer data, the thus configured problem is then employed to make predictions for the migration of radionuclides and colloids, which are in turn compared to respective experiments in order to validate the models. Furthermore, we perform artificial variations of the hydrogeological conditions and interaction parameters as well as extrapolations to safety case relevant time and spatial scales.

For the computer simulations a 2D as well as a 1D-transport code was used. This enables us to investigate the influence of dimensionality and complex flow fields on the form of the breakthrough curve. In particular, we intend to separate these effects from matrix diffusion. To the end colloidal transport and sorption effects were integrated into the 2D version of the program *r³t*. While the simulation of the CFM experiment in two dimensions leads to realistic run times, the computing demands of repository scale calculations force us to fall back on our 1D code TRAPIC [45, 46].

During the first phase of the CFM project, a series of tracer tests have been performed to evaluate suitable flow fields for long-term colloid migration experiments within the fractured shear zone. The modelling work investigates also the long-term flow and the transport of tracers in the fractured shear zone at two different locations where in-situ colloid and radionuclides migration experiments are planned to take place. The calculations were carried out using the finite element code ADINA-F [47]. The main objectives of the numerical analyses are:

- ⇒ Estimation of the flow and transport parameters from GTS hydraulic tests.
- ⇒ Numerical simulations of uranine tracer tests to support the in situ measurements [1].

2 Experimental Program

2.1 Laboratory program

2.1.1 Radionuclide Speciation in the groundwater porewater mixing zone

Abstract. The engineered barrier (bentonite) of the deep geological repository will be in contact with the host rock formation and consequently it can be expected that bentonite porewater will mix with formation groundwater. We simulate in this study the mixing of Grimsel groundwater (glacial melt water) with synthetic Febex porewater (assuming already saturated state) in a batch-type study and investigate the formation of colloids by laser-induced breakdown detection (LIBD) and SEM-EDX as well as the changes in radionuclide (U, Th, Eu) speciation via ultrafiltration or via time-resolved laser fluorescence spectroscopy (TRLFS) analysis in the case of Cm(III). Based on PHREEQC saturation index (SI) calculations a precipitation of calcite might be expected at low Febex porewater (FPW) admixtures (< 20%), fluorite precipitation at FPW admixtures < 60% and gibbsite precipitation at FPW admixtures above 10%. The colloids generated in the mixing zone aggregate when the synthetic FPW admixture exceeds > 10%. LIBD analysis of the time-dependent colloid generation/aggregation revealed a low concentration of colloids to be stable with an estimated plateau value around 100 ppt and an average colloid diameter around 30 nm after 70 days reaction time at Febex porewater admixtures > 10%. SEM/EDX mostly identifies Si/Al containing colloidal phases. TRLFS studies show that the Cm speciation is strongly influenced in the Febex pore water/Grimsel groundwater mixing zone at low Febex porewater admixtures (<20%) by colloid formation and Cm is almost quantitatively associated with colloidal phases.

Materials & Methods

The synthetic Febex bentonite pore water used throughout this study was freshly prepared according to the composition defined within the ACTAF project for saturated Febex bentonite [48] adjusted to pH 7 to avoid carbonate precipitation. The Grimsel groundwater used throughout this study was freshly sampled on the 22nd of May 2006 in Argon pre-flushed 50L Teflon coated stainless steel barrels. The barrel volume was exchanged eight times over a period of one day to avoid any artificial colloids from tubing, by fracture surface erosion or remaining dust in the barrel.

Two types of experiments were conducted with radionuclides and chemical radionuclide homologues, respectively:

- (1) For the colloid analysis via LIBD and separate SEM investigation on 50 nm track etch filter (Whatman Inc.) the Febex pore water solution was spiked with Eu(III), U(VI) and Th(IV) solution to obtain a concentration of $1 \cdot 10^{-8} \text{ mol} \cdot \text{L}^{-1}$ for each element. Afterwards, Grimsel groundwater (GGW) was added to the spiked Febex pore water in different admixture ratios. Analysis of the waters was performed by ICP-MS and ion chromatography after mixing.
- (2) For TRLFS studies, the Febex bentonite pore water was spiked with $9 \cdot 10^{-8} \text{ mol/L}$ ^{248}Cm and different aliquots of GGW water added. Only in those studies where we varied the pH of GGW the Cm was directly added to GGW. Selected samples were ultra-centrifuged for 60 minutes at 90,000 rpm (692,000g) to separate the colloidal fraction and fluorescence emission spectra were recorded in the colloid containing dispersion and the supernatant after centrifugation.

Geochemical modeling was performed with the program PHREEQC Version 2 [49] using the wateq4f database (23. Aug. 2005). Mixing simulation was obtained by the mix flag using different ratios of the two end member solutions GGW and Febex pore water. Colloid analysis was performed by a laser-induced breakdown detection (LIBD) system. The LIBD method and modes of calibration against reference polystyrene colloids and data evaluation are described elsewhere [50, 51]. Reaction vessels of PFA (perfluoro-alkoxyalkane) type were used. The vessels are directly connected via tubing to the quartz flow through cuvette of the LIBD equipment. To prevent any contamination by dust particles the air inlet is equipped with a 0.2µm filter. Additionally, water samples were filtered by Microsep ultrafiltration units ranging from 1 kDa to 1000 kDa and 50 nm Whatman track etch filter (for SEM-EDX analysis). The Cm speciation analysis in mixing waters and pure Grimsel groundwater or synthetic Febex pore water under variation of pH is made by TRLFS. Cm is used as a chemical probe for trivalent actinides due to its superior fluorescence properties compared to Am [20, 52-54]. $9 \cdot 10^{-8} \text{ mol} \cdot \text{L}^{-1} \text{ }^{248}\text{Cm}$ is added to Febex pore water solution. Cm is excited at one of its prominent absorption bands at 396 nm [52-54]. Details on the spectroscopic setup are given elsewhere [55].

Results & Discussion

Geochemical modeling results. Simulation of the Grimsel groundwater/ Febex pore water mixing zone by PHREEQC shows a strong pH gradient at low Febex pore water/Grimsel groundwater ratios up to approximately 30% before it levels off. In the same region also the highest changes in cation composition could be detected. Interestingly, the oversaturation (saturation index $SI > 0$) for calcite as well as for fluorite indicates that these phases might be formed in this range of low Febex pore water admixture. The Febex pore water is in equilibrium with quartz and under-saturated with respect to chalcedony, whereas it is clearly oversaturated with respect to gibbsite. It is interesting to notice that the simulation of different pore water/Grimsel groundwater ratios prognoses the potential formation of mineral phases that might re-dissolve with further increase of groundwater content, a phenomenon that has been seen in waste plume fronts [19]. Overall the calculations show that the mixing zone can be seen as a very dynamic environment with respect to mineral formation/dissolution processes. Based on the calculated saturation indices a formation of colloidal phases cannot be ruled out.

Colloid analysis by laser induced breakdown detection (LIBD) and SEM-EDX. The investigations on the evolution of the colloid concentration and average colloid size monitored by LIBD over a period of 70 d are presented in Figure 2-1. For the calculation of the colloid concentration a spherical shape and a mean mineral density of $2.2 \text{ g} \cdot \text{cm}^{-3}$ is assumed. In solutions with 10% Febex pore water the colloid concentration (~10ppb) as well as the mean colloid diameter ($152 \pm 18\text{nm}$) remain almost unchanged over the period of 70 d. The synthetic Febex pore water shows initially the highest colloid concentration and colloid size with 360 ppb and ~660 nm, respectively. However, with time a clear decrease in colloid concentration and colloid size can be observed indicating that the colloids found in the synthetic Febex porewater are probably impurities of the chemical used for preparation, which obviously sediment or dissolve with time. Colloid population in all solutions with variable pore water/groundwater ratios except for that with only 10% Febex pore water seem to converge over time to a stable concentration and colloid size under the conditions investigated. This plateau values can be estimated around 100 ppt for the colloid concentration and around 30 nm for the colloid diameter.

The impact of colloids on trace element speciation can be roughly estimated from the colloid characterization study discussed above. The colloidal surface area estimated from spherical colloids with a diameter of 30 nm and a colloid number concentration of $1.8 \cdot 10^6 \pm 1.1 \cdot 10^6 \text{ mL}^{-1}$

determined by LIBD for the final colloid concentration in high ionic strength solutions would be at maximum $8.2 \cdot 10^{-6} \text{ mL}^{-1}$. Assuming 7.49 sites/nm^2 for montmorillonite [56] approximately $6.2 \cdot 10^{13} \text{ sites}$ ($\sim 9.7 \cdot 10^{-11} \text{ mol}$) per liter would be available for metal complexation.

Further studies focused on the morphology and chemical analysis of colloidal material by SEM and EDX. Samples were filtered through filters with 50 nm poresize ca. 3h after mixture, after one day and after seven days. Interestingly, the morphology of the colloids formed during the reaction process changes greatly in the solution with 10% Febex pore water. Whereas at higher Febex porewater content typically large colloids/particles with well defined shape can be found, the sample with 10% porewater shows a high content of not well defined cloudy, round-shaped structures. EDX spectra analyses do not directly confirm the geochemical modeling results where a oversaturation with respect to gibbsite is expected in the range $> 15 \%$ Febex porewater content. One has, however, to state clearly, that the colloids potentially formed at higher synthetic Febex pore water content are not colloiddally stable and aggregate as can be seen in the LIBD analysis (Figure 2-1). These newly formed colloids can however influence the speciation of radionuclides.

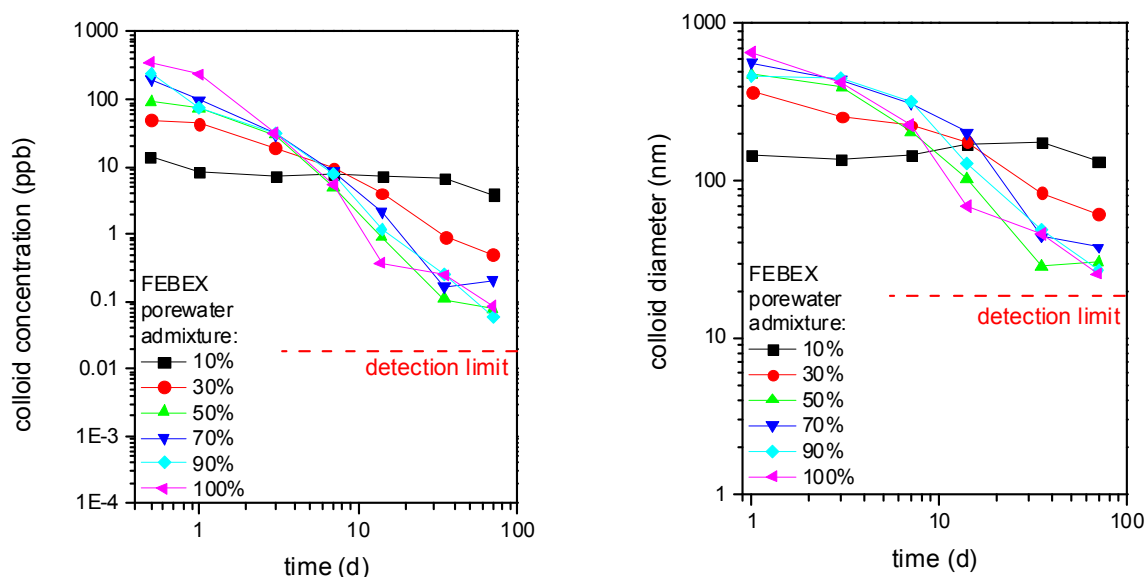


Figure 2-1: Time dependent evolution of colloid concentration and average colloid size as measured by laser-induced breakdown detection (LIBD). The dashed line indicates the detection limit of LIBD.

Radionuclide speciation. The synthetic Febex pore water was spiked with Eu(III), U(VI) and Th(IV) in a concentration of $1 \cdot 10^{-8} \text{ mol} \cdot \text{L}^{-1}$ for each element prior to Grimsel groundwater admixture and analysis by LIBD and SEM-EDX. According to the radionuclide speciation and solubility calculations performed for the synthetic Febex porewater used throughout this study [55], metal concentrations lie below the calculated solubility limit for Am(III) of $4 \cdot 10^{-6} \text{ mol} \cdot \text{L}^{-1}$ (solid phase $\text{NaAm}(\text{CO}_3)_2$) and U(VI) of $10^{-4} \text{ mol} \cdot \text{L}^{-1}$ (solid phase schoepite) and $4 \cdot 10^{-7} \text{ mol} \cdot \text{L}^{-1}$ (solid phase: $\text{Th}(\text{OH})_4$). The solution speciation is dominated by AmCO_3^+ , Am^{3+} , $\text{Th}(\text{OH})_3\text{CO}_3^-$, $\text{Th}(\text{OH})_{4\text{aq}}$ and $\text{UO}_2(\text{CO}_3)_3^{4-}$, $\text{UO}_2(\text{CO}_3)_2^{2-}$ in the Febex porewater and by $\text{Am}(\text{CO}_3)_2^-$, $\text{Am}(\text{OH})_2^+$, $\text{Th}(\text{OH})_3\text{CO}_3^-$, $\text{Th}(\text{OH})_{4\text{aq}}$ and $\text{UO}_2(\text{OH})_3^-$, $\text{UO}_2(\text{CO}_3)_3^{4-}$ in the GGW ($E_h = -70 \text{ mV}$) [55], respectively. Eu(III) and Cm(III) have been chosen in our work as chemical homologues to Am(III). Thermodynamic data for the aquatic chemistry are very similar for all those trivalent metal ions.

In order to check this estimate, ultrafiltration experiments are performed. Sample aliquots were directly ultra-filtered after mixture and analyzed by ICP-MS. Unfortunately, the sample volume allowed only a single filtration per filter size and therefore an error analysis cannot be performed. The ultrafiltration results (Figure 2-1) show that U(VI), as expected from the speciation calculation, is occurring as dissolved species and passes even the 1 kDa filter to more than 70 % in all experiments. The Th(IV) speciation seems to be dominated by large colloids. In all mixed solutions Th does not pass the 1000 kDa filter to more than 10 %. Ultrafiltration results for the sample containing 10 % pore water admixture are not shown, as Th and Eu concentrations in analysed samples are close to the detection limit of ICP-MS (samples had to be diluted prior to analysis due to insufficient sample volume and high dissolved solid concentrations). For solutions containing 30% to 90% pore water, the Eu(III) concentration filtered by 1000 kDa varies between 30 % to 50 % and the fraction filtered by the 1 kDa filter between 35% to 80%, respectively. Due to the strong changes in the pH value at different pore water admixture stages and the rather dilute solutions filtered, a strong interaction of Th(IV) and Eu(III) with sorption sites of the polyethersulfone membrane can not be excluded. This observation has already been made in earlier Th(IV) solubility studies comparing the ultrafiltration and ultracentrifugation method to separate Th(IV)-eigencolloids under different ionic strengths [56] . The experimental results suggest significant amounts of colloid-bound Th(IV) and Eu(III), even though ultrafiltration has to be considered very carefully under given conditions.

To further elucidate the speciation of trivalent actinides/lanthanides in the Grimsel groundwater/ synth. pore water mixing zone, time-resolved laser fluorescence spectroscopy (TRLFS) using Cm^{3+} as a fluorescence probe were applied. TRLFS provides speciation information through emission spectra and fluorescence relaxation. Fluorescence lifetimes can be correlated to the number of H_2O molecules in the metal ion hydration sphere through an empirical relationship. The hydration sphere of the non-complexed aquo ion contains 9 H_2O molecules and the corresponding fluorescence lifetime is at 65 μs . In a first step the end members Grimsel groundwater and synthetic Febex pore water were investigated under variation of the pH value in the range from pH 7.0 to 9.6. The pH variation in GW from 9.6 to 7 does not change significantly the shape or peak position of the fluorescence emission spectra with a maximum varying between 602.1nm and 602.8nm. At a first glance this is somewhat surprising as the speciation calculation predicts a change of the speciation from 42% $\text{Cm}(\text{CO}_3)_2^-$, 37% $\text{Cm}(\text{OH})_2^+$ and 16% $\text{Cm}(\text{CO}_3)^+$ at pH=9.6 to 48% Cm^{3+} , 27% CmF_2^+ and 20% $\text{Cm}(\text{OH})_2^+$. The predicted predominant aquo ion at pH=7 with an emission band maximum at 593.8 nm is not visible in the spectrum. All spectra show instead broad emission bands suggesting the coexistence of several species, however, rather independent of pH. In earlier studies, we have already discussed the Cm-speciation in Grimsel groundwater [15]. From combined ultracentrifugation and spectroscopy, the mainly colloidal character was stated. Our present study confirms this observation. Obviously, the Cm-species formed at high pH (=9.6) do not reequilibrate when pH is adjusted to 7 within hours. This points to rather slow reaction kinetics which is also expected in the presence of colloidal species. Measured fluorescence lifetimes showing multi-exponential decay and relatively long lifetimes point to the existence of colloidal species comparable to the Cm-silicate(II) species found in Panak et al. (2005) [58]. In the case of the Febex pore water the existence of Cm aquo ions at pH=7 and carbonate complexes at higher pH are deduced from spectra. However, lifetimes up to ~410 μs at pH=9.6 point again to the existence or co-existence of colloidal Cm species.

In a second step the fluorescence emission spectra of mixed solutions containing different pore water/groundwater ratios were measured and the respective spectra directly compared with those obtained in the end member solutions at the same pH value (Figure 2-2). In the solution containing $\geq 30\%$ pore water the fluorescence emission spectra for the mixed solutions and the pure Febex pore water solution are comparable. Interestingly, at lower pore

water contents (10-15%) the fluorescence emission spectra deviate significantly from end member spectra at given pH. The fluorescence decay in those solutions contains lifetimes components up to $\sim 200 \mu\text{s}$ compared to $\tau=80 \mu\text{s}$ measured in the porewater. At higher groundwater content lifetimes decrease to 140-170 μs . For Cm surface complexes such as $\equiv\text{Al-O-Cm}^+(\text{OH})_x(\text{H}_2\text{O})^{(5-x)}$ species found for Cm bound to α -alumina colloids [58] at high pH (peak maxima at 601.2nm and 603.3nm) and Cm-clay mineral surface complexes [58, Rabung et al. 2005) values for fluorescence lifetimes lie around 110 μs . Cm bound to hydroxyl-aluminosilicate (HAS) colloids (named Cm-HAS(II) in [20]) shows a lifetime of $88.3 \pm 5.2 \mu\text{s}$ and the maximum of the fluorescence emission is at 601.8 nm. The Cm-HAS(III) species found at higher pH is characterized by a peak maximum at 606.8 nm and a long fluorescence lifetime of $518 \pm 25 \mu\text{s}$ indicating complete incorporation of Cm into the colloid matrix with only $0.4 \pm 0.5 \text{ H}_2\text{O}$ molecules left in the Cm hydration sphere. Considering pure silicate systems, the colloidal Cm-silicate(II) complex found in [59] at $\text{pH} > 7$ has a peak maximum at 603.2 nm and a lifetime of $198.2 \pm 7.2 \mu\text{s}$ (2.4 ± 0.5 hydration water molecules), which is quite comparable to what we find in our mixed solutions with pore water contents of 10-15%. This species is attributed to Cm bound to silicate polymers, which have been observed to form even in silicate solutions being clearly undersaturated with regard to amorphous silica ($2.7 \times 10^{-4} \text{ mol/L Si}$) at $\text{pH} > 5$ [59]. Si concentrations in our solutions lie in the same range at 10^{-4} mol/L . To verify the Cm-colloid association the samples with 10% and 15% porewater content were ultracentrifuged to separate the colloidal fraction and the supernatant was measured by TRLFS. The fluorescence intensity almost disappeared in the supernatant of the solution containing 15% porewater indicating an almost quantitative association of Cm with colloidal phases. Additional tests performed with a higher (85%) porewater content still revealed association with colloids, however not complete. Fluorescence lifetime measurements in the supernatant of this sample showed monoexponential decay with short lifetimes in the range of $65 \pm 5 \mu\text{s}$. The calculated aquatic Cm-speciation is 10 % Cm^{3+} , 84% $\text{Cm}(\text{CO}_3)^+$ and 4% $\text{Cm}(\text{CO}_3)_2^-$ with associated τ -values of 64, 79 and 89 μs for the individual complexes. The lifetime measured in our experiments represents an average value. Carbonate complexes are known to have a ligand exchange rate faster than fluorescence relaxation so that observed emission life times in aqueous carbonate solutions are always monoexponential. Emission bands are also in agreement with the predominant existence of $\text{Cm}(\text{CO}_3)^+$ ($\lambda_{\text{max}}=598.5 \text{ nm}$).

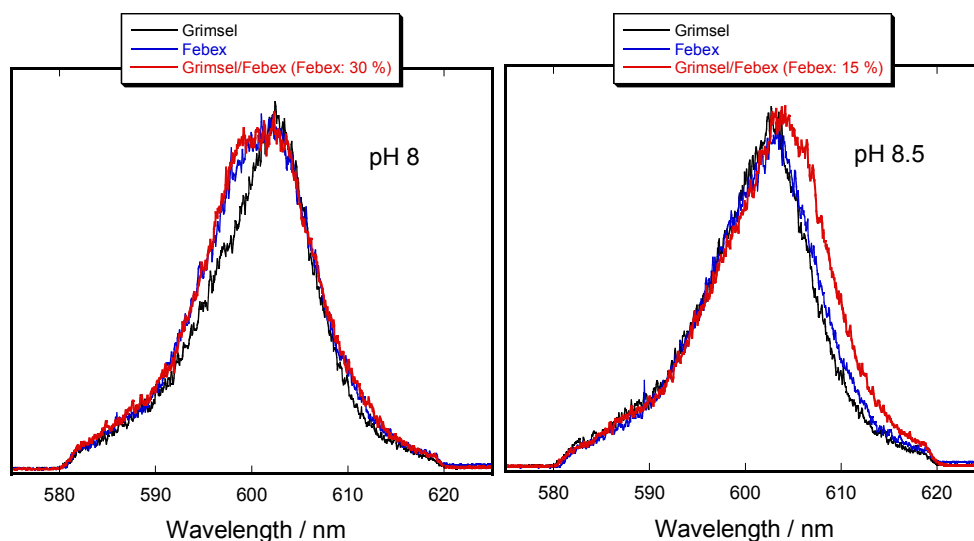


Figure 2-2: Comparison of TRLFS emission spectra taken of the end members Grimsel groundwater and synth. Febex pore water at pH 8 and 8.5 with spectra taken in mixed solutions at the same pH value. Percentage of Febex pore water admixture is 30 % (left) and 15 % (right), respectively.

Conclusions. The following conclusions can be drawn:

- Based on the PHREEQC saturation index (SI) calculations a precipitation of fluorite, calcite and gibbsite might be expected in the bentonite porewater/ Grimsel groundwater mixing zone.
- A low concentration of colloids with a estimated plateau value around 100 ppt after 70 days and colloid diameter around 30nm could be observed under the experimental mixing conditions.
- The colloids generated in the mixing zone aggregate when the pore water admixture to the groundwater exceeds > 10%.
- SEM/EDX mostly identifies Si/Al containing phases to be formed in mixing solutions.
- TRLFS studies show that the trivalent actinide speciation is strongly influenced in the Febex pore water/GGW mixing zone at low Febex pore water content via colloid formation and an almost quantitatively association to neo-formed colloids.

Further details to the study presented in this chapter can be found in:

- Kunze P., Seher H., Hauser W., Panak P. J., Geckeis H., Fanghänel T., and Schäfer T. (2008) The influence of colloid formation in a granite groundwater bentonite pore water mixing zone on radionuclide speciation. *Journal of Contaminant Hydrology* **102**, 263-272.

2.1.2 Sorption reversibility studies: Comparison of fracture filling material (FFM) from Grimsel (Switzerland) and Äspö (Sweden)

Abstract. Desorption kinetics of radionuclides from bentonite colloids and a possible subsequent sorption onto fracture filling material can influence colloid-facilitated radionuclide migration in groundwater. To shed light on the significance of these issues batch-type experiments using a cocktail of strongly and weakly sorbing radionuclides containing FEBEX bentonite colloids in the presence of fracture filling material from Grimsel and Äspö under Grimsel groundwater conditions have been conducted. Results show that tri- and tetravalent radionuclides, $^{232}\text{Th}(\text{IV})$, $^{242}\text{Pu}(\text{IV})$ and $^{243}\text{Am}(\text{III})$ are clearly colloidal associated in contrast to $^{233}\text{U}(\text{VI})$, $^{237}\text{Np}(\text{V})$ and $^{99}\text{Tc}(\text{VII})$. $^{232}\text{Th}(\text{IV})$, $^{242}\text{Pu}(\text{IV})$ and $^{243}\text{Am}(\text{III})$ concentrations decrease after ~ 100h showing bentonite sorption reversibility kinetics while $^{233}\text{U}(\text{VI})$ and $^{99}\text{Tc}(\text{VII})$ concentrations remain constant over the experimental time thus showing no sorption to the fracture filling material. In the case of $^{237}\text{Np}(\text{V})$, a decrease in concentration after ~300h is observed which can be explained either by a slow reduction kinetic to Np(IV) in accordance with the experimental pe/pH conditions reached and/or with a slow sorption kinetic on the fracture filling material. No influence of the different Grimsel fracture filling material size fractions (0.25-0.5mm, 0.5-1mm and 1-2mm) can be observed through comparison of surface normalized Kd values implying an independence of the kinetic processes under the given volume to mass ratio used throughout this study. The driving force of the observed reversibility could be the excess of FF material surface compared to the available surface area of introduced FEBEX colloids (76 to 1).

Materials & Methods

Fracture filling material characterization. A thorough mineralogical and chemical analysis of the Äspö diorite can be found in the literature, e.g. [57]. Here, only the most important features are summarized. From a petrological and mineralogical point of view, the Äspö “diorite” can be classified as a medium-grained and porphyritic quartz monzodiorite/

granodiorite with K-feldspar phenocrysts (1-2 cm) [57]. The Äspö diorite comprise of plagioclase, K-feldspar, biotite and calcite as major minerals and of muscovite, titanite, apatite, fluorite, zircon and opaque phases (mostly Fe-containing phases, e.g. magnetite) as accessory components. The Grimsel materials consist mainly of quartz, feldspar and micas. Further informations about the mineralogical, petrologic and geochemical composition can be found inter alia [58, 59]. For the batch type sorption studies fracture filling material (FFM) was crushed, sieved and freeze dried under atmospheric conditions. Three different size fractions, namely 0.25-0.5mm, 0.5-1mm and 1-2mm of the Grimsel FFM have been separated. The main part of the batch-type experiments concerning the Grimsel FFM is on the 1-2mm fraction. The Äspö FFM was taken at the Äspö-HRL. The material was also crushed and sieved and a size fraction of 0.5-1 mm was isolated and washed several times with ÄGW under anaerobic conditions (Ar). Fracture filling material from both sites has been characterized by scanning electron microscopy (SEM), energy dispersive x-ray microanalysis (EDX) as well as X-Ray diffraction (XRD) prior to the experiments. Figure 2-3a and b show SEM pictures of the Äspö FFM consisting of angular and sub-rounded shaped grains with heterogeneous and rough surfaces. EDX spectra of the Äspö FFM confirm the presence of alumina-silica oxide phases like e.g. feldspar and plagioclase. Grimsel FFM grains are characterized by a more angular morphology than the Äspö FFM which can be seen in Figure 2-3c and d. In accordance with the Äspö FFM rough heterogeneous grain surfaces are observed for the Grimsel FFM by the SEM pictures. As for the Äspö material the EDX spectra show mainly quartz grains and spectra for sheet-silicates, most likely of biotite-type.

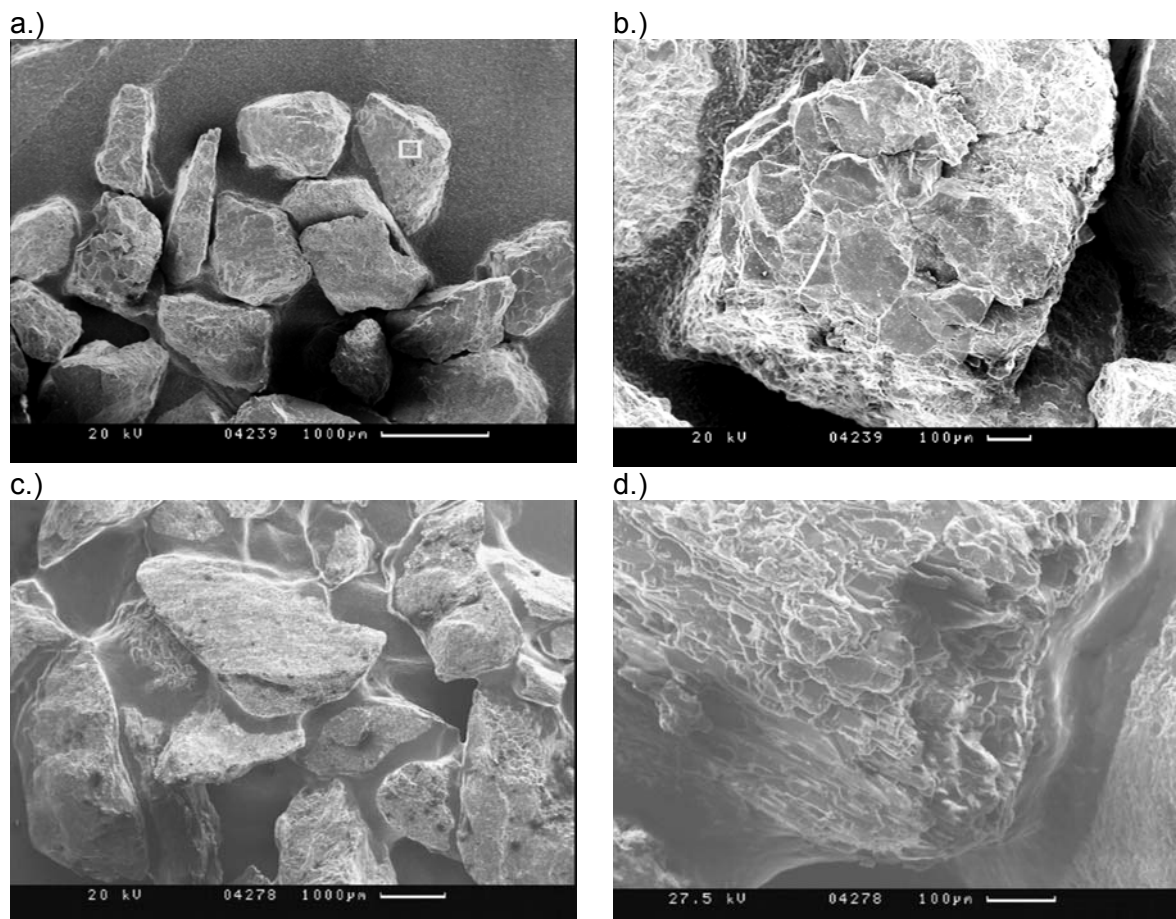


Figure 2-3: SEM pictures of the Äspö FFM [a.) and b.)] and of the Grimsel FFM [c.) and d.). The sizes fraction of the material is between 0.5 and 1 mm.

Specific surface areas of the different size fractions in case of the Grimsel FFM and of the Äspö FFM were determined by BET N_2 -adsorption. The samples were heated to 300°C and degassed. The determination of the surface was done via multiple point analysis and a subsequent fit with the BET isotherm. In all BET measurements care was taken to have sufficient total surface ($> 1m^2$) for reliable measurements. Specific surface area measurements (BET) for the 0.25-0.5mm, 0.5-1mm and 1-2mm Grimsel size fractions yielded values of 0.238m²/g, 0.187m²/g and 0.153-0.166m²/g, respectively. BET analysis for the Äspö FFM revealed a slightly higher specific surface area of 0.259 m²·g⁻¹ compared to the Grimsel materials which is approximately four times higher compared to independent literature data yielding a value of 0.05 m² g⁻¹ for fine grained granite of the size fraction 0.5 to 1mm [57].

Febex bentonite colloid characterization. For the experiments the FEBEX (full-scale engineered barrier experiment) bentonite from the deposit of Cabo de Gata, Almería (Spain) is used [60]. It is described as a smectite-rich bentonite [61]. The bentonite was sieved to obtain the $<63\mu m$ size fraction and equilibrated with 1 mol·L⁻¹ NaCl to transfer the bentonite to its mono-ionic Na-form. The sodium exchanged bentonite is washed with de-ionized (Milli-Q) water to remove excess salt after one week equilibration time. The suspension is centrifuged at 4,000 rpm (3360g) for 40 min. Afterwards the supernatant is discarded and the settlement re-suspended in Milli-Q water. This washing cycle is repeated three times. Each washing step is checked by electrical conductivity measurements and the final electrical conductivity after all washing cycles was 1.9 $\mu S\cdot cm^{-1}$. The final supernatant, containing bentonite colloids, is taken as a colloid stock dispersion and stored in a refrigerator until experiments were performed. The extracted colloidal fraction consists quantitatively of montmorillonite as proved by XRD analysis. The bentonite colloid concentration is determined via alumina ICP-MS measurements. Taking into account the structural formula of FEBEX bentonite given in [60], the bentonite colloid concentration could be calculated to be 640 mg·L⁻¹. The morphology of the Febex bentonite colloids was probed by AFM. A representative example is shown in Figure 2-4: A. The width of the particle is approx. 150 nm and the height approx. 2.25 nm resulting in a considerable lower aspect ratio than 1:10 found by [51].

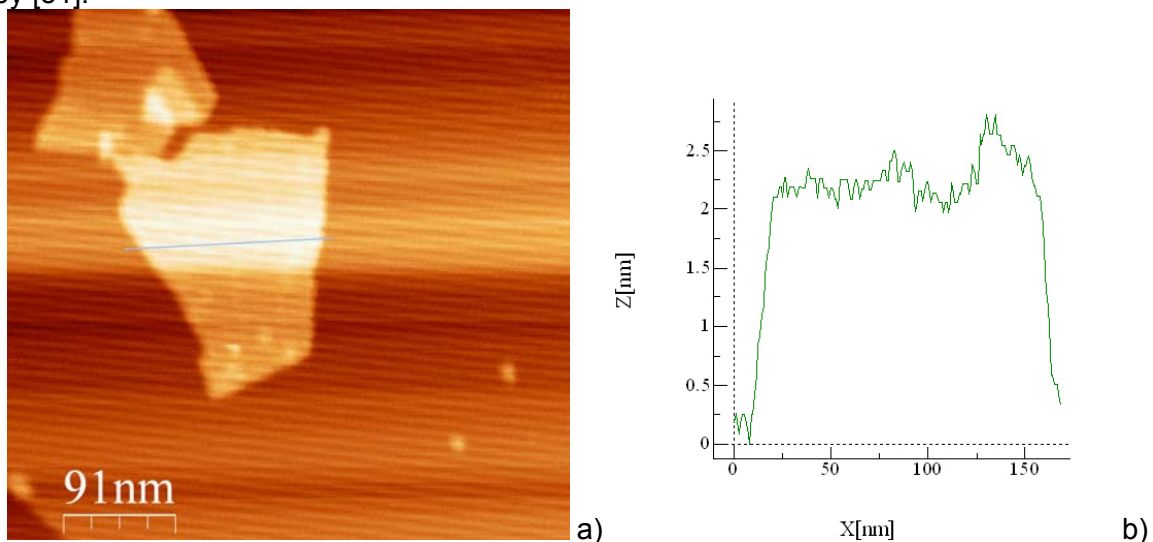


Figure 2-4: AFM picture of Febex bentonite colloids. The line in (a) represents the height profile shown in (b).

Chemical characterization of contact water evolution. In the present investigations Grimsel groundwater was used which was stored in Teflon coated aluminum barrels under argon atmosphere prior to the experiments. Water chemistry was analyzed via ICP-MS and colloid concentrations determined by laser-induced breakdown detection (LIBD). The chemical

composition is listed in [62]. Background colloidal concentration was determined to be around ~20ppb. The concentration of $[M^{2+}]$ ~0.25mM in the batch experiment contact water (Table 2-1) is below the critical coagulation concentration [CCC] of ~1mM for bentonite colloids as documented in [2] and this was used as milestone to start with the migration experiments. The 168h contact water solution with Grimsel FFM seems to be contaminated with Si/Al containing colloidal phases containing also La^{3+} , whereas the alumina concentration in all contact waters with Äspö FFM is considerably increased indicating a possible dissolution of Al containing phases under the alkaline pH of the GGW.

Table 2-1: Chemical composition of the original Grimsel groundwater (GGW) and after different contact time with Grimsel/Äspö FFM in the batch-type experiments.

	Grimsel GW (MI shearzone)	Grimsel FFM	Grimsel FFM	Grimsel FFM	Äspö FFM	Äspö FFM	Äspö FFM
Contact time	12.2.08*	24h	168h	500h	24h	168h	500h
pH	9.67	9.72	9.66	9.68	9.79	9.72	9.64
$E_{h(SHE)}$	n.d.	62	39	35	45	12	-5
$[Mg^{2+}]$	12.6 $\mu g \cdot L^{-1}$	42.2 $\mu g \cdot L^{-1}$	3.9 $mg \cdot L^{-1}$	35.6 $\mu g \cdot L^{-1}$	92.2 $\mu g \cdot L^{-1}$	74.3 $\mu g \cdot L^{-1}$	160 $\mu g \cdot L^{-1}$
$[Ca^{2+}]$	5.3 $mg \cdot L^{-1}$	5.3 $mg \cdot L^{-1}$	6.1 $mg \cdot L^{-1}$	6.5 $mg \cdot L^{-1}$	5.6 $mg \cdot L^{-1}$	5.8 $mg \cdot L^{-1}$	6.3 $mg \cdot L^{-1}$
$[Fe^{2+,3+}]$	< D.L.	< D.L.	7.5 $mg \cdot L^{-1}$	< D.L.	< D.L.	< D.L.	134 $\mu g \cdot L^{-1}$
$[Mn^{2+}]$	< D.L.	0.17 $\mu g \cdot L^{-1}$	141 $\mu g \cdot L^{-1}$	0.17 $\mu g \cdot L^{-1}$	1.3 $\mu g \cdot L^{-1}$	3.4 $\mu g \cdot L^{-1}$	6.5 $\mu g \cdot L^{-1}$
$[Sr^{2+}]$	182 $\mu g \cdot L^{-1}$	157 $\mu g \cdot L^{-1}$	180 $\mu g \cdot L^{-1}$	214 $\mu g \cdot L^{-1}$	148 $\mu g \cdot L^{-1}$	174 $\mu g \cdot L^{-1}$	203 $\mu g \cdot L^{-1}$
$[Cs^+]$	0.79 $\mu g \cdot L^{-1}$	0.02 $\mu g \cdot L^{-1}$	0.7 $\mu g \cdot L^{-1}$	0.03 $\mu g \cdot L^{-1}$	0.01 $\mu g \cdot L^{-1}$	0.03 $\mu g \cdot L^{-1}$	0.04 $\mu g \cdot L^{-1}$
$[La^{3+}]$	< D.L.	0.03 $\mu g \cdot L^{-1}$	0.68 $\mu g \cdot L^{-1}$	0.02 $\mu g \cdot L^{-1}$	0.08 $\mu g \cdot L^{-1}$	0.08 $\mu g \cdot L^{-1}$	0.05 $\mu g \cdot L^{-1}$
[U]	n.d.	0.55 $\mu g \cdot L^{-1}$	0.48 $\mu g \cdot L^{-1}$	0.47 $\mu g \cdot L^{-1}$	0.26 $\mu g \cdot L^{-1}$	0.18 $\mu g \cdot L^{-1}$	0.31 $\mu g \cdot L^{-1}$
$[Al^{3+}]$	42.9 $\mu g \cdot L^{-1}$	90.5 $\mu g \cdot L^{-1}$	4.7 $mg \cdot L^{-1}$	70.9 $\mu g \cdot L^{-1}$	178 $\mu g \cdot L^{-1}$	625 $\mu g \cdot L^{-1}$	404 $\mu g \cdot L^{-1}$
$[Na^+]$	14.7 $mg \cdot L^{-1}$	17.2 $mg \cdot L^{-1}$	16.7 $mg \cdot L^{-1}$	17.2 $mg \cdot L^{-1}$	17.3 $mg \cdot L^{-1}$	18.2 $mg \cdot L^{-1}$	17.3 $mg \cdot L^{-1}$
$[Cl^-]$	6.7 $mg \cdot L^{-1}$	7.12 $mg \cdot L^{-1}$	7.58 $mg \cdot L^{-1}$	31.53 $mg \cdot L^{-1}$	7.55 $mg \cdot L^{-1}$	8.70 $mg \cdot L^{-1}$	2.86 $mg \cdot L^{-1}$
[Si]	5.6 $mg \cdot L^{-1}$	4.9 $mg \cdot L^{-1}$	15.4 $mg \cdot L^{-1}$	4.9 $mg \cdot L^{-1}$	5.2 $mg \cdot L^{-1}$	5.4 $mg \cdot L^{-1}$	5.5 $mg \cdot L^{-1}$
$[SO_4^{2-}]$	5.8 $mg \cdot L^{-1}$	7.11 $mg \cdot L^{-1}$	6.99 $mg \cdot L^{-1}$	7.17 $mg \cdot L^{-1}$	7.32 $mg \cdot L^{-1}$	6.87 $mg \cdot L^{-1}$	6.59 $mg \cdot L^{-1}$
[F]	6.3 $mg \cdot L^{-1}$	6.60 $mg \cdot L^{-1}$	6.69 $mg \cdot L^{-1}$	6.61 $mg \cdot L^{-1}$	6.76 $mg \cdot L^{-1}$	6.73 $mg \cdot L^{-1}$	6.63 $mg \cdot L^{-1}$
$[Br^-]$	n.d.	n.d.	n.d.	n.d.	n.d.	n.d.	n.d.
$[NO_3^-]$	< D.L.						
$[HCO_3^-]$	3.0 $mg \cdot L^{-1}$						

n.d.: not determined, D.L.: detection limit, *: sampling date

Radionuclide cocktail characterization. The radionuclide cocktail was prepared in a glove box under Ar atmosphere by spiking radionuclides to Grimsel groundwater containing bentonite colloids (25.56 $mg \cdot L^{-1}$). After spiking of the radionuclides only a slight decrease of pH from 9.6 to 9.4 was measured, likely due to buffering capabilities of the bentonite colloids. Subsequently pH was readjusted using CO_2 -free NaOH. The prepared cocktail was equilibrated for 24 hours before aliquots of the radionuclide cocktail were spiked to the sample batches containing fracture filling material. Both strong and weak sorbing radiotracers have been used, namely: Am-243, Ba-133, Cs-137, Na-22, Np-237, Tc-99, Th-232, Pu-242 and Tritium. Pu-242 was added as Pu(III) after electrochemical reduction and quantitatively transferred to Pu(IV) through pH adjustment of the cocktail. Table 2-2 lists the concentration of the different elements and the corresponding measurement techniques. Na-22, Ba-133 and Cs-137 analysis via γ -spectrometry are in progress and data on these specific elements is not presented in this report. As shown in Table 2-2 Th(IV) and Am(III) are almost quantitatively bound to the bentonite colloids and for Pu(IV) ~15% are not colloid associated. For all other elements analyzed so far (U, Tc and Np) the colloid bound fraction is below 2% of the initial concentration (C_0).

Table 2-2: Characterization of the radionuclide cocktail including concentration, initial association to bentonite colloids determined by ultracentrifugation and the analytical method used in this study.

	Initial concentration C_0 (mol L ⁻¹)	Colloid bound concentration (%)	Analytical method
[HTO]			Liquid scintillation counting (LSC)
[Na-22]			γ-spectrometry
[Tc-99]	$1.5 \cdot 10^{-8}$	0.9	ICP-MS
[Ba-133]			γ-spectrometry
[Cs-137]	$2.7 \cdot 10^{-9}$		γ-spectrometry
[Th-232]	$1.7 \cdot 10^{-8}$	99.7	ICP-MS
[U-233]	$8.7 \cdot 10^{-7}$	1.6	ICP-MS
[Np-237]	$1.8 \cdot 10^{-6}$	0.1	ICP-MS
[Pu-242]	$1.3 \cdot 10^{-8}$	84.1	ICP-MS
[Am-243]	$8 \cdot 10^{-9}$	94.8	ICP-MS
[Colloid]	25.56 mg L ⁻¹		ICP-MS/ LIBD

Batch-type sorption studies. All experiments were conducted at room temperature (~ 21 °C) in a glove box under argon atmosphere (< 1ppm O₂). All pH measurements were undertaken using a Ross electrode and an Orion pH meter. The set-up was calibrated using commercial buffers. All FFM materials were equilibrated prior to the batch-type experiments with fresh Grimsel groundwater in Zinsser vials (20 mL HDPE) over a period of six weeks, exchanging the solution at least 5 times within this period. An aliquot of the last equilibration solution was taken for analysis. The solid to liquid ratio is 1:4 (g·mL⁻¹) for all experiments. After this equilibration phase the supernatant was exchanged with the radionuclide cocktail. The influence of the FFM on the initial Grimsel groundwater element concentrations is monitored by ICP-MS measurements. Triplicates of every sample were prepared: two of the 3 identical samples with 2g solid and 8 ml of cocktail solution and one sample with 4g solid and 16 ml of solution. First aliquots were taken 1h after spiking of the samples. The next aliquots after 24h, 48h, 120h, 336, 504h, 700h, 1000h and 2000h, respectively. An aliquot of every sample was ultra- centrifuged to remove the colloid associated radionuclides. Aliquots for ultracentrifugation were pipetted in ultracentrifugation vials, sealed and subsequently centrifuged for 1h at 70,000 rpm. Afterwards aliquots of the ultra- centrifuged supernatant were taken and subsequently analyzed by ICP-MS, liquid scintillation counting (LSC) and gamma-spectrometry.

Results & Discussion

As the radionuclide cocktail included several redox sensitive radionuclides (i.e. Pu(IV), Np(V), Tc(VII) and U(VI)) it was mandatory to monitor the contact time dependent evolution of the pH and the Eh value. The response time for the pH electrode was rather uncritical, whereas for the Eh measurement the criterion to accept the measured value is not well documented and established in the literature. In this study we monitored the time dependent change in the redox value although the automatic slope analysis of the Orion instrument already indicated a constant value after < 1h. As shown in Figure 2-5 the Eh drifted over several hours and we took the value, when a plateau was reached. The measured plateau values for pH dropped from pH 9.6 originally found in the Grimsel groundwater to 9.0 in the Grimsel FFM system and 9.1 in the Äspö FFM system after 7,500h. Meanwhile, the Eh_(SHE) values dropped from ~50mV to ~0mV within the first two days and remained ~ 0 mV with an exception of the measurement at 1,000h with values of ~ 50 mV in the Grimsel system.

Afterwards the redox potential started to decrease again to values of ~ -15 mV in the Grimsel FFM system and ~ -75 mV in the Äspö system after 7,500h.

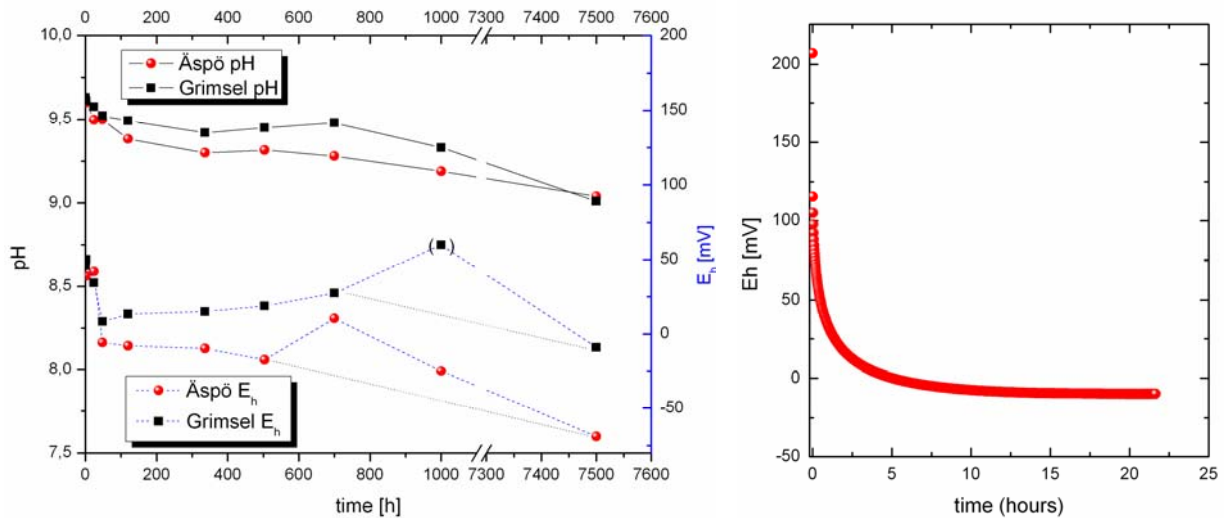


Figure 2-5: (left) Measured final pH and Eh for the RN batch-type studies as a function of contact time. (right) Eh measurement for a single point showing the response time of the redox electrode reaching a constant plateau value after several hours.

Figure 2-6 shows the time dependent evolution of Tc, U, Np, Th, Pu and Am concentration, both for ultracentrifuged (UC) and not ultracentrifuged (not-UC) samples. From a comparison of ultracentrifuged with not ultracentrifuged samples it is obvious that Tc, U and Np are not colloidal associated. The concentrations of Tc and U remain constant over the experimental period, indicating an absence of sorption to fracture filling material or reduction in both investigated systems. These observations are corroborated with the oxidation states expected from thermodynamic calculation as shown in Figure 2-7. Np concentration decreases after ~ 100 h in both systems which could either be explained by sorption to the fracture filling material or by a slow reduction to Np(IV). The borderline of Np reduction is around -60 mV (50% reduced Np), which is in the range of our measured Eh values of -76 mV for the Äspö system and -15 mV in the Grimsel system. Due to uncertainties in redox measurements these values are likely in the range of the borderline for reduction. The fact that the decrease in concentration first occurs after 100h corroborates the hypothesis of reduction because a concentration decrease due to adsorption should onset at earlier times. The reduction itself is known to be kinetically controlled and the experimental data obtained so far shows that the time frame is insufficient to reach equilibrium conditions. A partial reduction at shorter contact times might occur, but cannot be resolved within the analytical uncertainties.

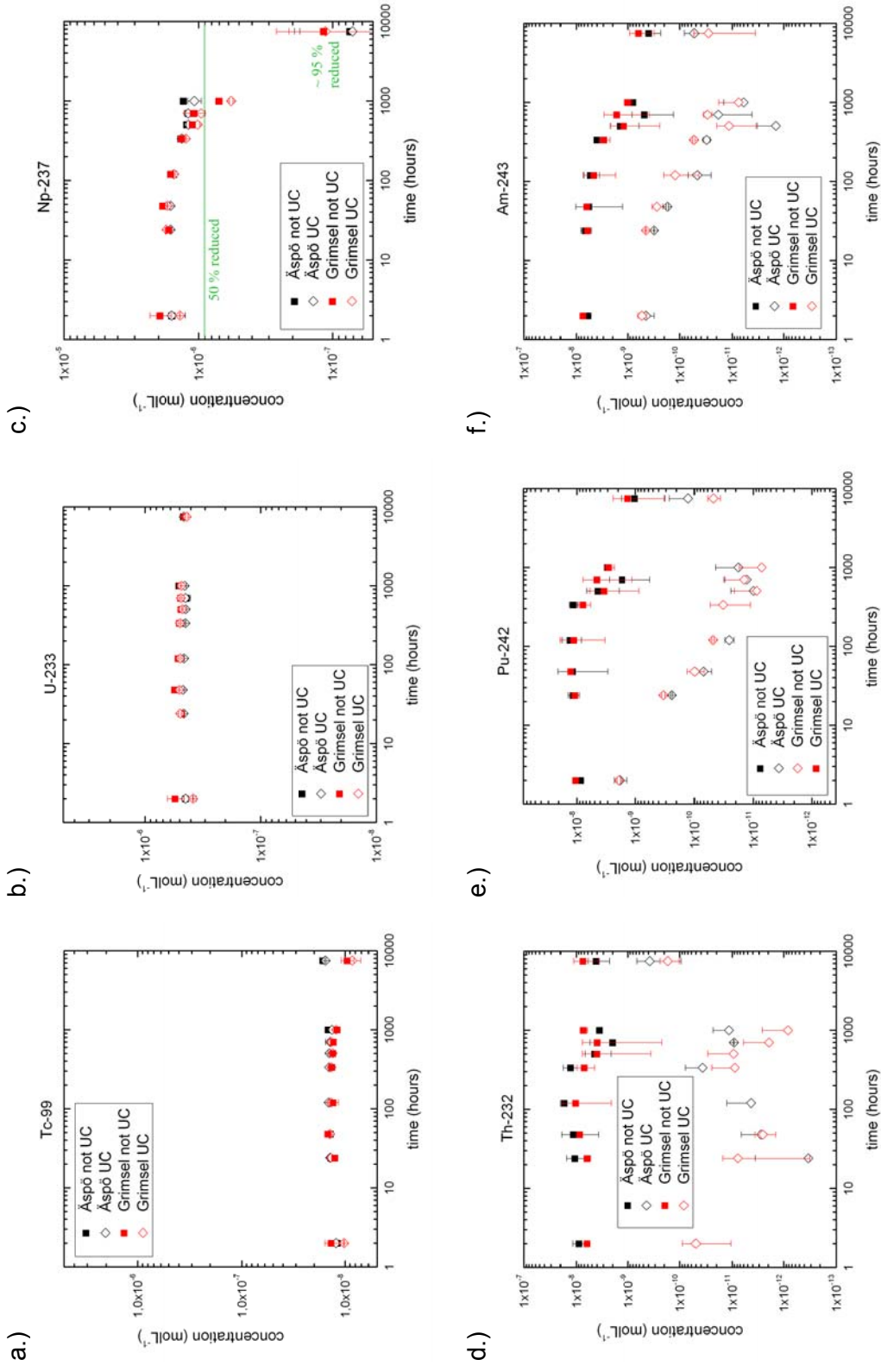


Figure 2-6: Time dependent evolution of radionuclide concentration for the Åspö (black symbols) and Grimseil FFM (red symbols) experiments. a.) Tc b.) U c.) Np d.) Th e.) Pu and f.) Am. Values are given both for ultracentrifuged (UC) samples and for not ultracentrifuged (not UC) samples.

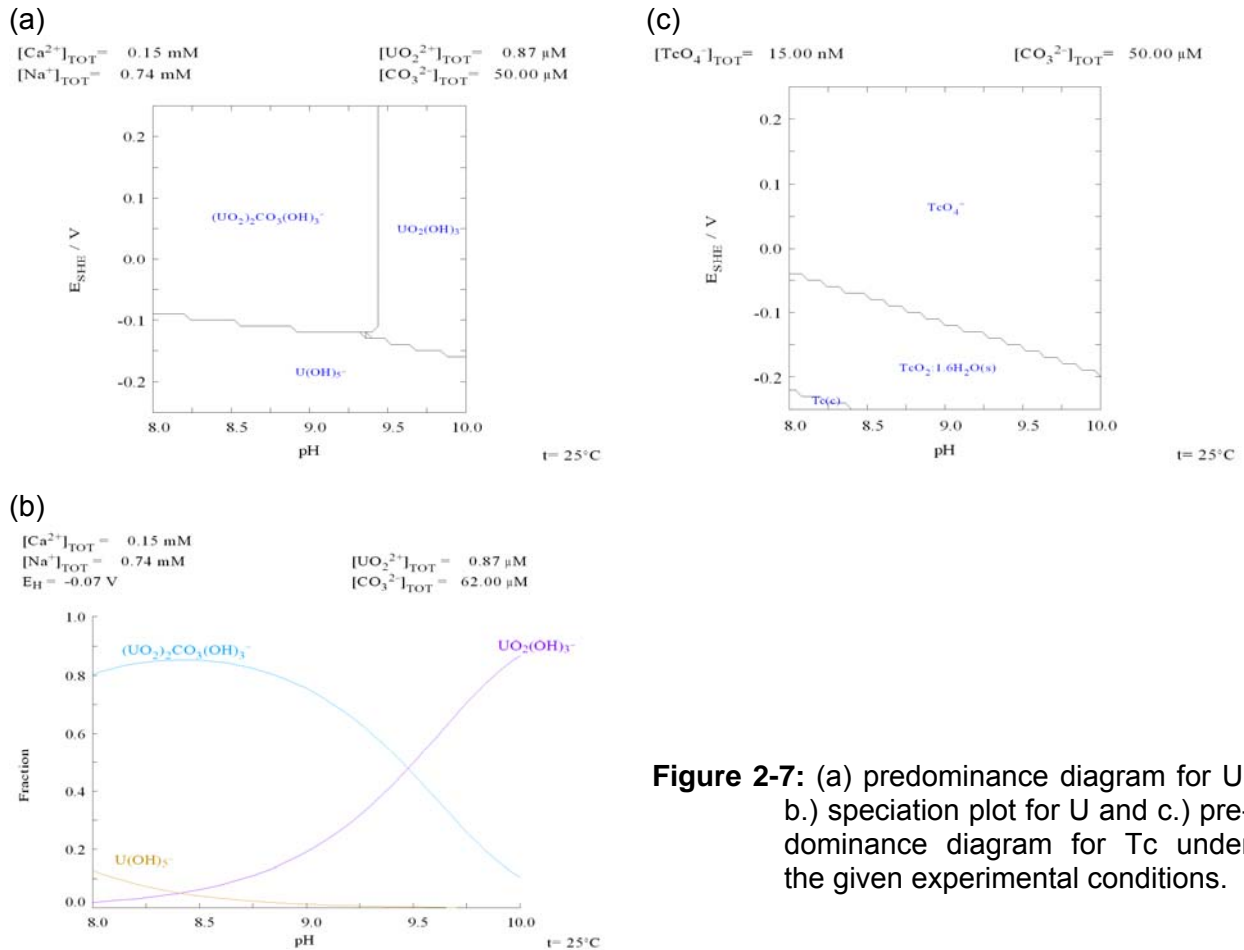


Figure 2-7: (a) predominance diagram for U; b.) speciation plot for U and c.) predominance diagram for Tc under the given experimental conditions.

Calculations based on Equation 1 [63] can be used to estimate the amount of reduced Np and thus deriving the concentration of radionuclides sorbed to the fracture filling material.

$$pe = \log K^{\circ}_{V-IVcoll} + \log [Np]_{tot} - \log (2) + \log \gamma_{NpO_2^+} - \log \{1 + \sum \beta'_{n,L} [L^Z]^{-n}\} \quad (\text{Equation 1})$$

Under the experimental conditions of pH 5-10 and $I \leq 0.1 \text{ M}$ background electrolytes and argon atmosphere the following simplifications can be made:

- Formation of hydrolysis species and other complexes can be neglected and the term $\{1 + \sum \beta'_{n,L} [L^Z]^{-n}\}$ can be omitted.
- Concerning the Np total concentration ($[Np]_{tot} = [Np(V)]^{\circ} = (1.8 \pm 0.2) \cdot 10^{-6} \text{ M}$) the SIT calculated activity coefficient $\log \gamma_{NpO_2^+}$ for NpO_2^+ in $I < 0.1 \text{ M}$ is negligible.

With $pe = 0.15 \pm 0.35$ the following equilibrium constant for $I=0$ can be obtained:

$$\log K^{\circ}_{V-IVcoll} = 5.0 \pm 0.4$$

Calculating the pe based on the values given above results in the borderline for 50% Np(V) reduction at $pe = \sim -1$ as given in Figure 2-8. This calculated pe is not far away from the measured pe values in the batch experiments, therefore a partial reduction of Np(V) on the FFM surface can be assumed.

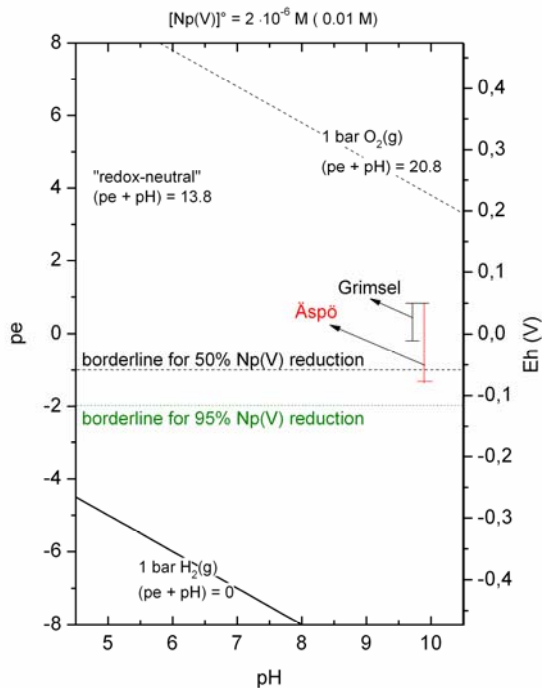


Figure 2-8: Pourbaix (pe/pH) diagram for the batch experiments showing the experimental pe/pH range and the pe borderline for 50% Np reduction. (orange: Grimsel FFM; grey: Äspö FFM)

In contrast, the tri- and tetravalent elements Th, Pu and Am are clearly colloid associated which again can be derived through a comparison between the UC and the not-UC samples. The differences in radionuclide concentration are 1-2 orders of magnitude which also reflect the effective separation of the colloids through the experimental procedure. This is furthermore documented in the Al ICP-MS signal, which gives information on the structural alumina of the Febex bentonite colloids. As shown in Figure 2-9 the Al concentration after UC is also reduced by around two orders of magnitude providing further confidence in the laboratory procedure to separate bentonite colloids from aqueous solution species. In addition the Al concentration remains within the analytical uncertainty constant over the observation period, which leads to the conclusion that no colloid attachment or at least a very low colloid attachment for both fracture filling materials under Grimsel groundwater conditions can be observed.

The tri- and tetravalent radionuclides show bentonite sorption reversibility kinetics after ~100h as evidenced by the radionuclide concentration decrease on the bentonite colloids (not UC samples). The onset of the reversibility process seems to start at roughly 100-300h after the addition of the bentonite cocktail and lasts until at least 1,000h. The last set of samples measured after 7,500h gives hint that the system might have reached equilibrium. The reason for the observed desorption in the presence of FFM can be the approximately ten times higher FFM surface area (76:1) available for radionuclide sorption compared to the bentonite surface area under the given experimental conditions.

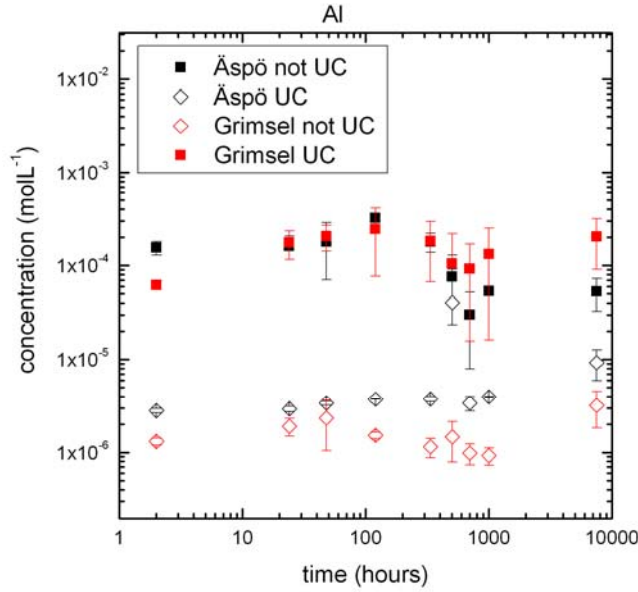


Figure 2-9: Comparison of the Al concentration in the ultracentrifuged and not ultracentrifuged samples for the Äspö FFM and Grimsel FFM system.

Figure 2-10 shows a comparison of our data for the Äspö and Grimsel FFM samples (not ultracentrifuged) with literature data in the presence of Febex bentonite colloids for Grimsel FFM using different grain sizes [64]. The data is presented as surface area normalized distribution coefficients. It can be expressed as follows:

$$K_d = \frac{\Gamma_{RN}}{[RN]} = \frac{(TOTRN - [RN])}{[RN]} / \phi m = \left(\frac{TOTRN}{[RN]} - 1 \right) / \phi m$$

whereas K_d = distribution coefficient in $L \cdot m^{-2}$; Γ_{RN} = surface excess of [RN] in $mol \cdot m^{-2}$; [RN] = dissolved [RN] concentration in $mol \cdot L^{-1}$; TOTRN = total [RN] concentration in $mol \cdot L^{-1}$; ϕ = surface area in $m^2 \cdot g^{-1}$; m = solid concentration in $g \cdot L^{-1}$.

Np shows slightly lower K_d values (~ 0.5 orders of magnitude) for both FFM systems investigated in this study compared to other data using the same FFM and same size fraction [62]. This information can be used as uncertainty estimation for the obtained distribution coefficients. Both independent data sets show an increase in K_d values of about one order of magnitude with time.

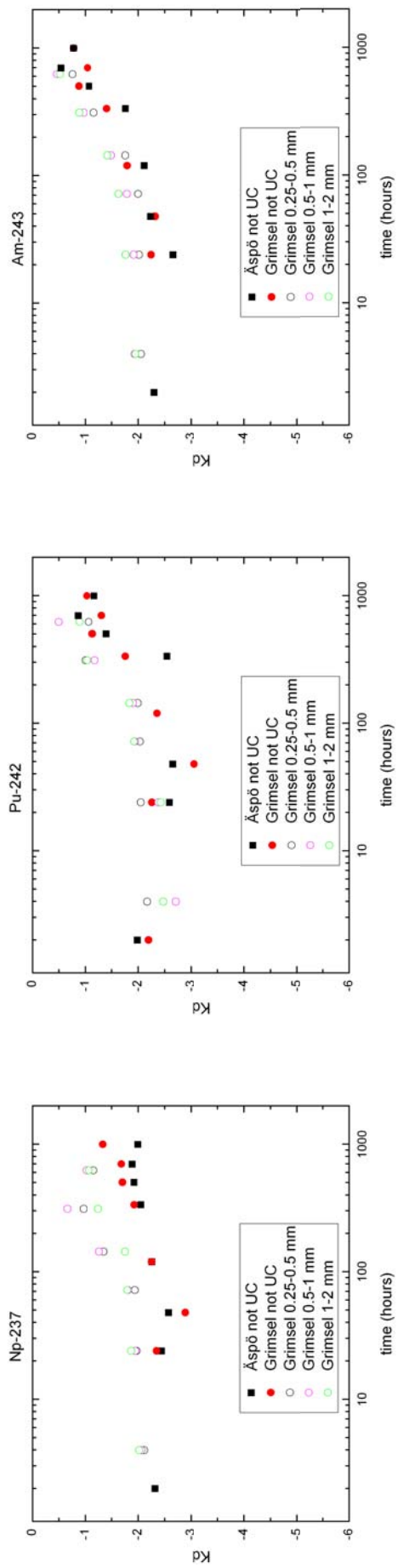


Figure 2-10: Surface area normalized log (K_d) values for Np (left), Pu (middle) and Am (right) in comparison to data from [64]. Data of this study are shown as filled symbols. The N₂ BET surface area taken for the calculation is: Åspö FFM: 0.2m²·g⁻¹, Grimsel FFM (1-2mm): 0.15m²·g⁻¹; Grimsel FFM (0.5-1mm): 0.19m²·g⁻¹; Grimsel FFM (0.25-0.5mm): 0.24m²·g⁻¹, respectively.

K_d values for Am(III) and Pu(IV) show a rise from K_d ~ -2.5 up to -0.5. This increase in K_d value can be explained by the kinetics of sorption reversibility and the subsequent sorption to the fracture filling material, whereas the observed trend in the Np K_d values reflect a combined effect of reduction and sorption. The envelope curves given in Figure 2-10 give an uncertainty margin of the FEBEX bentonite colloid reversibility kinetics that can be used in reactive transport modelling [65]. Overall, the results show that the desorption kinetics from bentonite colloids are rather independent from the FFM used and also from the grain size of the investigated material, at least in the size fraction range 0.25-2 mm.

Conclusions. Batch type experiments studying the radionuclide bentonite reversibility in presence of fracture filling materials from Äspö and Grimsel have been conducted using a cocktail of radionuclides spiked to natural groundwater from Grimsel.

- U(VI), Tc(VII) and Np(V) are not bentonite colloid associated. In the case of Np the observed decrease in the solution concentration could be explained by both sorption to the fracture filling material and by reduction to Np(IV) based on thermodynamic considerations using the pe/pH conditions reached.
- In contrast, the tri- and tetravalent radionuclides Th(IV), Pu(IV) and Am(III) are almost quantitatively associated to bentonite colloids. The tri- and tetravalent radionuclides show bentonite sorption reversibility kinetics which starts after about 100 h contact time with the fracture filling material (both Äspö and Grimsel).

Further details to the study presented in this chapter can be found in:

Huber F., Kunze P., Geckeis H. and Schäfer T. (submitted) Sorption and reversibility studies on the interaction of radionuclides with FEBEX bentonite under Grimsel groundwater conditions in the presence of fracture filling material. *Radiochimica Acta*.

2.1.3 Colloid stability

Abstract. In this study the critical coagulation concentration (CCC) of Febex bentonite colloids is determined by colloid coagulation studies under variation of pH, electrolyte concentration and fulvic acid (GoHy-573FA) content. For CaCl₂ electrolyte solution a pH independent Ca-CCC of 1 mmol·L⁻¹ was found. In the case of NaCl background electrolyte a pH dependent Na-CCC could be determined with 15 ± 5 mmol·L⁻¹ at pH 6, 20 ± 5 mmol·L⁻¹ at pH 7, 200 ± 50 mmol·L⁻¹ at pH 8, 250 ± 50 mmol·L⁻¹ at pH 9 and 350 ± 100 mmol·L⁻¹ at pH 10, respectively. The addition of 1 mg·L⁻¹ DOC FA increases the Ca/FA-CCC to 2 mmol·L⁻¹. An FA association with Febex bentonite colloids as surface coating and specific hot spots could clearly be identified by Scanning Transmission X-Ray Microscopy (STXM). The experimental bentonite stability results were described by means of a DLVO approach summing up hydration forces, short-range Born repulsion, van der Waals attraction and electrical double layer repulsion. The measured zeta (ζ) -potential of the bentonite colloids is used as platelet face charge and the edge charge is estimated by the combination of silica and alumina ζ-potential data in the ratio given by the Febex bentonite structural formula. Adjusting the montmorillonite face charge by a maximum of ± 12 mV was sufficient to successfully reproduce the measured stability ratios. However, the Na- CCC values could only be reasonably predicted using solely the edge-face interaction energy calculated. The strong deviations of the model predictions and the experimental determined Na- CCC values found at low electrolyte concentrations are explained by the spill-over of the platelet face electrical double layer (EDL) shielding the positive platelet edge charge.

Materials & Methods

Colloid preparation. Details on the colloid suspension used in this study can be found in chapter 2.1.2. The cation exchange capacity (CEC) was determined to 107 meq (100 g)⁻¹. The mean bentonite colloid size as determined by Photon Correlation Spectroscopy (PCS) is 185 nm with a half-width of 90 nm recalculated from the polydispersity index of 0.24.

Coagulation studies. The coagulation rate of the bentonite colloids is determined by photon correlation spectroscopy (PCS) using a ZetaPlus system (Brookhaven Inc.). The scattering light is measured perpendicular to the incident laser beam and the data evaluation is made by the instrument built-in software (Version 2.27). The hydrodynamic radius (r_h) is calculated from the measured diffusion coefficient (D) by the Stokes-Einstein equation assuming spherical colloid geometry:

$$r_h = \frac{k_B T}{6\pi\eta D} \quad (\text{Equation 2})$$

where k_B is the Boltzmann constant, T the absolute temperature and η is the viscosity of the fluid. The stability ratio is calculated based on the expression given by Kretzschmar et al. [26]:

$$W = \frac{\left[\left(\frac{dr_h}{dt}\right)_{t \rightarrow 0} / C\right]^{(f)}}{\left[\left(\frac{dr_h}{dt}\right)_{t \rightarrow 0} / C\right]} \quad (\text{Equation 3})$$

whereas W is the stability ratio, C the colloid concentration and the superscript (f) refers to measurements in the regime of fast solely diffusion controlled coagulation [24-26]. The region where fast diffusion controlled aggregation sets on is often called critical coagulation concentration (CCC). The advantage to determine colloid stability by means of W is the independency of the observation time used throughout the experiments [66] and that it is therefore possible to directly compare with published literature data. The solution used throughout the coagulation experiments has a concentration of $3.7 \cdot 10^{-4}$ % w/w with a pH of 5.9 ± 0.1 . Prior to each coagulation experiment the colloid size of the suspension is checked directly in the cuvette. Afterwards, to start the coagulation process, the electrolyte solution is added in a quantity to get the desired concentration. The pH is adjusted by addition of analytical grade NaOH. A measurement period of 10 sec. is combined to one data point by the software program. The measurement is stopped when the particle size has reached approx. 1000 nm. Experiments where this size is reached in $t < 180$ min were done in a single 5 ml cuvette. After removing the cuvette from the PCS the pH is checked with a Ross-electrode. Long-term experiments with $t > 180$ min were performed in 20 ml bottles. Here, the solutions are mixed in these bottles and an aliquot of the mixed solution is transferred into a cuvette for the particle size measurement. Ten measurements each with a 40 sec accumulation time are combined to one data point. The aliquot is back transferred to the experimental bottle and the pH adjusted. This measurement cycle is repeated until the particle size reaches approx. 1000 nm. The monitoring time of the slow aggregation experiments covered hours to weeks.

Surface potential determination. The electrophoretic mobility μ is measured with the ZetaPlus system using the PALS Zeta Potential Analyzer Software (Version 3.13) setting the data acquisition criterion to a target residual of 0.02. The ζ -potential measured in this study are calculated from electrophoretic mobility measurements using Smoluchowski's equation [66]:

$$\zeta = \mu\eta / \varepsilon_r \varepsilon_0 \quad (\text{Equation 4})$$

where ε_r is the relative permittivity of water, ε_0 the dielectric permittivity of vacuum and η is the viscosity.

For model calculations the measured ζ -potential was inserted as approximation of the surface potential. Due to the lower scatter angle (22°) in the electrophoretic mobility measurements the Febex bentonite colloid concentration was raised to $4 \cdot 10^{-3}$ % w/w. In order to estimate the bentonite colloid edge charge the ζ -potential of separately measured silica and alumina was combined as proposed by Williams and Williams [44]. The silica and α -alumina stock solutions were prepared by suspending Aerosil90 (Degussa) and TM-DAR (Taimicron) powder, respectively, in Milli-Q water. The bentonite edge charge was calculated with the ratio between silica and alumina given in the structural formula of Febex bentonite [60]:

$$\zeta_{edge} = 0.72 \cdot \zeta_{silica} + 0.28 \cdot \zeta_{alumina} \quad (\text{Equation 5})$$

The pH range in all measurements varied from 6 to 10. pH adjustment was performed by addition of analytical grade NaOH. For the measurements in CaCl_2 electrolyte solution the measurement setup was covered with a CO_2 free atmosphere to prevent the coprecipitation of calcium carbonate phases.

Scanning Transmission X-Ray Microscopy (STXM) studies. Two samples of bentonite colloids with addition of $1 \text{ mg} \cdot \text{L}^{-1}$ DOC (fulvic acid GoHy-573FA, [67]) were coagulated with CaCl_2 at a concentration of $0.33 \text{ mmol} \cdot \text{L}^{-1}$ at pH 6 and pH 8. The solution was ultra-centrifuged for 1 h at 90.000 rpm (502,135g). The concentrated settlement was used for the sample preparations. Carbon K-edge Near Edge X-Ray Absorption Fine Structure (NEXAFS) spectra were measured at the Scanning Transmission X-ray Microscopy (STXM) beamline X1A1 (NSLS), operated by the State University of New York at Stony Brook. The principle of the method is described in detail elsewhere [68]. The absorption by different carbon structures follows the Lambert-Beer law, i.e. the absorption is directly proportional to the mass absorption coefficients of different carbon functionalities as a function of the X-ray wavelength. The optical density (OD) is equal to the product of sample thickness d , the sample density ρ and the mass absorption coefficient $\mu(E)$, which is related to the quotient of the incident flux on the sample $I_0(E)$ and the flux detected behind the sample $I(E)$ via:

$$\text{OD} = -\ln \left[\frac{I(E)}{I_0(E)} \right] = \mu(E) \cdot \rho \cdot d \quad (\text{Equation 6})$$

STXM sample preparation was performed by drying $1 \mu\text{l}$ of concentrated settlement on a Si_3N_4 window (100 nm thick). The spectra was extracted from images taken at different energies across the absorption edge (so called stacks) after aligning them using cross-correlation [69]. Image regions free of particles gave the $I_0(E)$ information. Energy calibration of the spherical grating monochromator was achieved by using the photon energy of the CO_2 gas adsorption band at 290.74 eV [70]. For comparison of different NEXAFS spectra, all spectra were baseline corrected and normalized to 1 at 295 eV prior to peak fitting and deconvoluted following the procedure described in detail elsewhere [71-73].

Results and Discussion

Colloid stability. Colloid stability measurements are performed by measuring the time dependent change of the average colloid hydrodynamic radius. An electrolyte concentration dependent coagulation rate was observed, as expected (Figure 2-11). For CaCl_2 as

background electrolyte solution at pH 8 the fastest observed coagulation was at a concentration of $33 \text{ mmol}\cdot\text{L}^{-1}$. Lowering the electrolyte concentration to $3.3 \text{ mmol}\cdot\text{L}^{-1}$ no decrease in the detected coagulation rate within the analytical uncertainty could be observed. A first significant drop in coagulation rate occurs when the electrolyte concentration is furthermore lowered to $1 \text{ mmol}\cdot\text{L}^{-1}$.

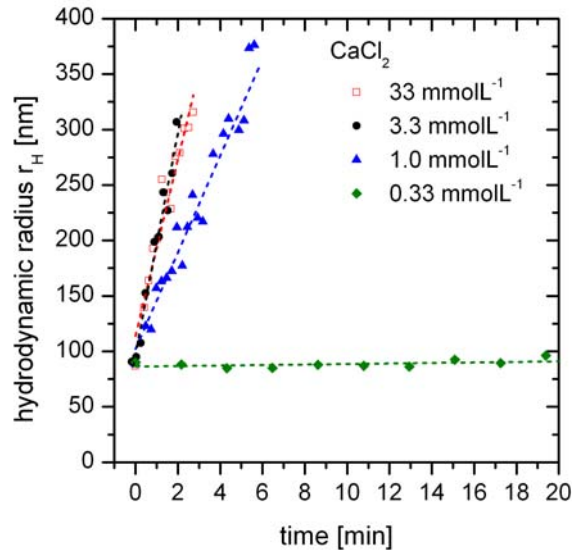


Figure 2-11: Time dependent hydrodynamic radius r_H increase for Febex bentonite colloids as a function of CaCl_2 background electrolyte concentration at pH 8.

The stability ratio W for each coagulation experiment under constant pH was calculated using (Equation 3) and plotted against the concentration for the adjusted pH values (Figure 2-12). The observed steep slopes of colloid size increase for concentrations above $1 \text{ mmol}\cdot\text{L}^{-1}$ result in a W between 1 and 2, whereas $W = 1$ represents by definition the critical coagulation concentration (CCC) of solely diffusion controlled aggregation. Taking into account the uncertainties in the linear slope analysis of the measured data, a variation of W between 1 and 2 has to be considered as CCC in this study. For lower background electrolyte concentrations the stability ratio W increases, which means that not every colloid-colloid collision results in a doublet formation. Taking the crossover of the linear regressions made for the different pH values investigated a pH independent CCC for CaCl_2 of $1 \text{ mmol}\cdot\text{L}^{-1}$ can be determined for Febex bentonite derived colloids (Figure 2-12). This value correlates well with the observations made by SKB [2] that the stability of suspended colloids is much decreased or in other words the stability of the buffer and backfill is enhanced if the concentration of divalent cations exceeds $1 \text{ mmol}\cdot\text{L}^{-1}$. SKB [2] therefore defines a safety function indicator of $[\text{M}^{2+}] > 1 \text{ mmol}\cdot\text{L}^{-1}$ for bentonite buffer stability. The Ca-CCC found in this study fits also well with published data for montmorillonite (SWy-1) and beidelite [74] and is slightly higher than published values of $0.4 \text{ mmol}\cdot\text{L}^{-1}$ determined by Lagaly and Ziesmer [75] for 0.025 % w/w Na-montmorillonite (Wyoming, M40A) as well as $0.3 \text{ mmol}\cdot\text{L}^{-1}$ reported by Chheda et al. [76] for 0.015 % w/w Na-montmorillonite (Fischer) (Figure 2-13). Comparing the layer charge of the Febex bentonite colloids determined to be 0.37 eq/formula unit with the variation generally found for montmorillonites of 0.25-0.4 eq/formula unit [77] and the layer charge of 0.28-0.31 eq/formula unit found for Wyoming M40A montmorillonite [75] Febex bentonite can be considered as a highly charged montmorillonite. However, the layer charge difference seems not to have a significant influence on the determined Ca-CCC.

For NaCl as background electrolyte the calculated W values are plotted against the concentration in Figure 2-12b. As expected, for the NaCl systems the concentrations needed to induce Febex bentonite coagulation are much higher than for CaCl_2 background

electrolyte following in general the trend predicted by the Schulze-Hardy Rule [66], but not inversely proportional to the sixth power of the cation valence. In contrast to the Ca-CCC, the Na-CCC is clearly dependent on the pH value of the system with a Na-CCC of 15 ± 5 $\text{mmol}\cdot\text{L}^{-1}$ at pH 6, 20 ± 5 $\text{mmol}\cdot\text{L}^{-1}$ at pH 7, 200 ± 50 $\text{mmol}\cdot\text{L}^{-1}$ at pH 8, 250 ± 50 $\text{mmol}\cdot\text{L}^{-1}$ at pH 9 and 350 ± 100 $\text{mmol}\cdot\text{L}^{-1}$ at pH 10, respectively. The Na-CCC values determined for the NaCl system are plotted as a function of the pH value in Figure 2-13. The determined Na-CCC values for pH 6 and pH 7 are in quite good agreement with published Na-CCC data for SWy-1 and the beidelite from Hetzel and Doner [74], Lagaly and Ziesmer [75] for pH 6.5 and Chheda et al. [76] for pH 6.8. Tombácz and Szekeres [78] however determined Na-CCC values at pH 6 for Wyoming montmorillonite SWy-1 & SWy-2 of 52 $\text{mmol}\cdot\text{L}^{-1}$, which are considerably higher than the Na-CCC values observed in this study for Febex bentonite.

Theoretical calculations by Liu et al. [79] predict based on the Febex bentonite colloids size of 185 nm and a calculated particle surface area S_p of $8.2 \cdot 10^4$ nm^2 (particle thickness δ_p 2.4 nm) a Na-CCC of 20-30 $\text{mmol}\cdot\text{L}^{-1}$ for pH 5 to ~ 6.5 , which is slightly above our measured values for pH 6.

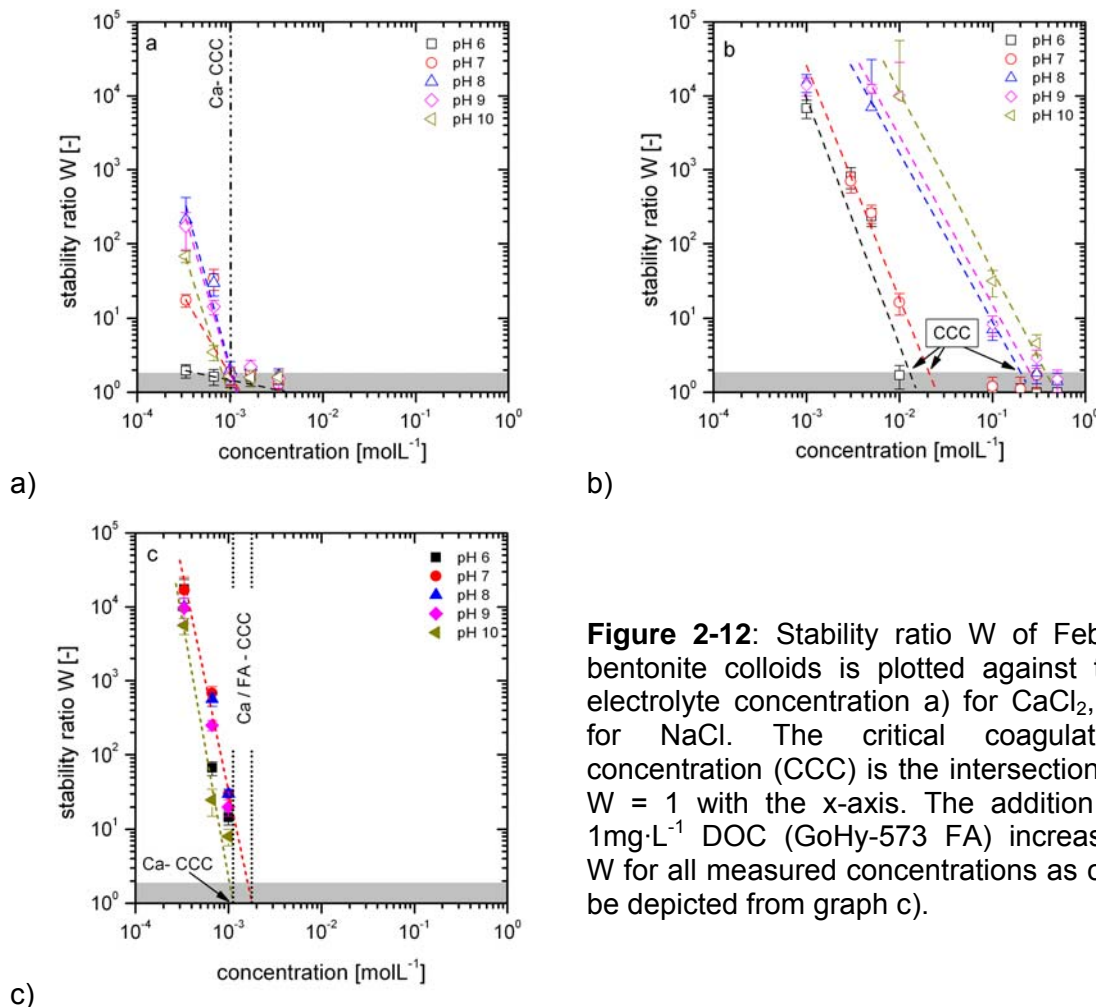


Figure 2-12: Stability ratio W of Febex bentonite colloids is plotted against the electrolyte concentration a) for CaCl_2 , b) for NaCl . The critical coagulation concentration (CCC) is the intersection of $W = 1$ with the x-axis. The addition of $1\text{mg}\cdot\text{L}^{-1}$ DOC (GoHy-573 FA) increases W for all measured concentrations as can be depicted from graph c).

The observed increase in Na-CCC above the isoelectrical point pH_{iep} of the montmorillonite edges might be explained by a full delamination of the montmorillonite platelets based on the approach of Liu et al. [79]. Asymmetrical Flow Field Flow Fractionation (AsFFFF) studies of fully delaminated Febex bentonite by Bouby [80] have shown a bimodal size distribution varying from 15-300 nm with peak maxima at 40 nm and 150 nm. Taking a particle thickness δ_p of 1.2 nm for fully delaminated platelets and the AsFFFF derived smaller colloid size peak

maxima of 40 nm a Na-CCC of approx. 200 mmol·L⁻¹ would be predicted, which is in fair good agreement with the measurements made at pH 8-10. However, it has to be noted that published Na-CCC data in the pH range 8-10 scatter considerably with highest values found by Tombácz et al. [81] of 350–400 mmol·L⁻¹ at pH 8 and lowest values of 18–40 mmol·L⁻¹ at pH 8-10 for SWy-1 [74] (see Figure 2-13).

A reason for the huge scatter found at high pH can be the difference in sample preparation and measurement techniques used. All referred literature data did transform there clays to its monoionic form by exchange with NaCl or NaClO₄. The cleaning step mostly includes centrifugation and washing, dialysis against Milli-Q water [76] or 0.01 mol·L⁻¹ electrolyte solution [74, 78]. Each treatment and differences in centrifugation times and speeds will lead to different clay colloid sizes and thicknesses. Other authors include pretreatment with Na₂CO₃ [81] or with citrate/H₂O₂ to removed iron oxides and humic substances [75] which can change the surface and edge properties of the colloids and influence the colloid stability, too.

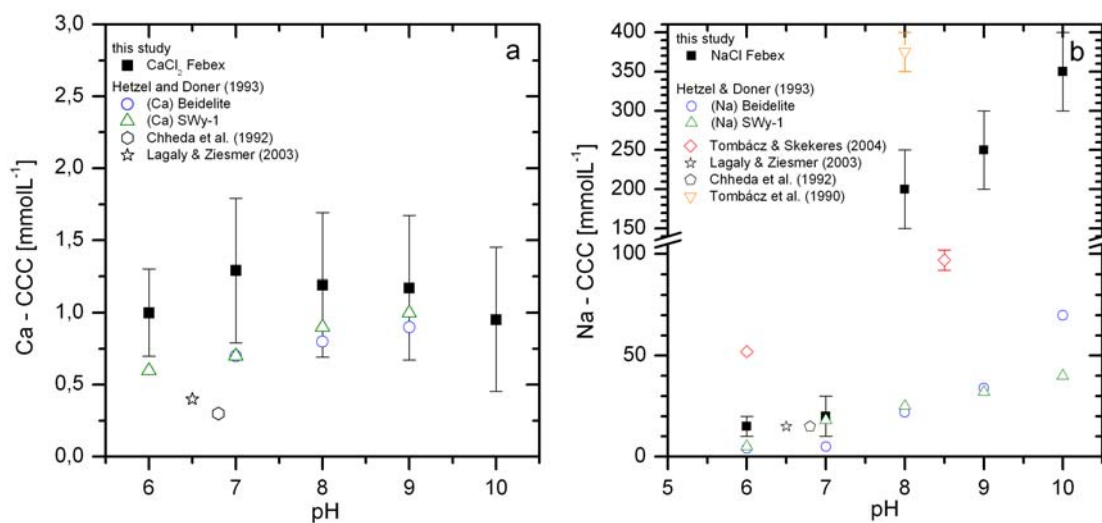


Figure 2-13: Critical coagulation concentration (CCC) plotted against pH for CaCl₂ a) and NaCl b). The Ca- CCC does not change within the analytical uncertainty for the investigated pH range. For comparison, the data from Hetzel & Doner [74] for montmorillonite (SWy-1) and beidelite is inserted. The Na- CCC values for pH 6 and 7 is within the range found in the literature, whereas for pH 8 to 10 a considerable variation is found. Possible explanations are given in the text.

The presence of humic substances can never be excluded in natural systems. For the Grimsel Test Site, Switzerland a DOC concentration of ≤ 1 mg·L⁻¹ is determined by Degueldre et al. [82] (0.24 mg·L⁻¹) and Schäfer et al. [32] (1.2 ± 0.2 mg·L⁻¹). The groundwater of the Äspö underground laboratory, Sweden has a higher DOC content of 10 – 22 mg·L⁻¹ [83], with maximum values found by Kienzler et al. [84] in the CHEMLAB2 borehole of 42.3 mg·L⁻¹. For the Whiteshell Research Area, Canada Vilks and Bachinski [85] report an average DOC concentration of 0.5 mg·L⁻¹. The addition of 1 mg·L⁻¹ dissolved organic carbon (DOC) as fulvic acid (GoHy-573FA) increases the colloid stability and the resulting W in CaCl₂ background electrolyte solution for the measured pH range (Figure 2-12c). Taking the intersection at W = 1 as calcium critical coagulation concentration in presence of fulvic acids (Ca/FA-CCC) for pH 10 only a marginal increase could be detected, which is within the analytical uncertainty. However, at lower pH values an increase in the Ca/FA-CCC to values ≤ 2 mmol·L⁻¹ could be determined.

In order to verify the fulvic acid surface association with montmorillonite colloids at pH 6 and 8 aliquots of the investigated suspensions were ultracentrifuged and the settlements investigated by carbon K-edge Scanning Transmission X-Ray Microscopy (STXM). The STXM method has been tested in various environmental systems including (a) natural particulate matter of ultra-oligothropic lakes [86], (b) distribution of natural organic matter in low carbon claystone formations [73], (c) chemical characterization of natural organic matter, humic and fulvic acids [87] and (d) their fractionation through metal complexation or mineral interaction [87-89] and proved to be a very sensitive technique.

The spectral features observed at the carbon K-edge include an absorption band at 285.2 eV, which is typical for aromatic carbon bonded either to carbon or a proton. The excitation around 286.6 eV is assigned to aromatic carbon bonded to oxygen $C(1s) \rightarrow \pi^*_{C-OH}$ as found in phenol or halogenated aromatics. The splitting is due to symmetry reduction and/or chemical shifts (higher electron affinity) associated with the ligand group [90]. The next higher excitation around 287.6 eV is not a π^* state but a low-lying 1s carbon transition to a mixture of 3p Rydberg orbital with a symmetrical antibonding C-H* orbital [90] as in aliphatic methyl and methylene groups. The most intense band in all fulvic acids spectras is around 288.2 eV to 288.8 eV and can be assigned to the large oscillation strength of the $C(1s) \rightarrow \pi^*_{C=O}$ of aromatic and aliphatic associated carboxylic groups [91]. An additional transition at around 289.5 eV is typically assigned to the O-alkyl group found in alcohols and carbohydrates.

In comparison to the pure fulvic acid (GoHy-573FA) the carbon K-edge spectra of the Febex bentonite colloid associated organics both sorbed at pH 6 and pH 8 show significant different spectra (Figure 2-14). The absorption band intensity at 285.2 eV is significantly weaker in the surface associated organics compared to the pure GoHy-573FA and can be interpreted with a higher amount of hydroxyl groups associated to the surface sorbed aromatic structures as found in comparative study between phenols and benzene [92]. This is cooperated by the stronger intensity of the $1\pi^*_{C=O}$ of aromatic and aliphatic associated carboxylic groups at 288.5 eV and a general higher content of oxygen containing functional groups ($\Sigma(\text{phenol-type} + \text{carboxyl-type} + \text{carbonyl-type})$) as quantified by de-convolution [71] of 81% for pH 6 and 77% for pH 8, respectively.

The high oxygen content of surface associated organics is very comparable to previous studies on natural organics associated with Febex bentonite (79%) [15] and significantly higher than the amount of oxygen containing functional found for pure GoHy-573FA with 67% (Figure 2-14a). The exact amount of Febex bentonite associated FA could not be determined within the uncertainty of the DOC measurements and the reproducibility of the sample preparation by ultracentrifugation. The ratio image taken at pH 6 (Figure 2-14b) shows organics associated with the Febex bentonite colloids as a rather homogeneous surface coverage with some hot spots of high C_{org} concentration. As clearly evidenced by these high resolution STXM images the fulvic acids added to the Febex bentonite colloid suspension at pH 6 are surface associated. The observed increase in colloid stability and CCC can therefore be attributed to a negative charge increase or charge reversal of colloid edge sites due to this fulvic acid association.

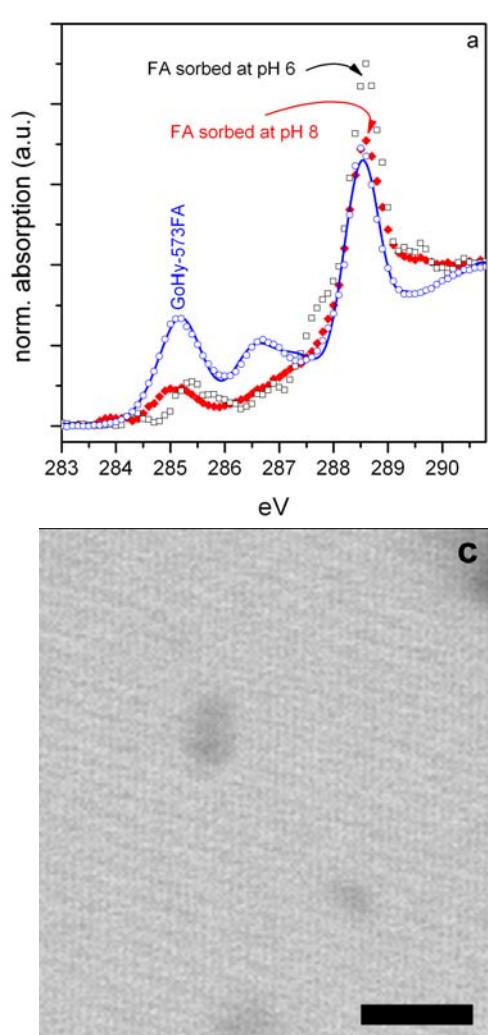


Figure 2-14: (a) XANES spectra of GoHy-573FA starting solution prior to Febex bentonite sorption (blue) and spectra of organics associated to Febex bentonite colloids at pH 6 and pH 8, respectively. The solid line represents a best fit of the fulvic acid spectra taking the de-convolution procedure as described in Schäfer et al. [93]. (b) Ratio image ($-\log(I[285.3\text{eV to } 295.0\text{eV}]/I_0[283\text{eV}])$) of organics associated with Febex bentonite colloids at pH 6. Brighter gray values indicate a higher concentration of organic material. (c) STXM image taken at 283eV below the carbon K-edge showing absorption of bentonite colloids and aggregates. Scale bar represents 2 μm .

Surface charge estimation and DLVO model predictions

CaCl₂-system: The ζ -potential for Febex bentonite colloids in two different CaCl₂ background electrolyte concentrations show negative charges over the investigated pH range from 6 to 10 with a slight charge decrease towards lower pH values (Figure 2-15a). The Febex bentonite colloid edge charges were estimated using equation (5) inserting the ζ -potential measurements of silica and α -alumina colloids (Figure 2-15b) taking into account the structural formula of Febex bentonite as given in Villar et al. [60]. The estimated bentonite edge charge for the 33 mmol·L⁻¹ CaCl₂ background electrolyte shows an isoelectrical point pH_{iep} of ~ 9.4 and positive edge charges below the pH_{iep} . The expected low colloid stability due to the positive edge charges is qualitatively in line with the observed fast coagulation ($W = 1$) based on the stability measurements in this CaCl₂ background electrolyte concentration range (see Figure 2-12a). For a CaCl₂ background concentration of 0.33 mmol·L⁻¹ a slow increase in colloid size was observed in the coagulation experiments (see Figure 2-11). The estimated edge charge as well as the measured ζ -potential for the Febex bentonite are both negative under these experimental conditions (pH 6-10), but with ζ -potentials of the estimated edge charge > -10 mV below pH 8.

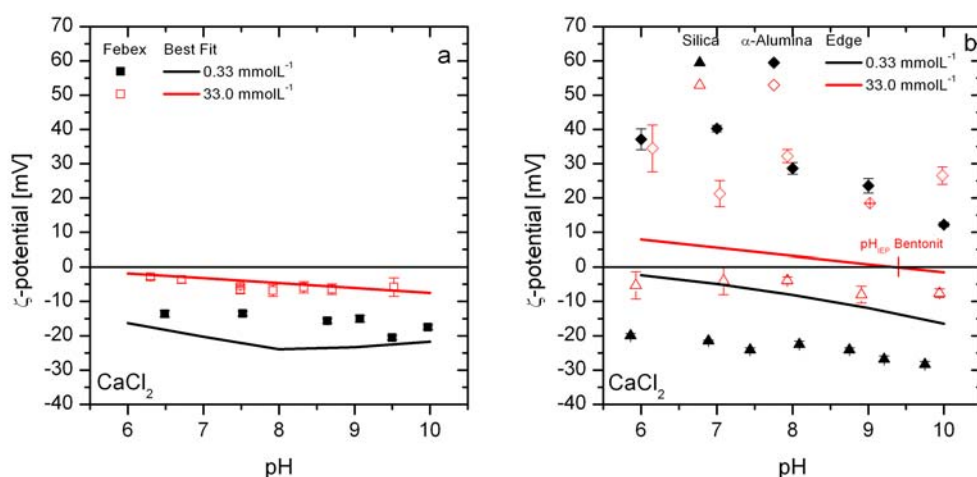


Figure 2-15: a) Febex bentonite colloid ζ -potential in CaCl_2 background electrolyte solution. Data points represent the measured ζ -potentials at $0.33 \text{ mmol}\cdot\text{L}^{-1}$ (filled squares) and $33 \text{ mmol}\cdot\text{L}^{-1}$ (open squares) as a function of pH. The solid lines represent the best fit for the surface potential to reproduce the measured stability ratio as given in Table 2-3. b) Silica (triangles) and α -alumina (diamonds) ζ -potential in CaCl_2 background electrolyte solution. Data points represent the measured ζ -potentials at $0.33 \text{ mmol}\cdot\text{L}^{-1}$ (diamonds) and $33 \text{ mmol}\cdot\text{L}^{-1}$ (triangles) as a function of pH. The lines indicate the estimated edge charge for the two electrolyte concentrations using equation (5).

NaCl-system: The Febex bentonite ζ -potential for the NaCl background electrolyte system (a) are considerably (~ -15 to -25 mV) lower compared to the CaCl_2 system (Figure 2-16a). The estimated edge charge as well as the ζ -potential of silica and α -alumina are plotted in Figure 2-16b. For α -alumina the isoelectrical point pH_{iep} is found to be at ~ 9.7 . This value is rather high compared to a pH_{iep} of 8 to 9 found in the literature [94]. For sensitivity analysis of the appropriateness of the used model alumina mineral for edge-charge estimation we compared the edge charge calculation of our α -alumina data with γ -alumina data (Figure 2-16c) published by de Lint et al. [95]. Here, the pH_{iep} was measured to be ~ 8.4 . The estimated edge charge based on equation (5) for the $100 \text{ mmol}\cdot\text{L}^{-1}$ NaCl background electrolyte shows a comparable pH_{iep} and ζ -potential curve for both alumina phases selected (α -alumina and γ -alumina). In the case of $1 \text{ mmol}\cdot\text{L}^{-1}$ NaCl background electrolyte an edge charge pH_{iep} of ~ 6 is found (Figure 2-16b) in the α -alumina, whereas calculations of the bentonite edge charge using γ -alumina revealed a negative edge charge over the entire pH range investigated (Figure 2-16c). The above mentioned discrepancy between α - and γ -alumina is almost negligible at pH 9-10, but becomes more pronounced with decreasing pH values, especially at pH 7-8 with a maximum difference of $\sim 10 \text{ mV}$.

The calculated positive edge charges for $100 \text{ mmol}\cdot\text{L}^{-1}$ NaCl at pH 6 to 7 are fully in-line with the coagulation found under these experimental conditions. Based on the experimentally determined Na-CCC of $15 \text{ mmol}\cdot\text{L}^{-1}$ for pH 6 the edge charge estimation based on γ -alumina seems to represent better the Febex bentonite coagulation behavior. In the case of α -alumina the edge charge has already for a $1 \text{ mmol}\cdot\text{L}^{-1}$ NaCl background electrolyte at pH 6 reached charge neutrality and strong coagulation should be expected. However, the general trend of increased bentonite stability with decreasing NaCl concentration can directly be deduced from the more negative values of the ζ -potential.

In a next step we used the measured face charges of the Febex bentonite together with the calculated edge charges to estimate the stability ratios retrieving the maximum energy barrier V_{\max} using the DLVO approach of Mahmood et al. [31] implementing the measured bentonite ζ -potentials (face charge) and the estimated edge-charge ζ -potentials (α -alumina or γ -alumina). Based on the V_{\max} the stability ratio W_{DLVO} is calculated by the equation given in Lewis [96]

$$W_{DLVO} = \exp\left(\frac{V_{\max}/k_B T}{2\kappa r_h}\right) \quad (\text{Equation 7})$$

where k_B is the Boltzmann constant, T the absolute temperature, κ the reciprocal double layer thickness and r_h the hydrodynamic radius of the colloid. The results show that the general trend of stability ratio variations is qualitatively predicted, but the calculated stability ratios W_{DLVO} under- or overpredicted the measured colloid stability W_{measured} sometimes by orders of magnitude (Table 2-3 and Table 2-4). Therefore, the DLVO model was modified insofar that the calculated edge charge ζ -potential was kept constant, while the bentonite face charge was varied until the best fit $W_{DLVO, \text{ best fit}}$ was obtained. The derived best fit bentonite face ζ -potentials are plotted as solid lines in Figure 2-15a and Figure 2-16a and the values are given in Table 2-3 and Table 2-4. The different energy contribution (edge-edge, edge-face and face-face) to the total interaction energy are the results for the interaction energy calculations based on the DLVO model of Mahmood et al. [31] and are plotted in Figure 2-17 as a function of the separation distance given in nm. The energy barrier V_{\max} is increasing with higher pH values under constant ionic strength, and therefore an increased colloid stability is expected based on equation (7). For the edge-edge (EE) and edge-face (EF) interaction an attractive interaction energy (Figure 2-17a,c) is calculated for pH < 8 (EE) and pH < 7 (EF) and therefore a fast coagulation in the edge-edge or edge-face mode would be expected. In the total interaction energy calculation (Figure 2-17g) an energy barrier V_{\max} still exists and therefore high stability ratios $W_{DLVO, \text{ best fit}}$ are predicted. For the face-face (FF) interaction energy at 1 mmol·L⁻¹ NaCl background electrolyte pure repulsive forces are predicted over the entire pH range with only minor variations as expected from the fitted surface potential of Figure 2-16a (Figure 2-17e). The FF mode calculation made in this study is comparable to standard DLVO-theory calculations and demonstrate the insensitivity to predict colloidal stability of heterogeneously charged colloids, as already pointed out by Missana and Adell [25].

In the case of 100 mmol·L⁻¹ NaCl background electrolyte the best fit bentonite surface potential decreases from pH 8 (-25 mV) to pH 6 (-12 mV), respectively and for pH 10 it is slightly lower than with 1 mmol·L⁻¹ NaCl background electrolyte (Figure 2-16a). For the higher salt concentration the electric double layer is drastically compressed and has no influence at distances > 5 nm away from the colloid surface and therefore attractive forces based on the van-der-Waals attraction can be calculated. The short range repulsive interactions are not strong enough to build up an energy barrier in the EE mode (Figure 2-17b). For the EF mode a slightly stronger electric double layer develops due to the lower surface potential. This increase in interaction energy is sufficient to develop a small energy barrier and a secondary minimum (Figure 2-17d).

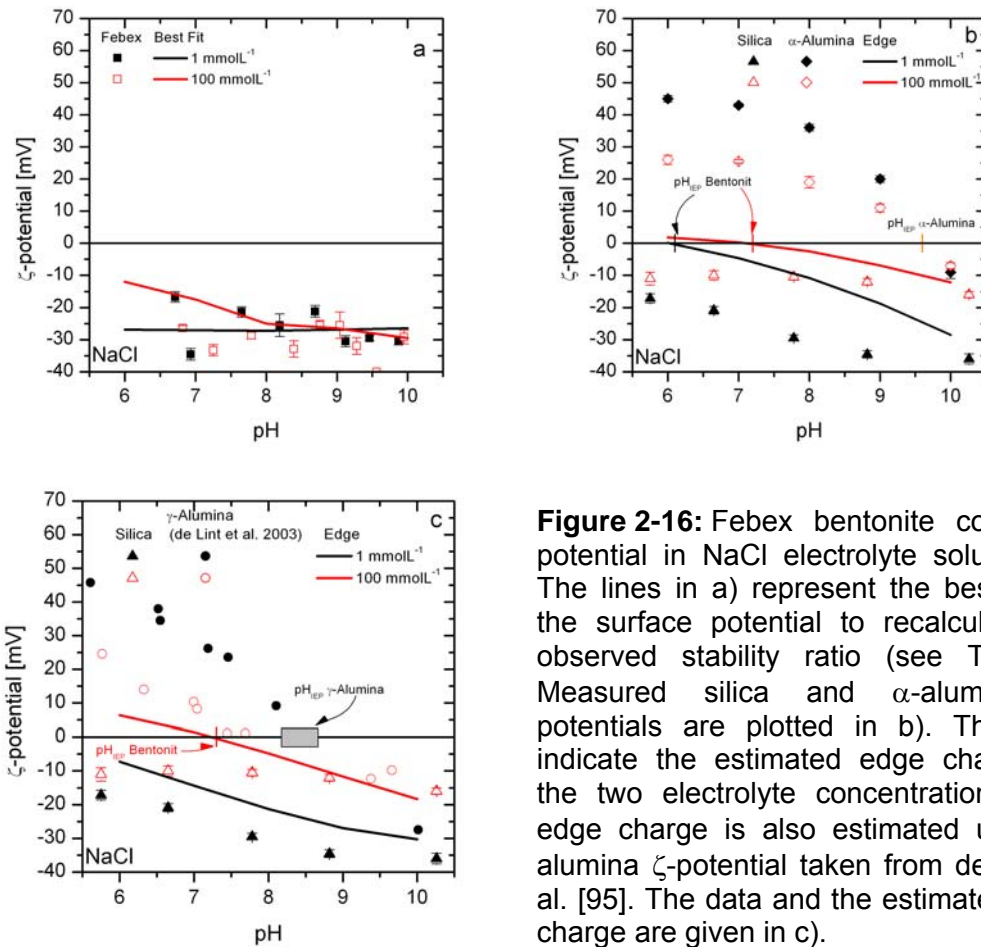


Figure 2-16: Febex bentonite colloid ζ -potential in NaCl electrolyte solution a). The lines in a) represent the best fit for the surface potential to recalculate the observed stability ratio (see Tab. 2). Measured silica and α -alumina ζ -potentials are plotted in b). The lines indicate the estimated edge charge for the two electrolyte concentrations. The edge charge is also estimated using γ -alumina ζ -potential taken from de Lint et al. [95]. The data and the estimated edge charge are given in c).

Table 2-3: Stability ratio W measured with and without addition of $1 \text{ mg}\cdot\text{L}^{-1}$ DOC (GoHy-573 fulvic acid), calculated and fitted for CaCl_2 electrolyte solution.

Concentration [mmol·L ⁻¹]	pH	W_{measured}	W_{DLVO}	$W_{\text{DLVO, best fit}}$	$W_{\text{measured FA}}$
0.33	6	2 ± 0.4	2	2	17373
0.33	7	18 ± 3.0	4	18	16950
0.33	8	211 ± 20	12	222	10000
0.33	9	173 ± 89	38	168	9596
0.33	10	69 ± 12	130	68	5614
33	6	1 ± 0.2	1	1	n.m.
33	7	1 ± 0.2	1	1	n.m.
33	8	1 ± 0.2	1	1	n.m.
33	9	1 ± 0.2	1	1	n.m.
33	10	1 ± 0.2	1	1	n.m.

Table 2-4: Stability ratio W measured, calculated and fitted for NaCl electrolyte.

Concentration [mmol·L ⁻¹]	pH	W_{measured}	W_{DLVO} α - alumina	W_{DLVO} γ -alumina	$W_{\text{DLVO, best fit}}$ α -alumina
1	6	6720 ± 1877	26	27	7105
1	7	9810 ± 220	202	230	9983
1	8	12900 ± 4138	2176	2896	14038
1	9	16000 ± 3856	33763	52949	15506
1	10	19100 ± 4604	794164	1305033	18901
100	6	1 ± 0.2	8	8	1
100	7	2 ± 0.3	17	17	2
100	8	5 ± 0.4	43	44	9
100	9	13 ± 1	130	134	14
100	10	34 ± 5	456	459	37

The energy barrier height can be overcome by thermal motion of the colloids if it lies between $V_{\text{max}} \leq 1 \text{ Jk}_B^{-1}\text{T}^{-1}$ [97] and $V_{\text{max}} \leq 10 \text{ Jk}_B^{-1}\text{T}^{-1}$ [98]. In order to check the reliability of our DLVO calculations for predictive modeling, we calculated the total interaction energy at concentrations of the measured Na-CCC, where by definition no energy barrier, or a barrier $< 10 \text{ Jk}_B^{-1}\text{T}^{-1}$ should be expected. In Figure 2-17h the total interaction for 350 mmol·L⁻¹, the Na-CCC at pH 10, is shown. A barrier height of $\sim 430 \text{ Jk}_B^{-1}\text{T}^{-1}$ still exists and the Na-CCC is not predicted correctly. However, due to the development of a secondary minimum a secondary minimum coagulation can be expected as proposed by some authors [99, 100].

Looking in detail on the different modes of clay platelet interaction, namely EE, EF and FF, reasonable predictions of the Na-CCC based on the energy barrier could solely be made for the EF interaction energy. By varying the electrolyte concentration and keeping the surface and edge potential constant for the pH value of interest, a Na-CCC could be calculated, where V_{max} is $\sim 1 \text{ Jk}_B^{-1}\text{T}^{-1}$ (Figure 2-18a). The determined EF-CCC values are plotted versus the experimentally determined Na-CCC values (Figure 2-18b). In the low pH range of 6 and 7 the EF-CCC is found to be lower than the experimentally determined Na-CCC.

Based on the montmorillonite platelet geometry with a particle thickness δ_p of $\sim 2\text{-}3$ nm and a mean particle diameter of 185 nm the high repulsive barrier of the platelet face might be responsible that the distances of attractive EF interaction cannot be reached. Tombácz and Szekeres [78] describe a shielding of the positive edge charge by the spill-over of the electric double layer (EDL) of the platelet face charge under low electrolyte concentration masking the positive edge charge. For higher electrolyte concentrations the EDL is decreasing and the positive edge charge is not any longer shielded [101, 102]. Secor and Radke [101] give a range of $< 10\text{-}100$ mmol·L⁻¹ electrolyte concentration, where this spill-over is expected, in line with our observed deviations for the calculated EF-CCC (shaded area in Figure 2-18b).

In the pH range ≥ 8 the deviation of the experimentally determined Na-CCC values and the EF-CCC vanishes and the data points approach asymptotically the 1:1 line shown in Figure 2-18b indicating a good agreement between the model predictions and the experimental observations.

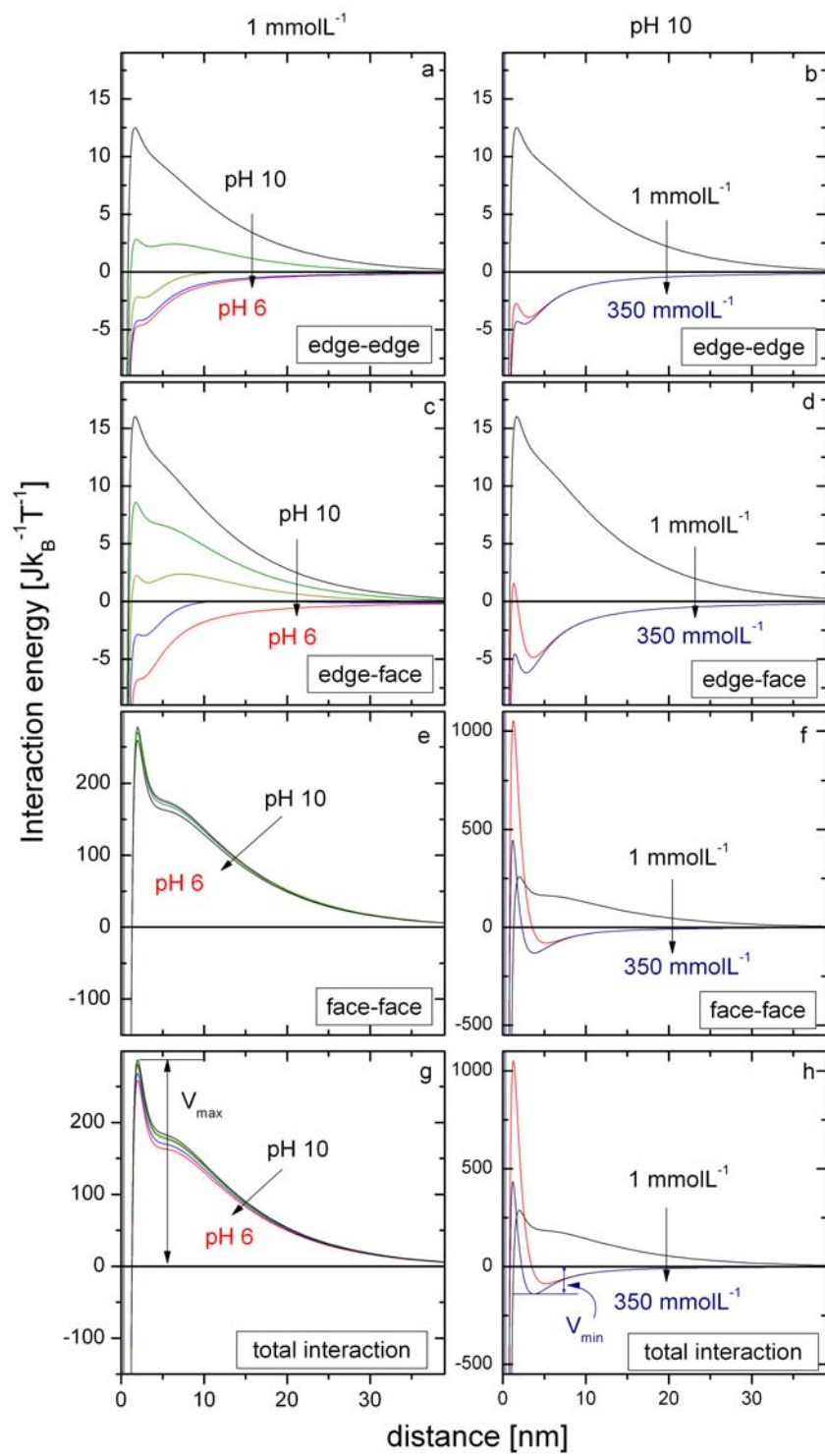


Figure 2-17: Interaction energy calculated for edge-edge (a,b), edge-face (c,d), face-face (e,f) and total (g,h) interaction for Febex bentonite colloids and 1 mmol·L⁻¹ NaCl electrolyte solution as a function of pH (left) and different concentrations at pH 10 (right) for the best fit surface potentials (solid line in Fig. 6a).

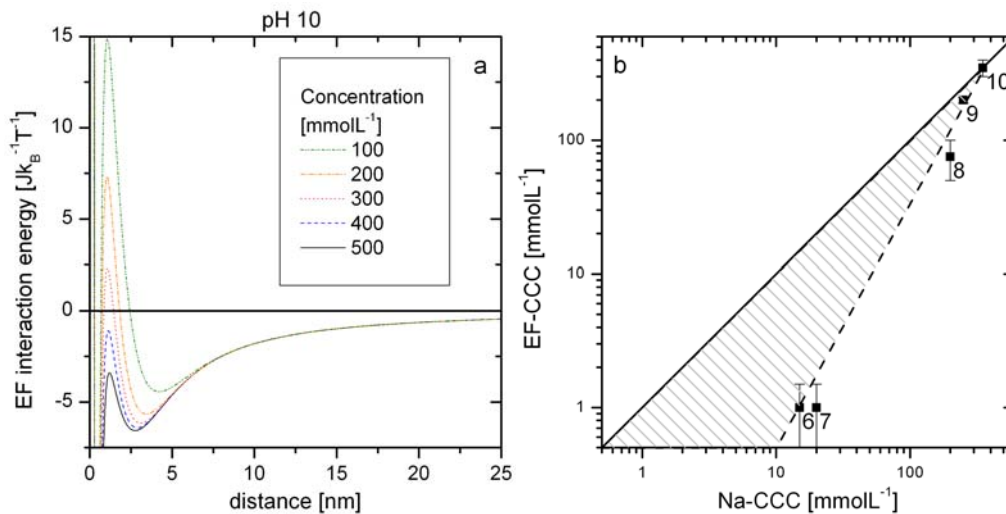


Figure 2-18: Interaction energy calculated for the edge-face (EF) mode of interaction for pH 10 under variation of the concentration variation (zeta- potential of platelet edge and face charge for 1 mmol·L⁻¹ NaCl inserted) (a). The energy barrier is decreasing with increasing electrolyte concentration. (b) Correlation between the measured Na-CCC values (Figure 2-13b) and the CCC derived from DLVO calculations (EF-CCC). The solid line (slope= 1) indicate perfect agreement between model and experiment (Na-CCC = EF-CCC). The shaded area in (b) shows the region of deviation and effect of edge charge shielding due to EDL spill-over.

Conclusions.

- The measurement of colloid stability by means of stability ratio was applied to determine the critical coagulation concentration (CCC) in dependence of pH and electrolyte concentration. For CaCl₂ background electrolyte solution a pH independent Ca-CCC of 1 mmol·L⁻¹ is found. This Ca-CCC gives further confidence in the the safety function criteria of $[\text{M}^{2+}] > 1 \text{ mmol}\cdot\text{L}^{-1}$ for prevention of bentonite buffer erosion as stated in SKB [2]. In NaCl electrolyte solution a pH dependent Na-CCC is determined with $15 \pm 5 \text{ mmol}\cdot\text{L}^{-1}$ at pH 6, $20 \pm 5 \text{ mmol}\cdot\text{L}^{-1}$ at pH 7, $200 \pm 50 \text{ mmol}\cdot\text{L}^{-1}$ at pH 8, $250 \pm 50 \text{ mmol}\cdot\text{L}^{-1}$ at pH 9 and $350 \pm 100 \text{ mmol}\cdot\text{L}^{-1}$ at pH 10, respectively. The Na-CCC values for $\text{pH} \leq 7$ are in good agreement with published data for SWy-1 and beidelite [74]. The size dependence of the CCC can explain the high Na-CCC values for $\text{pH} \geq 8$ found in this study and the scatter of literature data. Fully delaminated Febex bentonite derived montmorillonite platelets show a maximum in the size distribution with the size fraction of 40 nm [103]. For a particle thickness of δ_p of 1.2 nm and this colloid size theoretical calculations by Liu et al. [104] predict a Na-CCC of 200 $\text{mmol}\cdot\text{L}^{-1}$ in very good agreement with our experimental results.
- The addition of 1 $\text{mg}\cdot\text{L}^{-1}$ DOC by fulvic acid (GoHy-573FA) simulating this natural background DOC concentration in granitic environments increases the Ca/FA-CCC to 2 $\text{mmol}\cdot\text{L}^{-1}$. The surface charge is compensated by the adsorbed organic material on the surface of the colloids as could be shown in STXM investigations presented in this study.

- The DLVO model approach by Mahmood et al. [31] takes into account the clay colloids platelet geometry and difference in edge and face charge and was used in this study. The calculations with the measured ζ -potentials of the bentonite (face) and the approximated edge charge following the approach of Williams and Williams [44] show the general trend of higher colloid stability with higher pH value but overestimate the observed colloids stability as shown by comparison of the measured stability ratio W_{measured} and the calculated stability ratio W_{DLVO} . Adjusting the montmorillonite face charge by a maximum of ± 12 mV was sufficient to successfully reproduce the measured stability ratios. Having in mind that the ζ -potential do not represent the real surface charge needed in the DLVO calculations, the model approach could reasonable calculated the measured colloid stability. However, the Na- CCC values could only be reasonably predicted using solely the edge-face interaction energy calculated. The strong deviations of the model predictions and the experimental determined CCC values found at low electrolyte concentrations are explained by the spill-over of the platelet face electrical double layer (EDL) shielding the platelet edge charge.

Further details to the study presented in this chapter can be found in:

Seher, H., W. Hauser, H. Geckeis, T. Fanghänel, and T. Schäfer, (in preparation) Bentonite nanoparticle stability and effect of fulvic acids: experiments and modelling. *Applied Clay Science*.

2.1.4 Colloid generation at the compacted bentonite water interface

Abstract. Bentonite colloid generation was investigated for mono- and divalent electrolytes (Na^+ , Ca^{2+}) with various ionic strengths, pH and filter pore sizes (2 μm , 10 μm , 100 μm). Colloid concentration and average colloid diameter was measured with Laser-induced Breakdown Detection (LIBD). A pH and ionic strength dependent colloid generation was observed. For ionic strengths lower than the CCC a colloid generation can be confirmed. The strong pH dependency of colloid stability in the sodium system previously investigated in coagulation experiments was confirmed in the colloid generation experiments presented in this study. A filter pore size dependent colloid generation mechanism could not be observed in the course of this study. In all experiments the colloid concentration reaches in time a plateau value. Exchange of the contact water lead to a rapid neof ormation of colloids reaching again a plateau value showing a dynamic generation/aggregation equilibrium.

Materials & Methods

Material. For the experiments the smectite-rich Febex (full-scale engineered barrier experiment) bentonite from the deposit of Cabo de Gata, Almería (Spain) is used [60]. The exchangeable cation composition was determined prior to the experiment to be 99 ± 2.1 meq $\cdot 100^{-1}\text{g}^{-1}$. An overview of the used electrolytes, ionic strength and filter pore size in each experiment is given in Table 2-5.

Table 2-5: Experimental conditions for bentonite erosion experiment

Nr.	Density [g $\cdot\text{cm}^{-3}$]	Electrolyte	Ionic strength [mmol $\cdot\text{L}^{-1}$]	Filter pore size [μm]	Filter material	pH start	pH end
E1	1.6	NaHCO_3	10	100		8.7	8.9
E2	1.6	NaHCO_3	5	100		9.5	9.6
E3	1.6	GTS GW*	0.964	100		7.7	7.2
E4	1.6	CaCl_2	1	100	stainless	6.1	7.7
E5	1.6	CaCl_2	5	100	steel	6.0	7.5

E6	1.6	NaCl	10	100		6.5	5.0
E7	2.0	GTS GW*	0.964	2		9.5	n.n.
E8	2.0	GTS GW*	0.964	10		9.5	9.5
E9	2.0	GTS GW*	0.964	10	peek	9.5	9.5

(* GTS GW: Grimsel Test Site ground water)

Experimental setup. A bentonite pellet is confined with a filter plate in all experiments. Two different experimental setups are used. The first setup (Figure 2-19) consists of a stainless-steel cylinder in which the bentonite pellet is squeezed in between two filter plates of 100 μm pore size (CIEMAT setup), for more details see [14]. This reactor is submerged in 0.5 L electrolyte solution and experiments are performed under stagnant conditions.

The INE setup (Figure 2-19) consists of a two sided reactor. A bentonite pellet (19 mm diameter, 10 mm height) with a filter plate and a water tight spacer is inserted into both sides. The reactor has two tubing connections on top and on the bottom of each side to pump the electrolyte solution in circulation through the reactor. One connector is located directly above the filter plate to mimic in later experiments flow induced shear stress on the bentonite surface (for the studies presented here this connection is sealed) and the second connection is designed 6 cm above the filter surface. The volume inside the reactor is 11.6 mL and the reservoir has a total volume of 1 L capacity. The flow velocity at the filter plate surface is calculated with ADINA-F to be in the range of $3.3 \cdot 10^{-6} \text{ m} \cdot \text{sec}^{-1}$. The Reactor is constructed with stainless steel or PEEK material (see Table 2-5).



Figure 2-19: (left) Reactor of the CIEMAT setup in different assembly stages. The bentonite pellet is squeezed into a stainless-steel cylinder by two filter plates. (right) Stainless steel reactor version of the KIT-INE experimental setup. Two bentonite pellets with the PEEK spacer and the filter plates are inserted.

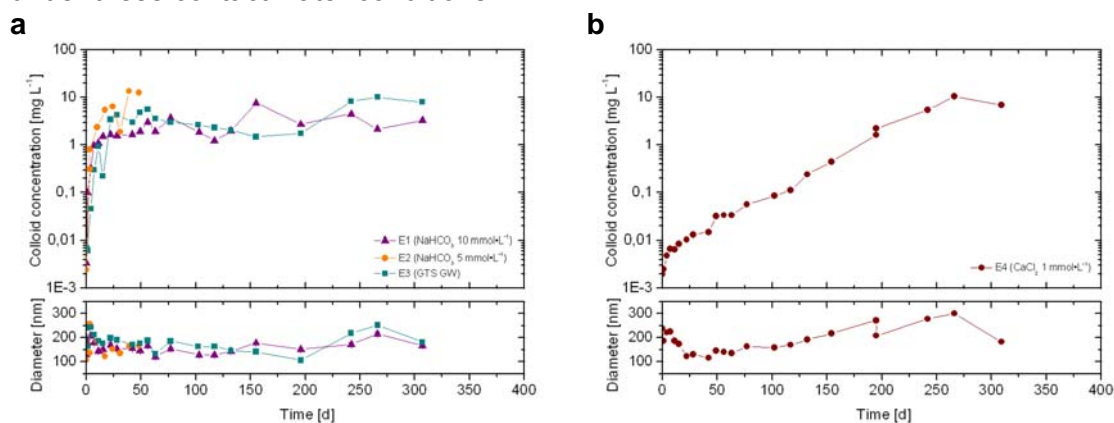
Analytical Methods. The colloid concentration and number-weighted average colloid diameter is determined with a Laser-induced Breakdown Detection (LIBD) system [50]. The sample solution is pumped through a silica flow-through cell. A dielectric breakdown is produced in the focus region of a pulsed laser beam (Nd: YAG-laser, Frequency: 15 Hz, Wavelength: 532 nm). The plasma generated by the breakdown event is monitored by a CCD-camera attached to an image-processing system. The system is calibrated with polystyrene reference particles. Sample aliquots are taken to quantify the bentonite colloid concentration via ICP-MS Al-signal measurement. Additionally pH, Eh and Temperature are measured to monitor changes in the electrolyte solutions.

Results and discussion

The time dependent evolution of the colloid concentration and the number-weighted average colloid diameter determined by LIBD for the different experiments are presented in Figure 2-20. In order to compare the experimental results of the different experimental configurations used (experiment number E1 to E6 CIEMAT setup and E7 to E9 INE setup) all measured concentrations were recalculated to a volume of 1 L contact solution. The data presented here is discussed on the basis of the critical coagulation concentration (CCC), which is the concentration where the aggregation of colloids is solely diffusion controlled [66]; see chapter 2.1.3.

In the NaHCO_3 -system with 5-10 mmol ionic strength (experiments E1 to E2) and a pH variation of pH 8.7-9.6 a comparable colloid concentration increase to a plateau value scattering between $7.1 \pm 4.1 \text{ mg}\cdot\text{L}^{-1}$ and $2.6 \pm 1.1 \text{ mg}\cdot\text{L}^{-1}$, respectively, after approximately 17 days could be observed. Both experiments are with respect to the sodium concentration below the CCC ($\sim 0.3 \text{ mol}$; [105]) and colloid coagulation is not expected. The compacted bentonite in contact with Grimsel ground water (GTS GW) shows from the start of the experiments lower pH values (pH ~ 7.7) compared to the fresh GTS GW, which could be attributed to an influence of atmospheric CO_2 . However, even under this circum- neutral pH the contact water solution ionic strength is below the CCC concentration of $\geq 20 \text{ mmol}\cdot\text{L}^{-1}$ found for monovalent ions. Therefore, the comparable colloid generation observed in the experiments E1 to E3 is in line with the knowledge from colloid stability investigations. The average number-weighted colloid size was in the 5 and 10 mmol $\cdot\text{L}^{-1}$ NaHCO_3 contact solution $158 \pm 19 \text{ nm}$ and $159 \pm 30 \text{ nm}$, respectively, whereas in the GTS GW a slightly higher average colloid diameter of $182 \pm 27 \text{ nm}$ could be detected.

The experiment in contact with a CaCl_2 solution of $1 \text{ mmol}\cdot\text{L}^{-1}$ ionic strength with pH variation ranging from 6.1 to 7.7 (experiment E4; Figure 2-20b) shows a stronger colloid release kinetic with a steady increase in colloid concentration over a period of approx. 250 days reaching uppermost concentration of $10.6 \text{ mg}\cdot\text{L}^{-1}$ and a plateau value of $5.3 \pm 2.7 \text{ mg}\cdot\text{L}^{-1}$ in the latest measurements. Based on the pH independent CCC for CaCl_2 of $1 \text{ mmol}\cdot\text{L}^{-1}$ ($I=3 \text{ mmol}\cdot\text{L}^{-1}$ through $I= \frac{1}{2}\cdot c_j \cdot z_j^2$) reported in [2] and independently determined for Febex bentonite to be in the same range (data not shown) a mobilization of colloids is expected under these contact water conditions.



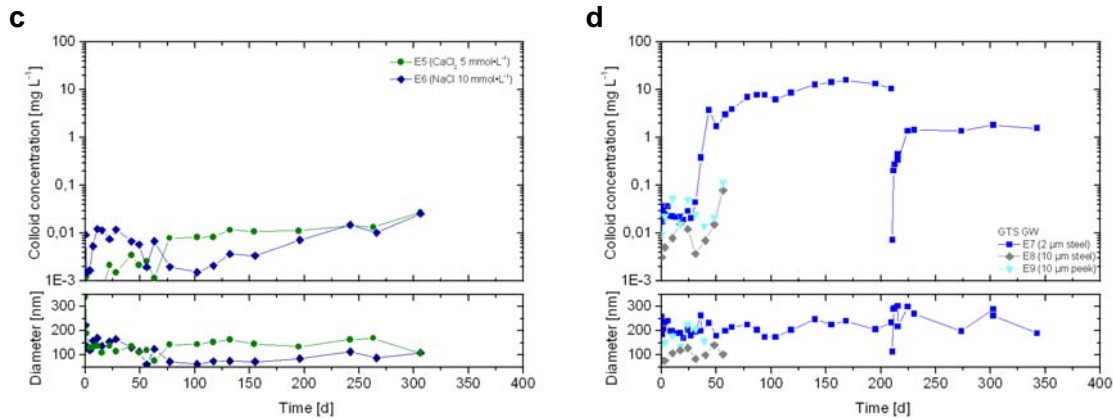


Figure 2-20: Time dependent evolution of the LIBD determined colloid concentration and number-weighted average colloid diameter. The electrolyte concentrations are given as ionic strength.

Interestingly, the average colloid size within 155 days is around 189 ± 52 nm, but in the observation period after 200 days onwards this average colloid size increases to a value of 248 ± 50 nm. Here, the colloid concentration plateau value observed could be explained with a dynamic equilibrium of colloid generation and colloid agglomeration (as indicated by the increasing average colloid size) in the supernatant. Further investigations are in progress to elucidate this hypothesis. For a calcium concentration above the CCC ($1.7 \text{ mmol}\cdot\text{L}^{-1}$ or $I = 5 \text{ mmol}\cdot\text{L}^{-1}$) no colloid generation can be observed (experiment E5), which is fully in line with the colloid stability investigations and the determined CCC.

A further test with $I = 10 \text{ mmol}\cdot\text{L}^{-1}$ NaCl was started at pH values ranging from 5.0 to 6.0. This comparison was needed as the CCC in the sodium system is strongly pH dependent [105] and the value of $10 \text{ mmol}\cdot\text{L}^{-1}$ was determined previously to be the CCC at pH 6. The results of these erosion experiments show clearly that within the observation period the colloid concentration found in solution remains almost constant around $7.3 \pm 4.3 \mu\text{g}\cdot\text{L}^{-1}$ with minimum values of $1.5 \mu\text{g}\cdot\text{L}^{-1}$ and maximum values of $25.8 \mu\text{g}\cdot\text{L}^{-1}$ in the latest measurement. The average colloid size was found to be the lowest observed in all experiments with 116 ± 42 nm.

An explanation for the observed lack in colloid generation under these slightly acidic pH conditions is the protonation of bentonite edge charges and therefore attraction to the permanently negative charged clay platelet faces (due to isomorphous substitution in the tetrahedral or octahedral layers) [27]. This colloid attraction responsible for the aggregation from solution also effectively hinders the release of colloids under these pH values, whereas under the same ionic strength at pH 8-9 due to the deprotonation of these edge groups edge charges a repulsive force is expected and also observed in the colloid generation experiments (see experiment E1; Figure 2-20a). The different colloid generation rates observed in this study can qualitatively be explained by the Schulze-Hardy-Rule [66], where lower concentration of divalent cations are needed for colloid coagulation compared to monovalent cations.

The experiments under variation of the filter pore size (experiment E7 and the newly started experiments E8 & E9) in contact with GTS GW reach a plateau value after ~90 days with colloid concentration plateau values around $9.3 \pm 3.4 \text{ mg}\cdot\text{L}^{-1}$. This is very comparable to the concentrations of $7.1 \pm 4.1 \text{ mg}\cdot\text{L}^{-1}$ and $2.6 \pm 1.1 \text{ mg}\cdot\text{L}^{-1}$ observed for the experiments with 100μm pore size filter frits. The average colloid size in this experiment with 2μm average pore size filter is 210 ± 24 nm and very comparable to the average colloid size found for the

100µm filter frits of 182 ± 27 nm. A delay in the onset of colloid generation is observed for all three experiments which can be explained by the design of the set-up and the calculated traveling time in the reactor from the surface of the filter plate to the injection hole. The flow velocity at the injection hole of $2.8 \cdot 10^{-2} \text{ m} \cdot \text{min}^{-1}$ drops to $3.3 \cdot 10^{-6} \text{ m} \cdot \text{min}^{-1}$ at the filter plate as calculated by ADINA-F simulations. The higher delay in the onset of in experiments E8 and E9 is due to the lower initial flow velocity chosen. Overall, a pore size dependency on colloid generation or the colloid size mobilized could not be observed in our experiments, but might be effective if the filter thickness (here 0.16 mm) is increased based on classical filtration theory [106]. To investigate a fully developed gel layer the water in experiment E7 was exchanged after 210 days. An instantaneous increase in colloid concentration can be observed and after 14 days a plateau value is again reached at concentrations of $1.5 \pm 0.2 \text{ mg} \cdot \text{L}^{-1}$. Furthermore, the mobilized average colloid size is considerably larger with 261 ± 43 nm after contact water exchange. Our current data clearly shows a dynamic equilibrium responsible for the observed colloid concentration plateau value, but further investigations are in progress or planned to gain detailed process understanding.

Conclusions.

- A pH and ionic strength dependent colloid generation from a compacted bentonite source was observed. For ionic strength lower than the CCC determined by colloid aggregation studies a colloid generation can be confirmed, whereas in experiments above the CCC bentonite erosion within the observation period is negligible. The experiments furthermore showed that the strong pH dependency of colloid stability found in the sodium system has the same effect on the colloid generation.
- An effect of the filter pore size (2, 10 & 100µm) on the colloid generation could not be observed, but the effect of filter thickness has to be investigated in new experiments.

Further details to the study presented in this chapter can be found in:

Seher, H. (to be submitted) Influence of colloids on the migration of radionuclides (in German). *PhD Thesis*, University of Heidelberg, Faculty of Chemistry and Earth Sciences.

2.1.5 Colloid – Mineral surface interactions (microscopic approach)

Abstract. The mobility of radionuclides in the far-field strongly depends on sorption/desorption processes with mineral surfaces of the geological barrier. Previous experiments have shown that the interaction of colloids as nanoscopic radionuclide carriers with natural mineral surfaces is complex. Process understanding is made difficult by the fact that multiple processes can act in parallel, e.g., the chemical heterogeneity of the surfaces, the surface roughness, discrete surface charges (on mineral edges or planes) or the surface contamination due to organic matter. Thus, the aim of this work was to gain insight into the interaction of negatively charged model colloids with natural mineral and rock surfaces. This was accomplished using different surface sensitive methods: sorption experiments were carried out with fluorescing carboxylated latex model colloids and Grimsel granodiorite rockforming minerals (quartz, biotite, muscovite, feldspar, apatite, titanite and additionally sapphire as clay mineral model). Sorption of the colloids was made visible by fluorescence

microscopy. By using SEM-EDX those mineral phases were identified on which predominant colloid adsorption took place. Complementary Atomic Force Microscopy (AFM) force spectroscopy experiments using the “colloid probe” technique were undertaken to gain insight into colloid (carboxylated latex sphere) -mineral surface interaction forces. Carboxylated latex spheres were taken as model particles for natural negatively charged colloids. Both experimental approaches showed strong adsorption or attractive forces, respectively, at pH values close to or below the points of zero charge (pH_{pzc}) of the mineral surfaces. The influence of metal cations such as Eu(III) , UO_2^{2+} , and Ca(II) and natural Grimsel groundwater on colloid-mineral interaction was investigated. The experiments indicated that the adsorbed cations may reduce the overall repulsive interaction at pH values higher than the individual mineral pH_{pzc} , but still no colloid adsorption on most of the minerals (quartz, biotite, muscovite, feldspar, titanite, sapphire) was observed in the alkaline regime. However, adhesion forces were significantly enhanced and repulsive forces reduced at high pH in presence of 10^{-4} M Ca^{2+} ions. The shear forces due to groundwater flow were estimated and found to be not high enough to overcome the measured colloid adhesion under all observed conditions. The short-term experiments carried out in this work are not directly transferable to long time scales. DLVO calculations show that the experiments can be well predicted by theory but that the calculations do not regard possibly present hydration forces at separation distances < 5 nm which may prevent a possible colloid adsorption. Results of this study prove that the interaction of colloids with mineral surfaces is determined by electrostatic interactions. According to the results, instantaneous colloid adsorption in alkaline regime can be expected on apatite in presence of Ca(II) or with Grimsel groundwater. The probability of colloid attachment at high pH is significantly increased if Ca(II) is present as compared to pure NaCl systems.

Materials & Methods

Colloids. For the colloid sorption experiments, fluorescent carboxylate-modified polystyrene colloids (functionalized during polymerization) with a diameter of 25 nm were purchased from Postnova Analytics (Landsberg/Lech, Germany). The nanospheres were rhodamine-labeled with an excitation wavelength of 552 nm and an emission wavelength of 580 nm. The concentration of the stock suspension was 10 g/l. The polydispersity index was provided by the manufacturer as < 0.1 and the density of COOH groups is 0.12 mmol/g. The pH of the stock suspension was 4.3. Sample solutions were prepared by diluting the colloid stock suspension with 10^{-2} M NaCl in Milli-Q water to a final colloid concentration of 0.05 g/l. Natural FEBEX-Bentonite (Cabo de Gata deposit, Almeria, Spain) according to the procedure described in detail in chapter 2.1.2.

Sample solutions. Teflon bottles were used to prepare the sample solutions in order to avoid adsorption of colloids or cations on the bottle material itself. The ionic strength was held constant at 10^{-2} M NaCl in the sorption and force spectroscopy experiments. All experiments with background electrolyte only or in presence of Ca(II) were carried out from pH 2-10. The Ca(II) concentration was set to 10^{-4} M; this corresponds to the Ca(II) concentration in Grimsel groundwater. All experiments $> \text{pH } 6$ were carried out in an Ar-atmosphere to prevent CO_2 absorption by the sample solutions. From pH 2-10 Ca(II) exists as free aquo-ion, as proven by speciation calculations with ECOSAT 4.8 (Wageningen University, Wageningen, Netherlands). All experiments in the presence of Eu(III) (CertiPUR Europium ICP Standard, Merck, Germany) were undertaken in the pH range of 2-6 only, since Eu(III) undergoes hydrolysis and may precipitate under alkaline conditions [107]. Under the conditions of our experiments, the Eu(III) -aquo ion exists in solution and interacts with the colloid or the mineral surfaces. The Eu(III) concentration in the sorption and force spectroscopy experiments was set to 10^{-5} and 10^{-6} M. Eu(III) is taken as a surrogate for trivalent actinide ions (Am, Pu, Cm). Additional experiments with UO_2^{2+} as a main component of spent nuclear fuel. Experiments in the presence of 10^{-6} M UO_2^{2+} were carried out in the pH range of 2-6.

The speciation of UO_2^{2+} in water is very complex, since various hydrolysis species (dependent on pH, ionic strength and UO_2^{2+} concentration) exist. Figure 2-21 shows the speciation of UO_2^{2+} in aqueous solution calculated also with ECOSAT 4.8. It can be seen that under the conditions of our experiments the species mainly present species are UO_2^{2+} , $(\text{UO}_2(\text{OH}))^+$, $((\text{UO}_2)_3(\text{OH})_5)^+$, $(\text{UO}_2(\text{OH}_3))^-$ and $(\text{UO}_2(\text{OH})_2)$. More information about the speciation of UO_2^{2+} can be found in [108].

Force spectroscopy and sorption experiments were also carried out with natural Grimsel groundwater to compare measured values obtained from synthetic waters with the natural groundwater. The element concentration in the Grimsel groundwater was determined by ICP-MS (Perkin-Elmer ELAN 6000). As can be seen, the main dissolved constituents present in the groundwater are composed of Na, Si and Ca (Table 2-6). The ionic strength of the Grimsel groundwater is about 10^{-3} M, the pH is 9.6 [32]. In the colloid sorption experiments with Grimsel groundwater, the colloid concentration was set to 0.05 g/l.

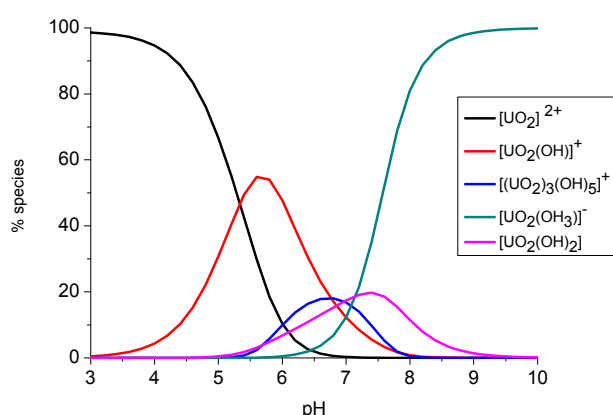


Figure 2-21: Speciation of UO_2^{2+} in aqueous solution, in absence of CO_2 . $[\text{UO}_2^{2+}] = 10^{-6}$ M, $I = 10^{-2}$ NaCl. [108] (see text) [109].

Table 2-6: Element concentration of Grimsel groundwater

Element	concentration [mol/l]
Li	1.05E-05
Na	4.01E-04
Mg	3.18E-06
Al	6.97E-07
Si	1.87E-04
K	5.26E-06
Ca	1.27E-04
Mn	1.16E-06
Ni	4.09E-08
Cu	2.20E-08
Zn	2.22E-06
Rb	1.99E-08
Sr	1.58E-06

Grimsel granodiorite sorption experiments. The individual Grimsel granodiorite samples were equilibrated for three years in Grimsel groundwater (pH 9.6, ionic strength 10^{-3} M; [15]). For the sorption experiments using fluorescent latex colloids, a piece of Grimsel granodiorite

(2×3 cm) was withdrawn from the groundwater and rinsed thoroughly with MQ-water. Then the granodiorite was dipped into the colloid suspension (volume 3 ml). Colloids were allowed to adsorb from fluid to sample surface for 15 min (T = 22 °C). This sorption time was chosen because sorption experiments with longer sorption times up to 2 hours showed no increase in colloid adsorption. The samples were then withdrawn from the suspension and thoroughly rinsed with MQ-water in order to remove any non-adsorbed latex colloids. After drying in an oven at 40°C, the rock samples were investigated by fluorescence microscopy. SEM/EDX was used to identify the minerals on which a predominant colloid adsorption took place. To gain insight into the desorption of colloids from Grimsel granodiorite, an additional long-term desorption experiment taking 37 days was carried out. The colloids were adsorbed onto the granodiorite for 30 min at pH 4, I = 10⁻² M NaCl. The colloid concentration was set to 0.05 g/l. These conditions were chosen to ensure maximum colloid adsorption while minimizing mineral dissolution, which generally increases with decreasing pH values. The Grimsel granodiorite sample was then placed in an electrolyte solution (pH 10 and I = 10⁻² M NaCl). The sample was withdrawn after different time intervals and the fluorescence intensity sure release on the element composition evolution of ÄGW (TRUE-1 site, F measurement to ensure that the rock sample interacts with colloid-free solution. Again SEM/EDX was used for identification of the mineral phases.

Single mineral sorption experiments. All single minerals (biotite, albite, K-feldspar, apatite, quartz and titanite) were commercially available (Krantz Mineralien Kontor, Bonn, Germany). Muscovite was purchased from Plano GmbH (Wetzlar, Germany) and sapphire from Mateck GmbH (Jülich, Germany). With the exception of sapphire, all these minerals are rockforming in the Grimsel granodiorite. Additional experiments with sapphire (001 plane) were carried out since this mineral can be regarded in some respects as a model for clay minerals and analogous iron phases. First, mineral surfaces were cleaned to remove any organic fluorescing impurities on the mineral surface. The minerals were immersed in and rinsed with chloroform, methanol and MQ-water. After this procedure the samples were placed in an oven at 40°C for approximately 3 hours. Sheet silicates like muscovite or biotite were freshly cleaved in order to obtain clean surfaces. Sorption experiments were carried out as described for the granodiorite.

SEM/EDX was applied to determine the elemental composition of the mineral phases. The samples were sputtered with a thin chromium layer and investigated with an acceleration voltage of 15 kV in order to minimize the penetration depth of the electron beam. On each sample, several areas (size 200×300µm) were analysed. The averaged values of the elemental compositions (in atom %) are summarized in Table 2-7. The error of the EDX measurements is estimated to 0.5 - 1.1 atom-%, depending on sample matrix and acceleration voltage.

Table 2-7: EDX data for the single minerals used in the sorption experiments (elemental composition in atom %, values < 1 % not included)

Element	albite	orthoclase	biotite	muscovite	quartz	apatite	titanite	sapphire
Si	21	22	8	10	30		12	
Al	8	7	4	8				43
Na	7							
Mg			4					
K		6	2	3				
Ca						23	15	
P						13		
Fe			2					

O	61	62	63	63	66	61	57	58
Ti							15	

Force spectroscopy experiments with single minerals. AFM Force spectroscopy measurements were carried out on the relevant minerals present in the Grimsel granodiorite (muscovite, biotite, quartz, K-feldspar, apatite, titanite). Surface roughness measurements of the minerals were undertaken in contact mode (in air) directly after the cleaning procedure. The scanning area was 25 μm^2 . The RMS roughness, defined as the root-mean-square of all the distances from the center line of the roughness profile, calculated over the profile length, was obtained using SPIP[®] analysis software (Image Metrology, Hørsholm, Denmark). The measured surface roughness of the minerals is shown in Table 2-8.

Table 2-8: Mineral surface roughness determined by AFM

mineral	RMS roughness [nm]
muscovite	< 0.1 - 0.3
biotite	0.4 – 1.4
quartz	3.4 – 4.2
K-feldspar	1.9 - 3.2
apatite	2.2 - 3.4
titanite	6.1 – 7.2

SEM/EDX (CS44FE Field Emission SEM, CamScan, Cambridge, UK) was applied to determine the average elemental composition of the minerals used for the force spectroscopy experiments. On each sample, several areas (size 200 x 300 μm) were analysed. The results are summarized in Table 2-9. The error of the EDX measurements was estimated as 0.5-1.1 at.%, depending on sample matrix and acceleration voltage.

Table 2-9. EDX data for the single minerals (elemental composition in atom %, values < 1 % not included) used in the force-spectroscopy experiments

Element	K-feldspar	biotite	muscovite	quartz	apatite	titanite
Si	25	8	10	30		12
Al	8	4	8			
Na	1					
Mg		4				
K	8	2	3			
Ca					26	15
P					17	
Fe		2				
O	58	63	63	66	50	57
F					6	
Ti						15

Results & Discussion

Sorption experiments with fluorescent polystyrene colloids. Sorption experiments under varied geochemical conditions with fluorescent polystyrene colloids and Grimsel granodiorite

and its component minerals were carried out in the initial phase of this work. The aim was to detect adsorbed colloids on the natural surfaces by fluorescence microscopy. By measuring the fluorescence intensity a semi-quantitative measure of the adsorbed colloids on the individual mineral surfaces (identified by SEM/EDX) could be achieved. The colloid surface coverage on the individual mineral surfaces was determined by correlating fluorescence intensities of adsorbed colloids on muscovite (measured by fluorescence microscopy) with the number of colloids per unit area (determined by atomic force microscopy (AFM)). Sorption of colloids on muscovite was used here as reference system because adsorbed colloids could be easily detected on the atomically flat surface. Colloid concentration was varied in the range 0.5 - 2 g/l in order to find a sufficient number of colloids on a selected image area. Eu(III) was added with a concentration of 10^{-5} M to increase the colloid adsorption. Images were obtained by tapping-mode AFM on dried samples. The number of colloids per μm^2 was counted at several image areas with different fluorescence intensities. An image of latex colloids adsorbed onto muscovite is shown in Figure 2-22. The height of the colloids in Figure 2-22 was determined as ~ 25 nm and the diameter was in the range of 50-100 nm. It is well-known that lateral dimensions are strongly overestimated due to the common AFM tip artefact, i.e. when the size of a feature is in the range of the tip radius. This is the case for the colloidal particles. The artefacts can be corrected by geometrical models. In the literature, various methods are proposed for the correction of tip artefacts [110, 111]. The PCS measurements also did not show any coagulation of the colloids. Therefore, it can be concluded that mainly single colloids on muscovite were found. Some aggregation on the surface, however, can not be excluded. The area (A) occupied by a single spherical colloid was calculated by $A = \pi r^2$, where r is the nominal colloid radius (12.5 nm). The surface coverage was obtained summing up values of A and relating this sum to the total image area. Surface coverage is given in percent. A fairly linear relation between surface coverage and the fluorescence intensity is found. From the standard deviation (3σ) of the fluorescent background signal (17 ± 0.3 counts) the detection limit of the method was estimated to around 2 colloids/ μm^2 corresponding to a surface coverage of around 0.1 %.

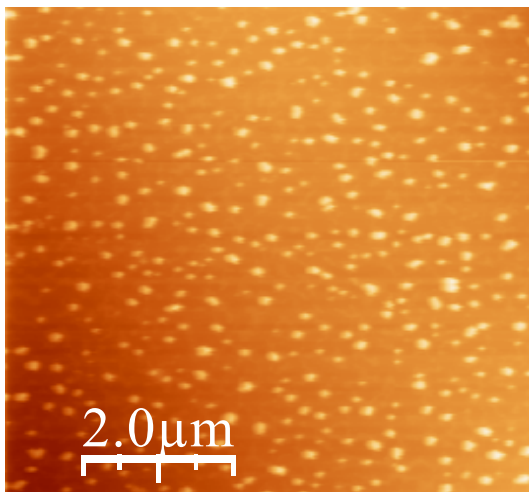


Figure 2-22: AFM image of muscovite surface with adsorbed latex colloids (pH = 4, $I = 10^{-2}$ M NaCl, $C_{\text{colloids}} = 2$ g/l, Eu(III) = 10^{-5} M) (see text)

Carboxylated latex spheres - rockforming mineral interaction

Single minerals relevant for the Grimsel granodiorite system were contacted with various suspensions containing fluorescent carboxylated latex colloids at different pH and Eu(III) concentrations. Additional experiments were carried out with Grimsel groundwater also containing the carboxylated latex colloids. In the fluorescence images, different regions with characteristic features can be distinguished. Sorption on surface areas with mineral edges

was indicated, when fluorescence was detected along straight or wound lines. Sorption on the mineral planes was evident, when homogeneous fluorescence intensity was detected on a certain area without a characteristic morphology. Further experiments were carried out with sapphire which, although, is not a component mineral of Grimsel granodiorite, is regarded in some studies as a model for minerals in this context only selected results will be presented.

Sheet silicates (muscovite and biotite). Figure 2-23 (a) and (b) show fluorescence-optical images of muscovite surfaces after adsorption of fluorescent polystyrene colloids at pH 4 in absence (a) and presence (b) of 10^{-5} M Eu(III). The black coloured areas in Figure 2-23 (a) represent the basal planes where measured intensity values were in the range of the background signal and, thus, no adsorption could be detected. In the bright areas increased fluorescence intensities were measured indicating colloid adsorption. Fluorescence signals could only be detected along straight lines or similar features which are typical for mineral edges. Figure 2-23 (b) shows that in presence of Eu(III) colloid sorption increased and took also place on the muscovite basal planes.

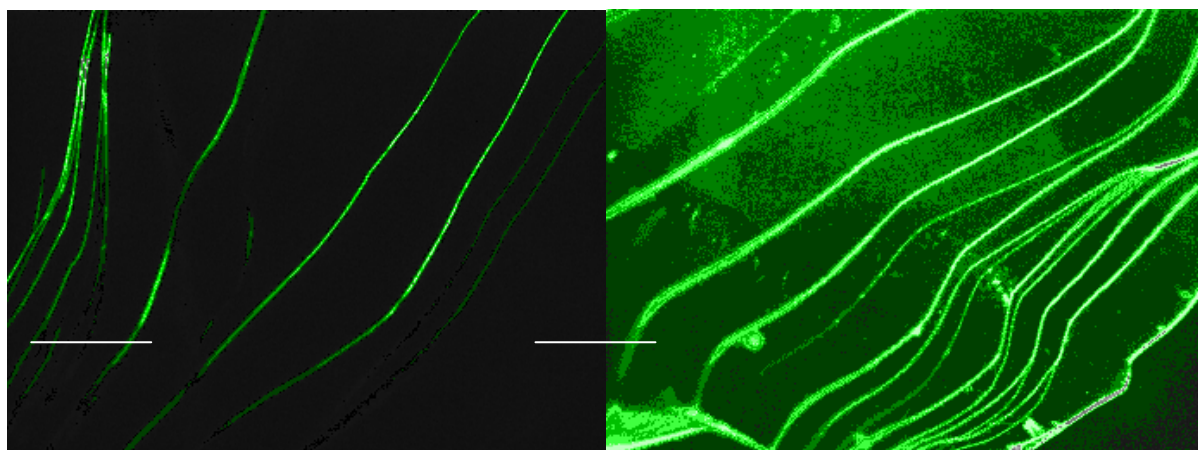


Figure 2-23: Fluorescence-optical image of muscovite (a) after adsorption of fluorescent colloids (pH = 4, $I = 10^{-2}$ M NaCl, $C_{\text{colloids}} = 0.05$ g/l) and (b) in the presence of Eu(III) (pH = 4, $I = 10^{-2}$ M NaCl, $C_{\text{colloids}} = 0.05$ g/l, Eu(III) = 10^{-5} M) (see text)

Figure 2-24 shows fluorescence intensity/surface coverage vs. pH obtained from the adsorption of carboxylated colloids on muscovite in the presence/absence of Eu(III). Figure 2-25 shows similar experimental data obtained for biotite.

Colloid adsorption with Grimsel groundwater. No adsorption of colloids was detected on muscovite and biotite.

Colloid adsorption in the absence of Eu(III). A significant fluorescence signal was detected on the mineral edges (diagonally lined bars in Figure 2-24 and Figure 2-25) under acidic conditions which decreased from pH 2 to 6. In contrast, under alkaline conditions, there was no fluorescence detected at the edges (pH 8-10, not shown).

Colloid adsorption in the presence of Eu(III). In the presence of Eu(III), a significant increase of fluorescence intensity was observed both on edges and planes. In Figure 2-23(b) it can be seen, that sorption also took place on the basal planes of muscovite. Black bars in Figure 2-24 and Figure 2-25 represent fluorescence intensities on basal planes in the presence of 10^{-5} M Eu(III). In the case of biotite, fluorescence was also detectable with a lower Eu(III) concentration (10^{-6} M) (white bars in Figure 2-25). At the edges of both sheet silicates

increased fluorescence intensities were found in the presence of 10^{-5} M Eu(III) from pH 2 to 6 (horizontally lined bars in Figure 2-24 and Figure 2-25). At lower Eu(III) concentration (10^{-6} M) fluorescence intensities at the edges were for both minerals comparable to those obtained in absence of Eu(III) (cross-hatched bars in Figure 2-24 and Figure 2-25).

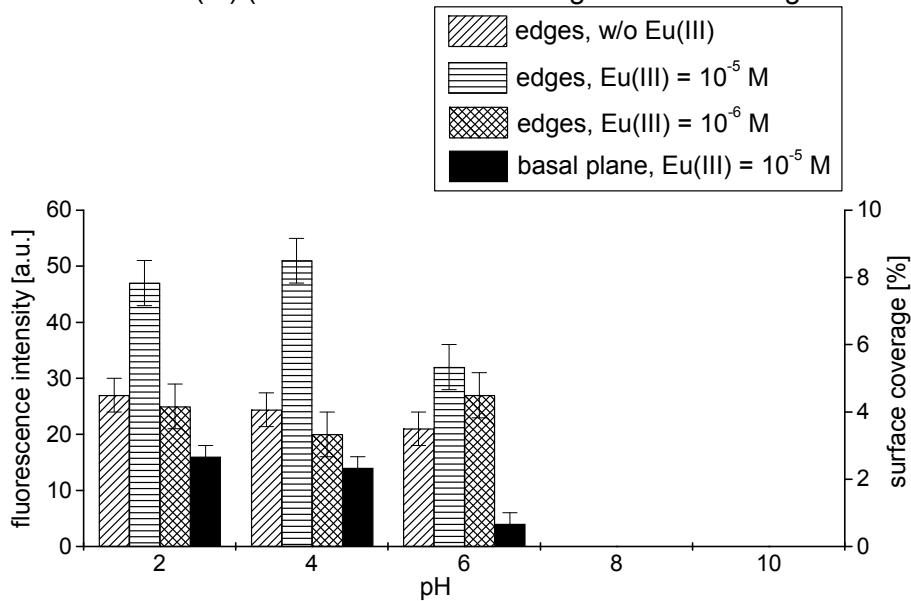


Figure 2-24: Fluorescence intensity/surface coverage vs. pH for muscovite in the presence and absence of Eu(III). All measurements were undertaken at pH 2, 4, 6, 8, 10

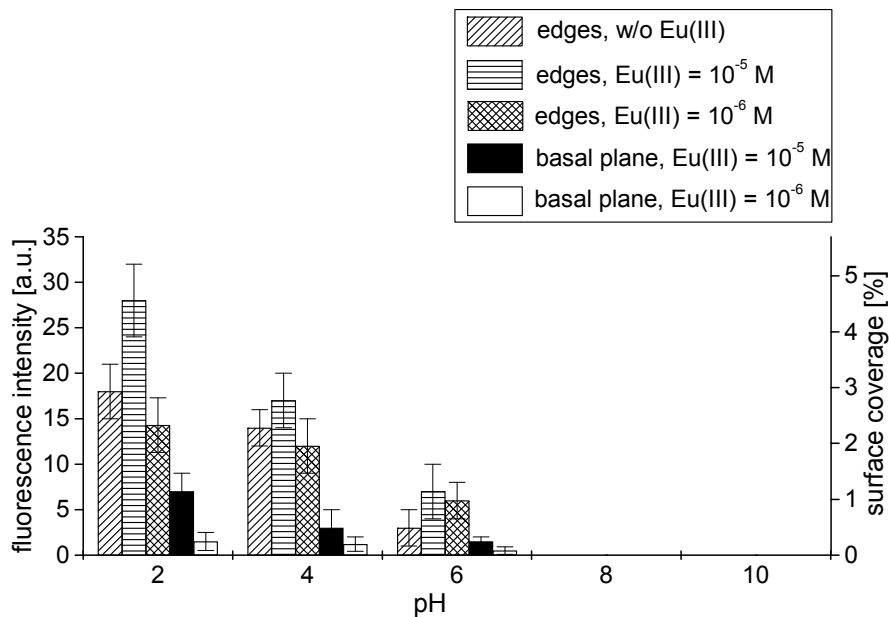


Figure 2-25: Fluorescence intensity/surface coverage vs. pH of biotite in the presence and absence of Eu(III). All measurements were undertaken at pH 2, 4, 6, 8, 10 (see text)

AFM force spectroscopy experiments

With the sorption experiments discussed above, valuable insight into colloid adsorption behaviour under various geochemical conditions was gained. However, these investigations were partly restricted by limited detection sensitivity and quantification of interfacial forces

being active under unfavourable conditions (alkaline pH) was not possible. For this reason, complementary AFM force spectroscopy experiments were undertaken. The force spectroscopy experiments were conducted with the colloid probe technique (a carboxylated polystyrene colloid of 1 μm diameter was attached onto the cantilever as probe) and different relevant mineral phases composing the Grimsel granodiorite. In the following section, the snap-in and adhesion forces derived from the force-spectroscopy measurements will be presented separately. The adhesion force can be seen as the force required to detach an adsorbed particle from the mineral surface, for example by shear forces due to groundwater flow. The snap-in forces can be seen as the responsible forces for the colloid adsorption onto mineral surfaces. The error bars of the measured values are shown exemplary. In this context, only selected results are presented.

Sheet silicates (muscovite and biotite). Figure 2-26 shows snap-in forces measured on muscovite. Black squares represent measurements in the presence of background electrolyte only. Snap-in forces were measured at pH 2 and 3. No obvious influence of Eu(III) and Ca(II) was observed at pH 2 and 3. In the presence of 10^{-5} M Eu(III) (grey diamonds) snap-in forces were also measured at pH 4-6 and were significantly increasing with pH. Experiments with 10^{-6} M Eu(III) (black triangles) showed only comparatively weak snap-in forces at pH 4-6. In the presence of 10^{-4} M Ca(II) (black asterisk), no snap-in forces were measured at pH values ≥ 4 . Similarly, no snap-in forces were observed in the experiments carried out with 10^{-6} M UO_2^{2+} and Grimsel groundwater (not shown).

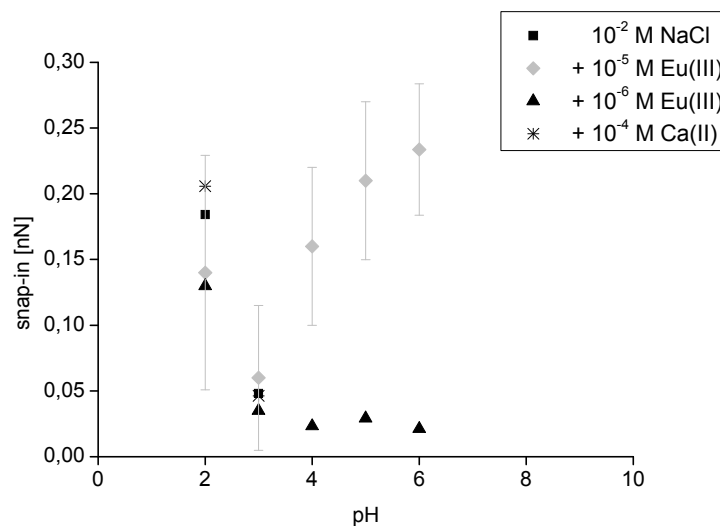


Figure 2-26: Experimental snap-in forces on muscovite (see text)

Figure 2-27 shows adhesion forces measured on muscovite. Measurements with 0.01 M NaCl showed decreasing adhesion forces with increasing pH (black squares). No attractive forces were detected at pH 8 and 10 (not shown). Again, no significant influence of cations was observed at pH 2 and 3. At pH 4-6 an increasing influence of Eu(III) was observed (grey diamonds/black triangles), whereas the higher Eu(III) concentration also had a significant influence on the measured adhesion forces. In the presence of 10^{-4} M Ca(II), adhesion forces at pH 4-10 were significantly increased (black asterisk). The same is true for the experiments with muscovite in presence of 10^{-6} M UO_2^{2+} at pH 4-6 (black diamonds). Experiments with Grimsel groundwater also showed increased adhesion forces (black cross) and were within the same range as the adhesion forces observed with Ca(II) at pH 10.

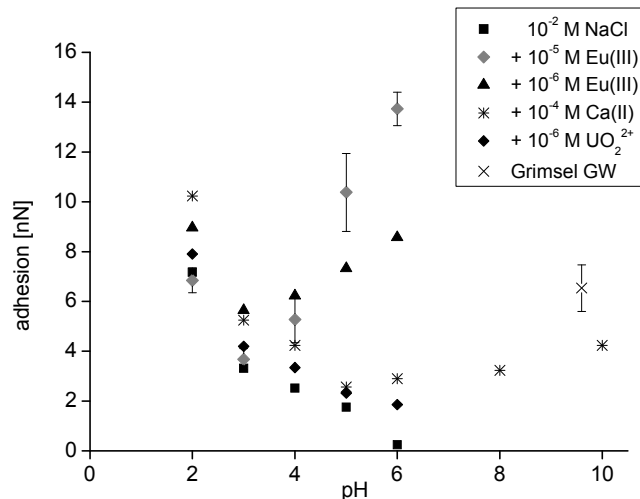


Figure 2-27: Experimental adhesion forces on muscovite (see text)

Figure 2-28 shows measured snap-in forces on biotite. Black squares represent values of experiments carried out with background electrolyte only. Snap-in forces were observed at pH 2 and 3; repulsion sets in at pH 4-10. In the presence of 10⁻⁵ M Eu(III) (grey diamonds) no significant influence was observed at pH 2 and 3, whereas at pH > 4 increased snap-in forces were observed. The presence of 10⁻⁶ M Eu(III) also leads to a slight increase in snap-in forces at pH 4-6 (black triangles). In the presence of 10⁻⁴ M Ca(II) (black asterisk), 10⁻⁶ M UO₂²⁺ and with Grimsel groundwater no influence on the snap-in forces was observed (not shown). Figure 2-29 shows measured adhesion forces on biotite. Black squares represent measured adhesion forces in the presence of background electrolyte only. Adhesion decreased with increasing pH and no attractive forces were measured at pH 8 and 10. In the presence of 10⁻⁵ M Eu(III) significantly increased adhesion forces were observed at pH 4-6 (grey diamonds). 10⁻⁶ M Eu(III) also increased adhesion forces at pH 4-6 (black triangles). 10⁻⁴ M Ca(II) increased the measured adhesion forces at pH 5-10 (black asterisk). With 10⁻⁶ M UO₂²⁺ an increase in adhesion forces was observed at pH 5 and 6. Significant adhesion forces were also observed with Grimsel groundwater (black cross) in about the same range as the measurements with 10⁻⁴ M Ca(II).

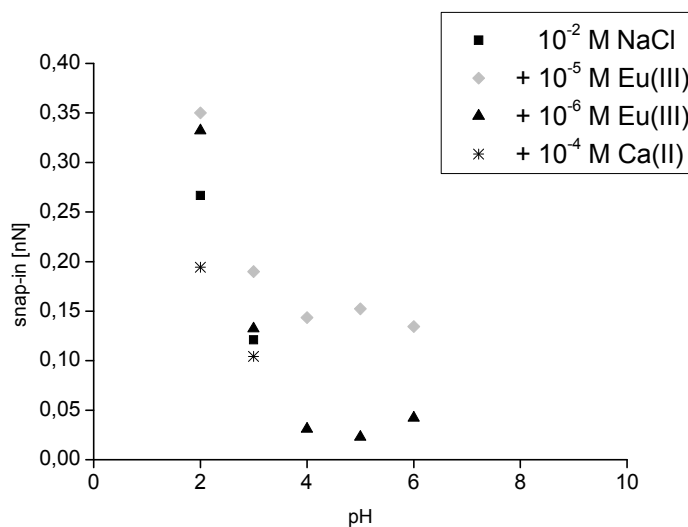


Figure 2-28: Experimental snap-in forces on biotite (see text)

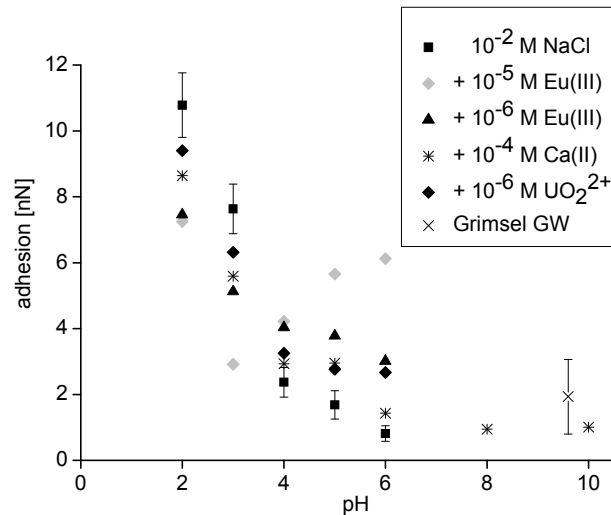


Figure 2-29: Experimental adhesion forces on biotite (see text)

In the present work a novel approach consisting of a combination of fluorescence optical, scanning electron and atomic force microscopy and spectroscopy with adsorption theory was applied for a better understanding of colloid adsorption processes on mineral surfaces.

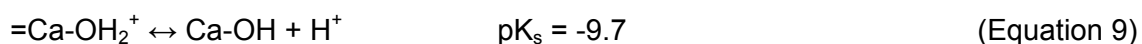
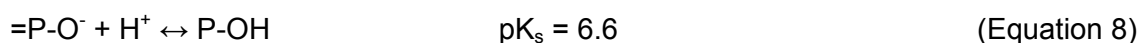
Adsorption of fluorescent carboxylated latex colloids (which act as a model for negatively charged natural colloids, e.g. bentonite colloids) on Grimsel granodiorite and a number of its single component minerals was studied by fluorescence microscopy and SEM/EDX. Although single colloids (< 500 nm) could not be resolved with the experimental setup, it was demonstrated to be very sensitive to quantify colloid adsorption processes. As a complementary technique AFM force spectroscopy with carboxylated latex colloids – used as colloid probes - was used. With this method it was possible to quantify and identify forces responsible for the colloid interaction with mineral surfaces with high sensitivity. Sorption and force spectroscopy experiments were conducted under variation of the geochemical conditions. Adhesion and snap-in forces can be directly quantified by AFM force spectroscopy. However, there are always some imponderables in determining these forces. The adhesion force can be seen as the force required to detach an adsorbed particle from the mineral surface, for example by shear force due to groundwater flow. The snap-in forces can be seen as the responsible (van der Waals) forces for the colloid adsorption onto mineral surfaces. The adhesion forces are always greater than the snap-in forces. This occurs for several reasons: (a) during the contact, some chemical bonds or adhesive bonds may engender non-DLVO forces. (b) during the contact, the colloid probe and/or the sample may be deformed, increasing the contact area, which can lead to increased adhesion forces. Differences between absolute values for snap-in forces and adhesion forces remain approximately constant and lie in the order of ~1 nN. This is quite similar to what is assumed as a typical value for hydration forces in extended DLVO model approaches: 1.6 nN/nm² assuming a contact area of about 943 nm². The different forces in approach and retract modes may thus be explained by short range hydration forces (see also Pashley, R.M., Israelachvili, J.N., 1984: Forces between mica surfaces in Mg²⁺, Ca²⁺, Sr²⁺, and Ba²⁺ chloride solutions. *Journal of Colloid and Interface Science* 97, 446.). In this case the appearance of snap-in forces indicates conditions where colloids manage to cross the hydration barrier. Respective adhesion forces give a measure for the “binding” strength of the colloid to the surface. Furthermore, it is known that adhesion forces decrease with increasing surface roughness (= decreasing contact area) [112]. It can also be assumed that surface roughness may exhibit heterogeneously distributed surface charges which may increase or decrease the snap-in forces as compared to measurements undertaken on smooth surfaces. In the

following text, the results obtained from the measurements and from theory are discussed with special attention to the different sample surfaces.

In the case of the colloid sorption experiments with background electrolyte on sheet silicates, albite, K-Feldspar, quartz and sapphire the decreasing fluorescence intensities with increasing pH can be explained by electrostatic repulsion. With increasing pH, the aluminol- and silanol-(edge) sites of the sheet silicates, feldspars, quartz (only silanol-sites), sapphire (only aluminol-sites) and the colloid carboxyl groups deprotonate resulting in increasing repulsive electrostatic forces. The pH_{pzc} values of muscovite and biotite surfaces were determined as 6.6 and 6.5, respectively. Therefore, both the muscovite and biotite surfaces are negatively charged at alkaline pH values and repulsion towards negatively charged colloids dominates. This corresponds to the finding that on the permanent negatively charged sheet silicate basal planes no colloid adsorption was detected in the alkaline pH regime and in the absence of Eu(III). At pH 2, the surface charge of quartz, albite and K-feldspar is close to its pH_{pzc} ($pH_{pzc} = 2.6$ [113]) and the surface charge of the carboxylated latex particles is relatively low. The neutralization of surface charge (and thus overall reduction of repulsive interactions) resulted in maximum values for colloid adsorption. However on albite and K-feldspar, weak fluorescence was detected even at pH 4, and in the case of albite also at pH 6, where both mineral and colloid surface can be assumed to be negatively charged. This observation cannot be explained by a simple electrostatic description. According to Ryan and Elimelech [114] colloid sorption under repulsive conditions may be attributed to surface roughness and/or chemical heterogeneities. Surface non-idealities, such as cracks, dislocations, geochemical impurities may lead to a nonuniform charge distribution known as "surface charge heterogeneity" [115-119].

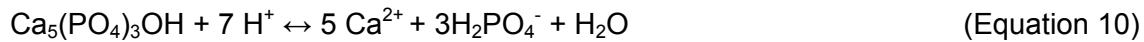
Song et al. [120] developed a theoretical approach for the calculation of a colloid deposition rate onto heterogeneously charged surfaces. They found that even minor charge heterogeneities result in increased deposition rates compared with a homogeneous charge distribution. Theoretical calculations by Adamczyk et al. (1983) [121] showed increased colloid adsorption on solid surfaces due to surface roughness and chemical heterogeneities. Hoek and Agarwal [122] concluded from numerical simulations that rough surfaces are more favourable for colloid deposition due to long range (attractive) van der Waals interactions. Therefore, it can be expected that colloid adsorption is strongly influenced by surface roughness, charge distributions and chemical heterogeneities, especially under electrostatically unfavourable conditions. The colloid sorption experiments with apatite and background electrolyte showed that highest fluorescence intensity was found at low pH values and decreased with increasing pH. But due to the comparatively high pH_{pzc} (about 7.6-8.1) colloid adsorption was observed even at pH 8. The observed trends are (as the minerals discussed above) in accordance with a simple electrostatic description of a positively charged mineral surface at pH values below the pH_{pzc} of negatively charged colloids.

Wu et al. (1991) [123] propose for fluorapatite $=Ca-OH_2^+$ and $=P-O^-$ as dominating surface groups which are characterized by the following equilibrium constants (10^{-1} M NaCl, 25°C):



Based on these equilibrium constants, the same authors expect for hydrous fluorapatite a pH_{pzc} of 8.15 - a value which is close to the pH_{pzc} of hydroxyapatite mentioned above. Solubility data for hydroxyapatite show that increased dissolution of this mineral takes place

with decreasing pH [124]. The dissolution reaction of hydroxyapatite, consuming protons, can be written as follows for acidic pH values [125]:



from the apatite (used in the sorption experiments) was determined by varying pH values from 2 – 8 at constant ionic strength (10^{-2} M NaCl) for 15 min. At pH 2 a weak dissolution of apatite during the experiment was observed resulting in a Ca concentration of about 5×10^{-5} M determined by ICP-MS. This low Ca concentration does not increase the ionic strength of the solution significantly and thus should not have a noticeable impact on colloid stability.

The force spectroscopy experiments on the sheet silicates could only be carried out on the basal planes of the sheet silicates as the mineral edges were not accessible in a defined way. In contrast to the sorption experiments, in the force spectroscopy experiments at low pH and 0.01 M NaCl attractive snap-in forces were detectable on the sheet silicates. A reason for this contradiction may be the larger area of interaction of the larger colloid ($\sim 1 \mu\text{m}$) compared to the smaller colloids ($\sim 25 \text{ nm}$) used in the sorption experiments. An effective contact area A between the $1 \mu\text{m}$ diameter colloid probe and a flat surface can be estimated to 943 nm^2 by using the Langbein approximation [112]: $A=2\pi rx$, where r is the colloid radius and x the separation distance. At contact x can be estimated to 0.3 nm . In contrast, the effective contact area of the fluorescent polystyrene colloids can be estimated to only 23 nm^2 . Because of the larger interaction area it may be that attractive snap-in forces lead to colloid adsorption at low pH values (where the negative surface charge of the basal planes and colloids are already minimized). Another reason for the different behaviour of fluorescent dyed polystyrene particles and the colloid probe is their different surface charge being lower for the particles used for the colloid probes. In agreement with the sorption experiments, no attractive snap-in forces were measured $> \text{pH } 3$ due to the increasing repulsion between the surfaces. The force spectroscopy measurements with K-feldspar and quartz showed that, in the absence of additional cations, snap-in forces have maximum values at low pH corresponding to maximum fluorescence intensities in the sorption experiments. The observation that snap-in forces were detected on K-feldspar even at pH 4 and that these forces were not detectable above this pH also agrees with the results of the sorption experiments. Since the pH_{pzc} of the quartz used in the force spectroscopy experiments was determined to 3.8 this observation can be explained by electrostatic attraction.

The corresponding force measurements with apatite and background electrolyte contrasted somewhat with the sorption experiments: maximum snap-in forces were observed at pH 5 and with decreasing pH they also decreased, whereas in the sorption experiments the fluorescence increased with decreasing pH. Above the pH_{pzc} , no attractive snap-in forces were measured, an observation which corresponds again with the sorption measurements. The decrease of attractive forces with decreasing pH is an unexpected result, since an increase of positive mineral surface charge is expected with decreasing pH. Furthermore, the colloid surface charge will become less negative with decreasing pH. It is known from the literature that with decreasing pH dissolution of the mineral surface takes place [124]. AFM contact mode images at different pH clearly prove the increasing surface roughness with decreasing pH. It can be assumed that mineral dissolution results in a smaller effective contact area between the colloid and mineral surface. This in turn can significantly reduce the attractive van-der-Waals and adhesion forces [34, 112, 126, 127]. It can only be speculated why the force spectroscopy measurements show contradictory behaviour compared to the sorption experiments: since different types of minerals were used in the sorption (hydroxyapatite) and force spectroscopy experiments (fluorapatite) colloid adsorption and mineral dissolution behaviour may differ.

Regarding the sorption experiments on the sheet silicates in the presence of Eu(III) a significant increase of fluorescence intensity both on mineral edges and planes was observed. Eu(III) also affected the colloid adsorption on the basal planes where no adsorption was observed in the absence of polyvalent cations. These observations are in agreement with a binding mechanism involving polyvalent cation bridges [128] and was also assumed in the case of colloid adsorption of negatively charged humic colloids on muscovite [129]. At the edges of both sheet silicates increased fluorescence intensities were found in the experiments with the higher Eu(III) concentration. Colloids can obviously adsorb under these conditions on the edge aluminol- and silanol groups [130]. The increase of colloid-mineral adsorption in the presence of polyvalent cations at low pH at first glance is surprising. Inner-sphere complexation to either carboxylic acid groups of colloids or surface hydroxyl groups of the minerals should not be relevant at pH 2. The colloid surface charge is not significantly influenced by the presence of Eu(III), even though Eu(III) is present in excess over the carboxylate groups (10^{-5} M Eu(III) vs. $6 \cdot 10^{-6}$ eq/l COOH). This indicates no or only low Eu(III) adsorption on the colloids, which is in agreement with the literature [131]. It can be assumed that at low pH Eu(III) is enriched at mineral surfaces by physisorption or cation exchange against, e.g., H^+ , K^+ , Ca^{2+} or Al^{3+} . The enhancement of colloid adsorption may be explained by surface bound Eu(III) which induces high local charge density. The force spectroscopy experiments with the sheet silicates in the presence of Eu(III) showed comparatively increased snap-in forces at pH values ≥ 4 . This corresponds to the sorption experiments carried out with the fluorescent colloids in which increased fluorescence was also seen in presence of 10^{-5} M Eu(III). In contrast to the sorption experiments, attractive snap-in forces could be measured on muscovite even at the lower (10^{-6} M) Eu(III) concentration. This observations speaks for an comparatively increased sensitivity of the force spectroscopy.

On the feldspars albite and K-feldspar and with sapphire a significant influence of Eu(III) on colloid adsorption was observed in the sorption experiments, which in the case of K-feldspar was dominated by the mineral edges. The colloid adsorption experiments in the presence of Eu(III) showed that the influence of this cation strongly depends on pH. Due to the protonation of the involved surfaces there was no influence of Eu(III) observed at pH 2. At pH 4 and 6, the influence of Eu(III) is more significant, depending on the Eu(III) concentration. This corresponds to the force spectroscopy measurements with K-feldspar, where a significant increase of the snap-in forces (dependent on Eu(III) concentration) at pH ≥ 4 was observed. Blum and Lasaga [132] and Walther [133] state that, for feldspars, $\{>(Al, Si)-OH_n^{n-}\}$ groups at the surface are the dominant charged species which are potential binding sites for Eu(III). Similar findings were observed in the sorption experiments with quartz. In the presence of the lower Eu(III) concentration no effect could be detected, although one can assume that Eu(III) adsorbs on the quartz surface at pH > 4 . This was supported by the fact that in the presence of the higher Eu(III) concentration a weak colloid adsorption was detected at pH 6. Eu(III) binds to the silanol-groups on the quartz surface and thus increases the positive mineral surface charge. In analogy to the sorption experiments, snap-in forces were observed on quartz at pH 6 in the presence of Eu(III). But compared to the sorption experiments, the force measurements detected snap-in forces also at pH 4. This observation can again be seen as an evidence for a comparatively increased sensitivity of the force measurements.

The colloid sorption experiment with apatite in the presence of Eu(III) showed an increase of the measured fluorescence intensities only with high Eu(III) concentrations. This observation might be explained by a complexation of Eu(III) with remaining negative complexing groups on the mineral surface, thus increasing the positive mineral surface charge. This idea is supported by the fact that the strongest colloid fluorescence was found at pH 6. The force spectroscopy experiments with apatite did not show any influence of Eu(III) (pH 2-6)

compared to the measurements in absence of these cations. Due to the increased mineral dissolution Eu(III) are possibly not adsorbed on the apatite surface.

Regarding the force spectroscopy experiments with the sheet silicates, K-feldspar and quartz in presence of Ca(II) and UO_2^{2+} no conceivable influence of these cations on the snap-in forces could be observed. It can be assumed that these cations will adsorb onto the mineral surfaces at pH values ≥ 4 but the resulting snap-in forces were not detectable in our experiments. The force spectroscopy experiments with apatite (from pH 2-8) in presence of Ca(II) and UO_2^{2+} also showed no measurable influence of these cations. Due to the increased mineral dissolution of apatite Ca(II) and UO_2^{2+} are also possibly not adsorbed on the apatite surface.

At pH 10, the adsorption of Ca(II) onto apatite and the colloid may increase the apatite surface potential which leads to the increased adhesion and snap-in forces. For apatite the measured snap-in forces are highest as compared to all other mineral surfaces under investigation showing the strong affinity of the surface towards negatively charged colloids. One may thus assume that the impact of sorbing cations is of second order and does not significantly modify the apatite surface charge properties.

The sorption and force spectroscopy experiments with quartz, K-feldspar, the sheet silicates, sapphire (only sorption experiment) and titanite and Grimsel groundwater proved that significant colloid adsorption did not take place since neither fluorescence nor snap-in forces were detected. Cations present in the groundwater may adsorb onto the involved surfaces but apparently still the repulsive forces are not sufficiently minimized to allow for (detectable) colloid adsorption. The experiments with Grimsel groundwater and apatite showed that both types of experiments complement each other well: snap-in forces and colloid adsorption were detected and thus colloid adsorption can be expected under natural conditions on this mineral. It can be postulated that the Ca(II) ions dissolved in the groundwater will adsorb onto the mineral and colloid surface thus reducing the overall negative potential.

Three positions on the muscovite basal planes are available to cations: (1) as counter-ions in the diffuse layer, (2) as adsorbed hydrated ions at the Stern plane and (3) as dehydrated ions residing in the lattice cavities of the basal sheet [134]. An adsorption of these cations onto the surface of the sheet silicates at pH > 4 is likely but obviously the repulsive energy barrier can not be overcome by the colloids at least during the time period of the experiments. Both sorption and approach mode force spectroscopy experiments carried out with Grimsel groundwater did not show any attractive colloid-surface interaction.

The adhesion forces measured on the sheet silicates, K-feldspar and quartz decreased with increasing pH in the presence of background electrolyte. This observation can be explained by the increasing negative surface charges (and thus repulsive interaction) both on the mineral and on the colloid surface. Eu(III), Ca(II) and possibly also UO_2^{2+} adsorb on the colloid and also on the mineral surface at pH values ≥ 4 reducing repulsive forces and thus leading to increased adhesion forces. To sum up, the observed trends of the adhesion forces on the minerals named above can be explained also by electrostatic interactions. Highest adhesion forces with background electrolyte were observed in the experiments with muscovite and biotite followed by apatite, K-feldspar and finally quartz. Regarding the snap-in forces, the highest values were observed on apatite, muscovite, biotite, K-feldspar and quartz. Thus, it can be concluded that apatite and the sheet silicates are most prone to colloid adsorption, whereas on quartz the least adsorption of colloids can be expected.

Force-volume measurements. In the force-volume measurements no significant deviations of the snap-in or adhesion forces from those obtained in the single point measurements were

observed. It can be assumed that the size of the colloidal particle plays an important role because the net force acting between colloid and surface depends on the interaction area. As stated above, the effective contact area between colloid probe and flat surface can be estimated to around 940 nm². Possible variations of surface charge will be averaged over this relatively large contact area. Thus, a possible effect of surface charge heterogeneities under all measurement conditions will depend on the relative size of the particle with respect to the relative size of the heterogeneously charged regions.

Grimsel Granodiorite. In the Grimsel granodiorite system, colloid sorption mainly takes place on the minerals apatite, illite, titanite, biotite (pH 2-6) and K-feldspars (pH 2-4). No adsorption could be detected at alkaline pH in measurements with background electrolyte only and with Grimsel groundwater. In the presence of Eu(III) increased colloid sorption on granodiorite is detected. These observations agree with those made with the single minerals. The desorption experiment with Grimsel Granodiorite showed that colloid adsorption is reversible. This was expected because in the corresponding force spectroscopy experiments with pH = 10 and I = 10⁻² M NaCl only repulsive interaction was detected on the Grimsel granodiorite main component minerals. Furthermore, in the colloid adsorption experiments under the same conditions no colloid adsorption was found.

To assess whether the adsorbed colloids might be sheared off the mineral surfaces by groundwater flow an approximation of the shear forces generated by water flow was developed by Nasr-el Din [135]: $F_D = 1.7009(6\pi\mu_v r v_x)$ where r is the colloid radius, μ_v the dynamic viscosity and v_x the fluid velocity. Under natural conditions, groundwater flow velocities of about 1 - 10 m/a can be expected, whereas in the Grimsel system the groundwater flow velocity is about 1 m/a [40]. Shear forces in the range of 8·10⁻⁷ nN – 8·10⁻⁶ nN were estimated for flow velocities of 1m/a and 10 m/a, respectively. Since all measured adhesion forces were significantly higher than the estimated shear forces, it can not be expected that the colloids, once adsorbed, will be remobilised from the surface due to ground water flow. Even with the artificially generated higher flow velocities in the CRR project in the GTS [16] no colloid mobilisation can be expected. Estimated shear forces were here in the range of 10⁻² nN, which is still slightly lower than the lowest experimental adhesion forces except if groundwater chemistry changes.

Some studies [32, 136] showed significantly colloid retention in laboratory and field studies under unfavorable colloid attachment conditions. If electrostatic interaction, as shown here, can be ruled out as the origin of colloid retention under repulsive conditions, other mechanisms for colloid retention must exist. Missana et al. [137] studied the dependence of colloid recovery on colloid concentration and water flow rate in a Grimsel granodiorite core. At very low flow rates and low colloid concentrations the colloid recovery was near 100 %, whereas decreased recoveries of only 20 % with high colloid concentration were found. The authors concluded that in the highly concentrated clay suspensions stronger particle-particle interactions may lead to ripening effects: a multi-layer adsorption of the colloids onto the surface of the stationary phase may take place. As a consequence, the deposition rate of colloids increases with increased number of adsorbed particles. Another reason for decreased colloid recoveries under repulsive conditions may be plugging of the flow paths: if colloids cannot be totally washed out from the fractures, they might plug the flow path as pointed out by Sen and Khilar [138]. According to these authors, entrapment of colloids can occur due to colloid size exclusion, e.g., at pore constrictions, multiparticle bridging and surface deposition. The probability of entrapment of colloids is relatively high for porous media (such as occurs in fractured zones having small pore constriction size distributions [40]). Increased colloid filtration under repulsive conditions may also occur since mineral surfaces will always have a certain surface roughness which might influence the colloid adsorption behaviour. Ryan and Elimelech (1996) reported higher than predicted colloid-rock

attachment under repulsive conditions and hypothesised the role of the surface physical heterogeneities, i.e., surface roughness.

Our experiments all were carried out in a comparatively short time. Colloid attachment to surfaces, however, is strongly kinetically driven. The probability for colloid “sticking” to the surface directly depends on the height of the repulsive energy barrier. At high Coulomb barriers colloid attachment may exist but is then only visible after long experimental times. It is thus remarkable that even 10^{-4} mol/L Ca^{2+} induce a significant reduction of the repulsive barrier even under high pH and low ionic strength conditions and thus favour colloid attachment. The low Ca^{2+} concentration may therefore contribute to a colloid retention at slow groundwater velocities. In this sense, short-term experiments carried out in this work are not transferable onto long time scales. Finally, we have to note that our carboxylated latex colloids cannot entirely mimic clay colloid behaviour. Clay colloid edge and basal planes exhibit different pH dependent surface charge properties leading to e.g. unique agglomeration mechanisms such as edge to edge, edge to plane and plane to plane agglomeration under specific geochemical conditions. At the high pH conditions of the Grimsel groundwater, however, all crystal planes should be equally negatively charged. Measured zeta potentials for clay colloids are in addition lower than those of the used latex colloids. Clay colloid tendency to attachment should thus be higher than those of carboxylated latex spheres.

Conclusions.

- The results of this study show that the interaction of colloids with mineral surfaces is mainly controlled by electrostatic interactions. Strongest attractive forces are observed close to or below the individual pH_{pzc} of the minerals.
- According to the results, colloid adsorption in alkaline regime (e.g., Grimsel groundwater conditions) can only be expected on apatite in the presence of $\text{Ca}(\text{II})$ or with Grimsel groundwater. Since apatite occurs only in trace concentrations in the Grimsel Granodiorite, only negligible colloid retention (due to electrostatic interaction) would be expected in the Grimsel system. However, carboxylated latex spheres can not fully be regarded as surrogates for clay colloids. Their adsorption behaviour thus may be to some extent different.
- Further research is necessary to understand colloid filtration under repulsive conditions, especially the role of physical heterogeneity and plugging effects, e.g., by carrying out colloid transport or adsorption experiments on (e.g., chemically inert) surfaces with defined surface roughness. Another focus has to be set to the possibility to study clay colloid interaction with mineral surfaces without taking model colloids.

Further details to the study presented in this chapter can be found in:

Filby, A., M. Plaschke, H. Geckeis, and T. Fanghänel (2008): Interaction of latex colloids with mineral surfaces and Grimsel granodiorite. *Journal of Contaminant Hydrology*, 102(3-4): p. 273-284.

2.1.6 Core migration studies

Abstract. The transport of Eu(III), Tb(III), Th(IV) and U(VI) has been studied in core migration experiments with a natural fracture overcored at the Grimsel test site, Switzerland using natural Grimsel groundwater (GGW, Ionic strength $0.964 \text{ mmol}\cdot\text{L}^{-1}$, pH 9.6). Colloid breakthrough is measured with Laser-induced breakdown detection (LIBD) and ICP-MS analysis. As tracer cocktail Febex colloids, Eu(III), Tb(III), Th(IV) and U(VI) (each $10^{-7} \text{ mol}\cdot\text{L}^{-1}$) and NaBr ($10^{-2} \text{ mol}\cdot\text{L}^{-1}$) as conservative tracer are injected. Eu(III), Tb(III) and Tb(IV) are quantitatively attached to the colloids prior to the injection as proven by ultracentrifugation and ICP-MS analyses. The colloid breakthrough curve (BTC) maximum is observed prior to the conservative tracer BTC as expected. The metal ion recovery decreases as a function of residence time with Eu(III) and Tb(III) showing faster bentonite colloid desorption compared to Th(IV). The U(VI) BTC could not be detected within the observation period of the experiments.

Materials & Methods

Grimsel granodiorite core: The core used in the transport experiments was provided by NAGRA, Switzerland. It was drilled in elongation of the MI-Shearzone in the VE tunnel of the Grimsel test site (GTS), Switzerland. The core consists of medium to coarse grained Grimsel granodiorite with a structural discontinuity of brittle and ductile deformation. The granodiorite consists mainly of 23 vol.% quartz, 23 vol.% plagioclase, 20 vol.% potassium feldspar and 25 vol.% sheet silicates (biotite, muscovite and chlorite) [139]. The shear zones in the granodiorite were formed during a ductile deformation. Afterwards a brittle deformation destroyed the mylonitic structures and formed the fracture filling material as well as the flowpaths. The fracture filling material shows high content of biotite (41 vol.%), albite (28 vol.%) and detectable quantities of clay minerals (0-1 vol.%) [139]. The granite core was not water tight due to the overcoring and core retrieval process. An epoxy resin was used to seal the core at the surface (Figure 2-30a). The upper and lower side of the core was cut plane after the coating was applied. A borehole with 4 cm diameter was placed in the middle of the core with a 90° angle to the fracture (Figure 2-30b). The final height of the core is 28 cm and the diameter 23. The flow path from the borehole in the middle of the core to each side is 12 cm. A packer system, produced by Solexperts AG (Switzerland), was inserted into the borehole and screwed into place (Figure 2-30c). The tracer cocktail can be injected into 8 different Peek pipes. Grimsel groundwater (GGW) is pumped from the bottom through the core in the transport experiments with a peristaltic pump (Ismatec). The tracer cocktail and additional GGW is pumped through one pipe in the packer system with a second peristaltic pump (Gilson). For very low flow velocities syringe pumps (Kd-Scientific) are used instead of the peristaltic pump.

Tracer cocktail: The colloid tracer cocktail was prepared with GGW. The metal ions Eu(III), Tb(III), Th(IV) and U(VI) were added after the addition of Febex bentonite colloids into the GGW from a $10 \text{ mg}\cdot\text{L}^{-1}$ ICP-MS standard solution with a final concentration of $1\cdot 10^{-7} \text{ mol}\cdot\text{L}^{-1}$. NaBr as conservative trace is added in a concentration of $1\cdot 10^{-2} \text{ mol}\cdot\text{L}^{-1}$. Each tracer cocktail was prepared 2-3 days before the experiments and stored under argon atmosphere. The pH was fixed to the natural GGW pH value of 9.6 by addition of NaOH. The bentonite colloid concentration was determined via ICP-MS Al concentration. The metal ion association with the bentonite colloids is tested by ultracentrifugation of aliquots at 90,000 rpm for 60 minutes ($\sim 5\cdot 10^5 \text{ g}$) and ICP-MS analysis (Table 2-10 to Table 2-12). The bentonite colloid size is monitored with PCS throughout the duration of the experiment.

a)

b)

c)



Figure 2-30: Preparation of the core from the Grimsel test site, Switzerland, for the transport experiments. At the surface of the core epoxy resin is used as sealing material (a). Afterwards both ends were cut and a borehole was drilled in the middle of the core with a 90° angle to the fracture zone (b). The packer system and drilled core from the location where the packer system is placed into the Grimsel core (c).

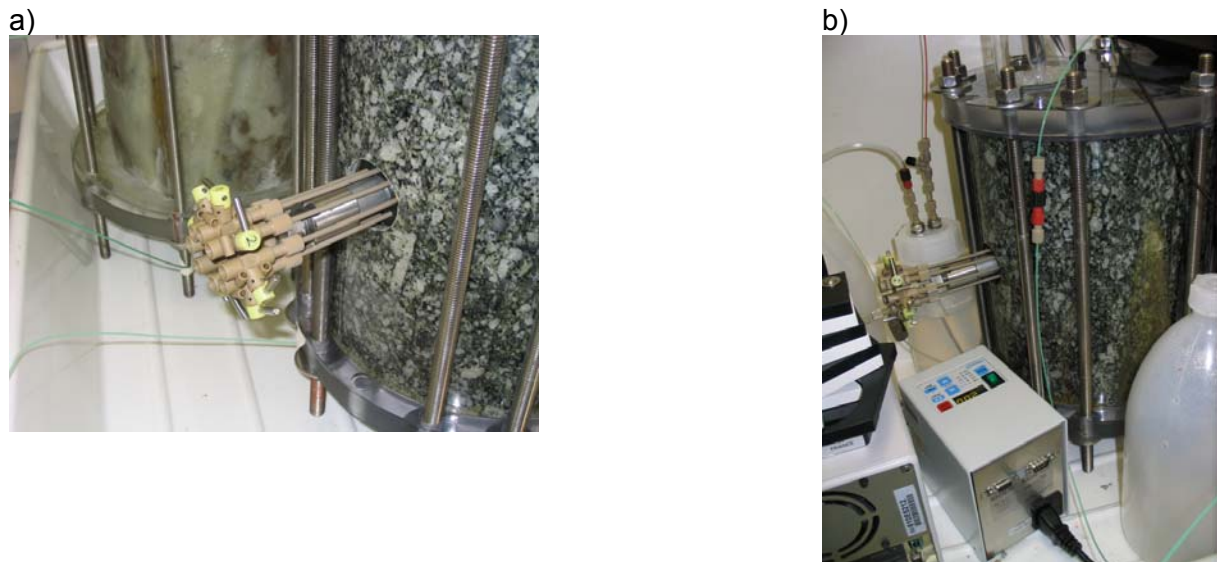


Figure 2-31: Core with installed packer system (a). At the end all PEEK pipes are closed with a check valve. Final experimental setup in the laboratory (b). A peristaltic pump is used to pump the water from the bottom of the core through the fracture. Another pump is injecting the tracer cocktail and GGW through the packer system. For details see text.

Table 2-10: ICP-MS analysis of the tracer cocktail of experiment Tr1.

Element	Tracer cocktail [μgL^{-1}]	Tracer cocktail ultracentrifuged [μgL^{-1}]	Sorbed on colloids [%]
Al	2528.9 ± 45.4	22.3 ± 3.8	99.1
Eu(III)	14.4 ± 0.3	0.7 ± 0.02	94.8
Tb(III)	15.3 ± 0.3	0.6 ± 0.03	95.9
Th(IV)	22.6 ± 0.4	0.1 ± 0.04	99.6
U(VI)	24.6 ± 0.4	23.2 ± 0.5	5.8

Table 2-11: ICP-MS analysis of the tracer cocktail of experiment Tr2.

Element	Tracer cocktail [μgL^{-1}]	Tracer cocktail ultracentrifuged [μgL^{-1}]	Sorbed on colloids [%]
Al	619.1 \pm 0.8	0.0	100
Eu(III)	15.6 \pm 0.2	1.0 \pm 0.01	93.5
Tb(III)	16.5 \pm 0.06	0.9 \pm 0.0	94.8
Th(IV)	25.1 \pm 0.3	0.1 \pm 0.03	99.5
U(VI)	27.5 \pm 0.2	26.2 \pm 0.2	4.4

Table 2-12: ICP-MS analysis of the tracer cocktail of experiment Tr3.

Element	Tracer cocktail [μgL^{-1}]	Tracer cocktail ultracentrifuged [μgL^{-1}]	Sorbed on colloids [%]
Al	361.1 \pm 27.3	4.4 \pm 0.0	98.8
Eu(III)	11.3 \pm 0.1	0.1 \pm 0.01	98.9
Tb(III)	11.9 \pm 0.2	0.1 \pm 0.0	99.1
Th(IV)	22.4 \pm 0.1	0.1 \pm 0.0	99.4
U(VI)	24.6 \pm 0.04	21.7 \pm 0.1	11.7

Analytical methods. The colloid concentration and number-weighted average colloid diameter is determined with a Laser-induced Breakdown Detection (LIBD) system [50]. The sample solution is pumped through a silica flow-through cell. A dielectric breakdown is produced in the focus region of a pulsed laser beam (Nd: YAG-laser, Frequency: 15 Hz, Wavelength: 532 nm). The plasma generated by the breakdown event is monitored by a CCD-camera attached to an image-processing system. The system is calibrated with polystyrene reference particles. This LIBD is referred to as mobile LIBD. Additionally s-curve analysis where performed with another LIBD system. Here the laser pulse energy is varied [140, 141]. The laser pulse energy where the first breakdowns of the colloids can be detected is called breakdown threshold. The breakdown threshold is increasing with decreasing colloid size. The slope of the s-curve is increasing with increasing colloid concentration when the colloid size is kept constant. This method is referred to as acoustic LIBD since the location of the breakdown event is done via acoustic location. The metal ion concentrations are measured via ICP-MS. Additionally the Al-concentration is used to detect the colloid breakthrough. The NaBr concentration is measured by a Br ion selective electrode.

Results & Discussion

Based on the speciation calculation of the metal ions (Eu, Tb, Th and U) used in this study [142] a metal concentration below the the solubility limit of the relevant solid phases in GGW was adjusted. However, amorphous hydroxide "eigen-colloid" can form due to local oversaturations. The metal ions where added to the tracer cocktail after the addition of the Febex bentonite colloids. It can therefore be assumed that the metal ions are sorbed onto the bentonite colloids. ICP-MS analysis of aliquots of the tracer cocktails (Table 2-10 to Table 2-12) show, that U(VI) is found to 88-96 % as solution species. This result is comparable to the investigations of the groundwater porewater mixing zone (see chapter 2.1.1). Eu(III), Tb(III) and Th(IV) are colloid associated to 95 – 100 %. This is comparable to measurements of Missana et al. [143] with colloid associated Eu(III) and Pu(IV) of > 75 % as well as from Schäfer et al. [32] with ~ 80 % colloid associated Th(IV) and Eu(III). Geochemical calculations with PHREEQC show negative saturation indexes for different mineral phases

(gibbsite, fluorite, quartz, calcite and chalcedony) in GW [144]. A precipitation and colloid formation of these phases can therefore be neglected.

Colloid/conservative tracer breakthrough: The measured NaBr and colloid concentrations are given in Figure 2-32. The bentonite colloid BTC peak maximum arrival time is earlier in experiments Tr1 and Tr2 and together with the peak arrival time of the conservative tracer in experiment Tr3 (NaBr, Table T4).

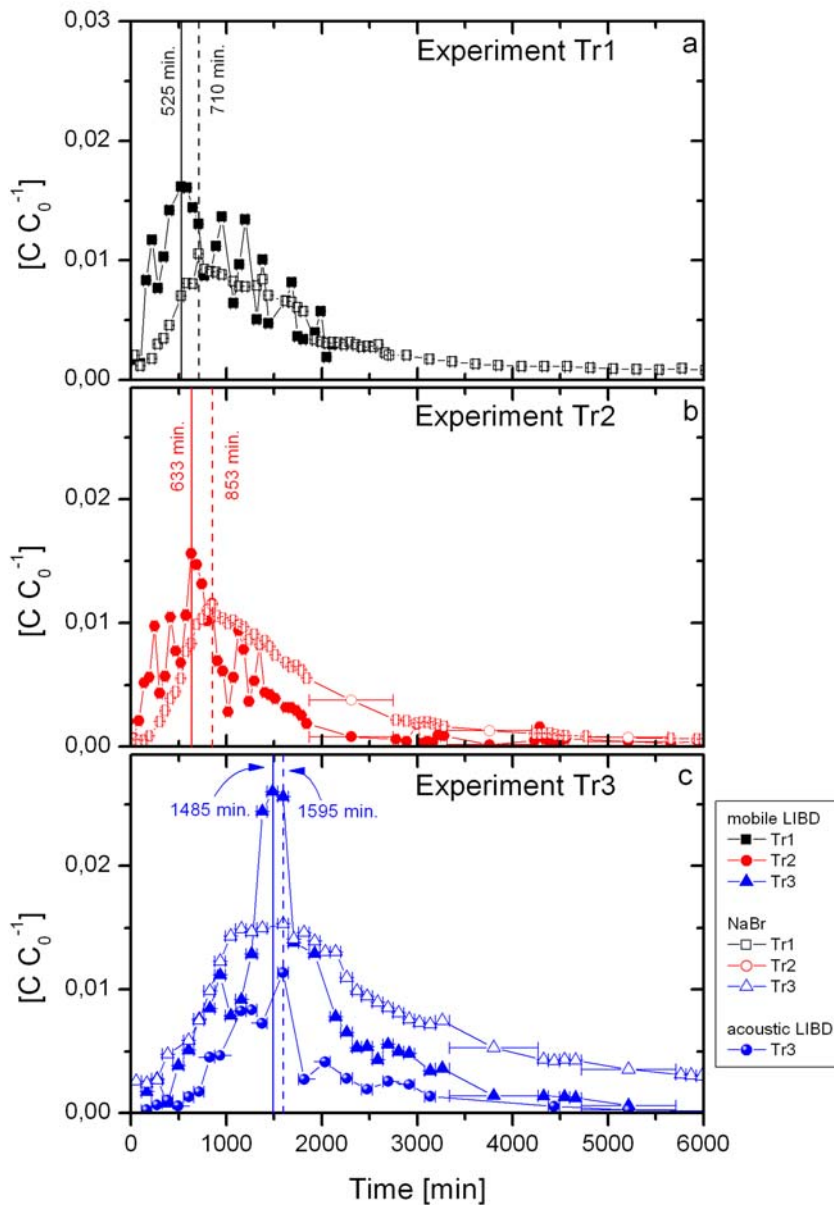


Figure 2-32: Breakthrough curves of Febex bentonite colloids and NaBr in experiment Tr1(a), Tr2(b) and Tr3(c). For NaBr the C_0 concentration in all experiments is $1 \cdot 10^{-2} \text{ mol} \cdot \text{L}^{-1}$. The C_0 concentration measured with the mobile LIBD varies for the bentonite colloids between $69.9 \text{ mg} \cdot \text{L}^{-1}$ (Tr1), $34.3 \text{ mg} \cdot \text{L}^{-1}$ (Tr2) and $57.0 \text{ mg} \cdot \text{L}^{-1}$ (Tr3), respectively. The C_0 concentration determined via acoustic LIBD in Tr3 is $62.9 \text{ mg} \cdot \text{L}^{-1}$.

The bentonite colloid and metal ion transport was also determined via ICP-MS analysis. In experiment Tr1 the concentration of Al, Tb(III), Eu(III) and U(VI) is increasing, but a peak maximum can not be determined (Figure F4). The Th(IV) concentration shows a clear peak between 404 and 535 minutes. The Th(IV) breakthrough curve as well as the location of the peak maximum is comparable to the bentonite colloids with a peak maximum after 525 minutes (Table T4). This shows a strong association of the Th(IV) transport with the bentonite colloids. The colloid breakthrough can also be observed in the measured colloid size. The biggest colloid size is measured after 648 minutes. This point in experimental observation time of the biggest colloid size lies within the measured peak maxima of the colloid concentration at 535 minutes and of the conservative tracer at 710 minutes.

Table 2-13: BTC parameters determined for the migration experiments

Experiment	Tr1	Tr2	Tr3
Peak maximum NaBr [min]	710	853	1595
$v_{a, dom}$ [$m a^{-1}$]	88.8	73.9	39.5
Peak maximum mobile LIBD [min]	525	633	1485
$v_{a, dom}$ [$m a^{-1}$]	120	99.7	42.5
Peak maximum acoustic LIBD [min]			1595
$v_{a, dom}$ [$m a^{-1}$]			39.5

The colloid breakthrough could be followed in the LIBD measurement, but not with the Al concentration in experiment Tr1. The injection volume is increased for experiment Tr2 in order to be able to follow the breakthrough in Al concentration. A time dependent increase in Al concentration could be measured in experiment Tr2. But Al-concentrations were low and showed pronounced scatter so that a peak maximum could not be located (Figure 2-33). Eu(III) and Tb(III) concentrations could be determined during the bentonite colloid breakthrough, but again the measured concentrations are too low to identify a clear peak maximum. The Th(IV) concentration increases again together with the bentonite colloid breakthrough determined via mobile LIBD. The peak maximum after 688 minutes lies again in between the peak maximum of the colloid concentration after 633 minutes and the peak maximum of the conservative tracer after 853 minutes (Table 2-12). The concentration for U(VI) was too low to detect a peak in experiment Tr2. Bentonite colloid breakthrough showed a maximum after 853 minutes in Tr2 and after 1485 and 1595 minutes in Tr3 (Figure 2-35 and Figure 2-36b). No difference between peak maxima of bentonite colloids and the conservative tracer could be recognized. Th(IV) shows a breakthrough behavior similar to that of the bentonite colloids. These observations show again that the transport of Th(IV) is bentonite colloid associated. During colloid breakthrough an increase in colloid size is observed. The s-curve analysis shows bentonite colloids in two size fractions of 80–150 nm as well as 150–300 nm. The highest colloid concentration is determined for the 150–300 nm size fraction. In the tracer cocktail the highest concentration was determined in the 80–150 nm size fraction. However, a size chromatographic effect could not be determined.

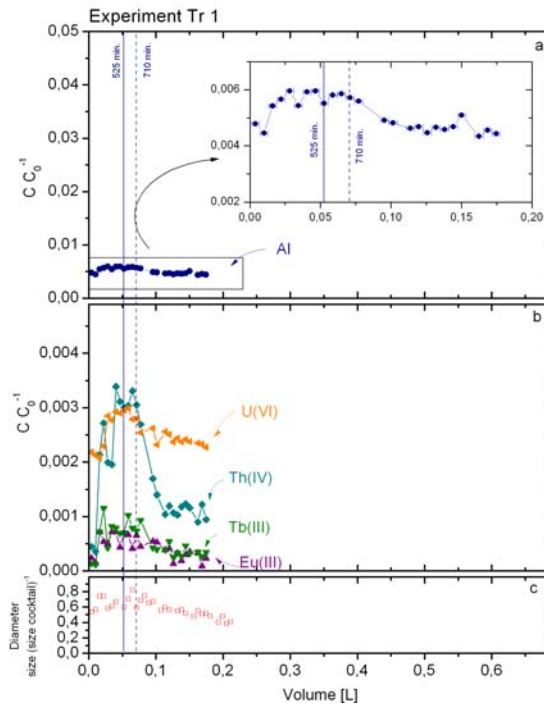


Figure 2-33: Breakthrough curves of Aluminum (a), Eu(III), Tb(III), Th(IV) and U(VI) (b) and the colloid diameter (c) in experiment Tr1. The colloid size was divided by the colloid size measured in the tracer cocktail.

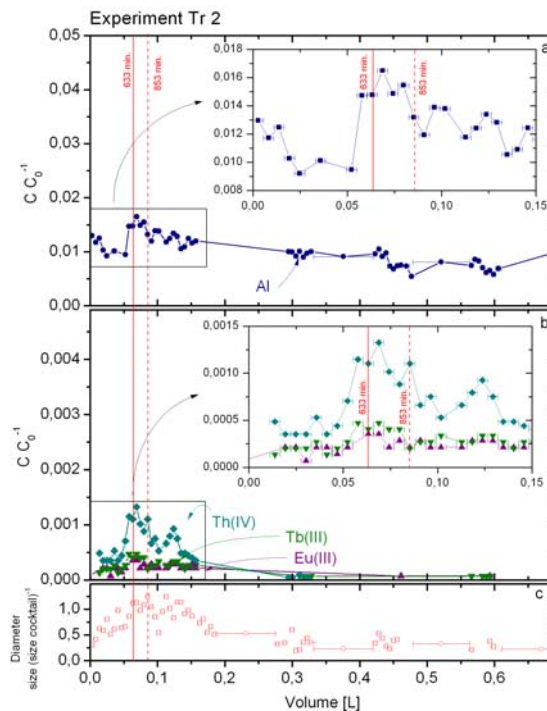


Figure 2-34: Breakthrough curves of Aluminum (a), Eu(III), Tb(III), Th(IV) and U(VI) (b) and the colloid diameter (c) in experiment Tr2 with a flow velocity of 99.7 m a^{-1} and an injection volume of 2 mL. The C_0 concentrations are the measured concentrations in the tracer cocktail (Table 2-11). The colloid size was divided by the colloid size measured in the tracer cocktail.

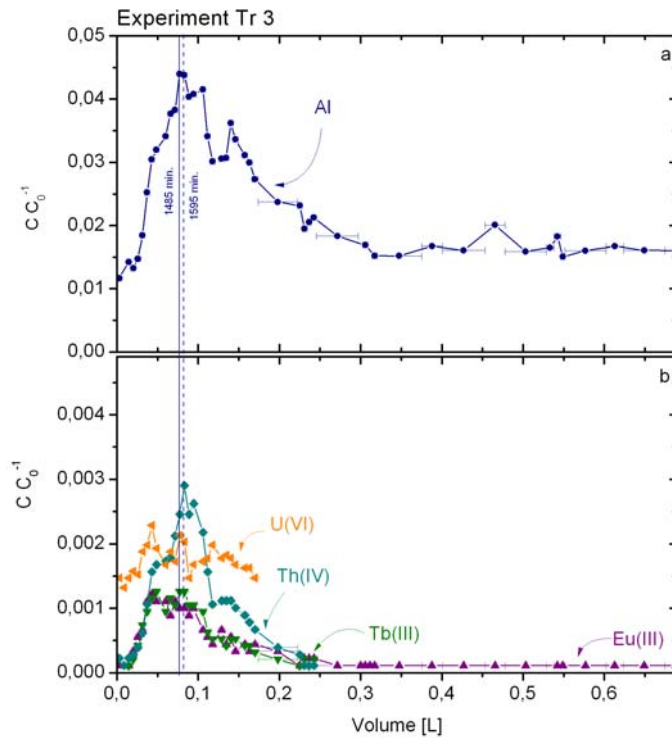


Figure 2-35: Breakthrough curves of Aluminum (a), Eu(III), Tb(III), Th(IV) and U(VI) (b) in experiment Tr3 with a flow velocity of 42.5 m a^{-1} and an injection volume of 2 mL .

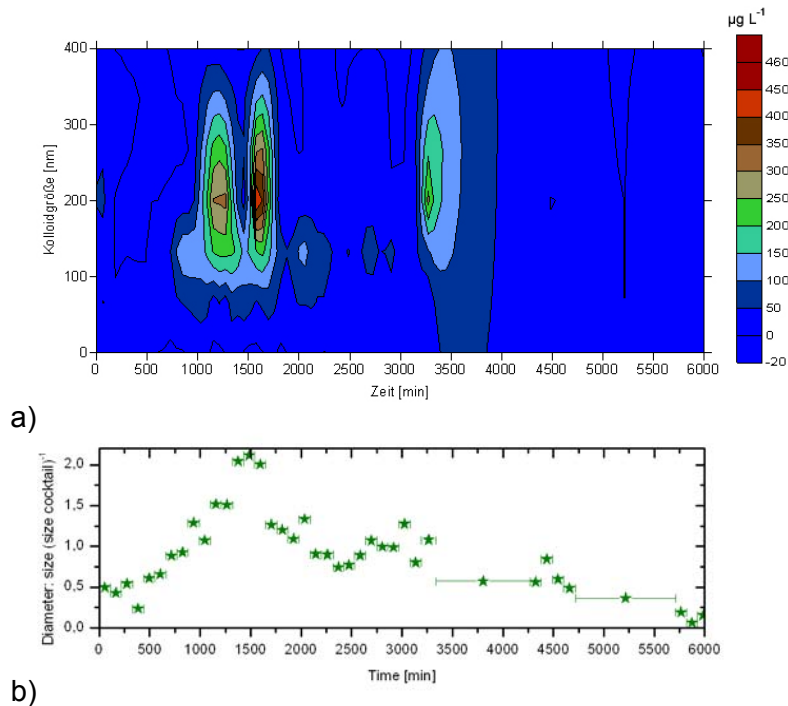


Figure 2-36: Colloid size distribution measured by s-curve analysis (a). Colloid size determined by mobile LIBD divided by the colloid size measured in the tracer cocktail (b).

The determined peak maxima (t_{dom}) can be used to calculate the retardation factor (R_f , Table 2-14) with σ density, Φ porosity and K_d distribution coefficient:

$$R_f = 1 + \frac{\sigma}{\Phi} K_d = \frac{t_{dom} \text{ colloids}}{t_{dom} \text{ conservative Tracer}}$$

The R_f value is < 1 if the tracer arrives before, and it is > 1 when it arrives after the conservative tracer. The bentonite colloid peak maxima are always measured before or together with the peak maxima of the conservative tracer. Therefore all calculated colloid R_f values are ≤ 1 . The reduction in flow velocity inside the Grimsel core leads to a comparable breakthrough curve of conservative tracer and bentonite colloids. The distance x which the colloids can travel by purely diffusive Brownian motion inside the fracture zone increases with increasing residence time t and constant diffusion coefficient D [145]: $x = \sqrt{2 \cdot D \cdot t}$. Therefore, depending on the residence time colloids can diffuse into slow flowing parts of the fracture as the conservative tracer and exclusion effects (e.g. Taylor dispersion, hydrodynamic chromatography) are negligible and colloids show similar transport behavior to the conservative tracer [146-148].

Table 2-14: Calculated retardation factors (R_f) for Febex bentonite colloids and Th(IV).

Exp.	Colloids (mobile LIBD)	Colloids (acoustic LIBD)	Th(IV)
Tr1	0.78 ± 0.04		0.74 ± 0.2
Tr2	0.77 ± 0.03		0.77 ± 0.03
Tr3	0.97 ± 0.03	1.0	1.0

The calculated bentonite colloid and Th(IV) retardation factor are comparable and converge to 1 for decreasing flow velocities. This can be expected, since Th(IV) is colloid associated. The calculation of a R_f value for Eu(III), Tb(III) and U(VI) was not possible due to the lack of clear breakthrough behavior.

Colloid size: The colloid sizes in experiment Tr1, Tr2 and Tr3 are given in relative colloid size. The mobile LIBD system did suffer an electrical defect after experiment Tr1. Before experiments Tr2 and Tr3 a new calibration of the mobile LIBD system had to be made. The colloid size varies between the two LIBD calibrations and the colloid sizes can not be compared correctly. The colloid size was therefore divided by the colloid size measured in the injection cocktail. The colloid breakthrough can be observed as an increase in colloid size in all 3 experiments. A small increase can be observed for experiment Tr1. The reason for this could be that the small injection volume of 1mL is diluted too much inside the experimental setup. A clear differentiation from the smaller background colloids in the groundwater was not possible. The injection volume was increased for experiment Tr2 and Tr3 to 2 mL. This injection volume increase leads to a clearly visible increase in colloid size in both experiments. The peak maximum colloid sizes in experiment Tr2 are comparable to the injected colloids. The maximum colloid sizes for experiment Tr3 is twice the size of the injected colloids. The colloid size of the tracer cocktail was monitored during the experiment and no increase could be found. Therefore, a simple colloid coagulation within the experimental duration cannot explain the observed colloid size increase in the peak maximum. Possibly, a mobilization of fracture surface associated larger colloids has occurred. The s-curve analysis of the bentonite colloid breakthrough in experiment Tr3 does not show a chromatographic effect. All size fractions are transported with the same velocity.

Recoveries: Recovery values for individual tracers are given in Table 2-15. The calculated recovery values as well as literature data are in addition plotted in Figure 2-37 as a function

of fracture residence time. U(VI) recoveries could not be determined (see discussion before). However, a breakthrough of U(VI) is only expected after the experimental observation period due to a high retardation [32, 143]. The ICP-MS analysis of the injection cocktails reveals only 4 – 12 % colloid bound U(VI), which should only partly elute (Figure F4 and F6).

Table 2-15: Recoveries for bentonite colloids and different metal ions. The recovery of a species was calculated with the respective concentration measured in the injection cocktail of this experiment.

	Tr1	Tr2	Tr3
Duration [d]	5	7	9.5
NaBr [%]	100 ± 8	96.4 ± 4	85 ± 2
Colloids (mobile LIBD) [%]	100 ± 5	73.5 ± 10	78 ± 8.5
Colloids (acoustic LIBD) [%]			38.9 ± 6.8
Al [%]	5.9 ± 3.7	82.6 ± 10	180 ± 20
Eu(III) [%]	4 ± 1	1.5 ± 0.5	5.3 ± 1
Tb(III) [%]	7 ± 2	2 ± 0.5	5.5 ± 1
Th(IV) [%]	33 ± 2	5 ± 2	11.3 ± 2

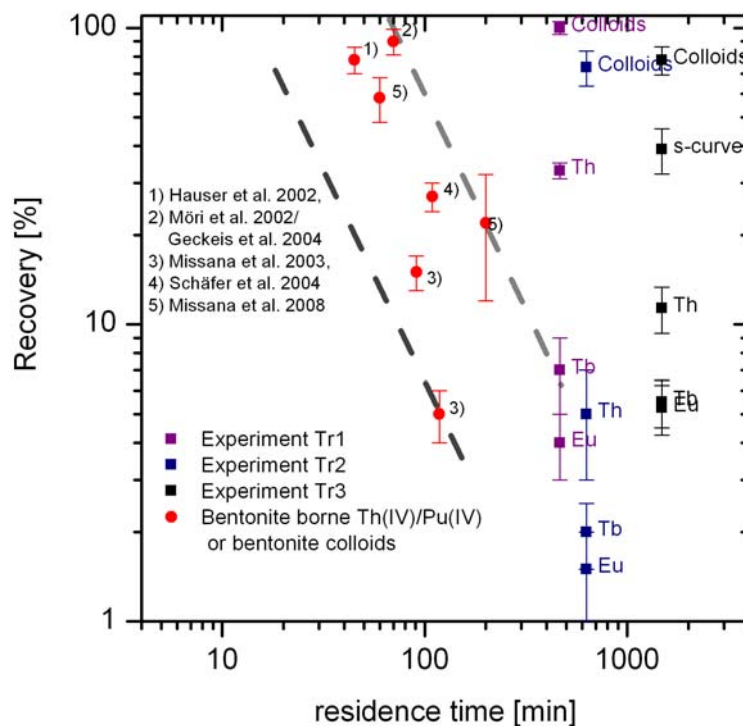


Figure 2-37: Recovery vs. residence time for bentonite colloids and metal ions used in the experiments. To compare the measured values in this work, literature data is also given Hauser et al. [149], Mōri et al. [139], Geckeis et al. [15], Missana et al. 2003 [150], Schäfer et al. [32] and Missana et al. 2008 [143].

The recoveries measured in experiment Tr1, Tr2 and Tr3 show the same general trend as the literature data of decreasing recovery with increasing residence time. The recoveries of the conservative tracer (NaBr) are quantitative in all experiments. The colloid recovery decreases to 59 ± 16 % in experiment Tr2 and stays at the same level considering the uncertainty for experiment Tr3 with 83 ± 23 %. It is noticeable, that the calculated colloid recovery based on the s-curve LIBD data is somehow lower with 40 ± 10 %.

The bentonite colloids, the surface of the fracture and the fracture filling materials are negatively charged under the geochemical conditions of the GW (low mineralisation, pH 9.6 [144]). The attachment of the bentonite colloids is therefore unfavorable under the experimental conditions. Ryan and Elimelech [151] report a difference between theoretically calculated and measured collision probabilities under unfavorable attachment conditions. A collision probability was measured in low concentration solutions where theoretical no collision probability should exist. Ryan and Elimelech [151] describe this discrepancy by surface charge heterogeneities and/or surface roughnesses. Missana et al. [143] could show under the same geochemical conditions as in the presented experiments, that the colloid recovery is decreasing with decreasing flow velocity until a plateau value of 26 ± 2 % is reached. Possible reasons for the decrease in colloid recovery could either be surface roughness or charge heterogeneity effects. The observed decrease in colloid recovery to 38.9 ± 6.8 % for the acoustic LIBD measurement is therefore plausible. A higher Th(IV) recovery compared to Eu(III) and Tb(III) is observed for all experiments. The recoveries of Eu(III) and Tb(III) are comparable within the experimental error. The in-situ experiments of Geckeis et al. [15] and Möri et al. [139] show a higher recovery for Pu(IV), the chemical homologue of Th(IV), of 86 % compared to 70 % for Am(III), the chemical homologue of Eu(III) and Tb(III). The discussed literature additionally shows that the sorption of the metal ions onto the bentonite colloids is reversible.

Desorption kinetics: The desorption of metal ions with a desorption rate k_r from bentonite colloids can be described by a first order rate law: $[A]_t = [A]_0 \exp(-k_r t)$

The decrease of the metal ion concentration $[A]_t$ is faster at the beginning of the desorption process due to the exponential part of the equation. The desorption rate gets slower with increasing residence time t . A slower decrease in metal ion recovery for longer residence times as observed in experiment Tr2 and Tr3 can be therefore expected. The higher colloid association of Th(IV) compared to Eu(III) and Tb(III) was also observed in batch experiments to determine K_d values for the sorption of Am(III) and Pu(IV) on Grimsel fracture filling material [15]. The K_d value for sorption to fracture filling minerals in presence of clay colloids is increasing from 2 ml g^{-1} after 2 h for Am(III) and Pu(IV) up to 30 ml g^{-1} after 300 h for Am(III) and 8 ml g^{-1} for Pu(IV) respectively. Eu(III) and Th(IV) as chemical homologues of Am(III) and Pu(IV) show the same behavior of stronger sorption of Th(IV) onto the bentonite colloids than Eu(III)/Tb(III). Bouby [152] could show a complete desorption of Eu(III) within three years when a competing ligand (humic acid, HA) is added. But a fraction of ~ 30 % of Th(IV) was still associated with the bentonite colloids after three years. It is possible that a plateau value for the recovery of Th(IV) is developing for even longer residence times. Missana et al. [143] observed a plateau value for the recovery of bentonite colloids as well as Bouby [152] for the desorption of Th(IV). But it could not be differentiated if the decrease in metal ion recovery is due to the desorption or a filtration of the bentonite colloids inside the core since the recovery of the bentonite colloids is varying considerably for different methods (LIBD and AI).

Conclusions.

Based on the results of these laboratory migration studies the following conclusions can be drawn:

- Febex bentonite colloids are at least partly mobile under the given experimental conditions.
- Metal ion recovery is decreasing with increasing residence time. This confirms earlier findings by other authors [15, 32, 139], which have been found for considerably shorter residence times.
- The bentonite colloid recovery could not be precisely quantified. The different detection methods used within this study (mobile LIBD, acoustic LIBD and ICP-MS Al concentration) revealed considerably different recovery values and more research is needed.
- The mechanism behind the decrease of metal ion recovery can not be specified since the bentonite colloid recovery could not clearly be determined due to instrumental problems. Desorption of the metal ions from colloids or filtration of the metal ion bearing colloids in the core are the possible mechanisms.
- Th(IV) is stronger associated with the bentonite colloids as compared to Eu(III) and Tb(III).
- A U(VI) breakthrough is not observed during the observation period of the experiment. A recovery can thus not be given.

2.2 Field experiments (AP 1.2) (Homologue test Run 08-01)

The field activities in the Grimsel Test Site (GTS) were heavily delayed due to the technical very demanding construction of the megapacker system to achieve low flow conditions within the migration shearzone. In the CFM project colloid tracer tests are performed in a low gradient flow field within the Migration (MI) shear zone at the GTS. The tunnel section of the MI shear zone was equipped with a three meter diameter steel tube which was sealed at both ends with large O-ring type packers (submountain packer). The objectives of the submountain packer were to lower hydraulic gradients within the shear zone towards the laboratory drift and therefore to realize near-natural ground water flow conditions.

For the first homologue test colloids and homologues were injected in borehole CFM 06.002 I1 (Run 08-01) without recirculation. The extraction point of this tracer test was the Pinkel surface packer resulting in a dipole length of 6.08m. Subsequently to Run 08-01 tracer test Run 08-02 was performed injecting solely uranine into the same flow field, however using recirculation. This difference will be discussed later forcing some difficulties in comparing directly the breakthrough curves. It was necessary to split the colloid/homologue and uranine injection because of possibly homologue complexation by elevated uranine concentrations. The average number-weighted colloid size as determined by LIBD for the Febex bentonite colloids is 144 ± 4 nm and therefore very similar to the colloid size injected in the homologue tests of the CRR project of 148 ± 4 nm. Ultracentrifugation (90,000 rpm for 60min) of the cocktail to check colloid association of the homologues as well as the colloidal nature of the Al-signal revealed that 98% of Al, 98% of Hf, 89% of Tb and 97% of Th, respectively, are associated to colloidal material that can be centrifuged off.

The injection of the homologue cocktail was performed by pressurizing a 1L HDPE bottle containing the tracer cocktail using argon gas. A total volume of 900 mL was injected in a time span of 89 min resulting in a linear injection flow rate of 10.1mL/min. This results in a total injected mass of 15.0 ± 4.2 mg Febex bentonite colloids, 23.4 ± 1.4 µg Hf, 14.3 ± 1.2 µg Tb and 19.8 ± 1.3 µg Th, respectively. The outflow rate at the Pinkel surface packer was held constant at 165mL/min.

Samples were collected for the partners AIST (AFM investigations), PSI-LES (single particle counting; SPC), KIT-INE (LIBD, ICP-MS) and the associated group CIEMAT (PCS). The sampling bypass had a flow rate of 100 mL/min.

The tracer test was stopped after 18846min (about 13 days) and a quantitative recovery of the injected bentonite colloids was determined by LIBD and ICP-MS via AI analysis within the analytical uncertainty of the respective method. The recovery of the homologues were quantified to be $56 \pm 9\%$ for Tb, $78 \pm 6\%$ for Hf and $93 \pm 6\%$ for Th, respectively. Comparing the first arrival times of the conservative tracer uranine and the homologues a retardation factor R_f of 0.78 could be determined. Due to the different injection methods used (circulation vs. non circulation) a direct comparison of the peak arrival times is not possible. Based on batch-type experiments of bentonite colloid radionuclide desorption kinetics and taking the residence time of Run 08-01 the expected recovery of tetravalent actinides is estimated to be in the range of $\sim 86\%$. Therefore, the observed recoveries of the tetravalent homologues in Run 08-01 are not in contradiction with the batch data on sorption/reversibility.

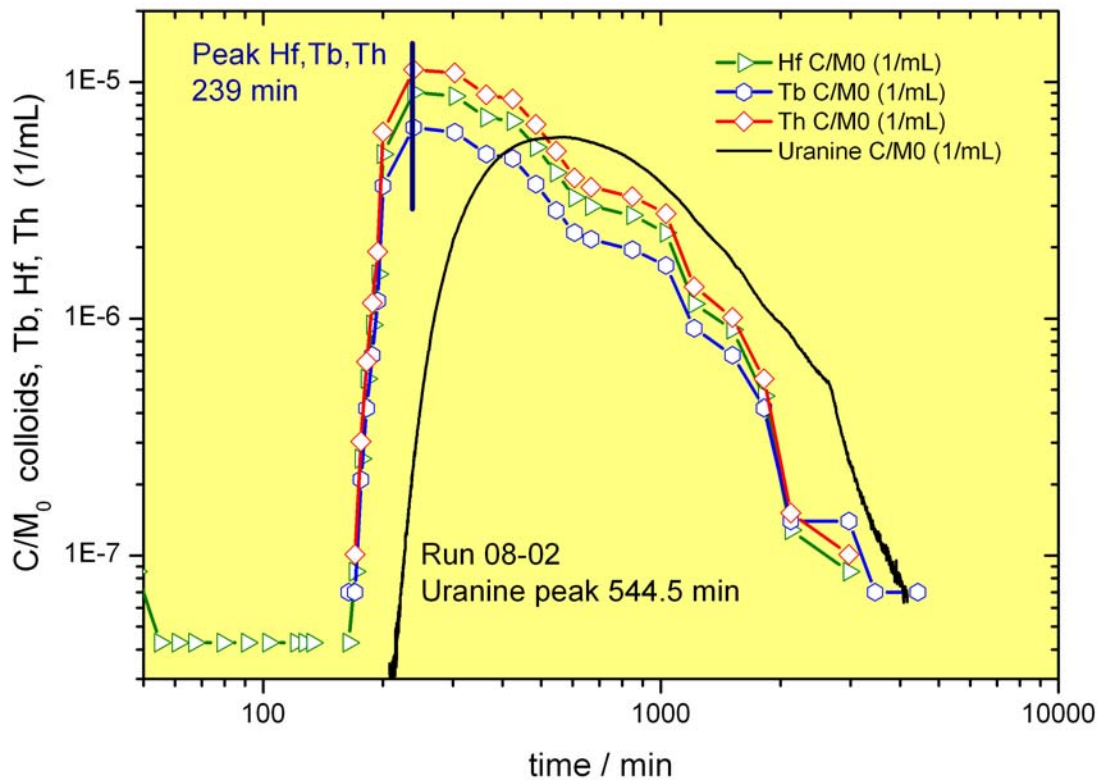


Figure 2-38: Breakthrough curves of the homologues Hf, Tb and Th in Run 08-01 in comparison to the conservative tracer uranine of Run 08-02 under the same hydraulic conditions, but using recirculation in the packer interval. The peak maximum for the homologues is after 239 min, whereas the peak maximum of the uranine peak is delayed through the recirculation used to 544.5 min.

Detailed analysis of the colloid size distribution in samples of the breakthrough curve could not resolve by SPC or LIBD a size dependent colloid elution (see Figure 2-39) as observed in laboratory column experiments [4]. Both, the observed high colloid recovery together with the not observed colloid size effect indicate that the flow path of Run 08-01 is a rather broad channel. In summary, the results of the first CFM homologue test together with data obtained within the CRR project clearly show the sensitivity of colloid mobility especially on the flow path geometry and heterogeneity of the fracture. Further in situ tests are planned in 2009

under variation of dipole geometry and at higher residence time to obtain detailed information on colloid filtration and radionuclide-colloid binding kinetics under near-natural flow conditions before emplacing the compacted bentonite block for the integral experiment.

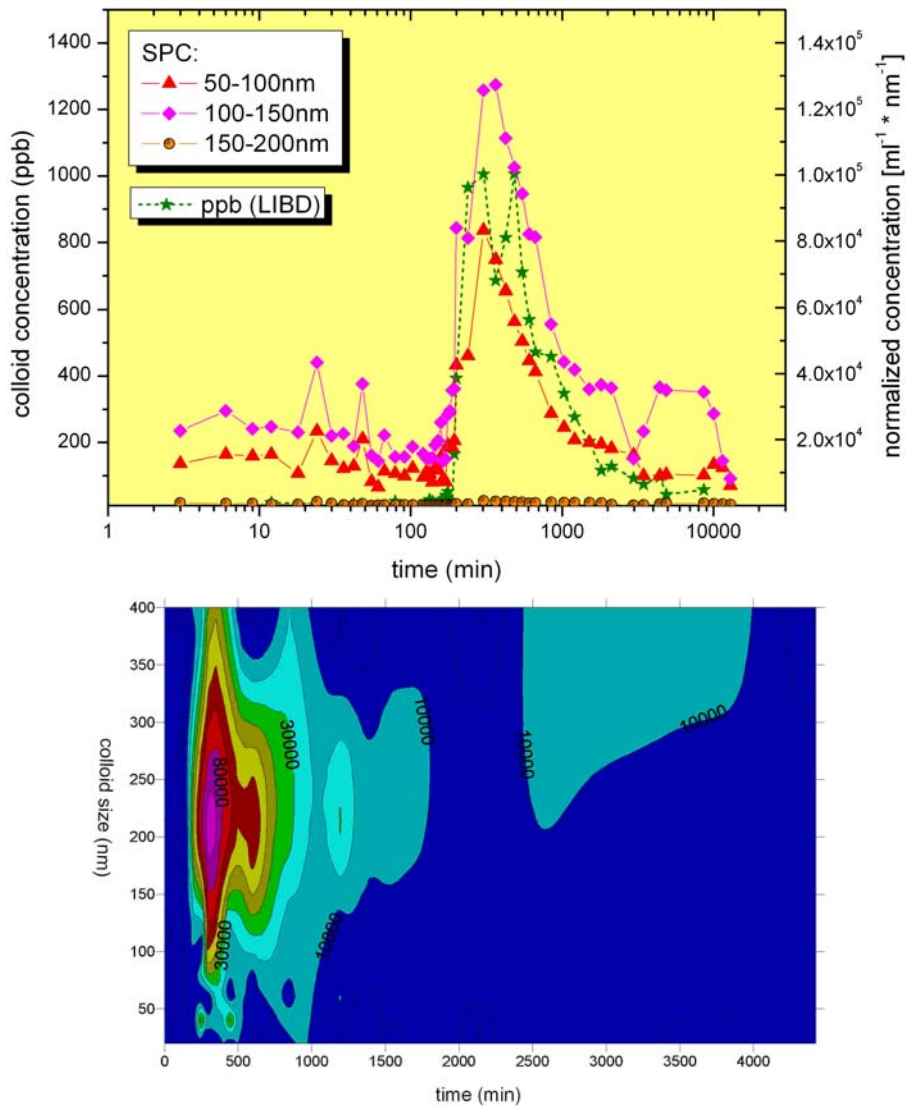


Figure 2-39: (top) Comparison of colloid breakthrough curves detected by LIBD and different channels of the single particle counting SPC (data C. Degueudre; PSI-LES). (bottom) Colloid breakthrough curve plotted as contour plot of colloid concentration (ppt) against the experimental time (x-axis) and colloid size (y-axis) taken from LIBD s-curve analysis.

3 Modeling

The objectives of flow and transport modelling are manifold. Modelling of the flow field and the transport of ideal tracers aims at understanding the flow conditions in the Grimsel shear zone and the impact of the different dipoles on the flow field. Further, predictions about the impact of reduced flow conditions – as planned in future homologue tests – are possible. Flow and transport modelling of a well characterised fracture in a bore core aims in understanding of the effect of heterogeneities on flow field and transport of tracers. Finally, the application of transport models including kinetically-controlled sorption reactions to describe the interaction between radionuclides, colloids and sediment matrix yields – based on the results from the experimental programme – in understanding the impact of the different processes on the shape of the break-through curves and on the recovery of the radionuclide tracers. It furthermore contributes to the qualification of the codes and sets the basis for calculations with regard to the long-term safety of deep geological repositories.

3.1 CFM hydraulics and transport modeling (AP 2.5)

Flow and transport equations. Assuming that fluid flow in the shear zone is laminar and isothermal, the momentum balance equation for fluid flow can be simplified to the well-known Darcy's law [153]. For 2D incompressible flow in a porous medium, the governing equation is:

$$\mathbf{V} = -1/\mu \mathbf{K} \cdot \nabla P \quad (\text{Equation 11})$$

where:

$\mathbf{V} = [v_y, v_z]^T$ is the vector of the components of averaged groundwater velocity in the y, z directions,

μ is the dynamic viscosity coefficient for water;

\mathbf{K} the intrinsic permeability tensor; and

∇P the water pressure gradient.

In the study described in this appendix, only conservative tracers are modelled, and thus only advection, diffusion and dispersion are relevant processes.

Advection: The contaminants are assumed to travel at the same rate as the average linear velocity of the groundwater. The average linear velocity can be calculated by dividing the Darcy velocity components by the effective porosity η_e .

Dispersion: Dispersion is a phenomenon arising from heterogeneities of flow velocities on all scales. The different flow paths and apertures create differences in the path length and velocities, which cause a spreading of migrating tracers in space and time. An important feature is the large scale heterogeneities of permeability distribution which cause spreading in all directions. Dispersion accounts for the complex features of the flow paths that cannot be modelled with the concept of average velocity. The dispersion term in the transport equation is mathematically described with Fick's law.

Molecular diffusion: Molecular diffusion is a process by which molecules move from areas of high concentration to areas of low concentration. This phenomenon can also be modelled by

Fick's law. If the flow velocities are high, then the effect of molecular diffusion is small compared with advection and dispersion.

Transport by these processes is modelled using the balance equation:

$$\partial C / \partial t = \nabla \cdot (\mathbf{D} \nabla C - \eta_e \mathbf{V} \nabla C) - S \quad (\text{Equation 12})$$

where C is the concentration of the species in the pore fluid. Molecular diffusion and the dispersion are jointly be represented by a hydrodynamic dispersion tensor \mathbf{D} . S is a source/sink term.

The coefficients of the hydrodynamic dispersion tensor are evaluated using the equation:

$$D_{kl} = (D_o + \alpha_T V) \delta_{kl} + (\alpha_L - \alpha_T) (v_k v_l) / V \quad (\text{Equation 13})$$

where D_o is the coefficient of molecular diffusion, α_L , α_T are the longitudinal and transverse dispersion lengths, δ_{kl} is the Kronecker delta, v_k , v_l are the components of the average groundwater velocity, V is the magnitude of the average groundwater velocity and the set (k, l) range over the indices y, z .

3.1.1 Numerical modelling of the field tracer tests

The tracer tests. In the first phase of the CFM project, different tracer tests with uranine as a conservative tracer were performed in the low gradient flow field within the shear. Prior to the tracer tests, the experimental tunnel was equipped with a 3 m-diameter surface packer system. The aim of installing this packer was to limit flow rates towards the drift, reduce the hydraulic gradient in the shear zone and hence achieve longer tracer travel times. The characteristics of the modelled tracer tests are given in Tracer Test Reports [154-156] and summarised in Table 3-1.

The model. In this study, it was assumed that groundwater flow and solute transport take place only in fractures within the shear zone filled with fault gouge, and that the shear zone at the test location is planar. The model thus represents a planar confined porous media with a constant porosity and an anisotropic permeability. The initial and boundary conditions assumed in the calculations are shown in the Figure 3-1. The groundwater flow in the model domain was calculated based on the assumption of impermeable top and bottom boundaries and a uniform, regional flow from left to right, with a velocity of 10 m per year. The uranine concentration curves that were measured at the injection hole in every test provided input functions for the model calculations. The present finite element model extends the relatively simple model used earlier in the CFM project. The 20m × 12m domain, including the drift and the injection and extraction holes, was meshed by 10564 four-node planar elements. The shear zone is assumed to be 1cm in thickness. The entire mesh and a detail of the mesh near the wells are shown in the Figure 3-2. The groundwater and the uranine were injected at one of the boreholes - BOMI 87.010 or CFM 06.002 - with flow rates as indicated in Table 3-1 and extracted at the surface packer at rates given also in the table.

Results & Discussion

The calculation starts with the modelling of the steady-state groundwater flow field in each dipole experiment. After these conditions are established, the injection of the uranine solution

is simulated. The uranine concentration was measured online in order to determine the input functions and then used directly in the numerical analysis.

The simulation of the uranine Run # 1 and test 07-02 have been used for the calibration of the numerical model for the Dipole 2 (between BOMI-87.010 and Pinkel surface packer) and the uranine tests 07-01 and 08-02 for the Dipole 1, respectively. Both dipoles are proposed as potential location for a final long-term radionuclide migration experiment.

Table 3-1: Summary of tracer tests used for model calibration

Tracer Test	Characteristics
Run #1 between BOMI 87.010 and Pinkel surface packer Distance 4 m	Injection flow rate: 4.5 ml/min Injected tracer volume 200 ml Uranine concentration 5.6 ppm Outflow rate 650 ml/min (from Pinkel and "crack")
Run 07-02 between BOMI 87.010 and Pinkel surface packer Distance 4 m	Injection flow rate: 3.4 ml/min (60 min) and 120 ml/min Injected tracer volume 204ml Tracer mass 2 mgr Recirculation flow rate 120 ml/min Outflow rate 120 ml/min
Run 07-01 between CFM 06.002 and Pinkel surface packer Distance 6 m	Injection flow rate: 9.18 ml/min Injected tracer volume 280 ml Tracer mass 14 mgr Recirculation flow rate 80 ml Outflow rate 165 ml/min
Run 08-02 between CFM 06.002 and Pinkel surface packer Distance 6 m	Injection flow rate: 10 ml/min Injected tracer volume 280.2 ml Tracer mass 15.4 mgr Recirculation flow rate 25 ml/min Outflow rate 165 ml/min (160 ml/min from annular gap)

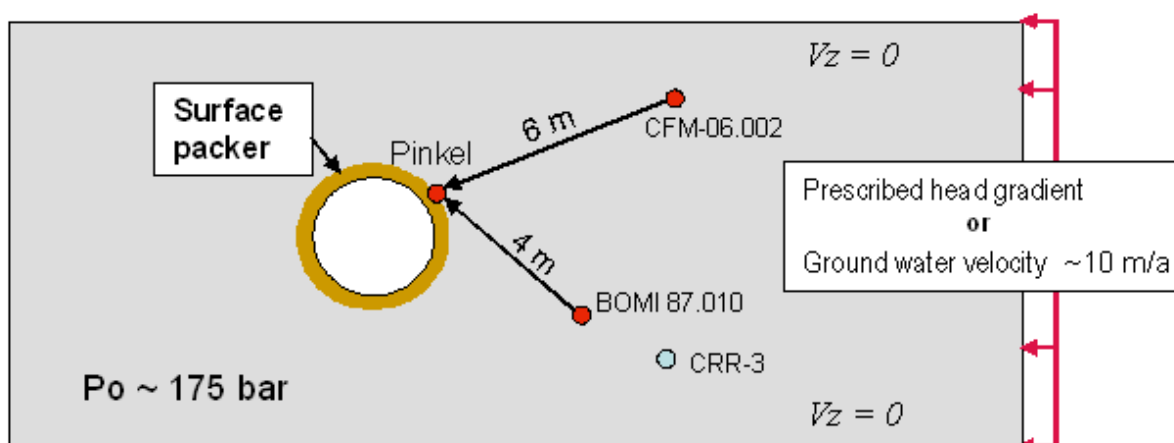


Figure 3-1: Definition of the model boundary condition for simulation of tracer tests

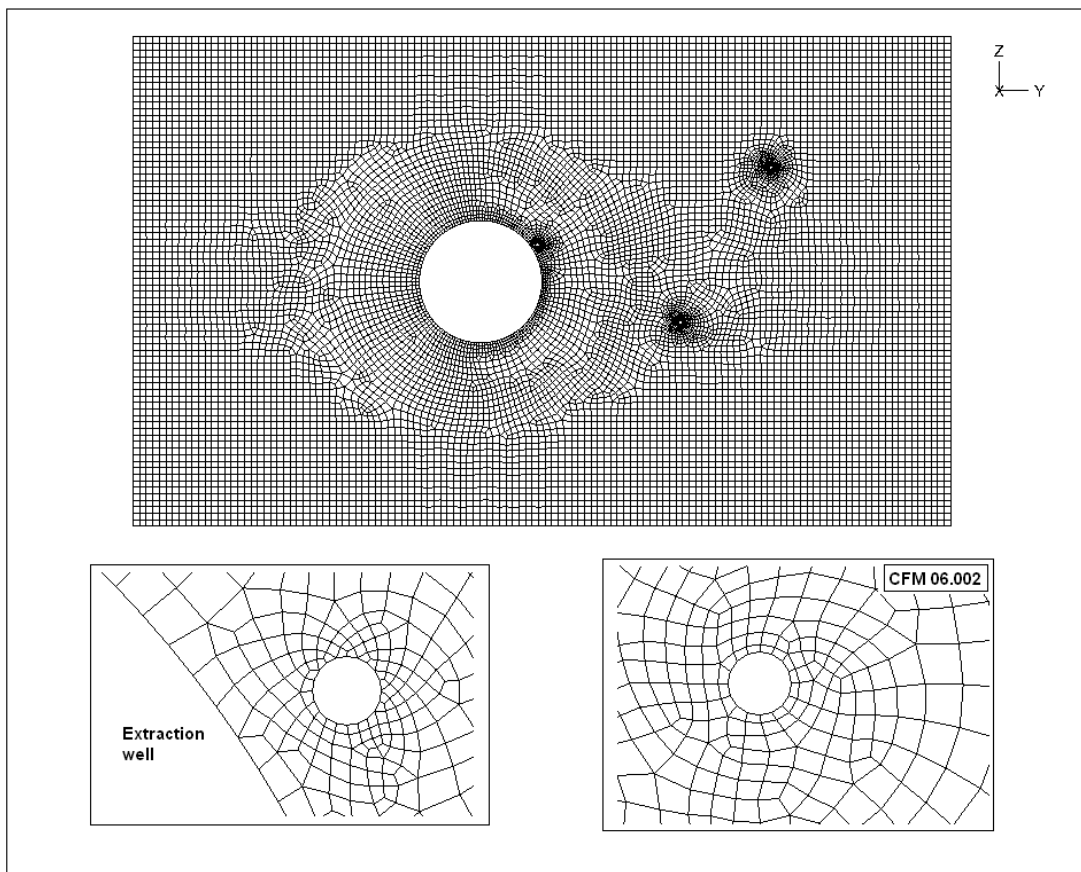


Figure 3-2: Finite element model used for calculation of tracer tests and detail of the mesh near the boreholes; dimensions of the model plane: 20 m × 12 m.

Simulation of the uranine breakthrough curves in Dipole 2. In the tracer test Run #1, uranine was injected at the borehole BOMI 87.010 and recovered at the Pinkel surface packer and at a fissure near this packer. The uranine concentration measured at the injection borehole is presented in Figure 3-3a. The material parameters used for the analysis are given in Table 2-1. The calculated and measured uranine breakthrough curves at the outflow borehole are plotted in Figure 3-3b. As can be observed, the simulation matches the concentration peak at the extraction hole quite well. However, the comparison of calculation results in the tailing part shows some differences. In the next step, uranine test 07-02 at relatively low outflow (120 ml/min) was modelled. The uranine concentration measured at the injection borehole is shown in Figure 3-3c. Figure 3-3d depicts the calculated and measured uranine breakthrough curves at the extraction hole (Pinkel). The model produces a reasonable fit to the experiment. There is clearly a good agreement between both curves regarding peak arrival time and the tailing following the peak. The long tailing seems to be induced by progressive release of the tracer late in the injection interval. The evolution of computed uranine concentration in the shear zone is presented in Figure 3-4. The plots show that the main flowpath of the tracer is towards the extraction hole, but a small amount of tracer passes below the drift. This is due to the diffusion and dispersion processes taking place during the long travel time in the weak dipole test.

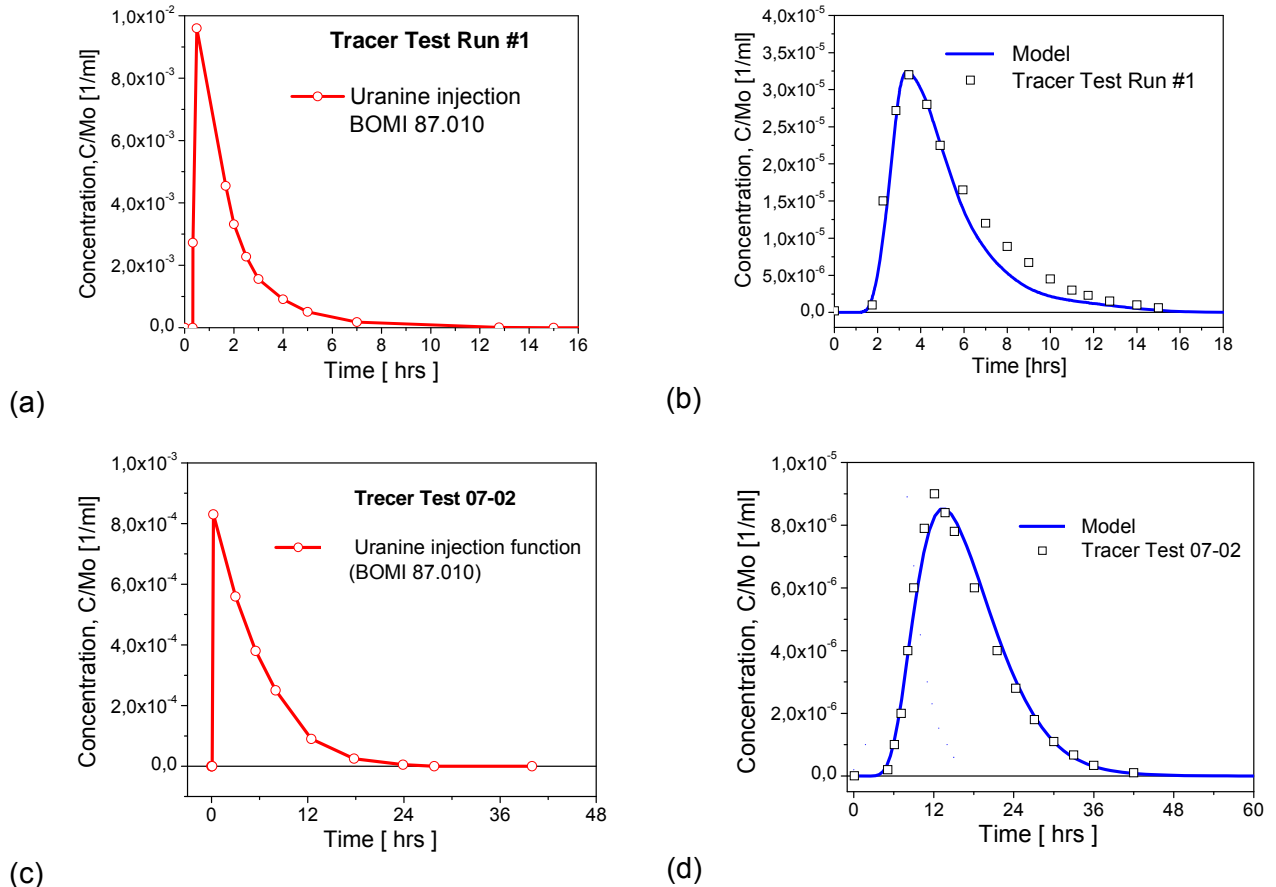


Figure 3-3: (a) Uranine concentration at the injection borehole (BOMI 87.010), (b) Calculated and measured break through curves at the extraction side, (c) Uranine concentration at the injection borehole (BOMI 87.010) for tracer test 07-02 and (d) Calculated and measured breakthrough curves at the extraction well (tracer mass recovery about 86%)

The results suggest that the use of an anisotropic hydraulic permeability of the shear zone, which was successfully applied to fit earlier tracer experiments [1, 157], does not work in this case. However, it seems that the heterogeneity of the shear zone material with respect to porosity and permeability in the model domain influence the transport processes under the low or natural hydraulic gradients.

The hydraulic parameters obtained from preview simulation of Run #1 (same dipole but different flow rates) were used firstly. However, it was necessary to perform further adjustments of these parameters due to the new test conditions (i.e. smaller pumping and extraction rates) to be able to fit the measured breakthrough curve. The calibrated input parameters are also given in Figure 3-5.

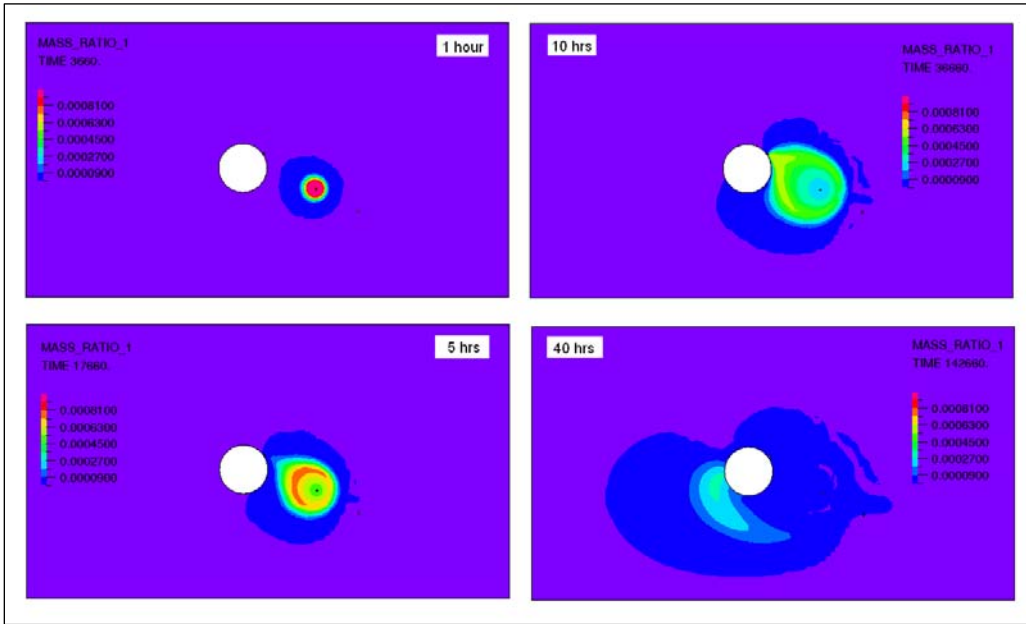
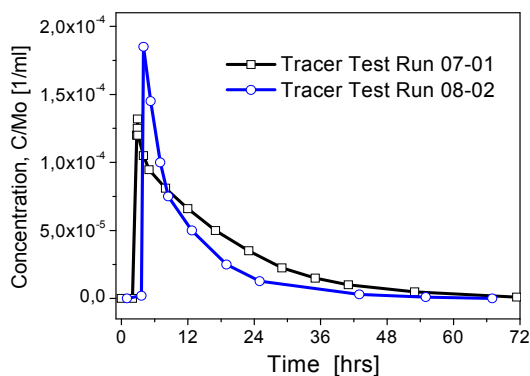


Figure 3-4: Distribution of the uranine concentration after different times.

Simulation of the uranine breakthrough curves in Dipole 1. In the tracer tests 07-01 and 08-02, uranine was injected at the borehole CFM 06.002 and recovered at the Pinkel surface packer. These tests were performed in a restricted flow field at outflow rates of about 165 ml/min. The uranine test 08-02 was carried out subsequent to the first homologue tracer test (run 08-01). The shapes of the two experimental breakthrough curves are quite different, due to technical problems during the test 07-01. After this experiment the injection equipment was changed. The uranine injection functions of both tests are presented in Figure 3-5a. A comparison of calculated and measured breakthrough curves is given in Figure 3-5b. The double peak observed in the concentration breakthrough curve of test 07-01 seems to be induced by the above-mentioned technical problem. No double peak was observed in subsequent tests (i.e. homologue test 08-01 and the tracer test 08.02). In a further model calculation, 30 minutes following the start of uranine injection, a 20 % increase in inflow rate was assumed. The double peak is then nearly reproduced and the calculated breakthrough curve is similar to the measurements.

(a)



(b)

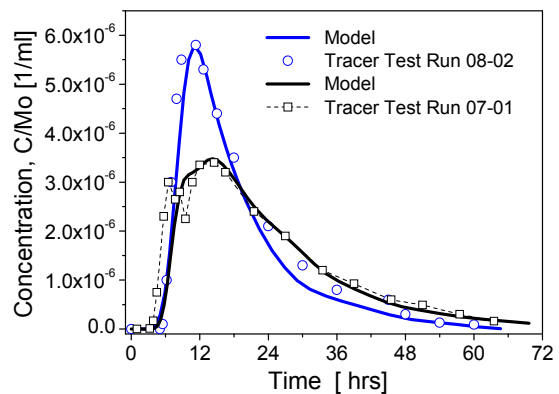


Figure 3-5: (a) Uranine injection functions of two different tests, (b) Comparison of measured and calculated break-through curves for two tracer tests.

Table 3-2: Comparison of hydraulic and transport parameters used to model the tracer tests

	Dipole 2		Dipole 1
	Run #1	Run 07- 02	Run 07-01 and 08-02
Flow porosity	0.1	0.1	0.12
Horizontal permeability (m ²)	2E-11	1E-11	2E-09
Vertical permeability (m ²)	1E-11	1E-11	1E-09
Longitudinal dispersion (m)	0.005	0.005	0.002
Transversal dispersion (m)	0.0005	0.0005	0.0002
Diffusion coefficient (m ² /s)	2E-11	2E-11	2E-11

For tracer test 08-02, the transport parameters have been kept the same as for run 07-01. In this case, the model reproduces the peak height position and width, as well as the shape of the tail. The computed piezometric head and the evolution of uranine concentration in the shear zone for the tracer test 08-02 are illustrated in Figure 3-6. The plots show that the mean flow pathway of the tracer is towards the extraction well.

Overall, regarding the hydraulic and transport properties obtained from this calibration work using tracer tests, it can be concluded that the area below the drift (dipole 2) is less permeable (transmissive) as the region around the dipole 1 (which confirm the in situ observations and the geostatistical model developed by [158]).

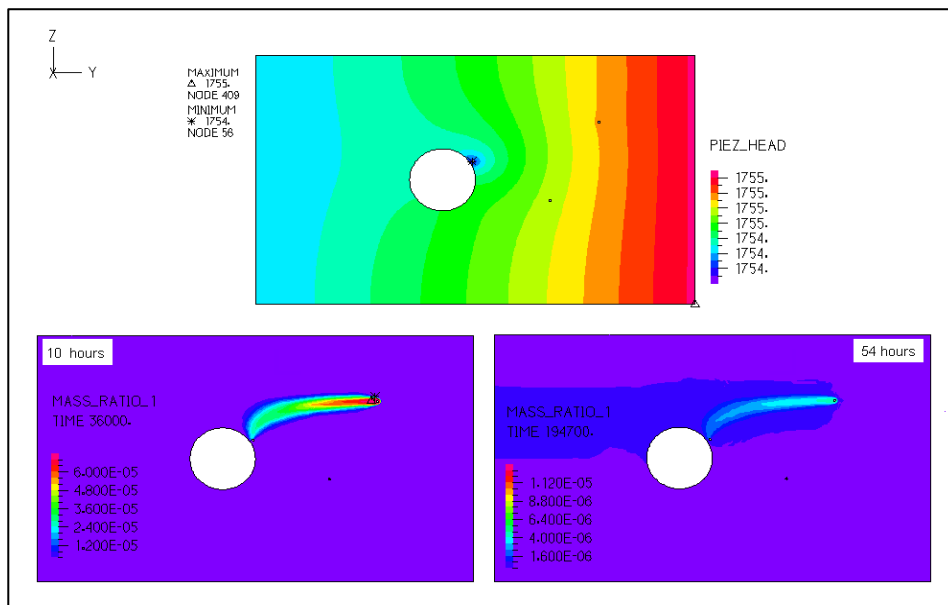


Figure 3-6: Distribution of piezometric head and uranine concentration 10 and 54 hours after injection.

In the next project step, further work is required to explore how the uncertainties on parameter estimation and the subsequent predictions at lower hydraulic gradients are affected by the choice of the present conceptual model. However, the test 08.01 with homologue radionuclides will be simulated using the transport parameters obtained by fitting the uranine tests.

3.2 Finite element modelling (ADINA-F) of flow and transport in a single fracture from the Äspö HRL (Sweden)

Abstract. Results are presented of a numerical study concerning the fluid flow and tracer transport through a single fracture in a granite drill core. The goal of this work is to investigate the influence of fracture geometry and surface roughness/heterogeneity on the flow velocity distribution which in turn has a direct impact on solute transport. Possible chemical processes which can lead to a retardation of solutes have been excluded, to solely investigate the influence of geometrical features. Geometrical information of the single fracture was obtained by means of a μ XCT with a spatial resolution of 80 μ m. This spatial information served as direct input for finite element simulations in Semi-2D and 3D using commercial finite element code ADINA-F to calculate flow velocity distribution and tracer transport. Experimentally obtained HTO breakthrough curves (BTC) with core#8 show a significant tailing reflecting complex flow and transport processes. Calculated BTCs also exhibit a distinct tailing due to Taylor dispersion and trapping of the tracer in so called low velocity zones near the irregular fracture walls. The results clearly indicate the impact of spatial heterogeneities on the coupled flow and transport processes occurring in fractured rocks leading to a dispersion and retardation of solutes and therefore to distinct tailings in the BTCs.

Introduction

Fluid flow as well as mass transport through fractured rock plays an important role in both scientific and industrial issues ranging from e.g. petroleum engineering to the storage of nuclear waste in a deep geologic repository. Fractured rock behaves completely different compared to porous media concerning fluid flow, especially fractured rock systems with very low matrix permeability. In contrast to porous media, fluid flow through fractured rocks is bound to discrete roughly shaped planes, which act as main flow paths. As a consequence this issue has been extensively studied in the past by several authors [158-161]. Both experimental and theoretical approaches have been applied to shed light on the processes governing flow and transport in single fractures as well as fracture networks. In most cases, fractures were treated with the parallel plate model or the streaming tube approach, where real natural fracture geometries are replaced by simplified and abstracted geometries. These simplifications have been made because of a more easily mathematical description resulting in a lesser computational effort. Besides, random fractures have been generated virtually by means of statistical and mathematical methods [162]. The governing equation describing fluid flow is the Navier-Stokes equation which represents a nonlinear system of partial differential equations, only to be solved numerically in 3D. Modern laboratory techniques, like e.g. computer tomography can serve as a non-destructive tool for characterisation of natural fractures in drill cores providing geometrical information which can be used directly in numerical codes to conduct flow and mass transport simulations on the measured scale. This more realistic approach has been applied in this study.

Materials & Methods

Core characterisation. The core used in this study comes from hard rock laboratory (HRL) in Äspö (Schweden) from the drill hole KOV 01 774.7-775.2. From a petrologic point of view, it would be classified as a diorite. For further geological, petrologic and geochemical details of the site, see [163]. Prior to characterisation, the core was sealed on the outside by sticking it in a custom made Plexiglas column. To gain information about geometry and orientation of the fracture and porosity and aperture distribution, it was scanned using a μ XCT. For further details about the applied experimental techniques it is referred to [164]. The size of the core is 13.528 cm in length and 5.048 cm in diameter. With the aforementioned method and setup

a resolution of 80 μm was achieved. The obtained CT data set were pre-processed using different computational tools for CT artefact reduction and segmentation of the fracture. By utilization of the complete CT dataset a connected porosity of 0.68% and an aperture distribution of the core could be derived. Figure 3-7 shows the fracture as rendered from the pre-processed data set. As expected for a real fracture, it possesses a complex 3D spatial geometry and fracture surface morphology. One side of the core shows a relatively sharp border, while the other side has a very irregular boundary. The last mentioned complex geometric feature is known/assumed to have a strong impact on the flow field and in consequence a strong influence for mass transport. Here occurrence of so called trapping zones is likely which can retard tracers and colloids when entering recirculation zones, e.g. through dispersion and/or diffusion [165].

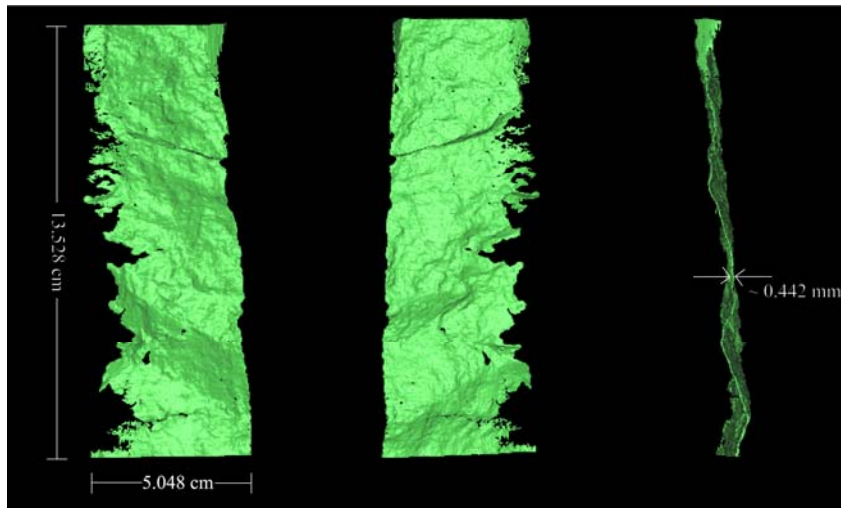


Figure 3-7: Rendered 3D image of fracture in Core#8 on the basis of the μXCT data set which shows the complex overall geometry and surface morphology. Notice the very irregular boundary on one side of the fracture.

Finite Element Model. Fluid flow and tracer transport through the fracture was modeled using the commercial finite element code ADINA-F [166, 167]. To study the effect of the fracture geometry two completely different models concerning the geometrical complexity have been generated. The first model in semi-2D dimension uses only mean values for the aperture, thus reducing most of the geometrical information of the CT data. The second model is a full 3D model using the complete CT data set, thus all of the geometrical information are considered. Mesh generation of the semi-2D was produced using the ADINA-F build-in mesh generator. The 3D volume mesh was generated out of the CT data set by means of the software 3-matic. Figure 3-8 shows both finite element meshes used in the study. All surfaces except the inlet at the bottom and the outlet at the top of the fracture are assigned no-slip (no-flow) boundary conditions.

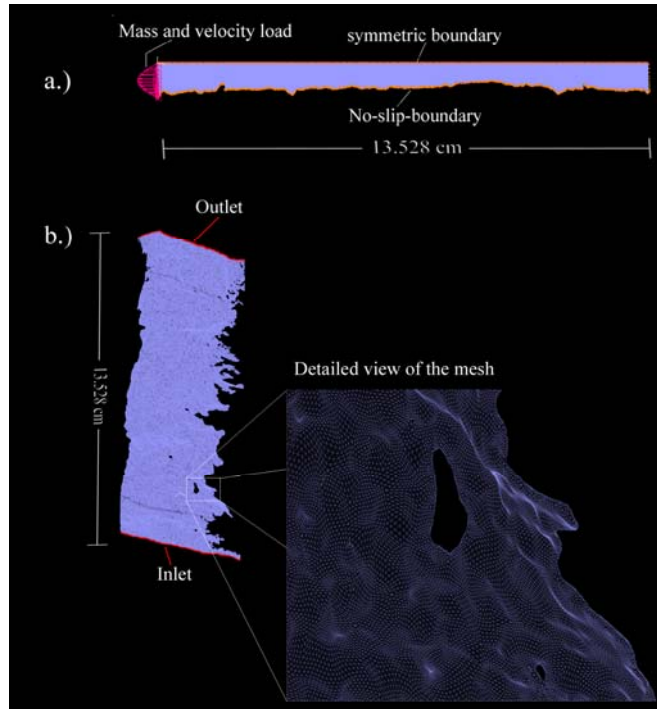


Figure 3-8: View of the semi-2D finite element mesh with the applied boundary and load conditions. Note that the aperture is shown as 30 times exaggerated for displaying reasons b.) 3D model with the inlet and outlet velocity boundary condition. The detailed view of a part of the 3D mesh shows an area inside the model where the fracture is closed.

In the semi-2D mesh a symmetric boundary has been applied at one side of the fracture. At the inlet of both models parabolic velocity profiles have been applied as velocity boundary condition and the exact tracer input function from the experiment is used as mass load boundary condition. The possible existence of matrix porosity in the vicinity of the fracture boundary and especially on the very irregular side of the fracture are completely ignored, to exclusively study the influence of geometry information on the velocity flow field and thus on the mechanisms dominating mass transport. Due to the same reason, calculations are conducted without regarding any chemical processes like e.g. sorption or sorptive reduction. The flow is laminar and water as fluid is incompressible with a density of 998.1 kg/m^3 and a viscosity of 0.001 kg/ms . A diffusion coefficient of $2.5 \cdot 10^{-9} \text{ m}^2/\text{s}$ for HTO has been used. Both models are used to calculate a HTO breakthrough curve obtained by a migration experiment on core #8 with a flux of 0.1 ml/min .

Mathematical description of fluid flow. The governing equation which describes complex fluid flow behaviour is the three-dimensional Navier-Stokes equation which is a non-linear system of partial differential equations satisfying the momentum, mass and energy conservation. For a steady state laminar flow of a Newtonian fluid with constant density and viscosity the equation can be written in vector form as [168]:

$$\rho(\mathbf{u} \cdot \nabla)\mathbf{u} = \mu \nabla^2 \mathbf{u} - \nabla p \quad (\text{Equation 14})$$

$$\nabla \cdot \mathbf{u} = 0 \quad (\text{Equation 15})$$

where ρ = fluid density, μ = fluid viscosity, $\mathbf{u} = (u_x, u_y, u_z)$ velocity vector and $p(x,y,z)$ = hydrodynamic pressure. Eq.(14) represents the momentum conservation and Eq.(15) the mass conservation. The inertial forces, viscous forces and pressure forces are described in

Eq.(14) by the first, second and third term, respectively. Depending on the ratio of inertial to viscous forces, which is known as the Reynolds number, a simplification of the Navier-Stokes equation can be achieved. This is the case when inertial forces are small compared to viscous and pressure forces, so the Navier-Stokes equation reduces to the so called Stokes equation which can be expressed as

$$0 = \mu \nabla^2 \mathbf{u} - \nabla p \quad (\text{Equation 16})$$

The Stokes equation forms a system of linear partial equations and thus can be solved more easily. By applying no-slip (=no-flow) boundary conditions at the boundary walls one component in the velocity vector \mathbf{u} (u_x , u_y , u_z) becomes zero which leads to a further simplification and thus lesser computational effort.

Results & Discussion

Calculated velocity, pressure and mass distribution of the semi-2D model are shown in Figure 3-9. As expected, a parabolic velocity profile has evolved and highest flow velocities correlate with zones of smaller aperture and vice versa. The pressure distribution shows a continuous gradient representing steady state flow conditions. A snapshot of tracer migration after 2250s reflects the parabolic velocity profile which leads to a dispersion. Figure 3-10 shows experimentally obtained breakthrough curves from migration experiments with core#8 in comparison with breakthrough curves calculated using the above described two finite element models. Regarding the semi-2D model, the peak correlates satisfactorily with the experimental peak position. A clear deviation in the tailing of the BTC is observed which can be explained by the averaging step of the geometrical information. The tailing is mainly produced by Taylor dispersion and to a lesser extent by molecular diffusion. It is obvious that the application of a mean aperture results in an averaging of the tailing in the calculated BTC.

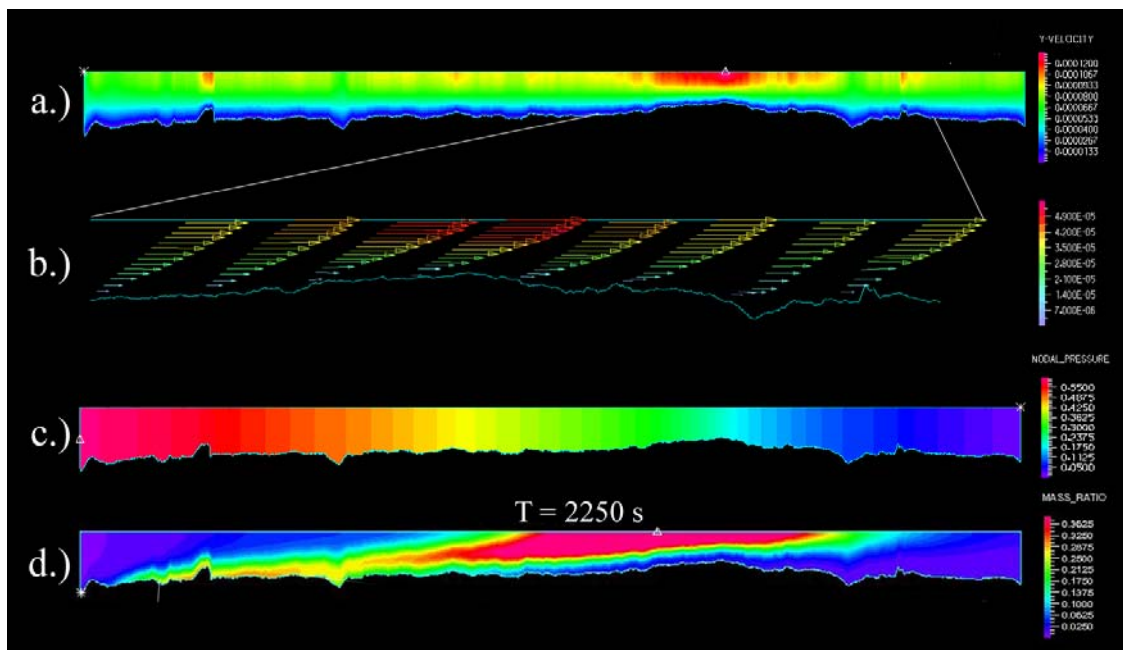


Figure 3-9: Results of the semi-2D model. a.) velocity distribution in the fracture. b.) detailed view of a part of the model showing velocity vectors. c.) calculated pressure distribution. c.) snapshot of the migrating tracer at time 2250 sec.

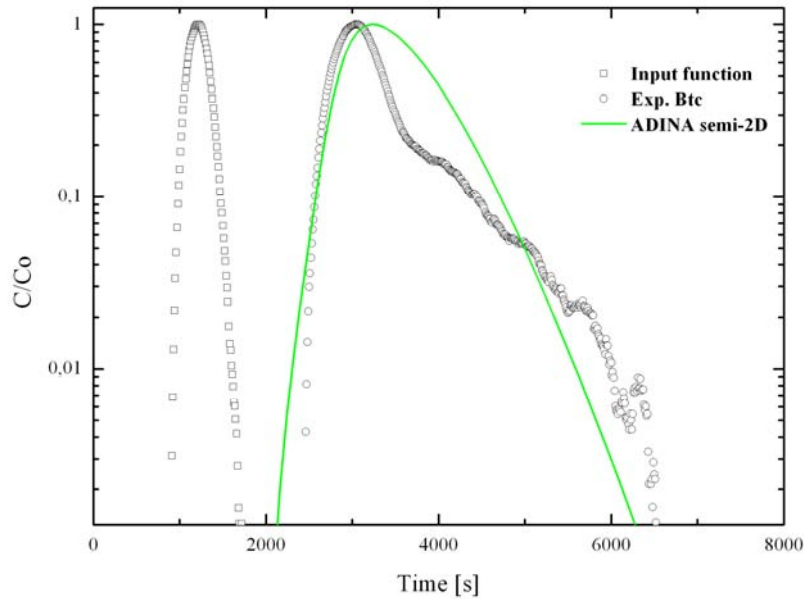


Figure 3-10: Normalized experimental HTO (open symbols) and calculated (line) BTC as function of time.

First calculations using the 3D model are conducted at the moment. First results show a peak position which is shifted to earlier times compared to the experimental BTC due to the fact that the same velocity has been used in the 3D simulations as in the semi-2D model. The velocity is some kind of a fitting parameter, because only the flux is known from the experiment which has to be recalculated by dividing it through the surface area of the inlet of the fracture. This surface is not exactly known because of the experimental setup and can only be roughly estimated. Nonetheless, the shape of the calculated peak is in relatively good accordance to the experimental HTO BTC. It has to be stated that no complete breakthrough curve has been simulated at the moment because of technical problems. From a visualization of the mass transport it can be derived that one can expect a distinct tailing in the BTC. Tracer distribution in the fracture shows a strong influence of the irregular side of the fracture where the tracer seems to be strongly retarded.

Conclusions

- Fluid and mass transport were simulated using the FEM approach on basis of datasets from a μ XTC (resolution $80\mu\text{m}$) of a single fracture in a diorite drill core to investigate the influence of real fracture geometry on the flow and transport behaviour.
- Two models have been tested. The semi-2D model only uses the averaged aperture of the fracture in contrast to the second model, a full 3D model using the full resolution of the CT dataset. Both models have been used to simulate a tracer migration experiment on the core#8.
- The semi-2D model results can reproduce the peak position quite satisfactorily but smoothes the tailing of the experimental BTC. These differences can be explained regarding the averaged fracture geometry information used in the model.
- The current 3D model cannot reproduce the peak position, but matches the shape of the peak quite good. This deviation is due to the fact, that there is uncertainty at the moment about the real velocity at the inlet of the fracture which can only be roughly

calculated from the used flux in the migration experiment. It has to be stated that the results of the 3D model are of preliminary nature. Despite the greater computational and technical effort in creating a 3D model on a basis of CT data, our results can be seen as a step towards a more fundamental understanding of the processes governing flow and mass transport in real single fractures.

3.3 1D and 2D flow and colloid facilitated transport modelling including kinetically controlled sorption processes

One of the goals of this section is to shed light on the multitude of different interaction processes between radionuclides, colloids and the sediment matrix. Especially we are interested in the consequences of kinetically controlled adsorption and desorption. To this end, we interpret laboratory geochemical data as measured by INE in terms of known theories. We are thereby able to assess the contribution of the processes involved. The sorption and filtration parameters extracted in the analysis provide necessary input for our transport calculations. Having calibrated the hydrogeological parameters with tracer data, the thus configured problem is then employed to predict the migration of radionuclides and colloids. Predictions are in turn compared to respective experiments in order to validate the models. Furthermore, we perform artificial variations of the hydrogeological conditions and interaction parameters as well as extrapolations to safety case relevant time and length scales.

For the computer simulations, we use a 2D as well as a 1D-transport code. This enables us to investigate the influence of dimensionality and complex flow fields on the form of the breakthrough curve. In particular, we intend to separate these effects from matrix diffusion. To this end colloidal transport and sorption effects were integrated into the 2D version of the program r^3t . While the simulation of the CFM experiment in two dimensions leads to realistic run times, the computing demands of repository scale calculations force us to fall back on our 1D code TRAPIC [45].

3.3.1 Experimental basis

The analysis relies on field data gathered in the CRR [15, 16, 169] and CFM campaigns [1] as well as on supporting laboratory results (e.g. [15, 62]). For a detailed description of the experimental basis, we refer the reader to sections 2.1.2 and 2.2. When applicable we will reiterate important aspects to ease the understanding of our modeling pipeline since intermediate results derived from the laboratory data are fed to the transport simulations.

3.3.1.1 Laboratory data input

For all elements, used as reactive tracers in the CRR-experiments, the time dependence of their sorption on the fracture infill material was measured in batch experiments by INE in solutions with and without colloids (concentration 20 mg/l) [15]. In the experiments, the radionuclides were shortly equilibrated with the solution and then brought into contact with the sediment. These data have been used in a first step to derive sorption coefficients and sorption rates for radionuclide adsorption to the sediment and to derive desorption rates from colloids for the tri- and tetravalent actinides (see section 3.3.3). We used the results of a new set of batch experiments, which have been performed by INE with an increased number of

sample points in time [170]. The data are listed in Table 3-3 and described in section 2.1.2. Experiments to investigate the interaction of colloids with the sediment matrix by INE are in progress (see section 2.1.5). Therefore, at this stage the interaction between colloids and sediment matrix has been described only by the theory of deep bed filtration (see section 3.3.4).

Table 3-3: Time dependence of the distribution coefficients [m^3/kg] of selected elements for the fracture infill material Grimsel [170]. The data have been determined for three size fractions of the infill material and are listed in this order: 1-2 mm, 0.5-1 mm, and 0.25-0.5 mm)

Time [h]	Np		Am		Pu	
	without colloids	with colloids	without colloids	with colloids	without colloids	with colloids
4	$1.9 \cdot 10^{-3}$	$2.0 \cdot 10^{-3}$	0.193	$2.3 \cdot 10^{-3}$	0.091	$7.0 \cdot 10^{-4}$
	$1.9 \cdot 10^{-3}$	$2.0 \cdot 10^{-3}$	0.193	$2.7 \cdot 10^{-3}$	0.091	$5.0 \cdot 10^{-4}$
	$2.1 \cdot 10^{-3}$	$2.2 \cdot 10^{-3}$	0.188	$2.6 \cdot 10^{-3}$	0.069	$2.0 \cdot 10^{-3}$
24	$4.0 \cdot 10^{-3}$	$2.8 \cdot 10^{-3}$	0.238	$3.6 \cdot 10^{-3}$	0.100	$8.0 \cdot 10^{-4}$
	$4.0 \cdot 10^{-3}$	$2.6 \cdot 10^{-3}$	0.238	$2.8 \cdot 10^{-3}$	0.100	$1.0 \cdot 10^{-3}$
	$4.7 \cdot 10^{-3}$	$3.1 \cdot 10^{-3}$	0.223	$2.9 \cdot 10^{-3}$	0.062	$2.6 \cdot 10^{-3}$
72	$2.19 \cdot 10^{-2}$	$3.3 \cdot 10^{-3}$	0.173	$4.8 \cdot 10^{-3}$	0.064	$2.5 \cdot 10^{-3}$
	$8.5 \cdot 10^{-3}$	$3.6 \cdot 10^{-3}$	0.084	$2.7 \cdot 10^{-3}$	0.030	$2.7 \cdot 10^{-3}$
	$9.9 \cdot 10^{-3}$	$3.3 \cdot 10^{-3}$	0.030	$3.0 \cdot 10^{-3}$	0.037	$2.7 \cdot 10^{-3}$
144	$4.48 \cdot 10^{-2}$	$3.7 \cdot 10^{-3}$	0.156	$7.9 \cdot 10^{-3}$	0.056	$3.0 \cdot 10^{-3}$
	$4.48 \cdot 10^{-3}$	$1.28 \cdot 10^{-2}$	0.156	$7.6 \cdot 10^{-3}$	0.056	$3.0 \cdot 10^{-3}$
	$2.14 \cdot 10^{-2}$	$1.3 \cdot 10^{-2}$	0.032	$7.6 \cdot 10^{-3}$	0.016	$3.0 \cdot 10^{-3}$
312	0.1144	$1.18 \cdot 10^{-2}$	0.192	$2.71 \cdot 10^{-2}$	0.354	$1.9 \cdot 10^{-2}$
	0.1007	$5.08 \cdot 10^{-2}$	0.278	$2.51 \cdot 10^{-2}$	0.273	$1.55 \cdot 10^{-2}$
	0.0943	$3.15 \cdot 10^{-2}$	0.287	$2.06 \cdot 10^{-2}$	0.296	$2.96 \cdot 10^{-2}$
624	0.0991	$1.84 \cdot 10^{-2}$	1.877	$5.27 \cdot 10^{-2}$	0.798	$2.55 \cdot 10^{-2}$
	0.1038	$2.21 \cdot 10^{-2}$	0.756	$6.68 \cdot 10^{-2}$	0.319	$6.39 \cdot 10^{-2}$
	0.1910	$2.06 \cdot 10^{-2}$	1.126	$4.44 \cdot 10^{-2}$	0.246	$2.46 \cdot 10^{-2}$

3.3.2 Field experiments

3.3.2.1 Colloid and radionuclide retention (CRR)

The colloid and radionuclide retention CRR experiment e.g. [15, 16, 169] was the first field experiment at the Grimsel test site dedicated to the study of the in-situ migration behavior of selected actinides and fission products in the presence and absence of bentonite colloids. In comparison with natural conditions, relatively high groundwater velocities have been chosen so as to restrict the travel times to a few hours. As a consequence, high recoveries of the RN have been yielded. Results from the CRR experiments have been used in the first phase of the project to derive input parameters for the interactions of RN with bentonite colloids and the fracture infill material and to check, whether the transport can be satisfactorily described with the model TRAPIC-1D and these values. The breakthrough curves for Am, Pu, Np and U and the respective recoveries for Am and Pu are shown in Figure 3-11. The maxima of the breakthrough curves of Am and Pu occur earlier than those of uranium and neptunium due to colloid-facilitated transport. The recovery of Pu is >90% whereas Am reaches lower values of

~60% after five hours. However, the data for Am have been measured close to the detection limit, a fact which might be responsible for the relatively low recoveries.

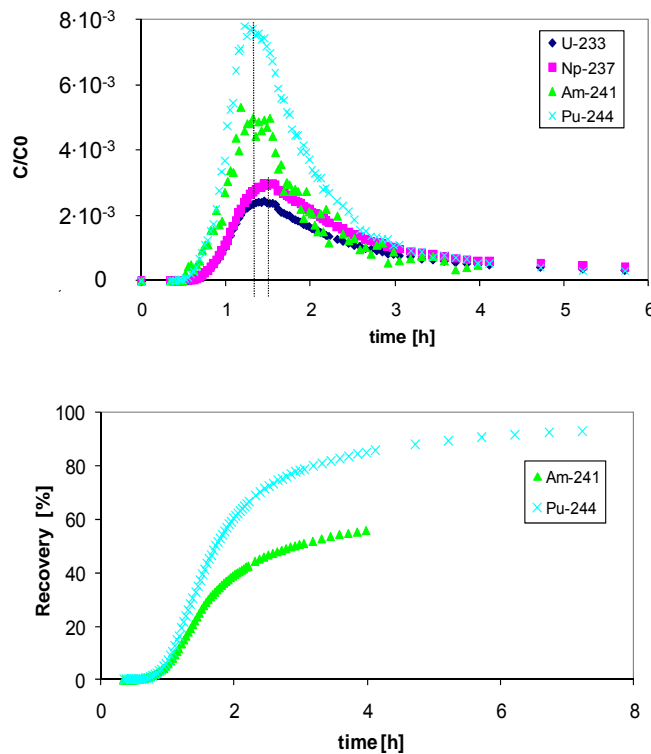


Figure 3-11: Breakthrough curves of Am, Pu, Np and U (top) and the respective recoveries for Am and Pu (bottom) in the CRR experiment #32 [15].

3.3.2.2 Colloid formation and migration (CFM)

One aim of the CFM project is to reduce the flow velocities and increase the travel times of the tracers to approach conditions as expected in a typical repository system and to better identify the effects of desorption and/or filtration on the recovery of the pollutants. A number of additional boreholes have been drilled for the CFM project. The new dipole established for the tracer test 08-02 and for the first homologue test 08-01 is constituted by the shear zone, the inflow borehole CFM 06.002 and the outflow area “Pinkel” as shown in Figure 3-12. In Run 08-02, which was performed two weeks after the homologue experiment, the injected uranine tracer solution was recirculated in order to measure the injection function. This was not done for the homologue experiment, i.e. no injection function is available.

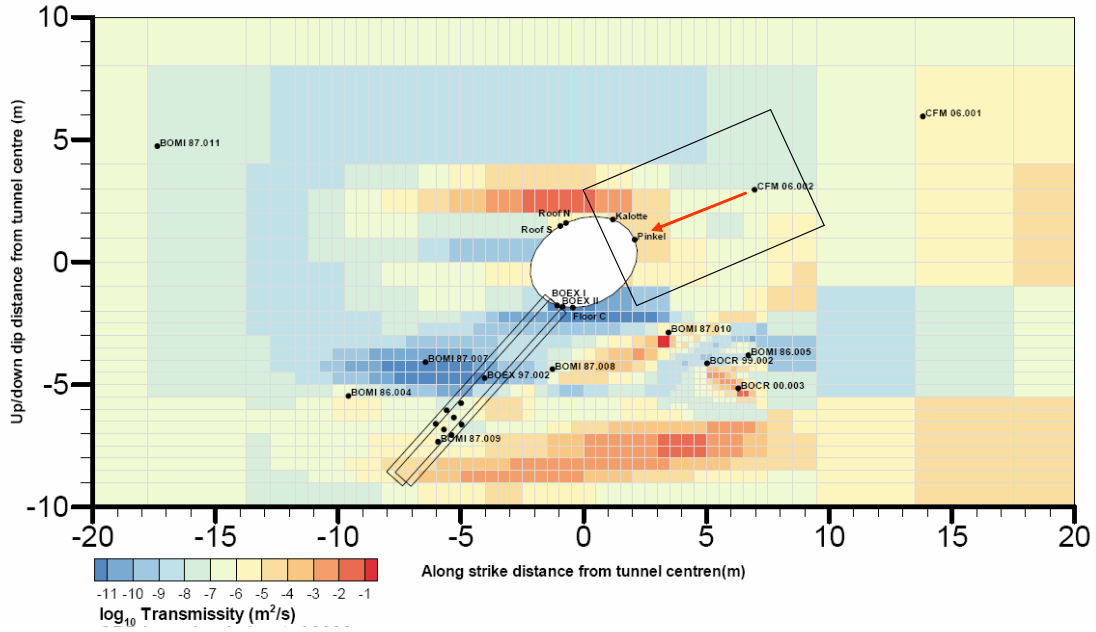


Figure 3-12: Transmissivity field and location of boreholes in the shear zone (after [171]). The dipole between borehole CFM 06.002 and Pinkel for the CFM homologue experiment is shown by the red arrow.

While the peaks of the breakthrough curves for the homologues occurred after 239 minutes, the peak of the uranine tracer arrived after 544.5 minutes. It is not yet clarified, why the colloid-bound homologues are transported so much faster than the conservative tracer. Judging from previously observed velocity acceleration factors for colloid transport close to one it is unlikely that this results from colloid-facilitated transport alone. This issue is discussed in section 2.2 and section 3.3.5.2.

Further homologue dipole experiments with increased travel times are under way. It is planned to reduce the flow velocity by reducing the water flux at the outflow borehole. These experiments will be analysed within a follow-up project.

3.3.3 Modelling of sorption processes

The adsorption and desorption rates for the radionuclides can be derived from the time-dependent concentrations measured in the batch experiments (cf. Figure 2-6) using the following system of equations:

$$\frac{\partial C_{Pb}}{\partial t} = -k_3(C_{Pb} - K_{d3}C_C C_{Pf}) \quad (\text{Equation 16})$$

$$\Theta \frac{\partial C_{Pf}}{\partial t} = k_3\Theta(C_{Pb} - K_{d3}C_C C_{Pf}) - k_1\rho(K_{d1}C_{Pf} - S_{Pf}) \quad (\text{Equation 17})$$

$$\frac{\partial S_{Pf}}{\partial t} = k_1(K_{d1}C_{Pf} - S_{Pf}) \quad (\text{Equation 18})$$

$$C_{Pb}(0) = C_{Pb,0}$$

$$C_{Pf}(0) = C_{Pf,0}$$

$$S_{Pf}(0) = S_{Pf,0}$$

with

C_{Pf} :	concentration of dissolved contaminants
C_{Pb} :	concentration of contaminants sorbed on mobile colloids
C_C :	concentration of mobile colloids
S_{Pf} :	mass of contaminants sorbed on sediment matrix per rock mass
K_{d1} :	distribution coefficient of dissolved contaminants on sediment matrix
k_1 :	rate for sorption of contaminants on sediment matrix
K_{d3} :	distribution coefficient of dissolved contaminants on mobile colloids
k_3 :	rate for sorption of contaminants on mobile colloids
Θ	effective porosity
ρ	dry density

The initial concentrations are marked with index 0. The system of equations was numerically solved with MATLAB. Figure 3-13 illustrates the denotation of the different interaction processes. The sorption process of the free pollutant on the sediment matrix is described by the rate k_1 . The sorption process of the free pollutant on mobile and immobile colloids is described by the rates k_3 and k_4 , respectively. The interaction process of the colloids with the sediment matrix is described by the rates K_2 and k_2 (cf. section 3.3.5).

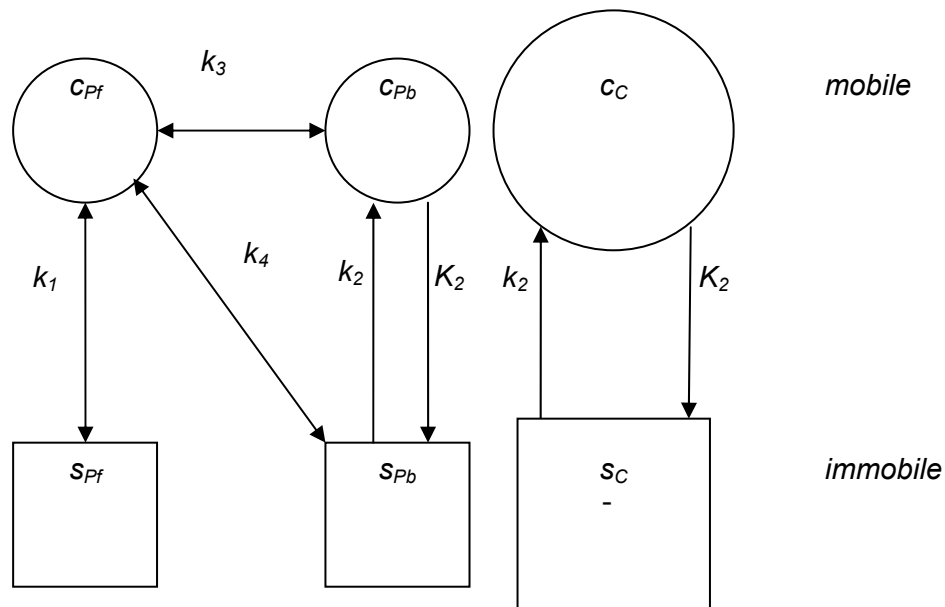


Figure 3-13: Nomenclature chosen for the concentrations of the pollutant and the colloid as well as for the sorption paths.

The effective porosity for the Batch-Experiment is calculated by

$$\Theta = \frac{1}{\frac{1}{\rho_f} \frac{M}{V} + 1} \quad (\text{Equation 19})$$

and the dry density by

$$\rho = \rho_f(1 - \Theta). \quad (\text{Equation 20})$$

For the rock density ρ_f a value of 2670 kg/m³ is assumed. With the V/M ratio of 4 ml/g the porosity results to 0.914 and the dry density to 229 kg/m³.

For the evaluation it is further assumed that the bentonite colloids do not sorb onto the sediment matrix. In this case $K_{d,tot}$ can be calculated by the ratio of the immobile and mobile pollutant concentrations as

$$K_{d,tot} = \frac{S_{Pf}}{C_{Pf} + C_{Pb}} = \frac{K_{d1}C_{Pf}}{C + C_C K_{d3} C_{Pf}} = \frac{K_{d1}}{1 + C_C K_{d3}} \quad (\text{Equation 21})$$

K_{d1} values are derived from experiments without colloids. Here the data point at the last point in time is used, i.e. it is assumed that at this time equilibrium conditions are reached. In the same way the $K_{d,tot}$ value can be arrived from the experiments with colloids. We considered two different cases in the data evaluation. There are strong indications that the desorption kinetics of the actinides from the bentonite colloids plays the most important role, namely that the adsorption process of the actinide to the sediment matrix is fast compared to the desorption process of the actinide from the colloid ($k_1 \gg k_3$). This assumption is realised in case A by use of a very high adsorption rate k_1 in the data evaluation. It is further assumed, that 98% of the actinides are initially bound to the colloids, as is observed under equilibrium conditions.

However, the data points for Am and Pu are characterised by a plateau appearing quite early (<100 h). These observations lead to the investigation of a second scenario. In experiments of Pu with colloids (without sediment) it was observed that the distribution coefficient of Pu on bentonite colloids (K_{d3}) increases from initially 100 m³/kg within three weeks to >1000 m³/kg [16]. Therefore, for the batch experiment with sediment it is important to know, how long the solution of actinides with bentonite colloids was equilibrated, before it was put into contact with the sediment. If a short equilibration time is assumed, it is likely that a distinct fraction of the actinides was not yet sorbed on colloids. This fraction might then sorb with a fast kinetics to the sediment and cause the plateau in the sorption curves. This is considered in case B.

The data indicate that a time dependent sorption of Np to the fracture filling material is observed without an influence of colloidal phases present. This is in contrast to experiments, performed in the CRR project [15], where no significant Np sorption was observed. A possible explanation is the change in the redox state from Np(V) to Np(IV) in these new experiments (cf section 2.1.2). Due to this uncertainty, we restricted the evaluation of data to Am and Pu. The results are presented in Table 3-4 and Figure 3-14 - Figure 3-16. Assuming that equilibrium in the sorption systems is reached after 624 h the K_{d1} value is about 0.5 m³/kg for Pu and 0.13 m³/kg for Am. The $K_{d,tot}$ values are derived from the simulations to 0.025 m³/kg for Pu and 0.058 m³/kg for Am. This is in good agreement with 0.025 m³/kg for Pu and 0.053 m³/kg for Am calculated by equation (Equation 21) using K_{d3} values of 1600 m³/kg. A K_{d3}

value of 1600 m³/kg corresponds to a 98 % colloid-bound fraction found in the CRR injection solutions for both elements under equilibrium [15].

In case A it is assumed that 96 % of Pu and Am are initially bound to colloids. The slightly decreased colloid-bound fraction is due to the slightly decreased colloid concentration in the batch experiments (0.0134 kg/m³) compared with the CRR field experiments (0.02 kg/m³). A value of 1 h⁻¹ is used for k_1 , i.e. 4 % of the elements sorb fastly onto the sediment matrix. The kinetics of the subsequent sorption is then determined by k_3 . The best simulations result in values of 0.0085 h⁻¹ and 0.009 h⁻¹ for Pu and Am, respectively. The data used are listed in Table 3-4. The model curves describe the experimental values quite well apart from the plateau, which is shown in Figure 3-14 and Figure 3-15.

Table 3-4: Parameters used for the best simulation of the Batch experiments for Pu and for Am (in brackets, when different from Pu)

parameter	unit	value		parameter	unit	Value	
		A	B			A	B
C_C	[kg/m ³]	0.0134		k_1	[h ⁻¹]	1	>0.05
$C_{Pb,0}$	[kg/m ³]	0.96	0.8 (0.7)	K_{d1}	[m ³ /kg]	0.56 (1.35)	
$C_{Pf,0}$	[kg/m ³]	0.04	0.2 (0.3)	K_{d3}	[m ³ /kg]	1600	
$S_{Pf,0}$	[kg/kg]	0		k_3	[h ⁻¹]	0.0085 (0.009)	0.007 (0.0065)

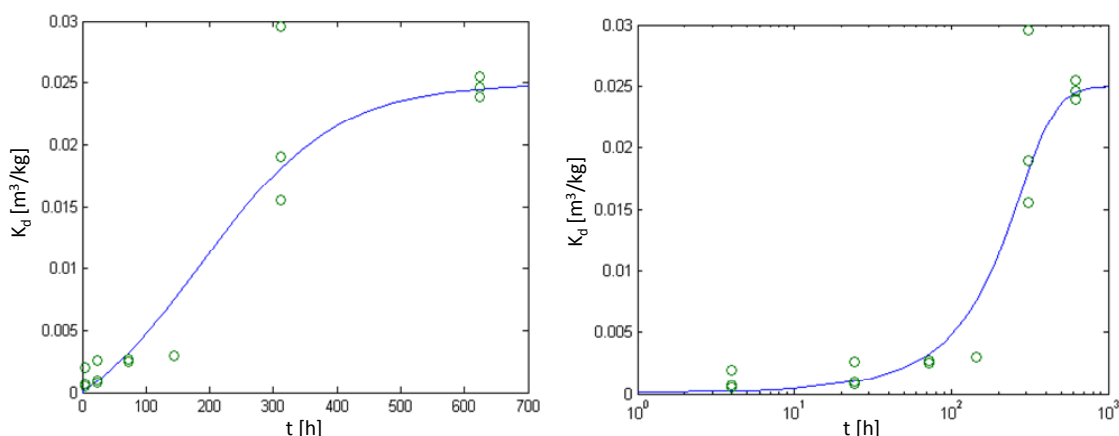


Figure 3-14: Case A: Distribution coefficients for plutonium as function of time. Data from experiments (dots) and model curves on linear and logarithmic time scales. Model parameters see Table 3-4.

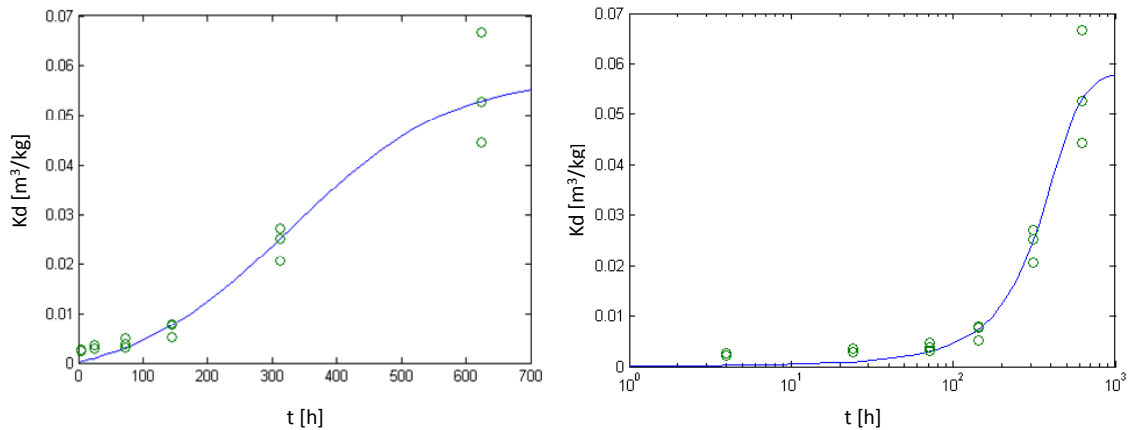


Figure 3-15: Case A: Distribution coefficients for americium as a function of time. Data from experiments (dots) and model curves on linear and logarithmic time scales. Model parameters see Table 3-4.

As observed in previous experiments, the curves for both americium and plutonium show only slight variations at times between 1 hour and 100 hours. As discussed above, this indicates that a higher element fraction than 4 % (as assumed in case A) sorbs with faster kinetics. This was evaluated in case B, where an increased initially not colloid-bound actinide fraction is regarded. Figure 3-16 shows the results of a simulation assuming that 20 % of plutonium and 30 % of americium are initially not bound to colloids, respectively. With an adsorption rate $k_1 > 0.05 \text{ h}^{-1}$ the plateau is well described by the resulting curves. The k_3 values are slightly lower than in case A.

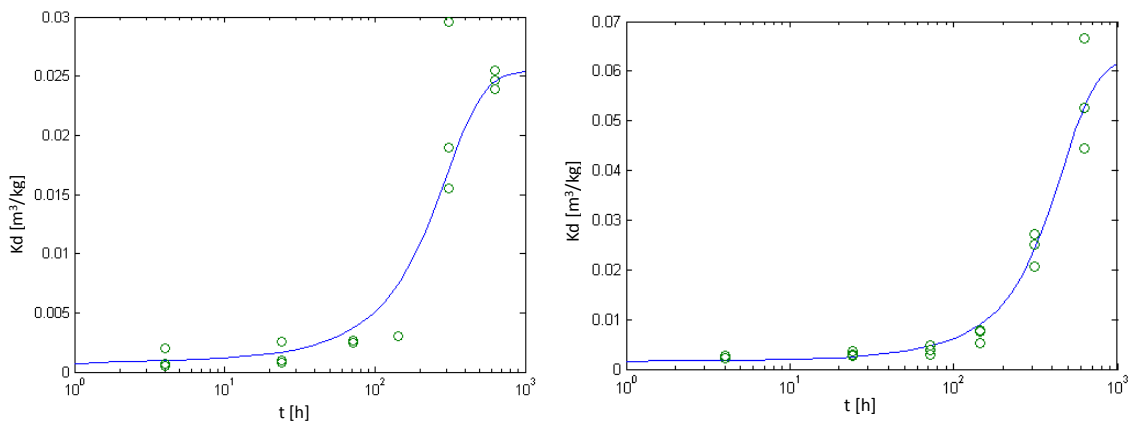


Figure 3-16: Case B: Distribution coefficients for plutonium and americium as function of time assuming 20% of Pu and 30% of Am not being initially sorbed to colloids. $k_1 = 0.05 \text{ h}^{-1}$. Other model parameters see Table 3-4

The results indicate that both actinides exhibit a similar behaviour regarding the desorption kinetics. The rates k_3 are in all cases in a range between 0.005 and 0.01 h^{-1} . The coefficient for actinide sorption onto the sediment matrix is increased by a factor of about two in case of Am. For the further calculations we take the reference value 0.0065 h^{-1} for rate k_3 .

3.3.4 Modelling of filtration processes

The interaction of colloids with the sediment matrix might also strongly impact the breakthrough curve and the recovery of the radionuclides. In order to estimate this impact, the deep bed filtration approach was applied here. In a later step, when modelling parameters from the respective laboratory experiments will be available, they will be compared to the results from the deep bed filtration approach. The deep bed filtration theory assumes that colloids, which come into contact with the sediment surface, are bound with a probability α . This bond is then irreversible. The process can be described by the following equation

$$\frac{\partial}{\partial t}(\rho_C S_C) = \lambda_f q_C C_C. \quad (\text{Equation 22})$$

The particle velocity is denoted as q_C . The efficiency of the filtration can be described by the filter coefficient λ_f . The mechanism is independent of the amount of already filtrated colloids. Important parameters are the porosity and pore size of the sediment, the diameter of the colloidal particles, and the viscosity. Here we refer to the model of Tien [172], Yao [106] and [173]. For the attachment of colloids on the sediment it is distinguished between three different processes: interception, sedimentation and diffusion. The model assumes the conditions for a particle passing a spherical collector. For this geometry a collector efficiency can be defined as

$$\eta = \frac{F_p}{q_C C_0 \pi d_C^2 / 4} \quad (\text{Equation 23})$$

with

F_p	particle flux reaching the surface,
q_C	particle velocity,
C_0	particle concentration in undisturbed medium,
d_C	collector diameter.

According to Yao et al [106] the collector efficiency is determined by the sum of the efficiencies of each individual process. The efficiencies for interception η_I , sedimentation η_S and diffusion η_D are calculated as follows

$$\eta_I = \frac{3}{2} \left(\frac{d_p}{d_C} \right)^2 \quad (\text{Equation 24})$$

$$\eta_S = \frac{(\rho_p - \rho) d_p^2 g}{18 \mu q_C} \quad (\text{Equation 25})$$

$$\eta_D = 0.9 \left(\frac{k_B T}{\mu d_p d_C q_C} \right)^{2/3} \quad (\text{Equation 26})$$

with

d_p	particle diameter,
d_C	collector diameter,
ρ_p	particle density,
ρ	fluid density,
μ	dynamic viscosity,
g	gravitation constant,
k_B	Boltzmann constant,
T	temperature.

The filter coefficient is then defined as

$$\lambda_f = \frac{3}{2} \frac{1 - \Theta}{d_c} \eta \alpha \quad (\text{Equation 27})$$

and related to the filtration rate K_2 in case of an irreversible filtration by

$$K_2 \Theta = \lambda_f q_c. \quad (\text{Equation 28})$$

The porosity is denoted by Θ . The attachment factor α describes the part of the colloid-matrix collisions which lead to binding. The attachment process of colloidal bentonite particles on granite infill material under Grimsel conditions has been investigated in experiments by De-gueudre et al. [40]. From these investigations an attachment factor of $2 \cdot 10^{-4}$ was determined. All other parameters, which are adapted to the conditions of the CFM experiment, are listed in Table 3-5.

Table 3-5: Parameters used for the deep bed filtration approach

parameter	unit	Value
particle velocity q_c	m/s	$5 \cdot 10^{-4}$
viscosity μ	Ns/m ³	$1 \cdot 10^{-3}$
fluid density ρ	kg/m ³	1000
colloid density ρ_p	kg/m ³	2670
collector diameter d_c	m	$5 \cdot 10^{-4}$
gravitation constant g	m/s ²	9.81
temperature T	K	298.15
Boltzmann constant k_B	J/K	$1.38 \cdot 10^{-23}$
porosity Θ		0.1
attachment factor α		$2 \cdot 10^{-4}$

The viscosity and fluid density are given for the low mineralised Grimsel groundwater. For the bentonite colloids the rock density of bentonite is applied. A collector diameter of $5 \cdot 10^{-4}$ m is selected as an average grain size of the fracture infill material according to data from Dollinger [171]. The particle velocity was derived from the maximum velocity of the colloids in experiment 08-02. Figure 3-17 illustrates the contribution of the three processes diffusion, interception and sedimentation to the collector efficiency. For small particle diameters $< 0.7 \mu\text{m}$ diffusion is the dominating process. At larger particle diameters the collector efficiency is determined by sedimentation; interception is not relevant for the size of the collector diameter assumed here.

For the particle diameter a reference value of $0.14 \mu\text{m}$ has been chosen for the calculations according to analysis from INE (cf. section 2.1.2). Using all other values listed in Table 3-5 the filtration coefficient λ_f amounts to $1.2 \cdot 10^{-3}$ and from equation (14) K_2 results to $5.9 \cdot 10^{-6} \text{ s}^{-1}$ ($\approx 2 \cdot 10^{-2} \text{ h}^{-1}$).

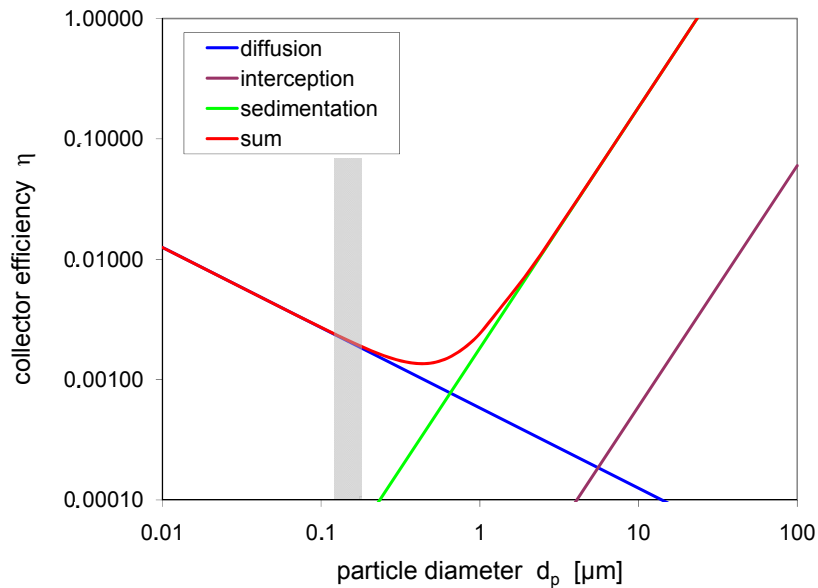


Figure 3-17: Collector efficiency vs. particle diameter for conditions listed in Table 3-5. Shaded area marks the range of colloid diameters observed under Grimsel groundwater conditions

3.3.5 Simulations

The shear zone of the CFM experiment consists of a network of open channels embedded into fracture infill material and enclosed by quasi-parallel granite walls whose distance is small compared to their extent. In our simulations it is assumed that the transport in this environment can be described by single phase flow in a 2D or somewhat less accurately in a 1D homogeneous porous medium on the given observation time and length scales. We model slow sorption processes with kinetic equations. Kinetic effects will likely not be relevant for the slow transport regime as expected under repository conditions, but they might be needed to understand the CFM experiment. The geochemical constants necessary for the simulation are derived from laboratory experiments as shown above. In contrast, because of model simplifications and the lack of detailed information about the fracture, the hydrogeological parameters have to take effective values. Therefore we carry out an additional calibration step by performing parameter variations in an effort to match the resulting breakthrough curves to the outcome of in-situ tracer experiments. In the 2D simulations our aim is not to reproduce the exact flow field but to approximate the distribution of flow path lengths which translate into the arrival time distribution of the tracer. The values for the hydrogeological parameters obtained in the calibration process are of course not unique. They might even be wrong in the sense that extrapolations to different experimental conditions fail to meet experimental results. An exhaustive search for a best fit in the set of all compatible values appears nevertheless impractical. The predictions of the simulations should therefore be treated with necessary care.

Colloids complicate the transport dynamics of the system consisting of rock matrix, solvent and radionuclides by introducing new interaction pathways and processes: they serve as sorption targets for the much smaller pollutants and may themselves interact with the matrix through filtration. The deep bed filtration approach employed here is explained in section 3.3.4. In this regard two assumptions are important for the following analysis: 1) the colloids, once attached to matrix, become permanently immobile 2) we presuppose that the resulting local alterations of the matrix porosity are negligible. A consequence of the particle size of

the colloids is a steric reduction of the accessible pore space the implications of which are also not taken into account. In particular colloids and pollutants both see the same effective matrix porosity. Moreover colloidal stability is taken for granted and matrix diffusion is not included in our model. We consider radioactive decay only in the repository-scale calculations.

We denote the concentration (mass per solvent volume) of mobile particles by c , whereas s represents the mass of immobile particles adsorbed to the matrix per mass rock matrix. The indexes P, Pb, Pf and C map these variables and several parameters to the populations and properties of pollutants in general (P), colloid-bound pollutants (Pb), colloid-free pollutants (Pf) and the colloids (C) respectively. A schematic view of the interaction system is depicted in Figure 3-13. The mathematical description of our model is given by the following system of diffusion-advection-reaction equations

$$\begin{aligned}
\partial_t(\theta_C c_C) + \nabla \cdot (c_C \mathbf{q}_C - \mathbf{D}_C \nabla c_C) &= -Q_2^C \\
\partial_t(\rho_C s_C) &= Q_2^C \\
\partial_t(\theta_P c_{Pf}) + \nabla \cdot (c_{Pf} \mathbf{q} - \mathbf{D} \nabla c_{Pf}) &= RD(c_{Pf}) - Q_1^P - Q_3^P - Q_4^P \\
\partial_t(\rho s_{Pf}) &= RD(s_{Pf}) + Q_1^P \\
\partial_t(\theta_C c_{Pb}) + \nabla \cdot (c_{Pb} \mathbf{q}_C - \mathbf{D}_C \nabla c_{Pb}) &= RD(c_{Pb}) + Q_3^P - Q_2^P \\
\partial_t s_{Pb} &= RD(s_{Pb}) + Q_2^P + Q_4^P
\end{aligned} \tag{Equation 29}$$

coupled by the source terms Q_i , $i = 1, 2, 3, 4$ and RD which arise from sorption/retention and radioactive decay, respectively.

$$\begin{aligned}
Q_1^P(c_{Pf}, s_{Pf}) &= k_1 \rho (f_1(c_{Pf}) c_{Pf} - s_{Pf}) \\
Q_2^C(c_C, s_C) &= K_2 \theta f_2(c_C) c_C - k_2 \rho_C s_C \\
Q_2^P(c_C, c_{Pb}, s_{Pb}) &= K_2 \theta f_2(c_C) c_{Pb} - k_2 s_{Pb} \\
Q_3^P(c_C, c_{Pf}, s_{Pf}) &= k_3 \theta (f_3(c_{Pf}) c_{Pf} - c_{Pb}) \\
Q_4^P(c_{Pf}, s_C, s_{Pf}) &= k_4 (\rho_C s_C f_4(c_{Pf}) c_{Pf} - s_{Pb})
\end{aligned} \tag{Equation 30}$$

with c : concentration of dissolved particles; s : mass fraction of matrix-attached particles; θ : effective matrix porosity; ρ : matrix bulk density; \mathbf{q} : Darcy velocity; \mathbf{D} : hydrodynamic dispersion tensor; k_i and K_i : transition rates, and f_i : sorption isotherms.

It should be noted that Q_2 can be made asymmetric. We employ this property of the process to simulate irreversible filtration by setting $k_2 = 0$ and interpreting K_2 as the filtration rate. Throughout this report we assume k_4 to be equal to k_3 .

3.3.5.1 1D

The objective of the 1D simulation is to check whether the breakthrough curves and, especially the recoveries of the in-situ experiments can be described with the parameters derived from the independent batch experiments. In particular, the range for desorption rates k_3 will be verified. Therefore model calculations for the conditions of the CRR experiment #32 [15] are performed and compared with the experimental data. Here it is assumed that no interac-

tions of colloids with the sediment matrix occur. In a second step parameter variations have been performed to estimate maximum concentrations and recoveries for experiments to be performed at longer travel times, as intended in the CFM project. In these parameter variations the impact of an irreversible colloid filtration is investigated, too.

Simulation of the CRR experiment. The pathway length is determined by the distance between injection and detection borehole, which is 2.2 m. The experiment was performed with an injection rate of 10 ml/min and an extraction rate of 150 ml/min, i.e. radionuclides are diluted during transport. This is considered by a constant volume flow of 150 ml/min in the whole 1D model area. Pore velocity and dispersion length are derived from the breakthrough curve of the conservative tracer I-131 (cf. Figure 3-18). This curve shows a strong tailing, which might be caused by matrix diffusion, and/or different pathway lengths of the particles in addition to dispersion. Both effects cannot be described in TRAPIC-1D causing the deviation between calculated and experimental curve. The porosity of the fracture is assumed to be 10 %. The cross section is chosen to $6 \cdot 10^{-2} \text{ m}^2$ in order to meet the correct pore velocity for the volume flow of 150 ml/min. The dispersion length is derived from the simulation for the conservative tracer. The width of the peak is met by a dispersion length of 0.1 m as shown in Figure 3-18 on the right, where the simulation curve was scaled to the maximum of the experimental curve (not taking into account the fraction of the tracer in the long-term tailing). All data are summarised in Table 3-6.

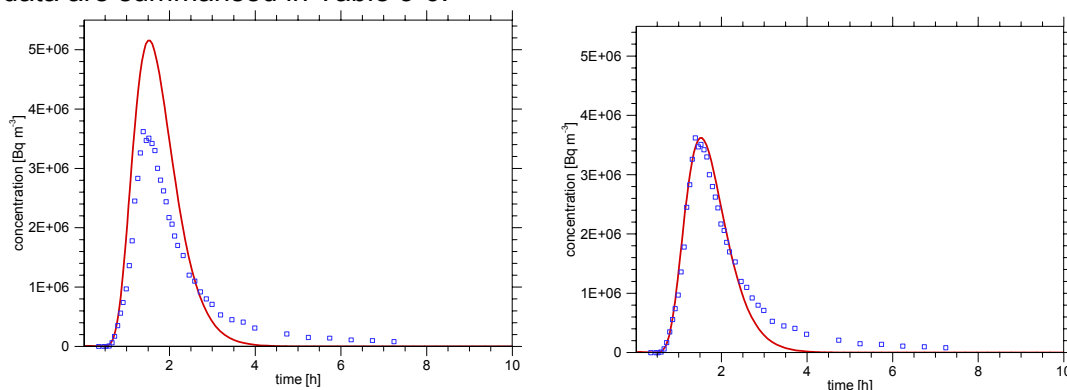


Figure 3-18: Breakthrough curve of the I⁻ tracer: dots = experiment, line = calculated (right side scaled)

Table 3-6: Geometrical and hydraulic data for CRR migration experiment #32

Parameter	unit	value
Pathway length	[m]	2.2
Cross section	[m ²]	$6 \cdot 10^{-2}$
Water flow	[m ³ /h]	$9 \cdot 10^{-3}$
Pore velocity	[m/h]	1.5
Porosity	[]	0.1
Dispersion length	[m]	0.1
Density	[kg/m ³]	2670

The most important parameter with respect to the maximum concentration of the breakthrough curves and the recovery is the desorption rate k_3 . This rate is very similar for Pu and Am. As discussed in section 3.3.3, the experimental data obtained in the CRR experiment for

Pu concentrations are more reliable than the Am data. Therefore, the transport calculations are exemplarily performed for Pu.

The data for the simulation calculations are taken from Table 3-4 and Table 3-6 apart from the concentration of bentonite colloids, which was set to 20 mg/l in accordance with the conditions in the field experiments. Since the equilibration time of the actinides with the injection water was several days the initially colloid-bound fraction of Pu is assumed to be 98%. The desorption rate k_3 was varied in the range between 0.0065 and 0.1 h⁻¹. The concentration of Pu in the injection solution is 1.64·10⁻⁶ kg/m³. A volume of 10⁻⁴ m³ was injected. The breakthrough curves and the recoveries for the simulations and experiments are shown in Figure 3-19. The maximum concentrations of the four simulation curves are slightly higher than in the experiment. However, the recoveries of the experimental and the calculated curves are more valuable for a comparison, since we consider the recovery as a measure for the desorption rate k_3 . If we assume that the tailing is caused by effects independent from the interaction processes between radionuclides, sediment and colloids, the contribution of the tailing should be included in the comparison of the experimentally observed and calculated recovery. The recovery curves are illustrated in Figure 3-19 (bottom).

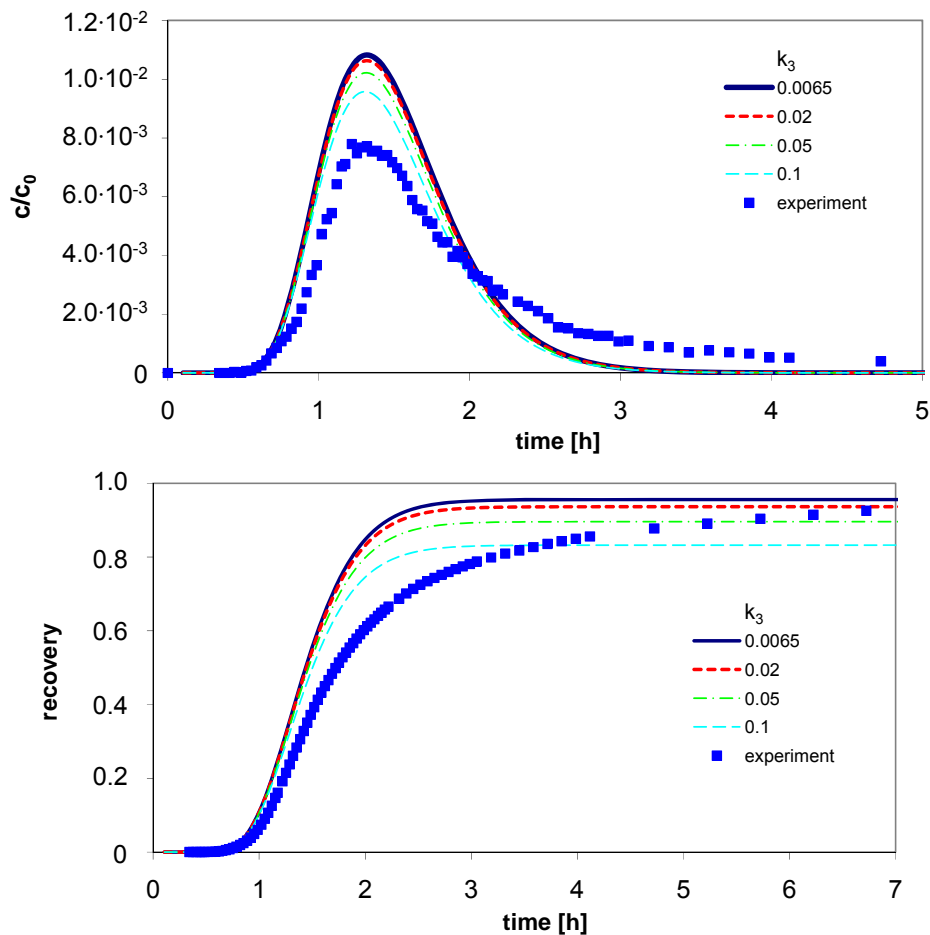


Figure 3-19: Breakthrough curves (top) and recoveries (bottom) for Pu in CRR experiment #32. Results from experiment and simulations

The model curve for a desorption rate of $k_3 = 0.0065$ h⁻¹ shows a recovery of 0.96, i.e. only 2 % of the initially injected Pu desorbs during transport from the colloids. With increasing rate k_3 the recovery decreases, approaching 0.83 for $k_3 = 0.1$ h⁻¹. The recovery of the experimental curve reaches a value of about 0.93 after seven hours with still increasing tendency. The results confirm the upper limit of the range for the sorption rates k_3 derived from batch ex-

periments. They indicate that adequate values for k_3 are below 0.02 h^{-1} . However, longer travel times are necessary to see a more pronounced effect of the desorption kinetics and to better determine the kinetic rates in the flow experiments. It could be further shown that there is no significant influence on the shape and maximum of the breakthrough curves for different k_1 rates $>0.05 \text{ h}^{-1}$, i.e. the adsorption process is fast even for $k_1 = 0.05 \text{ h}^{-1}$ compared to the characteristic time scale of the desorption process.

Parameter variations. The aim of the parameter variations is to estimate radionuclide concentrations in breakthrough curves and recoveries to be obtained in experiments carried out under more natural conditions, i.e. with lower flow rates than in the CRR experiment. The results should help to design the CFM experiments, e.g. to check whether radionuclide concentrations are still detectable at distinct groundwater travel times as given by the ratio of pathway length and pore velocity. In this respect the effects of the kinetically controlled desorption and filtration are of particular interest, since the impact of both processes increase with travel time. Therefore, calculations for similar model conditions as in CRR, with a slightly increased pathway length of 10 m have been performed. The most important data for the model are listed in Table 3-7. For the desorption rate k_3 a range between 0.005 and 0.01 h^{-1} is considered. For the filtration a reference value of $2 \cdot 10^{-2} \text{ h}^{-1}$ and a range between $8 \cdot 10^{-5} \text{ h}^{-1}$ (nearly no impact of filtration) and $2 \cdot 10^{-2} \text{ h}^{-1}$ is chosen. The pore velocity is varied between 0.01 and 5 m/h , which corresponds to groundwater travel times between 1500 and 3 hours. The assumptions concerning the injection solution and injection time are the same as in the CRR experiment. 98 % of Pu of the injection solution is assumed to be bound to bentonite colloids. The colloid concentration is 0.02 g/l .

Table 3-7: Geometrical and hydraulic data for parameter variations

Parameter	unit	value
Pathway length	[m]	10
Cross section	[m ²]	$1.5 \cdot 10^{-1}$
Water flow	[m ³ /h]	varied between $1 \cdot 10^{-4}$ and $5 \cdot 10^{-2}$
Pore velocity	[m/h]	$1 \cdot 10^{-2} - 5$
Travel time	[h]	3 - 1500
Porosity	[]	0.1
Dispersion length	[m]	0.1
Density	[kg/m ³]	2670

The maximum concentrations of the calculated breakthrough curves of colloid-bound are shown in Figure 3-20 for a desorption rate $k_3 = 0.005 \text{ h}^{-1}$. In the case of very low filtration rates (black solid line) the maximum concentration is above 10^{-7} mol/l for more than 300 hours travel time. In the case of filtration with a rate $K_2 = 2 \cdot 10^{-2} \text{ h}^{-1}$ the Pu concentration drops below $1 \cdot 10^{-7} \text{ mol/l}$ after about 50 hours and below $1 \cdot 10^{-10} \text{ mol/l}$ after 300 hours.

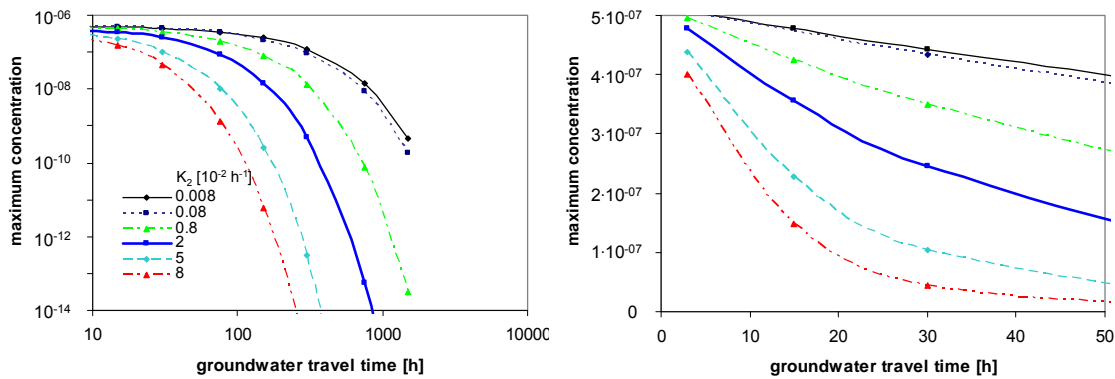


Figure 3-20: Concentration of Pu [mol/l] at the peak maximum of the breakthrough curve vs. groundwater travel time for different filtration rates. $k_3 = 0.005 \text{ h}^{-1}$: linear scale (left) and logarithmic scale (right)

For the same calculations the recoveries are shown in Figure 3-21 and Figure 3-22. The recoveries were obtained by integrating the breakthrough curves up to the time point twice the average groundwater travel time. The curves with filtration rates of $8 \cdot 10^{-5} \text{ h}^{-1}$ and $8 \cdot 10^{-4} \text{ h}^{-1}$ are very similar indicating that for a filtration rate of $8 \cdot 10^{-5} \text{ h}^{-1}$ the recovery decrease is only caused by the desorption of Pu from the colloids during transport. If no filtration processes occur the recovery will be reduced within 50 hours only down to 80% ($k_3 = 0.005 \text{ h}^{-1}$) and down to 60% ($k_3 = 0.01 \text{ h}^{-1}$). In this case travel times of at least 20 to 30 hours should be applied to identify an effect on the recovery.

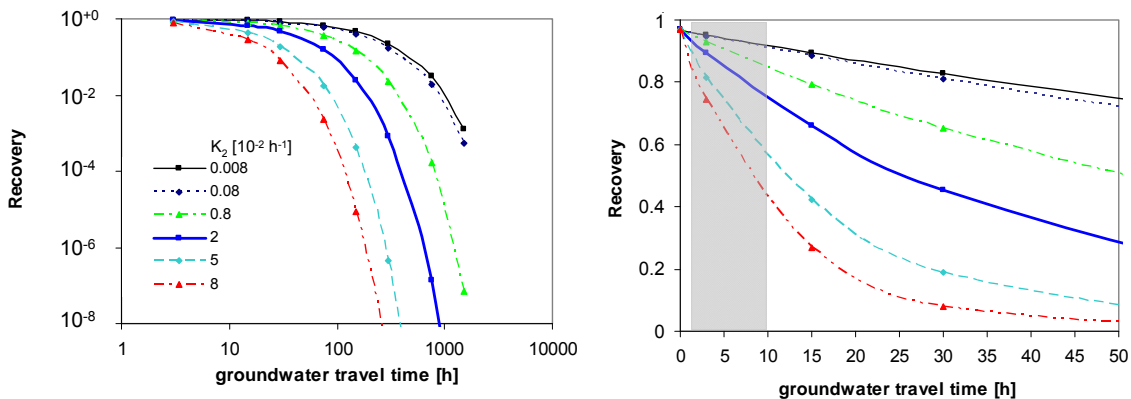


Figure 3-21: Recoveries vs. groundwater travel time for four different filtration rates: logarithmic (left) and linear (right) scale. $k_3 = 0.005 \text{ h}^{-1}$. The shadowed area indicates the range of travel times applied so far in the CRR and CFM experiments

The calculations with a filtration rate $K_2 = 2 \cdot 10^{-2} \text{ h}^{-1}$ derived from the deep bed filtration approach are marked as bold blue line. In these calculations the recovery is reduced within 10 hours to values of 30% to 20% and after 20 hours already to values $< 60\%$.

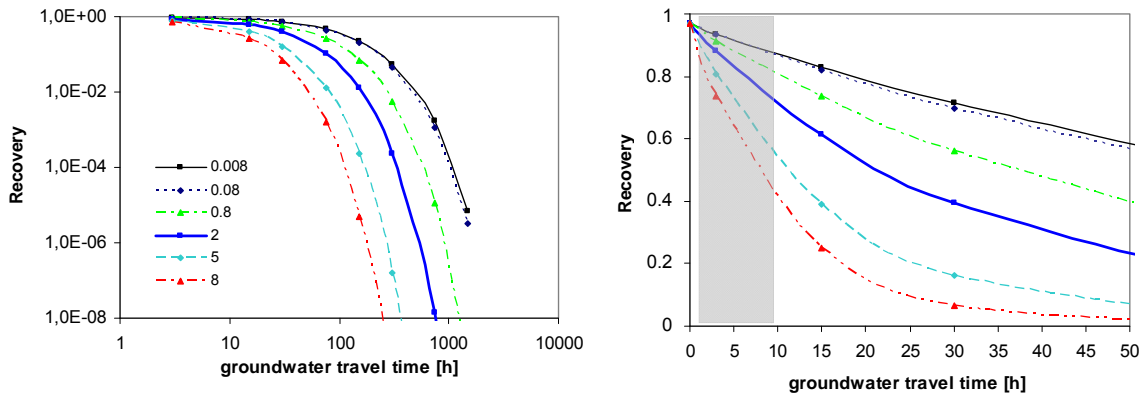


Figure 3-22: Recoveries vs. groundwater travel time for four different filtration rates: logarithmic (left) and linear (right) scale. $k_3 = 0.01 \text{ h}^{-1}$. The shadowed area indicates the range of travel times applied so far in the CRR and CFM experiments

3.3.5.2 2D

All 2D migration simulations are performed using the program r^3t based on stationary velocity fields calculated by d^3f . In order to simulate pollutant transport influenced by colloidal particles we had to enhance the code with the respective coupled sorption dynamics. The description of the implementation details of this new program version called $r^3t\text{-col}$ are relegated to the appendix.

We kept our computer representation of the CFM experiment intentionally simple in order to capture just the main characteristics of the problem. Only the cylindrical tunnel wall obstructs the transport and no inhomogeneities or anisotropies of the hydrogeological parameters shape the flow field. Mirror symmetry is assumed with regard to the x-axis so that computing resources can be saved by simulating only the upper half of the model area as illustrated in Figure 3-23 which also shows the chosen boundary conditions. The transformation of the 3D experimental constraints into the boundary conditions of the 2D model requires the introduction of a virtual homogeneous shear zone thickness which we set to $d=0.01\text{m}$ on the grounds of typical widths found in rock samples from the CFM site and in accordance with the CFM modellers group agreement.

The tunnel wall and the symmetry boundary elements are experimentally and implicitly sealed to transport respectively. For r^3t the measured concentration input function is transformed into a mass flux constraint and the experimentally prescribed solution volume rates at the in- and outflow areas are passed to d^3f in the form of velocities. All other walls are virtual and only serve to confine the model to a finite area. There constant pressure values cause the flow field to be solely determined by the dipole. The disappearing normal derivatives of the pollutant concentration prevent spurious dispersive fluxes due to artificial gradients, which would otherwise occur at the respective boundaries.

Out of the two CFM field experiments undertaken so far at the dipole “CFM-06.002 – Pinkel” we could arguably utilise only the results of the tracer test CFM-08-02 since the data for the transport of the homologues in CFM-08-01 exhibit two major inconsistencies with the configuration run:

1. the input function was not monitored

- the colloid break through curves indicate a much faster dynamics than observed for the tracer hinting at changed hydrogeological conditions either caused by natural instability or forcibly impaired by the experiment.

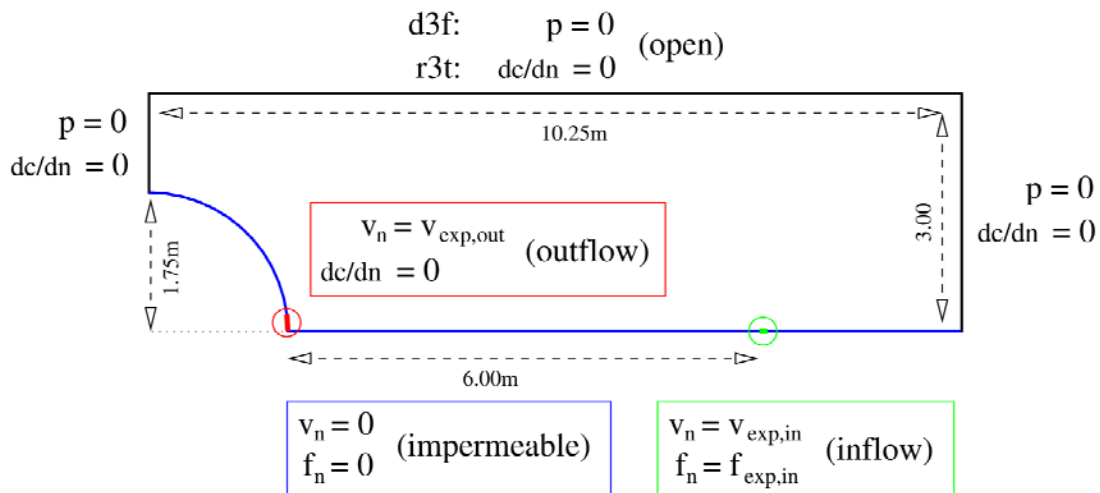


Figure 3-23: Geometry and hydrogeological/transport-related boundary conditions of 2D the computer model. Green: inflow, red outflow, blue: sealed tunnel wall and symmetry axis, black: permeable virtual boundaries within the shear zone. Notation: c = concentration; p = pressure; v = fluid velocity; f = pollutant mass flux; n is used either as a subscript to denote the normal component or in fractions in which symbolises the normal derivative of the respective variable.

In order to get an idea though, how interactions influence our results we artificially furnished the normally inert tracers with the plutonium sorption properties (see section 3.3.3: $K_{d1} = 0.56 \text{ m}^3/\text{kg}$, $k_1 = 2.7778 \cdot 10^{-4} \text{ s}^{-1}$, $K_{d3} = 1600.0 \text{ m}^3/\text{kg}$, $k_3 = 2.78 \cdot 10^{-6} \text{ s}^{-1}$) and measured the effects on the break through curves and the recovery rates in the presence of colloids which are optionally also subject to filtration by the matrix (see section 3.3.4: $K_2 = 6.0 \cdot 10^{-6} \text{ s}^{-1}$). The input function was borrowed from the tracer experiment and the injected solution consisted of 100% colloid-bound pollutants. Our simulated injection cocktail additionally contained a constant concentration of $0.02 \text{ kg}/\text{m}^3$ of pure colloids. No attempt should be made to compare the outcome of these simulations with other results in this report. Figure 3-24 displays the fit result of the tracer calibration procedure described above with an injection rate of $10 \text{ ml}/\text{min}$ and an extraction rate of $165 \text{ ml}/\text{min}$ based on the data and conditions of experiment CFM-08-02. We obtained the following values for the hydrogeological parameters: porosity = 0.055 , diffusion coefficient = $2.0 \cdot 10^{-11} \text{ m}^2/\text{s}$, dispersion length (longitudinal / transversal) = $7.0 \cdot 10^{-2} / 1.5 \cdot 10^{-2} \text{ m}$, and permeability = $2.0 \cdot 10^{-9} \text{ m}^2$. The rock density had been fixed at $2670.0 \text{ kg}/\text{m}^3$. For our setting, the (isotropic) permeability does not influence the dynamics since we prescribe the outflow velocity. The speed of the pollutants is mainly influenced by the porosity and the virtual shear zone thickness, which is fixed at $d = 0.01 \text{ m}$ and not varied in the calibration procedure as discussed above. This observation might help to explain the unusually low porosity (as compared to experimental values for the infill material), suggesting that the actual flow path is somewhat thinner than assumed or that the model of a homogeneous porous medium is only roughly applicable to the actual hydrological situation.

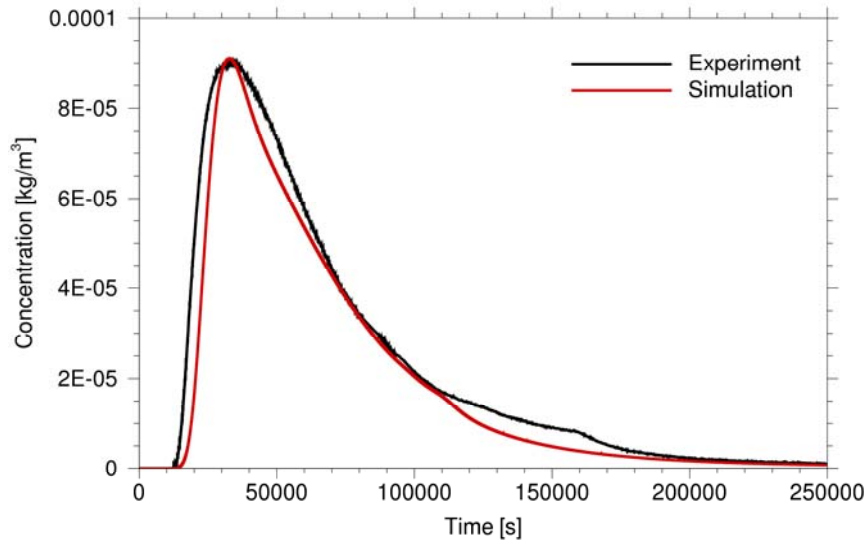


Figure 3-24: Determination of effective hydrogeological parameters by matching the outcome of the simulations to the experimental break through curve of the tracer.

Having calibrated the model we performed computer simulations using the experimentally determined sorption parameters for plutonium (see sections 3.3.3 and 3.3.4) with and without colloid filtration. In addition, extrapolations of our model to lower outflow rates, 50 ml/min and 10 ml/min, were investigated. The results are shown in Figure 3-25. As the outflow rate is throttled; a growing relative reduction in the amplitudes of the corresponding set of break through curves becomes apparent as can be expected from the increasing exposure times to sorption and filtration.

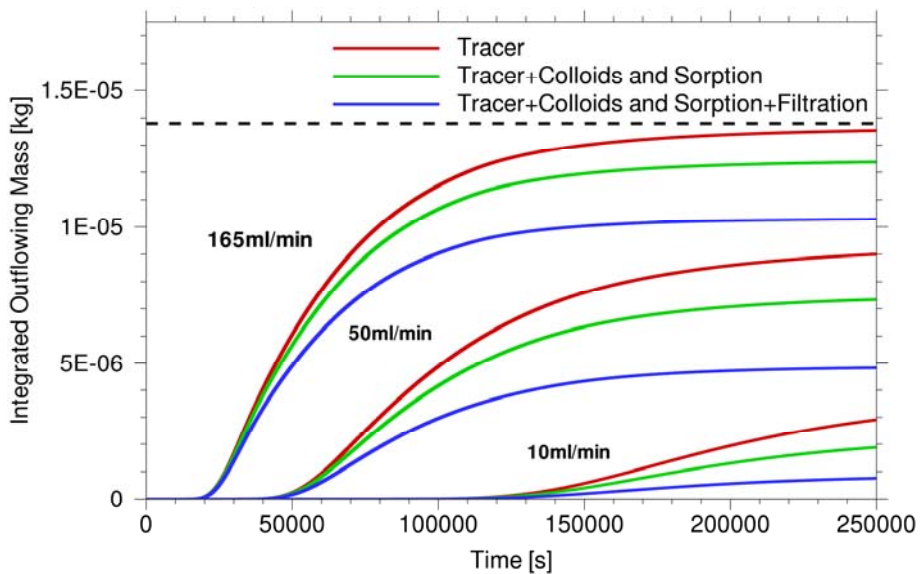


Figure 3-25: Time-dependent recovery of the injected pollutant mass. The dotted black line indicates the totally injected amount.

Figure 3-25 demonstrates that the recovered pollutant masses are simultaneously decreasing with increasing residence time. This results from the fact that the strength of the injection gets comparable to that of the extraction causing some transport pathways to be elongated and others to be totally disconnected from the outflow area as evidenced by Figure 3-26. The interpretation of the recovery curves is not completely straightforward

because of artificial and irreversible mass losses through the virtual model boundaries as observed in Figure 3-27 for 50 ml/min which do not occur at 165 ml/min (c.f. Figure 3-26). The recovered mass fractions measured for the different simulations at the experimental outflow rate of 165ml/min are 98% (tracer), 90% (tracer+colloids with sorption) and 75% (tracer+colloids with sorption+filtration).

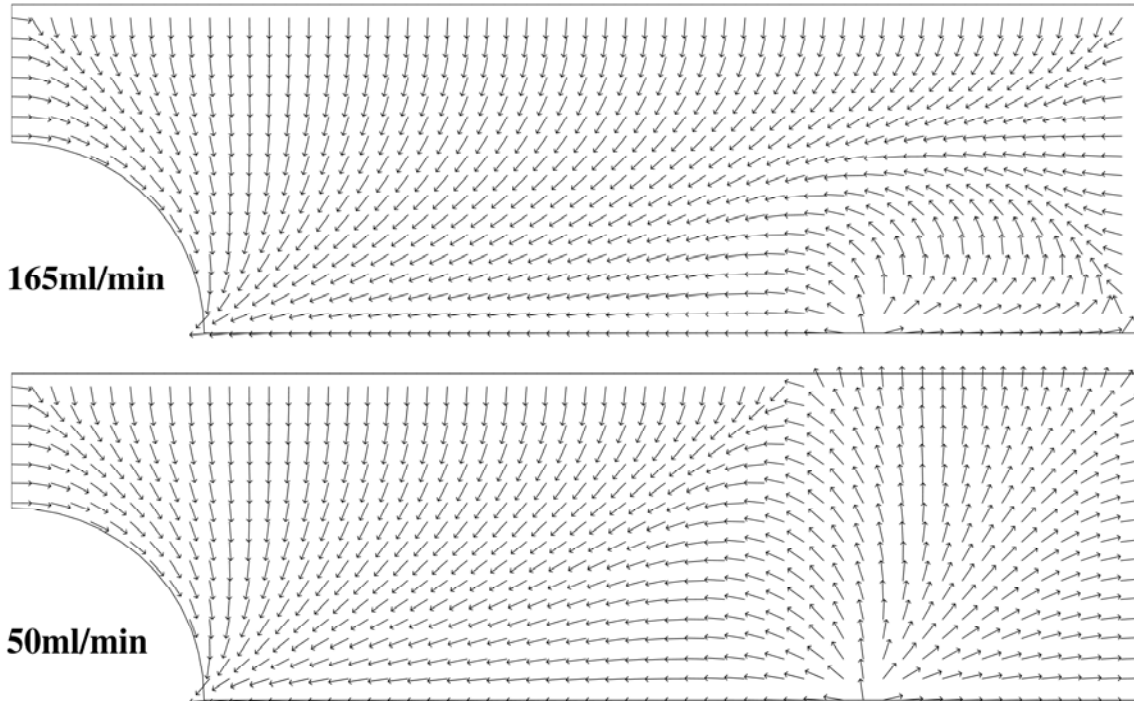


Figure 3-26: Stationary velocity direction field at outflow rates of 165ml/min (top) and 50ml/min (bottom). For illustration purposes, the length of the arrows is not scaled with the magnitude of the velocity.

In a scenario, where only (synthetic) plutonium and no colloids are injected into the model shear zone, the comparison of the simulation snapshots in Figure 3-28 demonstrates how strongly the sorption to the matrix impedes the pollutant transport. This calculation underlines the importance of the desorption rate k_3 which should therefore determine the time scale of the experiments.

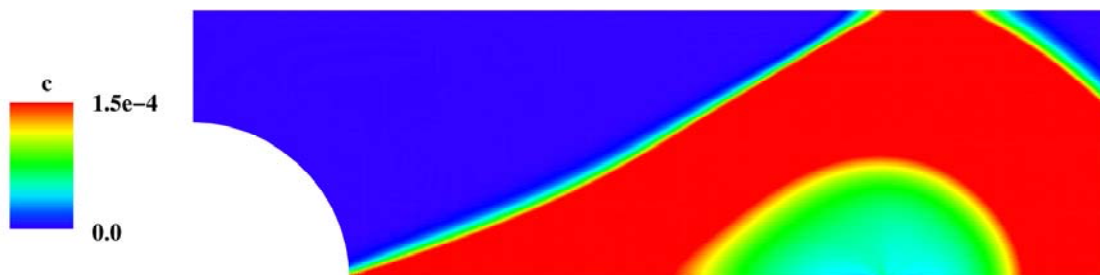


Figure 3-27: Snapshot of a tracer simulation with an outflow rate of 50ml/min illustrating problems with mass loss at permeable boundaries (right and top) due to the inadequate size of the model area for slow transport conditions.

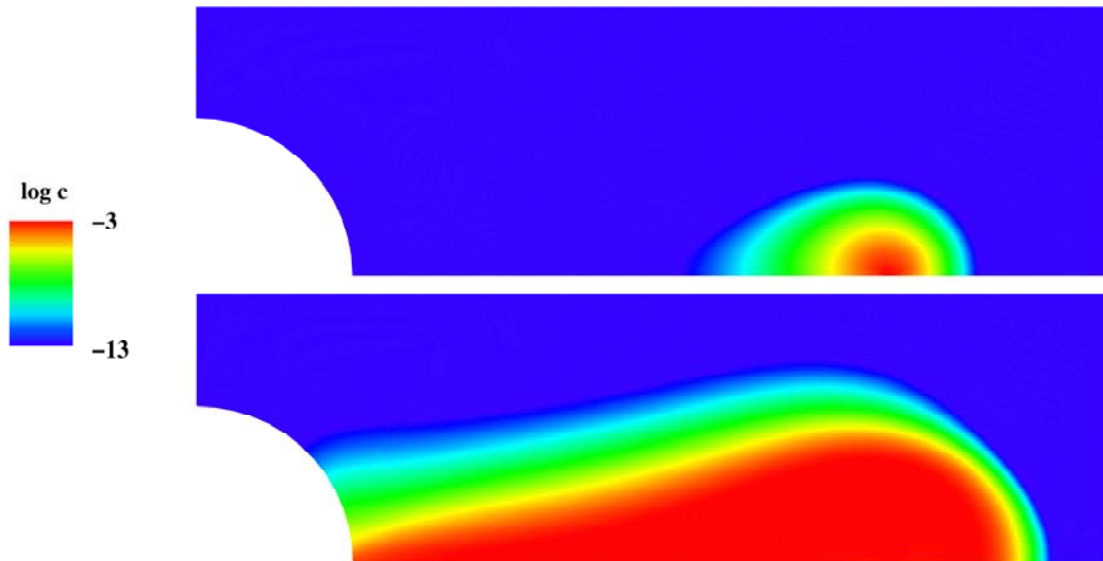


Figure 3-28: 2D logarithmic concentration profile of a simulation at $t = 32500$ s with active sorption processes but in the absence of colloids (top) compared with the equivalent image of the pure tracer experiment (bottom). The outflow rate is 165 ml/min and the snapshot time corresponds to the peak of the experimental tracer breakthrough curve.

Summarizing the results of this section it has been shown, that the tailing of the breakthrough curve could be explained by dimensional effects, i.e. a distribution of transport pathways. Our predictions for the homologue experiment will have to be validated by data from compatible experiments. The extrapolations to lower extraction flow rates suggest that not only the outflow but also the inflow will have to be reduced in order to recover a reasonable amount of the injected particles since transport paths are disconnected when the corresponding velocities become comparable. If this is experimentally not feasible, we will have to enlarge our model area to prevent spurious mass losses through virtual boundaries.

Our goal to analyse the importance of matrix diffusion for the migration experiment based on the tailing of the breakthrough curve has been precluded by the fact, that the experimental input function (cf. Figure 3-29) exhibits a long drawn-out tail itself which overshadows the effect to be investigated. This asymmetry of the input function results from the fact that the sample cocktail is not directly injected into the shear zone but via a void space, the annulus. Given in addition the existence of several, possibly heterogeneous flow paths the tailing is the results of a complex combination of difficult to separate influences.

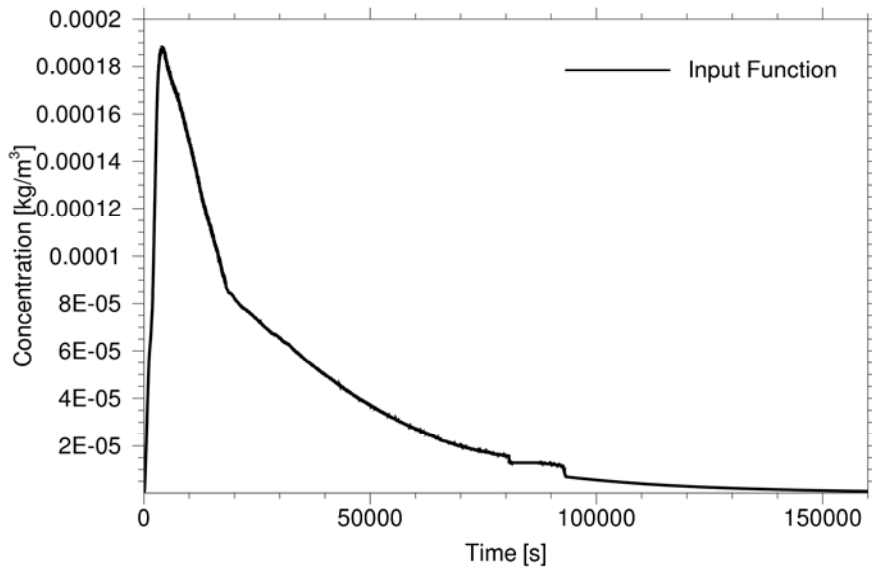


Figure 3-29: Input function: experimental concentration measured at the injection area. The samples were taken from annulus.

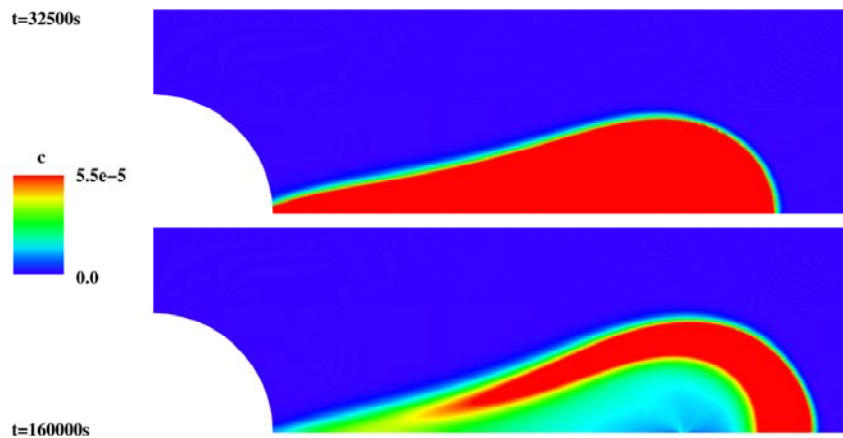


Figure 3-30: Two-dimensional colour-coded display of the concentration (kg/m^3) in the tracer simulation with an outflow rate of 165ml/min at the peak (top) and the tail (bottom) of the break through curve.

3.3.5.3 Repository conditions

Based on our results concerning the interaction parameters exploratory calculations with respect to the temporal and spatial scale of a repository system have been performed. The assumptions for the model calculation are based on the reference case for a repository in a fractured host rock in the German contribution to the European study Spent Fuel Performance Assessment (SPA) [174]. Here only the radionuclides from the four decay chains, mainly actinides are considered, since the highest impact is expected for them. All considered radionuclides and their half lives are listed in Table 3-8.

Table 3-8: Radionuclides and their half-lives considered in the calculations

Actinide	Half life [a]	Actinide	Half life [a]	Actinide	Half life [a]	Actinide	Half life [a]
Cm-248	$3.40 \cdot 10^{+5}$	Cm-245	$8.50 \cdot 10^{+3}$	Cm-246	$4.73 \cdot 10^{+3}$	Cm-247	$1.56 \cdot 10^{+7}$
Pu-244	$3.40 \cdot 10^{+7}$	Am-241	$4.32 \cdot 10^{+2}$	Pu-242	$3.75 \cdot 10^{+5}$	Am-243	$7.37 \cdot 10^{+3}$
Pu-240	$6.56 \cdot 10^{+3}$	Pu-241	$1.44 \cdot 10^{+1}$	U-238	$4.47 \cdot 10^{+9}$	Pu-239	$2.41 \cdot 10^{+4}$
U-236	$2.34 \cdot 10^{+7}$	Np-237	$2.14 \cdot 10^{+6}$	U-234	$2.46 \cdot 10^{+5}$	U-235	$7.04 \cdot 10^{+8}$
Th-232	$1.41 \cdot 10^{+10}$	U-233	$1.59 \cdot 10^{+5}$	Th-230	$7.54 \cdot 10^{+4}$	Pa-231	$3.28 \cdot 10^{+4}$
		Th-229	$7.88 \cdot 10^{+3}$	Ra-226	$1.60 \cdot 10^{+3}$		

It has been assumed that the radionuclide transport occurs via a 200 m long pathway in a porous medium with a porosity of 10 % and a rock density of 2670 kg/m³. The advective flow velocity has been assumed to be 2 m/a referring to a water flow of 200 m³/a and a cross section of 500 m². These conditions for a generic German site in granite are quite conservative with respect to the travel time. In reality the groundwater travel time is expected to be much higher than 100 years.

Since only Cm, Am, Pu and Th display high K_{d3} values for bentonite colloids at GRIMSEL conditions all other elements were not considered for colloid-facilitated transport. For Cm, Am, Pu and Th it was assumed that a fraction of 98 % of the injected nuclides is bound to colloids. The sorption and filtration parameters have been selected according to the results described in section 3.3.3 and 3.3.4. In all calculations similar K_d -values and sorption rates have been applied for Am, Cm, Pu and Th, since the values for the tri- and tetravalent actinides are very similar. The K_{dl} values for all other radionuclides have been selected from results from CRR experiment ($7 \cdot 10^{-3}$ m³/kg for U and $3.4 \cdot 10^{-3}$ m³/kg for Np and Pa) and from the SPA study ($5 \cdot 10^{-1}$ m³/kg for Ra), respectively.

It has to be denoted here that the assumptions are based on GRIMSEL conditions. Under these conditions e.g. uranium occurs in the redox state U(VI) and Np is expected to be at the transition between Np(V) and Np(IV). However, under different geochemical conditions the redox state of both elements might change. In a more reducing / lower pH environment the tetravalent forms of both elements might be dominating. The consequence would be a much stronger interaction of U and Np with colloids, similar to that observed for Th. The radionuclide inflow has been adapted to the results from the SPA study in a way that the maximum radionuclide flux at the interface bentonite/granite of each radionuclide has been taken into account. For each radionuclide a constant inflow over 1000 years is assumed (see Table 3-9).

Table 3-9: Radionuclide inflow for the six cases

Actinide	Inflow [Bq/a]						
Cm-248	$1.0 \cdot 10^{+1}$	Cm-245	$1.0 \cdot 10^{+3}$	Cm-246	$1.0 \cdot 10^{+3}$	Cm-247	$1.0 \cdot 10^{+1}$
Pu-244	$1.0 \cdot 10^{+1}$	Am-241	$1.0 \cdot 10^{+3}$	Pu-242	$1.0 \cdot 10^{+6}$	Am-243	$1.0 \cdot 10^{+5}$
Pu-240	$1.0 \cdot 10^{+5}$	Pu-241	$1.0 \cdot 10^{+3}$	U-238	$1.0 \cdot 10^{+3}$	Pu-239	$1.0 \cdot 10^{+6}$
U-236	$1.0 \cdot 10^{+3}$	Np-237	$1.0 \cdot 10^{+3}$	U-234	$5.0 \cdot 10^{+3}$	U-235	$1.0 \cdot 10^{+2}$
Th-232	$1.0 \cdot 10^{+1}$	U-233	$1.0 \cdot 10^{+3}$	Th-230	$1.0 \cdot 10^{+6}$	Pa-231	$1.0 \cdot 10^{+5}$
		Th-229	$5.0 \cdot 10^{+4}$	Ra-226	$1.0 \cdot 10^{+9}$		

We devised six parameter sets listed in Table 3-10 in order to assess the influences of k_3 variations and filtration on the repository time scale. For this purpose we measured the radionuclide concentrations at the end of the transport pathway. A realistic value of $k_3 = 55 \text{ a}^{-1}$ (about 0.0065 h^{-1}) is used as a reference value.

Table 3-10: Parameters for Cm, Am, Pu and Th for the six calculation cases for repository conditions

case	Sorption to sediment		Sorption to colloids		filtration	remark
	k_1 [a ⁻¹]	K_{d1} [m ³ /kg]	k_3 [a ⁻¹]	K_{d3} [m ³ /kg]	K_2 [a ⁻¹]	
1	1·10 ⁶	0.055	55	1600	no	k_3 – reference
2			1·10 ⁶		no	fast kinetics (equilibrium)
3			55		175	k_3 – reference / + filtration
4			5.5·10 ⁻²		175	k_3 – reduced / + filtration
5			5.5·10 ⁻²		no	k_3 – reduced (10 ⁻³)
6			5.5·10 ⁻⁴		no	k_3 – reduced (10 ⁻⁵)

The results of the calculations are shown in Figure 3-31 to Figure 3-34 for selected radionuclides. All main effects can be explained representatively by the behaviour of those radionuclides. In Figure 3-31 the results for Pu-242 are illustrated. It is clearly shown that the results for the calculations one and two are identical. This demonstrates that under repository-like conditions the kinetics of the interaction paths one and three are irrelevant, i.e. the assumption of equilibrium for the interaction between radionuclides and colloids is justified. Similar results are obtained for all other radionuclides. In case three, where additionally the filtration process is considered, a retardation of the major peak occurs; the peak maximum is shifted from $1.5 \cdot 10^{+4}$ to $6 \cdot 10^{+4}$ years. Sorption and filtration cause a decrease of the peak maximum by about a factor of 10. In case four the desorption rate is lowered by a factor of 1000. Under this assumption only a very slow desorption from filtered particles is possible, i.e. the radionuclides are more or less irreversibly bound to the colloids. The resulting curve shows, that an irreversible filtration on a 200 m long pathway and a groundwater travel time of 100 years efficiently retards the colloids and at the same time the radionuclides. The maximum concentration is further reduced by more than six orders of magnitude which is now additionally caused by radioactive decay.

Cases five and six have been selected to investigate how far the rate k_3 needs to be reduced to observe a strong impact on the maximum concentrations. In both cases no filtration is considered. Under these conditions a reduction of desorption rate causes an increase of the colloid-bound radionuclide fraction. In case 5, where the desorption rate is reduced by a factor of 1000 a significant fraction of Pu-242 is transported quite fast without retardation with a peak arrival after about 100 years. The maximum concentration of this peak is not increased in comparison to the case of equilibrium sorption. If the desorption rate is decreased by a factor of 10⁵, nearly all Pu-242 is transported on colloids causing a maximum concentration, which is increased by a factor of 10 in comparison to the equilibrium case. Behind the peak a long tailing with much lower concentrations occurs, due to the transport of low concentrations of Pu bound to the sediment matrix and desorbing with a low rate.

The curves for Am-243 are similar. The main difference is caused by the different half lives of both radionuclides. The shorter half life of Am-243 with $7.37 \cdot 10^3$ years causes a stronger decrease of the maximum concentrations by radioactive decay with increasing travel time,

whereas Pu-242 with a half life of $3.75 \cdot 10^5$ years only marginally decays within 10^5 years. This is also the reason, why for Am-243 no tailing beyond 10^5 years can be observed.

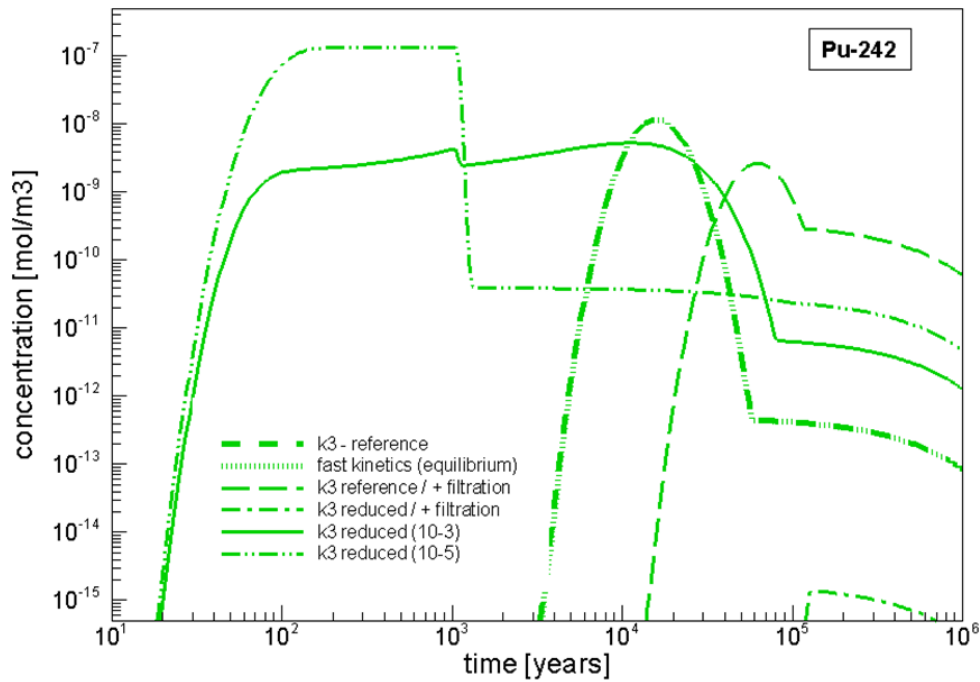


Figure 3-31: Breakthrough curves of Pu-242 for the different cases

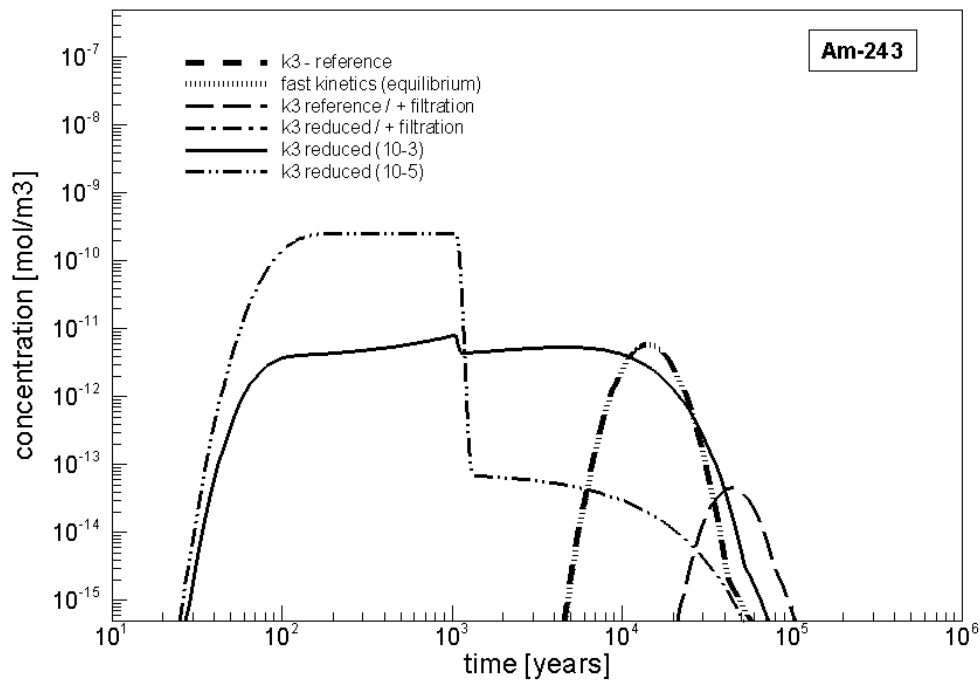


Figure 3-32: Breakthrough curves of Am-243 for the different cases

For U-236 the maximum concentration and the occurrence time of the major peak do not vary at all. This results from the fact, that the transport of uranium is assumed not to be im-

ected by colloids and for all calculations the same K_{d1} -value for sorption on the sediment is applied. However, the curves indicate a very small uranium fraction arriving much earlier at the outlet of the pathway. This fraction is built up by the decay of the mother nuclide Pu-240 and is highest for the calculation cases five and six, where extremely low desorption rates for the tri- and tetravalent radionuclides from the colloids are applied. In this case the major fraction of Pu-240 is transported without retardation on colloids and its peak arrives after 100 years which corresponds to the groundwater travel time.

The curves for Th-232 are in general similar to those from the trivalent actinides Pu-242 and Am-243, since the same interaction values are used. The main difference is caused by the very long half life of Th-232 ($1.41 \cdot 10^{10}$ years) and the impact of the mother nuclide U-236. Especially in case four, where filtration and a very slow desorption of radionuclides from colloids is assumed. Here, a strong peak occurs after $6 \cdot 10^5$ years, only one order of magnitude below the maximum concentration of case three, which is not the case for Pu-242 and Am-243. The plateau beyond 10^4 years in calculation three and most distinctive in calculation four is caused by the decay of the faster travelling nuclide U-236.

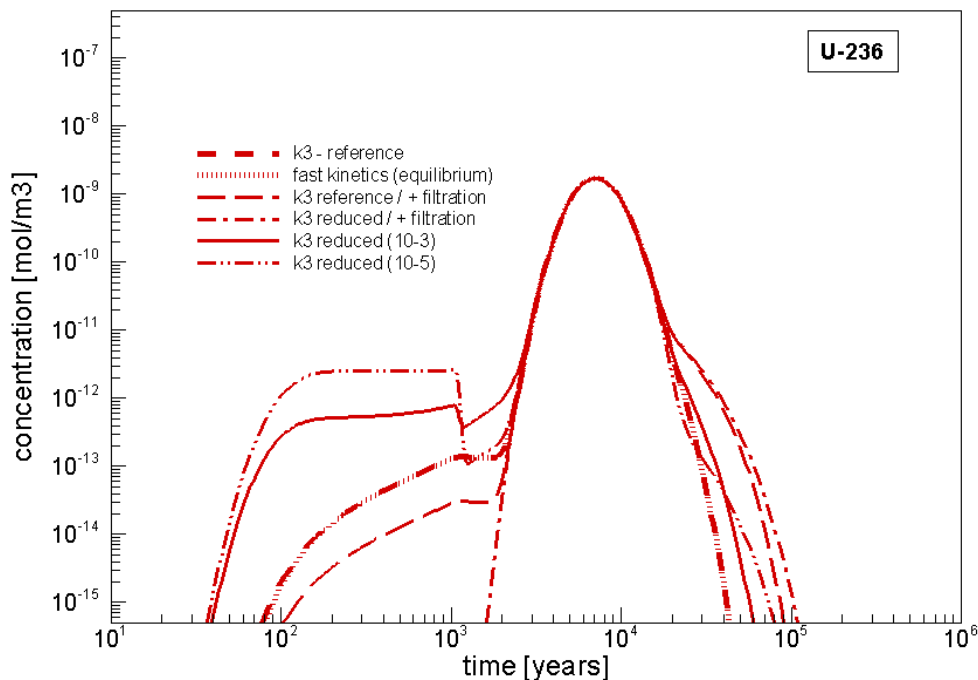


Figure 3-33: Breakthrough curves of U-236 for different calculation cases

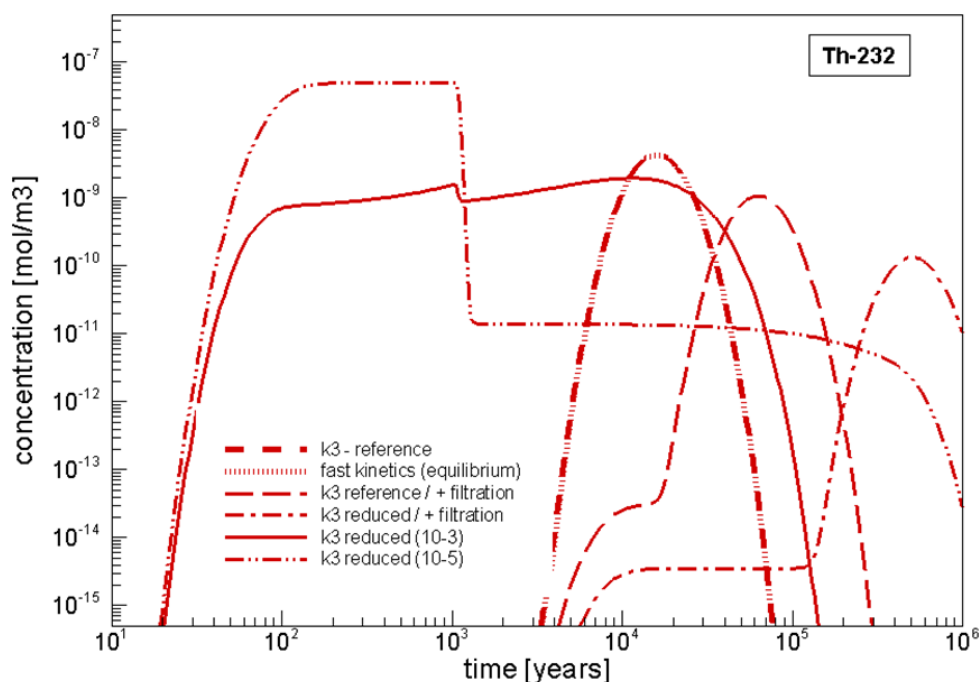


Figure 3-34: Breakthrough curves of Th-232 for different calculation cases

In conclusion, these calculations indicate that kinetic effects except those concerning filtration can be substituted by an equilibrium approach. In the synthetic cases five and six it was shown that a decrease of the desorption rate k_3 by three orders of magnitude is necessary to cause a significant fraction of tri- and tetravalent actinides to be transported by colloids without retardation. Only in case six it resulted in an increase of the maximum concentration of the respective actinides by about a factor of 10. The calculation cases based on the most likely data with regard to the available knowledge so far, are case one and case three. The effect of an irreversible colloid retention was investigated in cases three and four based on filtration rates K_2 derived from deep bed filtration theory. Applying a desorption rate $k_3 = 0.005 \text{ h}^{-1}$ observed in the batch experiments, a delay of the peak by app. 50 000 years is caused. For long-living actinides the reduction of the maximum concentration is then less than a factor 10. However, for those actinides with half lives much lower than 10^5 years the reduction is much higher due to radioactive decay.

If no filtration occurs the main impact of colloids here is the increase of the mobile concentration of tri- and tetravalent actinides and therewith a decreased sorption coefficient for actinides on the sediment. However, if the colloids are not stable this will cause an additional retention of the actinides.

It needs to be mentioned that the model applied here is to some extent oversimplified. In particular the approach of a porous medium might not be true for the fracture material of the granite fractures. At the Grimsel test site there are strong indications for partly open fractures or at least fracture areas with highly increased permeability. Nevertheless, we consider our model to be conservative with respect to the groundwater travel time. Sensibly only those areas of a granite host rock with low permeability will be selected for repositories and the groundwater travel times are likely in the range of thousands of years instead of 100 years.

4 Conclusions and outlook

The results of this project contribute in different ways to the safety case for a radioactive waste repository. On the one hand it contributes to the assessment basis, since the knowledge and understanding of processes, particularly on colloid/nanoparticle generation and colloid/nanoparticle stability has significantly increased. On the other hand the results from the experimental programme have been abstracted to a transport model for long-term safety assessment to directly estimate the consequences of colloid-facilitated actinide transport on the temporal and spatial scale of a repository system. The results of both aspects including an outlook with open questions are summarised in the following sections.

4.1 Understanding of colloidal/nanoparticle processes

A number of different aspects concerning the colloid/nanoparticle formation and fate have been tackled within the KOLLORADO project.

Groundwater- Bentonite porewater mixing zone. Geochemical gradients in a repository system may lead to secondary phase precipitation and colloid formation. For a repository in granite such geochemical gradients will establish at the bentonite barrier/groundwater interface. The present study could demonstrate both by geochemical modelling and experiment that various colloidal species indeed form. Interestingly, the colloid concentrations are found pretty low (in the range of ~100 ppt) and an estimation shows that the generated colloid surface site concentration is too low to significantly adsorb radionuclides. However, spectroscopic and ultrafiltration experiments showed that notably the speciation of polyvalent actinide ions such as Am and Pu is strongly influenced by colloid formation. Spectroscopic information points to significant actinide incorporation into colloid matrices. The study shows as well that colloids/nanoparticles provenance is very much driven by groundwater chemistry and mainly ionic strength. Increasing salinity destabilizes colloids and only very low colloid concentrations establish.

Reversibility of radionuclide- bentonite colloid binding. Experiments carried out in Grimsel groundwater and fracture filling materials from Äspö and Grimsel demonstrate the different interaction of long-lived radionuclides with colloids and mineral surfaces. Under given conditions U(VI), Tc(VII) and Np(V) do not significantly bind to bentonite colloids. In contrast, the tri- and tetravalent radionuclides Th(IV), Pu(IV) and Am(III) are almost quantitatively associated to bentonite colloids. It is very obvious that the major part of colloid-bound actinides are not irreversibly bound. Over time scales of ~ 1 year it appears that these metal ions desorb from colloids and partition between colloid surfaces and mineral surfaces. Dissociation rates seem to be rather insensitive to the origin of the fracture filling material either from Äspö or Grimsel. For Np(V) slow reduction and subsequent sorption is found consistent with respective speciation calculations taking the measured redoxpotential into account. Under given experiments actinides mostly form surface complexes. The results of the present project do not suspend from further research efforts to look to potential reactions leading to an 'irreversible' actinide inclusion into nanoparticles or into surface precipitates of colloids.

Colloid stability. Bentonite is discussed as backfill material for many repository concepts. Clay colloids can be released from such barriers and thus can be considered as a highly relevant colloid type for radionuclide transport. The present study provides data for describing clay colloid stability over a wide range of geochemical conditions and can thus be taken to predict colloid relevance for various repository concepts under varying geochemical boundary conditions. Critical coagulation concentrations (CCC) in dependence of pH and

electrolyte concentration are determined. For CaCl_2 background electrolyte solution a pH independent Ca-CCC of $1 \text{ mmol}\cdot\text{L}^{-1}$ is found. This Ca-CCC gives further confidence in the the safety function indicator criteria of $[\text{M}^{2+}] > 1 \text{ mmol}\cdot\text{L}^{-1}$ for prevention of bentonite buffer erosion as stated in SKB [2]. In NaCl electrolyte solution the CCC is found highly pH-dependent. The Na-CCC values for $\text{pH} \leq 7$ ($15\text{-}20 \text{ mmol}\cdot\text{L}^{-1}$) are in good agreement with published data for other clay minerals as SWy-1 and beidelite [74] and increase to 200 to $350 \pm 100 \text{ mmol}\cdot\text{L}^{-1}$ at $\text{pH} 8\text{-}10$, respectively. The colloid size dependence of the CCC can explain the high Na-CCC values for $\text{pH} \geq 8$ found in this study and the scatter of literature data [104]. The addition of $1 \text{ mg}\cdot\text{L}^{-1}$ DOC by fulvic acid (GoHy-573FA) increases the Ca/FA-CCC slightly to $2 \text{ mmol}\cdot\text{L}^{-1}$. The surface charge is thereby compensated by the adsorbed organic material on the surface of the colloids as could be shown in Scanning Transmission X-Ray Microscopy (STXM) investigations. Application of a DLVO theory based modeling approach by Mahmood et al. [31] shows the general trend of higher colloid stability with higher pH value but overestimates the observed colloids stability somewhat. Adjusting the montmorillonite face charge by a maximum of $\pm 12 \text{ mV}$, which is still within the range of experimentally obtained data, was sufficient to successfully reproduce the measured stability ratios. However, the Na- CCC values could only be reasonably predicted using solely the edge-face interaction energy calculated. The strong deviations of the model predictions and the experimental determined CCC values found at low electrolyte concentrations can be explained by the spill-over of the platelet face electrical double layer (EDL) shielding the platelet edge charge due to the aspect ratio of the clay platelets.

Colloid generation at the compacted bentonite fracture interface. A pH and ionic strength dependent extent of colloid generation from a compacted bentonite source was observed very much driven by the respective CCC. For conditions below the CCC, colloid generation is confirmed, whereas in experiments with an ionic strength lying above the CCC, colloid generation within the observation period is negligible. The experiments substantiate the important influence of the CCC for the potential release of clay colloids from bentonite. Colloid release models can now be parameterized with data determined here.

Colloid – Mineral surface interactions. The results of this study show that the interaction of colloids with mineral surfaces is mainly controlled by electrostatic interactions. Strongest attractive forces are observed close to or below the individual point of zero charge (pH_{pzc}) of the minerals. According to the results, colloid adsorption in alkaline regime (e.g., Grimsel groundwater conditions) can only be expected on apatite. Since apatite occurs only in trace concentrations in the Grimsel Granodiorite, only negligible colloid retention would be expected. Separate measurements show that Ca(II) concentrations as low as 10^{-4} M as present in Grimsel groundwater reduce colloid-mineral surface repulsive forces by a factor of about three and adhesion forces become detectable even at high pH. Therefore, the probability of colloid attachment to mineral surfaces increases also in low mineralized groundwater at high pH. Experimental observations of weak colloid retention in such systems can be qualitatively also explained by such kinetically controlled processes.

Colloid mobility. Based on the results of the laboratory migration studies Febex bentonite colloid mobility is relatively high and only small colloid fractions are found to be retained in the fracture under the Grimsel groundwater conditions. As mentioned above this finding is in qualitative agreement with colloid-mineral interaction studies. Compared to the colloid recovery the initially colloid associated metal recovery is significantly lower and decreases with increasing residence time clearly indicating the relevance of kinetically controlled desorption processes under these conditions. This confirms earlier findings obtained by other authors [15, 32, 139] at considerably shorter migration times. Tetravalent actinide ions such as Th(IV) show slower dissociation rates as compared to those of the trivalent metal ions Eu(III) and Tb(III). The time dependent decrease of metal ion recovery observed in column

experiments is again in qualitative agreement with the outcome of batch sorption tests. Both studies confirm the importance of considering radionuclide desorption kinetics for the assessment of colloid mediated radionuclide transport for nuclear waste disposal (see discussion below). Without this consideration, results of short-term laboratory experiments cannot be applied to make long-term predictions.

Impact on long-term safety assessment. Data and process understanding gathered within the present project allows a much better appraisal of the impact of colloid-facilitated radionuclide transport on the long-term safety assessment of a geological repository. In the presence of colloids/nanoparticles radionuclide transport might be increased or decreased, depending on the interaction between radionuclides, colloids and the sediment matrix. It is particularly important to know, firstly, the kinetics of radionuclide interaction with colloids and notably the dissociation rates, i.e. to what extent do initially colloid-bound radionuclides desorb from the colloids during their migration through the geological formation and, secondly, how strong the interaction of colloids with the sediment matrix is and what is the time dependence of processes involved.

Earlier approaches to the description of the colloid-mediated migration of pollutants and radionuclides by coupled reactive transport codes assuming instantaneous establishment of chemical equilibria usually failed to reproduce experimental data. As a consequence 'irreversible' sorption processes were often invoked to explain this discrepancy. The 'irreversibility' hypothesis, however, implies that otherwise strongly retarded polyvalent actinide ions can migrate via colloidal transport without any retention. Therefore, in our transport calculations most emphasis was placed on the investigation of kinetic effects supported by experimental data and their impact on the arrival time and recovery of radionuclides and colloids. One- and two dimensional models have been applied to describe the colloid-facilitated transport in laboratory and field experiments at the Grimsel site. Data for tri- and tetravalent radionuclide sorption onto colloids and sediment matrix and corresponding rates have been derived from batch experiments. For the filtration of colloids parameters have been derived from the deep bed filtration theory.

These parameters have been implemented into model calculations for the conditions of the CFM tracer experiment and results are summarised in Figure 4-1 in comparison to results available from all migration experiments performed within the Grimsel programme. The results are plotted as tracer recovery versus travel time. The model calculations using best estimate parameters are depicted by the yellow and green circles. The yellow circles show colloid recoveries which are influenced by filtration processes and the green circles show the recoveries of tri- and tetravalent actinides, which are reduced by colloid filtration and metal ion desorption from colloids with subsequent retention at rock surfaces. While calculated colloid recoveries are quite consistent with experimental data, actinide desorption and retention rates taken for the model are too low to match the results of the CFM in-situ experiment and the new drill core migration experiments. Apparently, desorption rates are higher in the migration experiments as compared to those derived from the batch experiments. This finding needs to be further investigated.

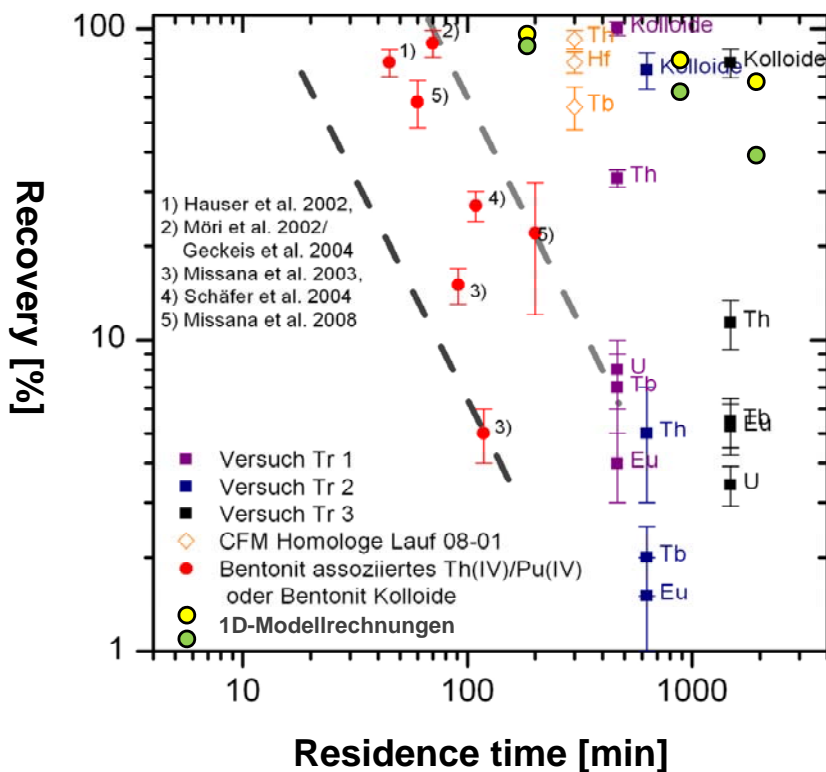


Figure 4-1: Comparison of experimental data with model calculations; only colloid filtration ($K_2 = 0.02 \text{ h}^{-1}$ yellow dots) and colloid filtration with radionuclide desorption ($k_3 = 0.01 \text{ h}^{-1}$ green dots).

Despite the divergence of calculated and experimental results, those model parameters have been applied to conditions more relevant to a radioactive waste repository system, i.e. with a transport pathway through the geosphere of about 200 m and a groundwater velocity of 2 m/a. Six different parameter sets have been applied with two basically different assumptions, i.e (a) considering no interaction of colloids with the sediment matrix and (b) considering irreversible colloid filtration. In both cases actinide desorption from colloids and reversible sorption to the rock was assumed by taking the reaction rates discussed above.

For case a) (no colloid filtration) a relevant impact of colloids on actinide transport could not be established unless desorption rates are reduced by at least two orders of magnitude below those derived from the batch laboratory experiments. Note that desorption rates observed in bore core and in-situ migration experiments are even higher. This is illustrated exemplarily for Pu-242 in Figure 4-2, where the curve for the desorption rate of 55 a^{-1} , the typical value measured in the batch experiments, represents the reference case. Then the desorption rate was step-wise reduced. A first strong visible impact on the breakthrough curve is observed for a desorption rate of 0.2 a^{-1} but still does not affect the maximum concentration and peak time.

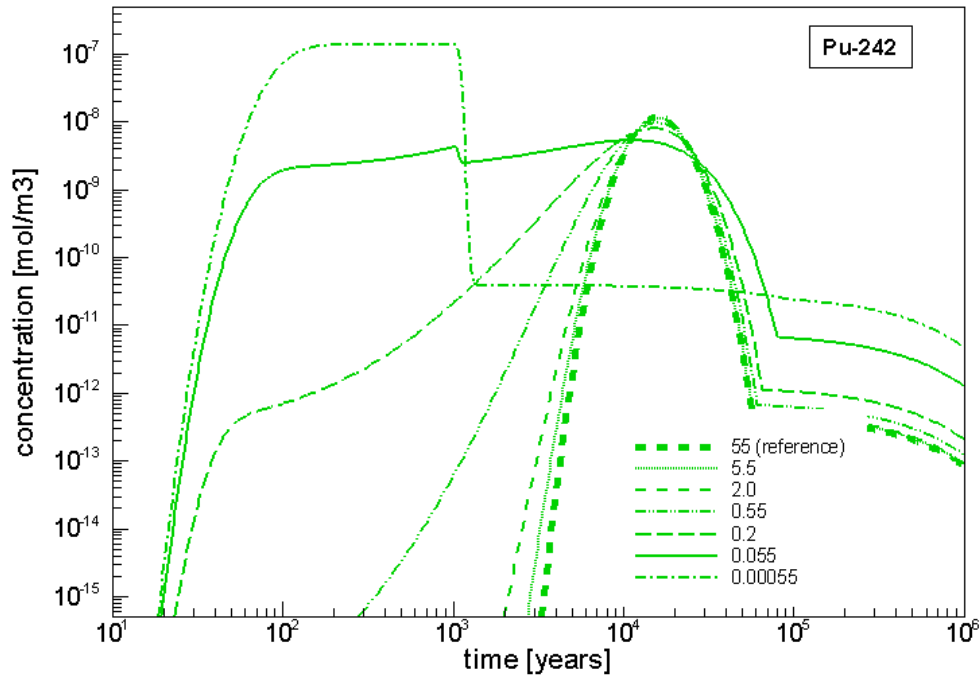


Figure 4-2: Impact of the desorption rate k_3 on the breakthrough curve of Pu-242. No colloid filtration assumed.

In case b) (colloid filtration is taken into account according to the deep bed filtration theory) a delay of the radionuclide breakthrough peak and a reduction of the concentration at peak maximum is observed (see fig. 3-32).

Both calculations show that colloid impact on actinide transport under given conditions (clay colloid concentration: 20 mg/L, Grimsel groundwater conditions with low ionic strength and high pH, migration through a stream tube with low dispersion) is very limited and can be described by an equilibrium approach. This conclusion holds for the assumption that colloids are stable and not filtered. Unretarded colloid-mediated transport only becomes relevant for very slow actinide desorption rates, which have hitherto not been observed in experiments. The only conceivable geochemical process leading to such low rates for actinide dissociation from colloids would be incorporation into colloid structures, e.g. in the course of secondary colloid phase formation processes as observed in the mixing zone at the bentonite/groundwater interface. Concentrations of those neo-formed colloids, however, has been found to be very low.

The calculations have been performed on the basis of experiments in fractured, granitic rock. For those repositories a bentonite buffer is currently the preferred component in the engineered barrier system (EBS) in many countries. The release of bentonite colloids/nanoparticles from the outer rim of a bentonite buffer (gellayer) into water conducting fractures is an important process notably for scenarios considering glacial meltwater intrusion that has to be addressed in the safety case.

With respect to other host rocks the following general conclusions can be drawn from the outcome of the present study. In several countries the EBS concept for repositories in clay or claystone is similar with regard to the buffer material, usually bentonite or other swelling clays, considered as preferred buffer around the waste containers. However, the characteristics of different host-rock types severely influences colloid mobility. Usually, the

pore sizes in claystone are very low (in the range of several nm), resulting in a mechanical filtration of colloids. Under these conditions the impact of clay colloids on radionuclide transport through the host rock is low. Colloid facilitated transport is only becoming relevant, if water conducting fractures or fissures appear in the claystone and stay open for considerable time frames. But even then clay colloids are only mobile if they remain stable in the groundwater. Clay formations in Northern Germany are characterised by rather saline porewaters. Based on the data set generated within this project, criteria can be established related to clay colloid stability in specific groundwater types. Critical coagulation concentrations lie thus at ≤ 0.4 mol/L NaCl and 1 mmol/L CaCl₂. As concentrations in saline porewaters exceed those values, bentonite colloids are not stable in such water. The effect of relatively high salinity on radionuclide-colloid-rock interactions has been demonstrated for granitic groundwater from the Äspö site, The Swedish underground rock laboratory operated by SKB. Under those conditions clay colloids lead to an even stronger retention of actinides due to sorption to agglomerating colloids. For the scenario of low mineralized glacial melt water intrusion, where colloids are presumably stable, the results obtained for radionuclide – colloid interaction reactions obtained in our studies in the Grimsel system should be transferable to some extent. Interaction parameters have however to be adapted to the specific geochemical conditions of a given site.

Bentonite is not the preferred material for buffer, backfill or sealing in a repository located in rock salt. Colloids may be generated from different sources such as e.g. secondary phase formation upon container or waste form corrosion. However, due to the very high ionic strength of the (in case of an unexpected repository evolution scenario) intruding saturated brines colloids are not expected to be stable. Of higher concern for a repository in rock salt are organic colloids in the overburden of the host rock. At Gorleben site humic colloids occur in quite high concentrations of up to 200 mg C/L. These colloids might act as radionuclide carrier in the far field of the repository.

4.2 Future directions

The data presented in this KOLLORADO final report reduce in many ways the uncertainties of colloid/nanoparticle effects on radionuclide mobility as documented above. However, from the scientific point of view a couple of open questions appeared and require further work. In the following those questions and possible research directions are mentioned:

- **Colloid stability** can be qualitatively predicted by DLVO-theory approaches as shown in this study. Predicted critical coagulation concentrations (CCC) in some cases overestimated experimentally obtained data. This would correspond to a modelling result that is in view of performance assessment ‘conservative’. However, it has to be stated clearly that several assumptions i.e. (a) approximation of surface potentials by zeta-potential measurements, (b) edge charge calculation based on the structural formula using zeta-potentials measured on pure Al- and Si- phases and (c) the geometry of clay platelets has been estimated as half-cylinder, have to be solidified. Here, new approaches e.g. based on the layer- charge distribution of clays have to be tested. Another aspect to be focused on are acid-base interactions as part of the non-DLVO forces, which are currently not implemented in the model. The presence of organic matter does not significantly modify bentonite colloid stability in Grimsel and Äspö groundwater, but influences sedimentation kinetics and acts as a complexing agent keeping tri- and tetravalent actinides in solution. Further studies should also investigate stability of humic-like substances under saline conditions.

- **Radionuclide-colloid interaction** has been identified in the present project to mainly take place by reversible surface sorption processes. Transport calculations suggest a lower limit for actinide desorption rates of $0.55-0.2 \text{ a}^{-1}$. At slower rates colloid mediated transport can under colloid stabilizing conditions have a significant impact for actinide migration. Future studies should therefore concentrate on the identification of processes which may potentially form colloidal species with extremely slowly dissociating actinides. Such processes might be coprecipitation phenomena. The challenge of such studies is to prove or disprove whether such processes are relevant for given repository scenarios.
- **Bentonite erosion.** Erosion experiments revealed that geochemical parameters determining colloid stability also control bentonite erosion. The generation of colloids from the gel/sol-layer has not been investigated in detail. Detailed post-mortem analysis of the bentonite erosion reactors to characterize the bentonite-water contact zone and retrieve informations on the mineralogy, size distribution and exchangeable cation composition will be studied. Furthermore, the development of a bentonite erosion model based on the experimental results is planned.
- **Colloid- surface interaction.** Fundamental aspects of colloid/nanoparticle mobility in the geosphere still require further studies. Within the present study carboxylated polystyrene colloids were taken to simulate clay colloid – rock interaction. It is clear that clay particle surfaces with anisotropic surface charge distribution are much more difficult to describe. Approaches, how to investigate surface forces between clay colloids and mineral surfaces are in the mean time available from the literature and will be adopted to cross check the data obtained within this project. Further questions will address the development of a model approach to convert measured surface forces into attachment factors required for transport calculations and to the role of colloid sorption mechanism on the reversibility and irreversibility of binding to the surface. The present study shows that colloids being attached in the primary potential minimum at the mineral surface cannot be released by shear forces induced by groundwater flow. Agglomeration/attachment in the secondary minimum may however be less strong and surface charge variations upon pH and salinity changes can lead to the release of attached colloids. Finally, research is necessary to understand colloid filtration under repulsive conditions, especially the role of physical heterogeneity and plugging effects, e.g., by carrying out colloid transport or adsorption experiments on (e.g., chemically inert) surfaces with defined microstructured surfaces (surface roughness).
- **Transport modeling.** Although the modelling approaches are able to describe the available migration experiments to some extent a further qualification of the model is needed. Therefore, predictive calculations for additional homologue tests within the CFM project under variable boundary conditions (particularly lower flow conditions) are planned. Distinguishing various origins of peak tailing caused by the heterogeneity of surface morphology and/or matrix diffusion will be possible through direct input of μCT (mikro computer tomography) data of the real fracture geometry. Furthermore, application of a PA model for fractured (not porous) media to estimate consequences for long-term safety assessment are planned. A challenge will be the modelling of the integrated field experiment planned within Phase II of the CFM project.

5 References

- [1] Smith, P.A., I. Blechschmidt, V. Cvetkovic, C. Degueldre, I. Gaus, K. Iijima, M. Küntzel, G.W. Lanyon, I. Neretnieks, U. Noseck, A. Pudewills, T. Schäfer, and P.W. Reimus, *CFM Phase I Modeling Report NAB 08-31*. 2008, NAB 08-31, Nagra: Wettingen (Switzerland).
- [2] SKB, *Long-term safety for KBS-3 repositories at Forsmark and Laxemar - a first evaluation; Main report of the SR-Can project. SKB Technical report TR-06-09*. 2006, Technical report TR-06-09, Svensk Kärnbränslehantering AB: Stockholm, Sweden. p. 620.
- [3] SKB, *Buffer and backfill process report for the safety assessment SR-Can*. 2006, Technical report TR-06-18, Svensk Kärnbränslehantering AB: Stockholm, Sweden. p. 620.
- [4] Alonso, U., T. Missana, H. Geckeis, M. Garcia-Gutierrez, M.J. Turrero, R. Möri, T. Schäfer, A. Patelli, and V. Rigato, *Role of inorganic colloids generated in a high-level deep geological repository in the migration of radionuclides: open questions*. Journal of Iberian Geology, 2006. **32**(1): p. 79.
- [5] Yoshida, H. and M. Takeuchi, Metcalfe, R., *Long-term stability of flow-path structure in crystalline rocks distributed in an orogenic belt, Japan*. Engineering Geology, 2005. **78**: p. 275.
- [6] Nagra, *Project Opalinus Clay - Safety Report - Demonstration of disposal feasibility for spent fuel, vitrified high-level waste and long-lived intermediate level waste (Entsorgungsnachweis)*. 2003, NTB 02-05, Nagra: Wettingen (Switzerland). p. 360.
- [7] SKB, *Interim process report for the safety assessment SR-Can*. 2004, SKB report R-04-33, Svensk Kärnbränslehantering AB.
- [8] Pusch, R., *Stability of bentonite gels in crystalline rock - physical aspects, SKBF/KBS report TR 83-04*. 1983, TR-report 83-04, University of Luleå: SKB was formerly: SKBF/KBS; SKBF - Svensk Kärnbränsleförsörjning AB.
- [9] Push, R., *Stability of bentonite gels in crystalline rock - Physical aspects*. 1983, TR 83-04, SKB: Stockholm.
- [10] Liu, J. and I. Neretnieks, *Physical and chemical stability of the bentonite buffer*. 2006, SKB Rapport R-06-103, Svensk Kärnbränslehantering AB.
- [11] Gallé, C., *Gas breakthrough pressure in compacted Fo-Ca clay and interfacial gas overpressure in waste disposal context*. Applied Clay Science, 2000. **17**(85-97).
- [12] Missana, T., T. Alonso, and M.J.S. Turrero, *Generation and stability of bentonite colloids at the bentonite/granite interface of a deep geological radioactive waste repository*. Journal of Contaminant Hydrology, 2003. **61**(1-4): p. 17-31.
- [13] Baik, M.H., W.J. Cho, and P.S. Hahn, *Erosion of bentonite particles at the in-terface of a compacted bentonite and a fractured granite*. Engineering Geology, 2007. **91**(2-4): p. 229-239.
- [14] Alonso, U., T. Missana, and M. García-Gutiérrez, *Experimental approach to study the bentonite colloid generation source term in different geochemical conditions*, in *2nd Annual Workshop Proceedings of the Integrated Project "Fundamental Processes of Radionuclide Migration" - 6th EC FP IP FUNMIG*, G. Buckau, et al., Editors. 2007, SKB: Stockholm. p. 329-335.
- [15] Geckeis, H., T. Schäfer, W. Hauser, T. Rabung, T. Missana, C. Degueldre, A. Möri, J. Eikenberg, T. Fierz, and W.R. Alexander, *Results of the Colloid and Radionuclide Retention experiment (CRR) at the Grimsel Test Site (GTS), Switzerland -Impact of reaction kinetics and speciation on radionuclide migration-*. Radiochimica Acta, 2004. **92**(9-11): p. 765-774.
- [16] Möri, A., W.R. Alexander, H. Geckeis, W. Hauser, T. Schäfer, J. Eikenberg, T. Fierz, C. Degueldre, and T. Missana, *The colloid and radionuclide retardation experiment at the Grimsel Test Site: influence of bentonite colloids on radionuclide migration in a fractured rock*. Colloids and Surfaces a-Physicochemical and Engineering Aspects, 2003. **217**(1-3): p. 33-47.
- [17] Zänker, H., W. Richter, and G. Hüttig, *Scavenging and immobilization of trace contaminants by colloids in the waters of abandoned ore mines*. Colloids and Surfaces a-Physicochemical and Engineering Aspects, 2003. **217**(1-3): p. 21-31.
- [18] Zänker, H., H. Moll, W. Richter, V. Brendler, C. Hennig, T. Reich, A. Kluge, and G. Hüttig, *The colloid chemistry of acid rock drainage solution from an abandoned Zn-Pb-Ag mine*. Applied Geochemistry, 2002. **17**(5): p. 633-648.

- [19] Wan, J., T.K. Tokunaga, E. Saiz, J.T. Larsen, Z. Zheng, and R.A. Couture, *Colloid formation at waste plume fronts*. Environmental Science & Technology, 2004. **38**: p. 6066-6073.
- [20] Kim, M.A., P.J. Panak, J.I. Yun, A. Priemyshev, and J.I. Kim, *Interaction of actinides(III) with aluminosilicate colloids in "statu nascendi" Part III. Colloid formation from monosilanol and polysilanol*. Colloids and Surfaces a-Physicochemical and Engineering Aspects, 2005. **254**(1-3): p. 137-145.
- [21] Buddemeier, R.W. and J.R. Hunt, *Transport of colloidal contaminants in groundwater: radionuclide migration at the Nevada test site*. Appl. Geochem., 1988. **3**: p. 535-548.
- [22] Kersting, A.B., D.W. Efurud, D.L. Finnegan, D.J. Rokop, D.K. Smith, and J.L. Thompson, *Migration of plutonium in ground water at the Nevada Test Site*. Nature, 1999. **397**: p. 56-59.
- [23] Vilks, P., H.G. Miller, and D.C. Doern, *Natural Colloids and Suspended Particles in the Whiteshell Research Area, Manitoba, Canada, and Their Potential Effect on Radiocolloid Formation*. Applied Geochemistry, 1991. **6**(5): p. 565-574.
- [24] Novich, B.E. and T.A. Ring, *Colloid stability of clays using photon correlation spectroscopy*. Clays and Clay Minerals, 1984. **32**(5): p. 400-406.
- [25] Missana, T. and A. Adell, *On the applicability of DLVO theory to the prediction of clay colloids stability*. J. Colloid Interface Sci., 2000. **230**: p. 150-156.
- [26] Kretzschmar, R., H. Holthoff, and H. Sticher, *Influence of pH and humic acid on coagulation kinetics of kaolinite: a dynamic light scattering study*. J. Colloid and Interface Science, 1998. **202**: p. 95-103.
- [27] Jasmund, K. and G. Lagaly, eds. *Tonminerale und Tone: Struktur, Eigenschaften, Anwendungen und Einsatz in Industrie und Umwelt*. 1993, Steinkopf: Darmstadt. 490.
- [28] Meunier, A., *Clays*. 2005, Berlin, Heidelberg: Springer. 472.
- [29] Derjaguin, B.V. and L. Landau, *Theory of the stability of strongly charged lyophobic sols and the adhesion of strongly charged particles in solutions of electrolytes*. Acta Physicochim. URSS, 1941. **14**.
- [30] Verwey, E.J.W. and J.T.G. Overbeek, *Theory of the stability of lyophobic colloids*. 1948, Amsterdam: Elsevier.
- [31] Mahmood, A., T. Amiratharajah, W. Sturm, and K.E. Denett, *A micromechanics approach for attachment and detachment of asymmetric colloidal particles*. Colloids and Surfaces A: Physicochemical and Engineering Aspects, 2001. **177**: p. 99-110.
- [32] Schäfer, T., H. Geckeis, M. Bouby, and T. Fanghänel, *U, Th, Eu and colloid mobility in a granite fracture under near-natural flow conditions*. Radiochimica Acta, 2004. **92**: p. 731-737.
- [33] Missana, T., U. Alonso, M. Garcia-Gutierrez, and M. Mingarro, *Role of bentonite colloids on europium and plutonium migration in a granite fracture*. Applied Geochemistry, 2008. **23**(6): p. 1484-1497.
- [34] Bowen, W.R. and T.A. Doneva, *Atomic force microscopy studies of membranes: Effect of surface roughness on double-layer interactions and particle adhesion*. Journal of Colloid and Interface Science, 2000. **229**(2): p. 544-549.
- [35] Alonso, U., T. Missana, A. Patelli, V. Rigato, and J. Ravagnan, *Colloid diffusion in crystalline rock: An experimental methodology to measure diffusion coefficients and evaluate colloid size dependence*. Earth and Planetary Science Letters, 2007. **259**(3-4): p. 372-383.
- [36] Patelli, A., U. Alonso, V. Rigato, T. Missana, and S. Restello, *Validation of the RBS analysis for colloid migration through a rough granite surface*. Nuclear Instruments & Methods in Physics Research Section B-Beam Interactions with Materials and Atoms, 2006. **249**: p. 575-578.
- [37] Stumpf, S., T. Stumpf, J. Lutzenkirchen, C. Walther, and T. Fanghanel, *Immobilization of trivalent actinides by sorption onto quartz and incorporation into siliceous bulk: Investigations by TR-LFS*. Journal of Colloid and Interface Science, 2008. **318**(1): p. 5-14.
- [38] Vakarelski, I.U., K. Ishimura, and K. Higashitani, *Adhesion between silica particle and mica surfaces in water and electrolyte solutions*. Journal of Colloid and Interface Science, 2000. **227**(1): p. 111-118.

- [39] Johnson, P.R., N. Sun, and M. Elimelech, *Colloid transport in geochemically heterogeneous porous media: Modeling and measurements*. Environmental Science & Technology, 1996. **30**(11): p. 3284-3293.
- [40] Degueldre, C., R. Grauer, A. Laube, A. Oess, and H. Silby, *Colloid properties in granitic groundwater systems .2. Stability and transport study*. Applied Geochemistry, 1996. **11**(5): p. 697-&.
- [41] Alonso, U., T. Missana, A. Patelli, V. Rigato, and J. Ravagnan, *μ PIXE study on colloid heterogeneous retention due to colloid/rock electrostatic interactions*. 2004. p. 68.
- [42] Velegol, D. and P.K. Thwar, *Analytical model for the effect of surface charge nonuniformity on colloidal interactions*. Langmuir, 2001. **17**(24): p. 7687-7693.
- [43] Taboada-Serrano, P., V. Vithayaverroj, S. Yiacoumi, and C. Tsouris, *Surface charge heterogeneities measured by atomic force microscopy*. Environmental Science & Technology, 2005. **39**(17): p. 6352-6360.
- [44] Williams, D.J.A. and K.P. Williams, *Electrophoresis and zeta potentials of kaolinite*. J. Colloid Interface Sci., 1978. **65**(1): p. 79-87.
- [45] Lührmann, L., *Modellierung des kolloidgetragenen Schadstofftransports mit dem Rechenprogramm TRAPIC*. 1999, Report GRS-149, Gesellschaft für Anlagen- und Reaktorsicherheit (GRS) mbH: Braunschweig.
- [46] Lührmann, L., U. Noseck, and C. Tix, *Model of contaminant transport in porous media in the presence of colloids applied to actinide migration in column experiments*. . Water Resources Research, 1998. **34**(3): p. 421-426.
- [47] Adina, *ADINA (Automatic Dynamic Incremental Nonlinear Analysis)*, A.R.D. Inc., Editor. 2007, Report ARD 01-09: Watertown, MA, USA.
- [48] Fernández, A.M., *Caracterización y modelización del agua intersticial de materiales arcillosos. Estudio de la bentonita de Cortijo de Archidona. (In Spanish)*. 2004, Universidad Autónoma de Madrid. Editorial CIEMAT: Madrid. p. 505.
- [49] Parkhurst, D.L. and C.A.J. Appelo, *User's guide to PHREEQC (Version2)-A computer program for speciation, batch-reaction, one-dimensional transport, and inverse geochemical calculations*. 1999, Water-Resources Investigations Report 99-4259, U.S. Geological Survey. p. 310 p.
- [50] Hauser, W., H. Geckeis, J.I. Kim, and T. Fierz, *A mobile laser-induced breakdown detection system and its application for the in situ-monitoring of colloid migration*. Colloids and Surfaces a-Physicochemical and Engineering Aspects, 2002. **203**(1-3): p. 37-45.
- [51] Plaschke, M., T. Schäfer, T. Bundschuh, T.N. Manh, R. Knopp, H. Geckeis, and J.I. Kim, *Size characterization of bentonite colloids by different methods*. Analytical Chemistry, 2001. **73**(17): p. 4338-4347.
- [52] Klenze, R., J.I. Kim, and H. Wimmer, *Speciation of Aquatic Actinide Ions by Pulsed Laser Spectroscopy*. Radiochimica Acta, 1991. **52-3**: p. 97-103.
- [53] Kim, J.I., R. Klenze, and H. Wimmer, *Fluorescence Spectroscopy of Curium(III) and Application*. European Journal of Solid State and Inorganic Chemistry, 1991. **28**: p. 347-356.
- [54] Fanghanel, T. and J.I. Kim, *Spectroscopic evaluation of thermodynamics of trivalent actinides in brines*. Journal of Alloys and Compounds, 1998. **271**: p. 728-737.
- [55] Chung, K.H., R. Klenze, K.K. Park, P. Paviet-Hartmann, and J.I. Kim, *A study of the surface sorption process of Cm(III) on silica by time-resolved laser fluorescence spectroscopy (I)*. Radiochimica Acta, 1998. **82**: p. 215-219.
- [56] Rozalén, M., P.V. Brady, and F.J. Huertas, *Surface chemistry of K-montmorillonite: Ionic strength, temperature dependence and dissolution kinetics*. Journal of Colloid and Interface Science, 2009. **333**(2): p. 474-484.
- [57] Byegård, J., H. Johansson, M. Skålberg, and E.-L. Tullborg, *The interaction of sorbing and non-sorbing tracers with different Äspö rock types. Sorption and diffusion experiments in the laboratory scale*. SKB Technical report TR-98-18. 1998 SKB Technical report TR-98-18, Svensk Kärnbränslehantering AB, Stockholm, Sweden.

- [58] Nagra, *Grimsel Test Site - Investigation Phase V "The CRR final project report series I: Description of the Field Phase - Methodologies and Raw data": Nagra Technical report NTB 03-01*, A. Möri, Editor. 2004, NTB 03-01, Nagra: Wettingen (Switzerland).
- [59] Nagra, *GTS Phase V (CRR Experiment): Supporting laboratory experiments with radionuclides and bentonite colloids. Nagra Technical Report NTB 03-02*, T. Missana, et al., Editors. in press, Nagra: Wettingen, Switzerland. p. 100.
- [60] Villar, M.V., P.L. Martin, M. Pelayo, B. Ruiz, P. Rivas, E. Alonso, A. Lloret, X. Pintado, A. Gens, J. Linares, F. Huertas, E. Caballero, C. Jimenez de Cisneros, J. Obis, A. Perez, and J. Velasco, *FEBEX bentonite: origin, properties and fabrication of blocks (full-scale engineered barriers experiment in crystalline host rock)*. 1998, 05/98, Enresa (empresa nacional de residuos radiactivos, s.a.): Madrid, Spain.
- [61] Cama, J., J. Ganor, C. Ayora, and A. Lasaga, *Smectite dissolution kinetics at 80°C and pH 8.8*. *Geochimica Et Cosmochimica Acta*, 2000. **64**: p. 2701-2717.
- [62] Nagra, *CFM Phase I - Status report of the laboratory programme. Nagra Arbeitsbericht NAB 07-41*, T. Schäfer and K. Iijima, Editors. 2007, NAGRA Arbeitsbericht NAB 07-41, NAGRA: Wettingen (Switzerland). p. 97.
- [63] Fellhauer, D., *Untersuchungen zur Löslichkeit und Redoxchemie von Neptunium*, in *Institut für Radiochemie*. 2008, Master thesis, Universität Heidelberg: Heidelberg.
- [64] Schäfer, T., F. Huber, P. Kunze, M. Bouby, and H. Geckeis, *Effect of available surface area on sorption reversibility*. unpublished.
- [65] Noseck, U. and D. Klotz, *Modelling of colloid-facilitated contaminant transport with the computer code TRAPIC: Theoretical basis and application*. Radionuclide Retention in Geologic Media, Workshop Proceedings, 2002: p. 231-239.
- [66] van Olphen, H., *Clay Colloid Chemistry - For Clay Technologists, Geologists and Soil Scientists*. second ed. 1977: John Wiley & Sons. 318.
- [67] Artinger, R., G. Buckau, S. Geyer, P. Fritz, M. Wolf, and J.I. Kim, *Characterization of ground-water humic substances: influence of sedimentary organic carbon*. *Applied Geochemistry*, 2000. **15**(1): p. 97-116.
- [68] Jacobsen, C., S. Williams, E. Anderson, M.T. Browne, C.J. Buckley, D. Kern, J. Kirz, M. Rivers, and X. Zhang, *Diffraction-limited imaging in a scanning transmission x-ray microscope*. *Optics Communications*, 1991. **86**: p. 351--364.
- [69] Jacobsen, C., S. Wirick, G. Flynn, and C. Zimba, *Soft X-ray spectroscopy from image sequences with sub-100 nm spatial resolution*. *Journal of Microscopy*, 2000. **197**(2): p. 173-184.
- [70] Hitchcock, A.P. and D.C. Mancini, *Bibliography of atomic and molecular inner-shell excitation studies*. *Journal of Electron Spectroscopy and Related Phenomena*, 1994. **67**: p. 1-132.
- [71] Schäfer, T., G. Buckau, R. Artinger, J.I. Kim, S. Geyer, M. Wolf, W.F. Bleam, S. Wirick, and C. Jacobsen, *Origin and mobility of fulvic acids in the Gorleben aquifer system: implications from isotopic data and carbon/sulfur XANES*. *Organic Geochemistry*, 2005. **36**(4): p. 567-582.
- [72] Schäfer, T., F. Claret, A. Bauer, L. Griffault, E. Ferrage, and B. Lanson, *Natural organic matter (NOM)-clay association and impact on Callovo-Oxfordian clay stability in high alkaline Solution: Spectromicroscopic evidence*. *Journal de Physique IV*, 2003. **104**: p. 413-416.
- [73] Schäfer, T., P. Michel, F. Claret, T. Beetz, S. Wirick, and C. Jacobsen, *Radiation sensitivity of natural organic matter: Clay mineral association effects in the Callovo-Oxfordian argillite*. *Journal of Electron Spectroscopy and Related Phenomena* 2009. **170**: p. 49-56.
- [74] Hetzel, F. and H.E. Doner, *Some Colloidal Properties of Beidellite - Comparison with Low and High Charge Montmorillonites*. *Clays and Clay Minerals*, 1993. **41**(4): p. 453-460.
- [75] Lagaly, G. and S. Ziesmer, *Colloid chemistry of clay minerals: the coagulation of montmorillonite dispersions*. *Advances in Colloid and Interface Science*, 2003. **100-102**: p. 105-128.
- [76] Chheda, P., D. Grasso, and C.J. van Oss, *Impact of ozone on the stability of montmorillonite suspensions*. *Journal of Colloid and Interface Science*, 1992. **153**: p. 226-236.
- [77] Mermut, A.R. and G. Lagaly, *Baseline studies of the Clay Minerals Society Source Clays: Layer-charge determination and characteristics of those Minerals containing 2:1 Layers*. *Clays and Clay Minerals*, 2001. **49**(5): p. 393-397.

- [78] Tombácz, E. and M. Szekeres, *Colloidal behavior of aqueous montmorillonite suspensions: the specific role of pH in the presence of indifferent electrolytes*. Applied Clay Science, 2004. **27**(75-94).
- [79] Liu, L.C., L. Moreno, and I. Neretnieks, *A Novel Approach to Determine the Critical Coagulation Concentration of a Colloidal Dispersion with Plate-like Particles*. Langmuir, 2009. **25**(2): p. 688-697.
- [80] Bouby, M., H. Geckeis, J. Lützenkirchen, S. Mihai, and T. Schäfer. *Interaction of bentonite colloids with Eu and Th in presence of humic acid: A Flow Field- Flow Fractionation study*. in *4th Annual Workshop Proceeding of integrated project "Fundamental processes of Radionuclide Migration" - 6th EC FP IP FUNMIG, FZKA report 7461*. 2009. p. 271-279.
- [81] Tombácz, E., I. Abraham, M. Gilde, and F. Szanto, *The pH dependent colloidal stability of aqueous montmorillonite suspensions*. Colloids and Surfaces, 1990. **49**: p. 71- 78.
- [82] Degueldre, C., H.R. Pfeiffer, W. Alexander, B. Wernli, and R. Bruetsch, *Colloid properties in granitic groundwater systems. I: Sampling and characterisation*. Applied Geochemistry, 1996. **11**(5): p. 677-685.
- [83] Tullborg, E.-L. and E. Gustafsson, *14C in bicarbonate and dissolved organics--a useful tracer?* Applied Geochemistry, 1999. **14**(7): p. 927-938.
- [84] Kienzler, B., P. Vejmelka, J. Romer, E. Fanghanel, M. Jansson, T.E. Eriksen, and P. Wikberg, *Swedish-German actinide migration experiment at ASPO hard rock laboratory*. Journal of Contaminant Hydrology, 2003. **61**(1-4): p. 219-233.
- [85] Vilks, P. and D.B. Bachinski, *Characterization of organics in whiteshell research area groundwater and the implications for radionuclide transport*. Applied Geochemistry, 1996. **11**(3): p. 387-402.
- [86] Schäfer, T., V. Chanudet, F. Claret, and M. Filella, *Spectromicroscopy mapping of colloidal/particulate organic matter in Lake Brienz, Switzerland*. Environmental Science & Technology, 2007. **41**(22): p. 7864-7869.
- [87] Naber, A., M. Plaschke, J. Rothe, H. Hofmann, and T. Fanghanel, *Scanning transmission X-ray and laser scanning luminescence microscopy of the carboxyl group and Eu(III) distribution in humic acid aggregates*. Journal of Electron Spectroscopy and Related Phenomena, 2006. **153**(3): p. 71-74.
- [88] Christl, I. and R. Kretzschmar, *C-1s NEXAFS spectroscopy reveals chemical fractionation of humic acid by cation-induced coagulation*. Environmental Science & Technology, 2007. **41**(6): p. 1915-1920.
- [89] Claret, F., T. Schäfer, J. Brevet, and P.E. Reiller, *Fractionation of Suwannee River Fulvic Acid and Aldrich Humic Acid on α -Al₂O₃: Spectroscopic Evidence*. Environmental Science & Technology, 2008. **42**(23): p. 8809-8815.
- [90] Stöhr, J., *NEXAFS spectroscopy*. Springer Series in Surface Sciences, ed. G. Ertl, R. Gomer and D.L. Mills. Vol. 25. 1996, Berlin: Springer. 403.
- [91] Dhez, O., H. Ade, and S.G. Urquhart, *Calibrated NEXAFS spectra of some common polymers*. Journal of Electron Spectroscopy and Related Phenomena, 2003. **128**(1): p. 85-96.
- [92] Francis, J.T. and A.P. Hitchcock, *Inner-shell spectroscopy of p-benzoquinone, hydroquinone, and phenol: Distinguishing quinoid and benzenoid structures*. J. Phys. Chem., 1992. **96**: p. 6598.
- [93] Schäfer, T., N. Hertkorn, R. Artinger, F. Claret, and A. Bauer, *Functional group analysis of natural organic colloids and clay association kinetics using C(1s) spectromicroscopy*. Journal de Physique IV, 2003. **104**: p. 409-412.
- [94] Kosmulski, M., *pH-dependent surface charging and points of zero charge II. Update*. Journal of Colloid and Interface Science, 2004. **275**(1): p. 214-224.
- [95] de Lint, W.B.S., N.E. Benes, J. Lyklema, H.J.M. Bouwmeester, A.J. van der Linde, and M. Wessling, *Ion Adsorption Parameters Determined from Zeta Potential and Titration Data for a gamma-Alumina Nanofiltration Membrane*. Langmuir, 2003. **19**(14): p. 5861-5868.
- [96] Lewis, J., A. , *Colloidal Processing of Ceramics*. Journal of the American Ceramic Society, 2000. **83**(10): p. 2341-2359.

- [97] Bagchi, P., *Test for particle size dependence in the theory of slow flocculation at a secondary minimum*. Colloid & Polymer Science, 1976. **254**(10): p. 890-894.
- [98] van de Ven, T.G.M., *Colloid Hydrodynamics*, ed. R.H. Ottewill and R.L. Rowell. 1989, London: Academic Press.
- [99] Litton, G.M., *Particle size effects on colloid deposition kinetics: evidence of secondary minimum deposition*. Colloids and surfaces A, 1996. **107**: p. 273-283.
- [100] Cortada, M., J.A. Anta, and J.A. Molina-Bolivar, *Secondary minimum coagulation in charged colloidal suspensions from statistical mechanics methods*. Journal of Physical Chemistry B, 2007. **111**: p. 1110-1118.
- [101] Secor, R.B. and C.J. Radke, *Spillover of the diffuse double layer on montmorillonite particles*. Journal of Colloid and Interface Science, 1985. **103**(1): p. 237-244.
- [102] Chang, F.-R.C. and G. Sposito, *The Electrical Double Layer of a Disk-Shaped Clay Mineral Particle: Effects of Electrolyte Properties and Surface Charge Density*. Journal of Colloid and Interface Science, 1996. **178**(2): p. 555-564.
- [103] Bouby, M., in *Annual Report 2008*, H. Geckeis and R. Klenze, Editors. 2009, Researchcenter Karlsruhe - Institute for Nuclear Wastes Disposal (INE): Karlsruhe (in press).
- [104] Liu, L., L. Moreno, and I. Neretnieks, *A Novel Approach to Determine the Critical Coagulation Concentration of a Colloidal Dispersion with Plate-like Particles*. Langmuir, 2009. **25**(2): p. 688-697.
- [105] Seher, H., T. Schäfer, H. Geckeis, and T. Fanghänel, *Febex bentonite colloid stability in ground water*, in *2nd Annual Workshop Proceedings of the Integrated Project "Fundamental Process of Radionuclide Migration" - 6th EC FP IP FUNMIG*, G. Buckau, et al., Editors. 2007, SKB: Stockholm. p. 397-402.
- [106] Yao, K.M., M.T. Habibian, and C.R. O'Melia, *Water and Wastewater Filtration: Concepts and Applications*. Environmental Science and Technology, 1971. **5**: p. 1105-1112.
- [107] Rabung, T., H. Geckeis, J.I. Kim, and H.P. Beck, *Sorption of Eu(III) on a natural hematite: Application of a surface complexation model*. Journal of Colloid and Interface Science, 1998. **208**(1): p. 153-161.
- [108] Huber, F., *Migration von Uranyl durch eine Quarz-Säule, Diploma Thesis*. 2007, Geoscience Department, Technical University Karlsruhe: Karlsruhe.
- [109] Lützenkirchen, J. and F. Huber, *Heterogeneities in adsorption from aqueous solution - An example of the effect of surface coverage*. Adsorption Science & Technology, 2007. **25**(7): p. 503-516.
- [110] Garcia, V.J., L. Martinez, J.M. Briceno-Valero, and C.H. Schilling, *Dimensional metrology of nanometric spherical particles using AFM*. Probe Microscopy, 1997. **1**: p. 107.
- [111] Ramirez-Aguilar, K.A. and K.L. Rowlen, *Tip characterization from AFM images of nanometric spherical particles*. Langmuir, 1998. **14**(9): p. 2562-2566.
- [112] Israelachvili, J.N., *Intermolecular and surface forces*. 1992, London: Academic Press.
- [113] Churchill, H., H. Teng, and R.M. Hazen, *Correlation of pH-dependent surface interaction forces to amino acid adsorption: Implications for the origin of life*. American Mineralogist, 2004. **89**(7): p. 1048-1055.
- [114] Ryan, J.N. and M. Elimelech, *Colloid mobilization and transport in groundwater*. Colloids and Surfaces A, 1996. **107**: p. 1-56.
- [115] McDowell-Boyer, L.M., J.R. Hunt, and N. Sitar, *Particle Transport through Porous Media*. Water Resources Research, 1986. **22**(13): p. 1901-1921.
- [116] Johnson, P.R., N. Sun, and M. Elimelech, *Colloid transport in geochemically heterogeneous porous media: Modelling and measurements*. Environmental science & technology, 1996. **30**(11): p. 3284-3293.
- [117] Brusseau, M.L., X.J. Wang, and Q.H. Hu, *Enhanced Transport of Low-Polarity Organic-Compounds through Soil by Cyclodextrin*. Environmental Science & Technology, 1994. **28**(5): p. 952-956.

- [118] Nazemifard, N., J.H. Masliyah, and S. Bhattacharjee, *Particle deposition onto charge heterogeneous surfaces: Convection-diffusion-migration model*. Langmuir, 2006. **22**(24): p. 9879-9893.
- [119] Duffadar, R.D. and J.M. Davis, *Interaction of micrometer-scale particles with nanotextured surfaces in shear flow*. Journal of Colloid and Interface Science, 2007. **308**(1): p. 20-29.
- [120] Song, L., P.R. Johnson, and M. Elimelech, *Kinetics of colloid deposition onto heterogeneously charged surfaces in porous media*. Environ. Sci. Technol., 1994. **28**: p. 1164-1171.
- [121] Adamczyk, Z., T. Dabros, J. Czarnecki, and T.G.M. Vandeven, *Particle Transfer to Solid-Surfaces*. Advances in Colloid and Interface Science, 1983. **19**(3): p. 183-252.
- [122] Hoek, E.M.V. and G.K. Agarwal, *Extended DLVO interactions between spherical particles and rough surfaces*. Journal of Colloid and Interface Science, 2006. **298**(1): p. 50-58.
- [123] Wu, L.M., W. Forsling, and P.W. Schindler, *Surface Complexation of Calcium Minerals in Aqueous-Solution .1. Surface Protonation at Fluorapatite Water Interfaces*. Journal of Colloid and Interface Science, 1991. **147**(1): p. 178-185.
- [124] Kohn, M.J., J. Rakovan, and J.M. Hughes, eds. *Phosphates - Geochemical, Geobiological, and Materials Importance*. Reviews in Mineralogy and Geochemistry. Vol. 48. 2002, Mineralogical Society of America and Geochemical Society: Washington, D.C. 742.
- [125] Valsami-Jones, E., K.V. Ragnarsdottir, A. Putnis, D. Bosbach, A.J. Kemp, and G. Cressey, *The dissolution of apatite in the presence of aqueous metal cations at pH 2-7*. Chemical Geology, 1998. **151**(1-4): p. 215-233.
- [126] Schutz, W. and H. Schubert, *Influence of Contact Pressure on Particle Adhesion*. Chemie Ingenieur Technik, 1976. **48**(6): p. 567-567.
- [127] Assemi, S., J. Nalaskowski, and W.P. Johnson, *Direct force measurements between carboxylate-modified latex microspheres and glass using atomic force microscopy*. Colloids and Surfaces a-Physicochemical and Engineering Aspects, 2006. **286**(1-3): p. 70-77.
- [128] Greenlan.Dj, *Interactions between Humic and Fulvic Acids and Clays*. Soil Science, 1971. **111**(1): p. 34-&.
- [129] Plaschke, M., J. Romer, R. Klenze, and J.I. Kim, *In situ AFM study of sorbed humic acid colloids at different pH*. Colloids and Surfaces a-Physicochemical and Engineering Aspects, 1999. **160**(3): p. 269-279.
- [130] Wang, Y.C. and M. Ferrari, *Surface modification of micromachined silicon filters*. Journal of Materials Science, 2000. **35**(19): p. 4923-4930.
- [131] Takahashi, Y., T. Kimura, Y. Kato, Y. Minai, and T. Tominaga, *Hydration structure of Eu-III on aqueous ion-exchange resins using laser-induced fluorescence spectroscopy*. Chemical Communications, 1997(2): p. 223-224.
- [132] Blum, A.E. and A.C. Lasaga, *The Role of Surface Speciation in the Dissolution of Albite*. Geochimica Et Cosmochimica Acta, 1991. **55**(8): p. 2193-2201.
- [133] Walther, J.V., *Relation between rates of aluminosilicate mineral dissolution, pH, temperature, and surface charge*. American Journal of Science, 1996. **296**(7): p. 693-728.
- [134] Lyons, J.S., D.N. Furlong, and T.W. Healy, *The Electrical Double-Layer Properties of the Mica (Muscovite)-Aqueous Electrolyte Interface*. Australian Journal of Chemistry, 1981. **34**(6): p. 1177-1187.
- [135] Nasr-el-Din , H.A., B.B. Maini, and P. Stanislav, *Fines migration in unconsolidated sand formations*. AOSTRA Journal of Research, 1991. **7**(1): p. 1-15.
- [136] Vilks, P. and M.H. Baik, *Laboratory migration experiments with radionuclides and natural colloids in a granite fracture*. Journal of Contaminant Hydrology, 2001. **47**(2-4): p. 197-210.
- [137] Alonso, U., T. Missana, A. Patelli, D. Ceccato, N. Albarran, M. García-Gutiérrez, T. Lopez-Torrubia, and V. Rigato, *Quantification of Au nanoparticles retention on a heterogeneous rock surface*. Colloids and Surfaces A: Physicochemical and Engineering Aspects. **In Press, Corrected Proof**.
- [138] Sen, T.K. and K.C. Khilar, *Review on subsurface colloids and colloid-associated contaminant transport in saturated porous media*. Advances in Colloid and Interface Science, 2006. **119**(2-3): p. 71-96.

- [139] Möri, A., W.R. Alexander, H. Geckeis, W. Hauser, T. Schäfer, J. Eikenberg, T. Fierz, C. Degeldre, and T. Missana, *The colloid and radionuclide retardation experiment at the Grimsel Test Site: influence of bentonite colloids on radionuclide migration in a fractured rock*. Colloids and Surfaces A: Physicochemical and Engineering Aspects, 2003. **217**(1-3): p. 33-47.
- [140] Bundschuh, T., W. Hauser, J.I. Kim, R. Knopp, and F.J. Scherbaum, *Determination of colloid size by 2-D optical detection of laser induced plasma*. Colloids and Surfaces A: Physicochemical and Engineering Aspects, 2001. **180**(3): p. 285-293.
- [141] Walther, C., H. Cho, and T. Fanghänel, *Measuring multimodal size distributions of aquatic colloids at trace concentrations*. Applied Physical Letters, 2004. **85**(26): p. 6329-6331.
- [142] Duro, L., *Prediction of the solubility and speciation of radionuclides in Febex and Grimsel waters*. 1999, An99-218, Nagra: Wetingen, Switzerland.
- [143] Missana, T., Ú. Alonso, M. García-Gutiérrez, and M. Mingarro, *Role of bentonite colloids on europium and plutonium migration in a granite fracture*. Applied Geochemistry, 2008. **23**(6): p. 1484-1497.
- [144] Kunze, P., H. Seher, W. Hauser, P.J. Panak, H. Geckeis, T. Fanghänel, and T. Schäfer, *The influence of colloid formation in a granite groundwater bentonite porewater mixing zone on radionuclide speciation*. Journal of Contaminant Hydrology, 2008. **102**(3-4): p. 263-272.
- [145] Zvikelsky, O. and N. Weisbrod, *Impact of particle size on colloid transport in discrete fractures*. Water Resources Research, 2006. **42**: p. W12S08.
- [146] Becker, M.W., P.W. Reimus, and P. Vilks, *Transport and Attenuation of Carboxylate-Modified Latex Microspheres in Fractured Rock Laboratory and Field Tracer Tests*. Ground Water, 1999. **37**(3): p. 387-395.
- [147] Taylor, G., *Dispersion of soluble matter in solvent flowing slowly through a tube*. Proceedings of the Royal Society A: Mathematical, Physical and Engineering Sciences, 1953. **219**: p. 186-203.
- [148] de Marsily, G., *Quantitative hydrogeology : groundwater hydrology for engineers*. 1986: Academic Press.
- [149] Hauser, W., H. Geckeis, J.I. Kim, and T. Fierz, *A mobile laser-induced breakdown detection system and its application for the in situ-monitoring of colloid migration*. Colloids and Surfaces A: Physicochemical and Engineering Aspects, 2002. **203**(1-3): p. 37-45.
- [150] Missana, T., Ú. Alonso, and M.J. Turrero, *Generation and stability of bentonite colloids at the bentonite/granite interface of a deep geological radioactive waste repository*. Journal of Contaminant Hydrology, 2003. **61**(1-4): p. 17-31.
- [151] Ryan, J.N. and M. Elimelech, *Colloid mobilization and transport in groundwater*. Colloids and Surfaces A: Physicochemical and Engineering Aspects, 1996. **107**: p. 1-56.
- [152] Bouby, M., *Colloid impact on radionuclide migration*, in *Annual Report 2008*, H. Geckeis and R. Klenze, Editors. 2009, Researchcenter Karlsruhe - Institute for Nuclear Wastes Disposal (INE): Karlsruhe. p. 40.
- [153] Bear, J., *Hydraulics of groundwater*. 1979, New York: McGraw-Hill Book Company. 569.
- [154] Trick, T., *GTS-CFM: Tracer Test Run #1, QLR*. 2005, unpublished report, NAGRA: Wetingen (Switzerland).
- [155] Trick, T. and I. Blechschmidt, *GTS-CFM: Tracer Test Run 07-02, QLR*. 2007, NAGRA Aktennotiz 07-342, NAGRA: Wetingen (Switzerland).
- [156] Trick, T. and I. Blechschmidt, *GTS-CFM: Tracer Test Run 08-02, QLR*. 2008, NAGRA Aktennotiz 08-165, NAGRA: Wetingen (Switzerland).
- [157] Smith, P.A., J. Guimerà, G. Kosakowski, A. Pudewills, and M. Ibaraki, *GTS Phase V: CRR Final project report series III: Results of the supporting modelling programme*. 2003, Nagra Technical Report NTB 03-03, NAGRA: Wetingen (Switzerland).
- [158] Meier, P.M., A. Medina, and J. Carrera, *Geostatistical inversion of cross-hole pumping tests for identifying preferential flow channels within a shear zone*. Ground Water, 2001. **39**(1): p. 10-17.
- [159] Carrera, J., *An Overview of Uncertainties in Modeling Groundwater Solute Transport*. Journal of Contaminant Hydrology, 1993. **13**(1-4): p. 23-48.

- [160] Moreno, L., Y.W. Tsang, C.F. Tsang, F.V. Hale, and I. Neretnieks, *Flow and Tracer Transport in a Single Fracture - a Stochastic-Model and Its Relation to Some Field Observations*. Water Resources Research, 1988. **24**(12): p. 2033-2048.
- [161] Tsang, Y.W., C.F. Tsang, I. Neretnieks, and L. Moreno, *Flow and Tracer Transport in Fractured Media - a Variable Aperture Channel Model and Its Properties*. Water Resources Research, 1988. **24**(12): p. 2049-2060.
- [162] Tsang, C.F., C. Doughty, and M. Uchida, *Simple model representations of transport in a complex fracture and their effects on long-term predictions*. Water Resources Research, 2008. **44**(8).
- [163] Laaksoharju, M., E.L. Tullborg, P. Wikberg, B. Wallin, and J. Smellie, *Hydrogeochemical conditions and evolution at the Aspö HRL, Sweden*. Applied Geochemistry, 1999. **14**(7): p. 835-859.
- [164] Enzmann, F. and M. Kersten, *X-ray computed micro tomography (μ -XRT) results of a granitic drill core*, in *1st Annual workshop Proceedings of IP FUNMIG, report CEA R-6122*, P. Reiller, et al., Editors. 2006, Commissariat à l'énergie atomique (CEA): Gif sur Yvette (France). p. 211-215.
- [165] Boutt, D.F., G. Grasselli, J.T. Fredrich, B.K. Cook, and J.R. Williams, *Trapping zones: The effect of fracture roughness on the directional anisotropy of fluid flow and colloid transport in a single fracture*. Geophysical Research Letters, 2006. **33**(21).
- [166] Bathe, K.J., H. Zhang, and M.H. Wang, *Finite-Element Analysis of Incompressible and Compressible Fluid-Flows with Free Surfaces and Structural Interactions*. Computers & Structures, 1995. **56**(2-3): p. 193-213.
- [167] Bathe, K.J., H. Zhang, and S.H. Ji, *Finite element analysis of fluid flows fully coupled with structural interactions*. Computers & Structures, 1999. **72**(1-3): p. 1-16.
- [168] Brush, D.J. and N.R. Thomson, *Fluid flow in synthetic rough-walled fractures: Navier-Stokes, Stokes, and local cubic law simulations*. Water Resources Research, 2003. **39**(4).
- [169] Kosakowski, G., *Anomalous transport of colloids and solutes in a shear zone*. Journal of Contaminant Hydrology, 2004. **72**(1-4): p. 23-46.
- [170] Schäfer, T. and K. Iijima, *CFM Phase I - Status report of the laboratory programme*. 2007, NAGRA Arbeitsbericht NAB 07-41, NAGRA: Wettingen (Switzerland). p. 97.
- [171] Gaus, I. and P.A. Smith, *Modellers dataset for the Colloid Formation and Migration Project Status: End of CFM Phase 1*. 2008, NAGRA Arbeitsbericht NAB 08-27, NAGRA: Wettingen (Switzerland).
- [172] Tien, C. and A.C. Payatakes, *Advances in deep bed filtration*. Am. Inst. Chem. Eng., AIChE, 1979. **25**(5): p. 737.
- [173] Grauer, R., *Zur Chemie von Kolloiden. Verfügbare Sorptionsmodelle zur Frage der Kolloid-rückhaltung*. 1990, PSI report 65, Paul-Scherrer Institut (PSI): Villigen, Switzerland.
- [174] Lührmann, L., U. Noseck, and R. Storck, *Spent fuel performance assessment (SPA) for a hypothetical repository in crystalline formations in Germany*. 2000, Report GRS-154, Gesellschaft für Anlagen- und Reaktorsicherheit (GRS) mbH: Braunschweig.
- [175] Vejmělka, P., T. Fanghänel, B. Kienzler, E. Korthaus, J. Römer, W. Schüssler, R. Artinger, and *Sorption and Migration of Radionuclides in Granite (HRL ÄSPÖ, Sweden)*. 2000, Wissenschaftliche Berichte, FZKA 6488, Forschungszentrum Karlsruhe.
- [176] Buckau, G., *Humic substances in performance assessment of nuclear waste disposal: actinide and iodine migration in the far-field : 2nd technical progress report 2004*, FZKA report 6969, Forschungszentrum Karlsruhe: Karlsruhe. p. 350.
- [177] Behrens, S.H., D.I. Christl, R. Emmerzael, P. Schurtenberger, and M. Borkovec, *Charging and aggregation properties of carboxyl latex particles: experiments versus DLVO theory*. Langmuir, 2000. **16**: p. 2566-2575.
- [178] Czigany, S., M. Flury, and J.B. Harsh, *Colloid stability in vadose zone aggregate. Hanford sediments*. Environmental Science & Technology, 2005. **39**(6): p. 1506-1512.
- [179] Scherbaum, F., R. Knopp, and J.I. Kim, *Counting of particles in aqueous solutions by laser-induced photoacoustic breakdown detection*. Applied Physics B, 1996. **63**: p. 299-305.

- [180] Fujimori, H., T. Matsui, T. Ajiro, K. Yokose, Y. Hsueh, and S. Izumi, *Detection of Fine Particles in Liquids by Laser Breakdown Method*. Jpn. J. Appl. Phys., 1992. **31**: p. 1514-1518.
- [181] Bundschuh, T., W. Hauser, and J.I. Kim, *Colloids and Surfaces A*, 2001. **180**: p. 285.
- [182] Hauser, W., R. Götz, H. Geckeis, and B. Kienzler, *In-situ colloid detection in granite groundwater along the Äspö HRL access tunnel*, M. Laaksoharju and S. Wold, Editors. 2005, Technical report TR-05-20, Svensk Kärnbränslehantering AB (SKB): Stockholm, Sweden. p. 57-76.
- [183] Kienzler, B., P. Vejmelka, J. Römer, D. Schild, and M. Jansson, *Actinide Migration in Fractures of Granite Host Rock: Laboratory and in Situ Investigations*. Nuclear Technology, 2009. **165**(2): p. 223-240.
- [184] Buckau, G. *Origin, stability and mobility of humic colloids in Äspö groundwater: Feasibility study*. in *The Colloid investigations conducted at the Äspö Hard Rock laboratory during the years 2000-2004*. 2005: SKB report, Appendix #4. p.
- [185] Duro, L., *Prediction of the solubility and speciation of radionuclides in Febex and Grimsel waters*. 1999, Nagra Aktennotiz AN99-218, Nagra: Wettingen, Switzerland. p. 44.
- [186] Bradbury, M.H. and B. Baeyens, *Modelling the sorption of Mn(II), Co(II), Ni(II), Zn(II), Cd(II), Eu(III), Am(III), Sn(IV), Th(IV), Np(V) and U(VI) on montmorillonite: Linear free energy relationships and estimates of surface binding constants for some selected heavy metals and actinides*. *Geochimica Et Cosmochimica Acta*, 2005. **69**: p. 875-892.
- [187] Dzombak, D.A. and F.M.M. Morel, *Surface complexation modeling- hydrous ferric oxide*. 1990, New York: Wiley & Sons. 393.
- [188] Dardenne, K., T. Schäfer, P. Lindqvist-Reis, M.A. Denecke, M. Plaschke, J. Rothe, and J.I. Kim, *Low temperature XAFS investigation on the lutetium binding changes during the 2-line ferrihydrite alteration process*. *Environmental Science & Technology*, 2002. **36**(23): p. 5092-5099.
- [189] Huber, F. and T. Schäfer, *Sorption and reversibility studies on the interaction of radionuclides with FEBEX bentonite under Grimsel groundwater conditions in the presence of Äspö and Grimsel fracture filling material*. *Applied Geochemistry*, 2009, in prep.
- [190] Milne, C.J., D.G. Kinniburgh, W.H. van Riemsdijk, and E. Tipping, *Generic NICA-Donnan Model parameters for metal-ion binding by humic substances*. *Environmental Science & Technology*, 2003. **37**: p. 958-971.

6 Appendix

6.1 Development of r³t-col

For the inclusion of the model for colloid-facilitated transport presented in section 3.3.5 the extended sorption dynamics was implemented within the framework of r³t. Moreover, r³t-col allows a scaling of the velocity field for the migration of colloids in order to reflect in a very simplified way the modified transport properties due to their size which can be of the order of the pore diameters. Up to now, the implementation was done for the two-dimensional case, only.

6.1.1 Overview

The programme consists of three software layers: a *framework* implemented as a suite of libraries of the UG package, a so called *problem class* which defines the general structure of equations and the numerical methods and finally the *application* layer which parametrises the equations.

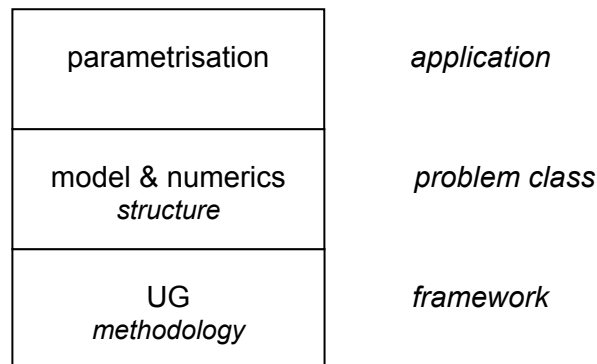


Figure 6-1: Software layers of r³t

The data interfaces are neglected within the simplified view of Figure 6-1.

Implementing a problem class is an expert's work who is closely acquainted with the the UG-framework and who has an expertise in the application of the numerical multigrid methodology. However, the extensions to be realised could be mapped with one limitation to the problem class offered by r³t, so that the programming took only place within the application layer.

Abstractly speaking, the problem class of r³t defines a system of differential equations

$$M \dot{y} = Ly + q + A(y)y + r \quad (2)$$

with y being the discretised model state consisting of $c_C, s_C, c_{Pf,1}, s_{Pf,1}, c_{Pf,2}, s_{Pf,2}, \dots$ where the index 1,2,3, ... counts the different components to be transported. The so called mass matrix M , the stiffness matrix A and its derivative $\partial_y A$ have to be set in the application layer, while the discretised transport operator L and the source term q are directly built from the input data for diffusion, dispersion and sources without being touched by the top layer. The source

term r denotes the term describing radioactive decay which is set within the application layer, where it can be manipulated if necessary.

The mass matrix is diagonal in the r^3t problem class preventing a direct implementation of the model with equilibrium sorption for the Q_2 -paths. The coupling of the colloid to the bound pollutant causes non-diagonal entries. The Q_3 - and Q_4 -path cannot be consistently modelled in equilibrium, as neither c_{pf} nor c_{pb} can be withdrawn from the transport process, i. e. be eliminated from the system of equations.

6.1.2 Mapping colloid-facilitated-transport phases on phases in r^3t

In the case of kinetic sorption r^3t creates two phases for each component, the dissolved mobile phase and the immobile phase adsorbed to the matrix. It is sufficient that a single sorption path is kinetic and all others are in equilibrium mode so that r^3t acts in this way for all components. Furthermore, r^3t creates phases for the immobile pore water if required by the input data.

In the case of colloid-facilitated transport two phases are needed for the colloidal component and four phases for each pollutant, two mobile and two immobile phases resulting from the interaction with the matrix and the colloid. No colloidal interaction is considered in the immobile pore water.

The colloid phases are directly mapped on the two phases of the kinetic sorption mode. Only the reaction path has to be modified. The four phases of each pollutant have to be mapped on the phases of **two** r^3t components, one component representing the free phases and the other component for the bound phases of the pollutant. Furthermore, it has to be taken into account, that the different sorption paths now have different structures and different parameterisation patterns. The primary change induced by the extended sorption process is the coupling of phase equations to the phases of different components, i.e. the coupling of three phases of a pollutant component to the colloidal phases and the coupling of the two bound phases to the free mobile phase of the same pollutant. This dependency pattern was the most challenging part to be implemented in a weakly documented code. The different behaviour of the free and the bound components with respect to sorption has to be considered by case differentiations in the source code.

6.1.3 Implementation of the velocity coefficient

The problem class of r^3t does not provide different flow fields for different components. But in the case of a scaling of the flow by a single positive factor

$$\mathbf{q}_c = \alpha \mathbf{q} \quad (3)$$

the transport equation

$$\partial_t(\theta_c c) + \nabla \cdot (c(\alpha \mathbf{q}) - \mathbf{D}_c \nabla c) = Q \quad (4)$$

can be equivalently written as

$$\partial_t \left(\frac{\theta_c}{\alpha} c \right) + \nabla \cdot \left(c \mathbf{q} - \frac{1}{\alpha} \mathbf{D}_c \nabla c \right) = \frac{Q}{\alpha} \quad (5)$$

This is a transport equation with advective flow \mathbf{q} and scaled parameters θ , \mathbf{D}_c and Q . Looking again at the structure provided by the problem class (eq. (2)) it is apparent that the scaling is easy to realise for M , A and r , which all appear in the application layer. For the source term q the factor has to be explicitly multiplied into the input data. This holds only for the source term parametrised by the input file `config/sourceterm`, not for the terms of the sorption processes which are “automatically” scaled. The same has to be done for the diffusion coefficient of the colloid and the bound pollutant components. The dispersion cannot be scaled independently for all components as the dispersion length is a property of the porous medium and does not change with the component. This means that apart from dispersion the scaling of the flow can be realised within the application layer if the proper input data for the source term and diffusion is provided.

6.1.4 Consequences of the component mapping

Usually, components of r^3t represent nuclides with nuclide specific properties. In some processes, e. g. non-linear sorption, not the nuclide but the element concentration has to be considered with the element concentration being the sum of the corresponding nuclide concentrations.

Because of the mapping of a component of the colloid-facilitated transport model onto two independent components of r^3t with different transport parameters the two r^3t -components cannot refer to the same nuclide nor to the same element in the sense of r^3t . So currently, processes referring to element concentrations cannot be calculated correctly. The implementation expects an alternating sequence of free and bound “nuclides” as well as a similar sequence of “elements”. Consequently, nuclides and elements have to be identified, i.e. the concept of an element referring to several nuclides cannot be used any more in r^3t -col.

To avoid this loss of functionality r^3t would have to provide components with four phases in the mobile pore water. This could have been realised, only, by an extension of the problem class of r^3t which was out of the scope of this project.

6.1.5 Extension of the r^3t -source code

6.1.5.1 The source code of `appl2d/cproblem_lgm.c`

r^3t defines several application classes on top of the r^3t problem class. The problem class needs a set of seven functions to parametrise its structures. Different application classes use different sets of functions. The standard application class *configurable* is initialized by the following piece of code.

```
static INT Init_ConfigurableProblem (void) {
    UserProcPtr coeffs [MAX_COEFFS];
    INIT_COEFFS;
```

```

coeffs[INITVALSFUNC] = Conf_InitialValues;
coeffs[TENSORFUNC]   = Configurable_DiffusionDispersion;
if (Velocity_str == NULL)
    coeffs[VELOCITYFUNC] = Configurable_ConvectionVelocity;
coeffs[FLUIDDENSITY] = Configurable_FluidDensity;
coeffs[VOLUMEINTEGR] = Configurable_VolumeIntegration;
coeffs[NONLINUPDATE] = Configurable_NonlinearUpdate;
coeffs[OPERATOR]     = Operator_Splitting ;
if (CreateProblem("configurable",Configurable_ProblemConfig,
                  DomainSize,Conf_BndCond, 0, NULL, MAX_COEFFS,
                  coeffs) == NULL) return 1;
return 0;
}

```

The function `CreateProblem` is a call to the UG framework. `r3t-col` simply adds a new application class *colloidal* to `r3t` which is an extension of the class *configurable*. This is done by a call to the function `Init_ColloidalProblem` which was added to the file `appl2d/cproblem_lgm.c`.

```

static INT Init_ColloidalProblem (void){
    UserProcPtr coeffs[MAX_COEFFS];
    INIT_COEFFS;
    coeffs[INITVALSFUNC] = Conf_InitialValues;
    coeffs[TENSORFUNC]   = Configurable_DiffusionDispersion;
    if (Velocity_str == NULL)
        coeffs[VELOCITYFUNC] = Configurable_ConvectionVelocity;
    coeffs[FLUIDDENSITY] = Configurable_FluidDensity;
    coeffs[VOLUMEINTEGR] = Colloidal_VolumeIntegration;
    coeffs[NONLINUPDATE] = Colloidal_NonlinearUpdate;
    coeffs[OPERATOR]     = Operator_Splitting ;
    if (CreateProblem("colloidal",Colloidal_ProblemConfig,
                    DomainSize,Conf_BndCond, 0, NULL, MAX_COEFFS,
                    coeffs) == NULL) return 1;
    return 0;
}

```

The function `Colloidal_VolumeIntegration`, `Colloidal_NonlinearUpdate` and `Colloidal_ProblemConfig` are implemented in the file `pclib/colloidal.c`. Another application *confcolloidal* was defined for testing the initialization procedure of the class *colloidal*.

```

static INT Init_ConfColloidalProblem (void){
    UserProcPtr coeffs[MAX_COEFFS];
    INIT_COEFFS;

```

```

coeffs[INITVALSFUNC] = Conf_InitialValues;
coeffs[TENSORFUNC]   = Configurable_DiffusionDispersion;
if (Velocity_str == NULL)
    coeffs[VELOCITYFUNC] = Configurable_ConvectionVelocity;
coeffs[FLUIDDENSITY] = Configurable_FluidDensity;
coeffs[VOLUMEINTEGR] = Configurable_VolumeIntegration;
coeffs[NONLINUPDATE] = Configurable_NonlinearUpdate;
coeffs[OPERATOR]     = Operator_Splitting ;
if (CreateProblem("confcolloidal", Colloidal_ProblemConfig,
                  DomainSize, Conf_BndCond, 0, NULL, MAX_COEFFS,
                  coeffs) == NULL) return 1;
return 0;
}

```

The class *confcolloidal* behaves like the class *configurable* but performs with a certain overhead provided for the colloid-facilitated processes.

The input file `config/geometry` controls which application class is being used.

6.1.5.2 The source code in `pclib/`

`pclib/cproblem.h` and `pclib/rsysfv.c`

In the source file `pclib/cproblem.h` the declarations for `colloid_density`, `colloid_sorption_coef`, `colloid_desorption_coef` are included. The size of the array `col_ind` is increased by 4.

In the source file `pclib/rsysfv.c` a single line in the function `TSFV_PreProcess` had to be generalized. The code

```

if (Configurable_VolumeIntegration(in, out) < 0)
    REP_ERR_RETURN(-1);

```

has changed to

```

VolumeIntegrals=MG_GetUserFct(mg, VOLUMEINTEGR);
if (VolumeIntegrals(in, out) < 0)
    REP_ERR_RETURN(-1);

```

`pclib/configure.c`

The file `pclib/configure.c` holds the code of the parametrising function of the application class *configurable*. The extensions for the class *colloidal* are implemented in `pclib/colloidal.c`. The most important changes to `pclib/configure.c` are the directives

```
#include "colloidal.h"
```

at the beginning and

```
#include "colloidal.c"
```

at the end of the file. Besides these only arrays for the management of matrix indices had to be extended.

pclib/colloidal.h and pclib/colloidal.c

The code of the source file `pclib/colloidal.h` declares the following functions:

```
INT Colloidal_ProblemConfig(INT argc, char **argv);
INT Colloidal_SetParameters(void);
INT Colloidal_VolumeIntegration(DOUBLE *in, DOUBLE *out);
INT Colloidal_NonlinearUpdate(DOUBLE *in, DOUBLE *out);
void Colloidal_ControlMessage(void);
```

These functions are implemented in the file `pclib/colloidal.c` with about 1900 non blank lines of code (comments included). The function `Colloidal_ControlMessage` only assures the user that the application class *colloidal* or *confcolloidal* is being called.

Extending the structure of the matrices for the new dependencies among the formerly independent components was the main difficulty. The different treatment of the colloid component and the free and the bounded components blows up the code. During initialization the function `Colloidal_ProblemConfig` calls `Colloidal_SetParameters` which calls `Configure_SetParameters` of the class *configurable*. The function `Colloidal_VolumeIntegration` parametrises the mathematical structures M , A and r . `Colloidal_NonlinearUpdate` does the same for $\partial_y A$.

6.1.5.3 The source code in `config/`

The files affected in the directory `config/` are `symbols.h`, `parser.y`, `scanner.l` and `template.c`. The files `parser.h`, `parser.c` and `scanner.c` are generated by the parser generator `yacc` and the scanner generator `flex`, respectively, during compilation. So, these files do not contain source code.

config/symbols.h

The declaration of a structure `COLLOID_PROP`

```
typedef struct colloid_prop {
    double density;
    double velocity_coef;
    double sorption_coef;
    double desorption_coef;
} COLLOID_PROP;
```

was added to the file `symbols.h`. This structure extends the structure `MATERIALS` as a sub-structure. Within the structure `ELEM_PROP` the size of the arrays `sorption`, `Kd`, `b`, `kappa`, `Kn1`, `p` and `rate` was increased from 2 to 4.

config/template.h and config/template.c

The function `WriteJsparseDaa` was enabled to write the extended dependency pattern of the application classes *colloidal* and *confcolloidal* to the output file `scripts/template.scr`. Therefore the signature of the calling function `WriteTemplates` also had to be extended from `(char *filename)` to `(char *filename, char *problemname)`. The string in `*problemname` is used to set the variable `is_colloidal`.

config/parser.y and config/scanner.l

The modifications to the files `config/parser.y` and `config/scanner.l` extend the user interface for the additional parameters needed for colloid-facilitated transport. The following tokens were added to the parser.

```
%token T_COLLOID_DENSITY
%token T_COLLOID_VELOCITY_COEF
%token T_COLLOID_SORPTION_COEF
%token T_COLLOID_DESORPTION_COEF
%token T_COLLOID DISSOLVED
%token T_COLLOID ADSORBED
```

`T_COLLOID DISSOLVED` replaces `T_COLLOID DILUTED`. The scanner links the above mentioned tokens to the strings `"COLLOID_DENSITY"`, `"COLLOID_VELOCITY_COEF"`, `"COLLOID_SORPTION_COEF"`, `"COLLOID_DESORPTION_COEF"`, `"COLLOID DISSOLVED"` and `"COLLOID ADSORBED"`, respectively. This match is not case sensitive, i.e. `"colloid_density"` also raises a signal for the token `T_COLLOID_DENSITY`.

The patterns added to the parser are `mat_colloidal`, `mat_colloidal_density`, `mat_colloidal_velocity`, `mat_colloidal_colloidal_sorption_coefs`, `mat_colloidal_sorption`, `mat_colloidal_desorption`, `retention_line_cd1`, `retention_line_ca1`, `retention_line_cd`, `retention_line_ca`, `retention_line_cd2` and `retention_line_ca2`.

These changes affect the input file `config/retention`, as explained below.

6.1.6 Extension of the interface

6.1.6.1 The file `config/geometry`

The application class to be used is determined by the parameter `problemname` in the file `config/geometry`. Setting

```
problemname = colloidal
```

or

```
problemname = confcolloidal
```

calls one of the newly added classes. For an unknown identifier the class *configurable* will be called as default. The identifier to be used for an application class is the first parameter of the call to `CreateProblem` in the source file `appl2d/cproblem_lgm.c`.

6.1.6.2 The file `config/pollutant`

Formally, nothing has changed for the file `pollutant` in the input directory `config/`. But the number of components declared has to be uneven if the application class *colloidal* or *confcolloidal* is to be called. The first component declared is interpreted as the colloid. The following is the free component of the first pollutant, the next its bound counterpart. Two components follow for the second pollutant, and so on. An example is given for the case of two pollutants.

```
pollutant
  model crr
  version ref
  Colloid
    PfA
    PbA
    PfB
    PbB
pollutant end
```

In general $1+2n$ components have to be declared for n pollutants, where $n = 0$ is possible. Violating this condition results in a run time error.

6.1.6.3 The file `config/retention`

The file `retention` is the place where all the extensions to the parser take effect. An example is given where all these changes are emphasised.

```
retention
model crr
version ref

hydrogeo2mat
  FRACTURE: Formation
hydrogeo2mat end

FRACTURE
  rock_density 2670.0
  porosity      0.0825
  porosity_im   0.0
  g             1.0
  diffusion     2.0E-11
  alpha_L      0.038
```

```

alpha_T      0.017
colloid_density      1.0
colloid_velocity_coef      1.0
colloid_sorption_coef      Csorption
colloid_desorption_coef      Cdesorption

Colloid
  mobile
    kinetic Henry Kd,mobile rate kmobile
  mobile end
Colloid end

PfA
  mobile
    kinetic Henry 0.03 rate 1.0
  mobile end
  colloid_dissolved
    kinetic Henry 0.0 rate 0.00
  colloid_dissolved end
  colloid_adsorbed
    kinetic Henry 0.00 rate 0.00
  colloid_adsorbed end
PfA end

PbA
  mobile
    kinetic Henry Kd,mobile rate kmobile
  mobile end
PbA end
...

FRACTURE end
retention end

```

Formally, the `colloid_dissolved` and `colloid_adsorbed` blocks can be declared for any component. The parser does not distinguish between colloidal, free and bound components, but only those of the colloid-free components affect the simulation. The sorption rate K_2 in the reaction path Q_2 of the model is the product of the value of `colloid_sorption_coef` times the rate and the first coefficient of the `mobile`-block of the colloidal and the bound components.

$$K_2 = C_{sorption} K_{d,mobile} k_{mobile} \quad (6)$$

The model parameter k_2 is the product of the value of `colloid_desorption_coef` and the rate, only.

$$k_2 = C_{desorption} k_{mobile} \quad (7)$$

6.2 Verification of r³t-col

6.2.1 General test setup

For the verification of r³t-col an intercomparison with TRAPIC1D was carried out on the basis of several quasi-1D test cases (TC). All tests were performed on a rectangular domain of 50 m (x) times 10 m (y) with the porosity uniformly set to $\Theta = 0.5$ (see Figure 6-2). A Darcy flow of $q = 0.5 \text{ m s}^{-1}$ propagates along the x-direction. Neumann-type boundary-conditions govern the outflow boundary and the lateral boundaries for all components whereas their inflow is exactly prescribed by a Robin-condition. The initial concentrations were chosen to be $c_C = 1 \text{ mol m}^{-3}$ for the colloid and $c_{P,i} = 0 \text{ mol m}^{-3}$ for all pollutants. With an inflow of $F_C = 0.5 \text{ mol s}^{-1} \text{ m}^{-2}$ the colloid concentration does not change if it is initially in equilibrium with the immobile colloid phase s_C . All parameters depending on the third spatial dimension (concentrations, fluxes) are calibrated for a test field thickness of $d = 1 \text{ m}$.

The test cases are devised in a way that at the outset only process Q_1 is analysed and then additional interactions are taken into account successively. For TC1 which only considers the classical sorption process of a pollutant with the matrix the pollutant inflow is set to $f_{Pf} = 1 \text{ mol s}^{-1} \text{ m}^{-2}$, while in all other simulations with an activated reaction path between the free and colloid-bound component the inflow is set to $f_{Pf} = 0.01 \text{ mol s}^{-1} \text{ m}^{-2}$ and $f_{Pb} = 0.99 \text{ mol s}^{-1} \text{ m}^{-2}$ for a time t_{inflow} of 10 s or 100 s, respectively. For further general and test case specific parameters please consult the tables Table 6-1 and Table 6-2. Results from TRAPIC1D are compared with those at the midpoint of the outflow boundary calculated by r³t-col.

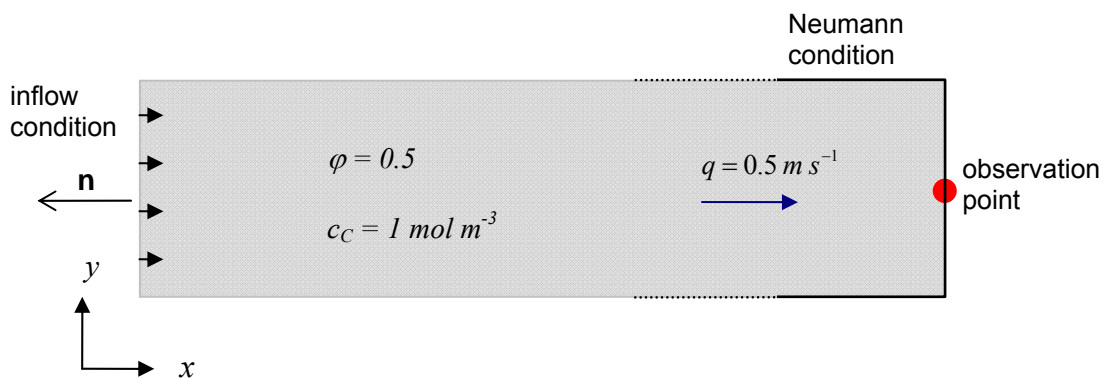


Figure 6-2: Test case setup for the comparison with TRAPIC1D

Table 6-1: Constant test case parameters

rock density	2500 kg m^{-3}	dispersion length (long.)	0.1 m
porosity	0.5	dispersion length (trans.)	0.01 m
diffusion coefficient	$10^{-6} \text{ m}^2 \text{ s}^{-1}$	Darcy velocity	0.5 m s^{-1}

Table 6-2: Variable test case parameters

		TC1	TC2		TC3	
			(1)	(2)	(1)	(2)
Q_1	$k_1 [s^{-1}]$	$10^{-3}, 10^{-2}, 10^{-1}, 10^0$	1	1	1	1
	$K_{d1} [m^3 kg^{-1}]$	0.003				
Q_2	$k_2 [s^{-1}]$	0	0	0	0	10
	$K_2 [s^{-1}]$	0	0	0	$10^{-3}, 10^{-2}, 10^{-1}, 10^0$	10, 30, 50, 100
Q_3	$k_3 [s^{-1}]$	0	$10^{-3}, 10^{-2}, 10^{-1}, 10^0$	1	10^{-3}	10^{-4}
	$K_{d3} [m^3 kg^{-1}]$	0	1	$10^{-1}, 10^0, 10^{+1}, 10^{+2}$	1	1
Q_4	$k_4 [s^{-1}]$	0	0	0	10^{-3}	10^{-4}
	$K_{d4} [m^3 kg^{-1}]$	0	0	0	1	1

6.2.2 Results

Summarizing the results of the test cases detailed in the following subsections, the time courses of the break-through curves computed by r^{3t}-col and TRAPIC1D match almost perfectly with visible differences in some of the predicted amplitudes. These aberrations are possibly attributable to numerical dispersion effects and the root of this problem should be investigated. In general, our findings inspire reasonable confidence in the outcome of future calculations of colloid-facilitated transport in two dimensions with r^{3t}-col, so that the influence of complex flow fields can be studied.

6.2.3 TC1: sorption process Q_1 , variation of the sorption rate k_1

In order to check the functionality of the non-extended version of r^{3t} with regard to kinetic sorption, the first test case only considers the classical sorption process between the free pollutant and the matrix, i.e. no colloid-facilitated transport can occur. This aspect of the program has not been verified previously.

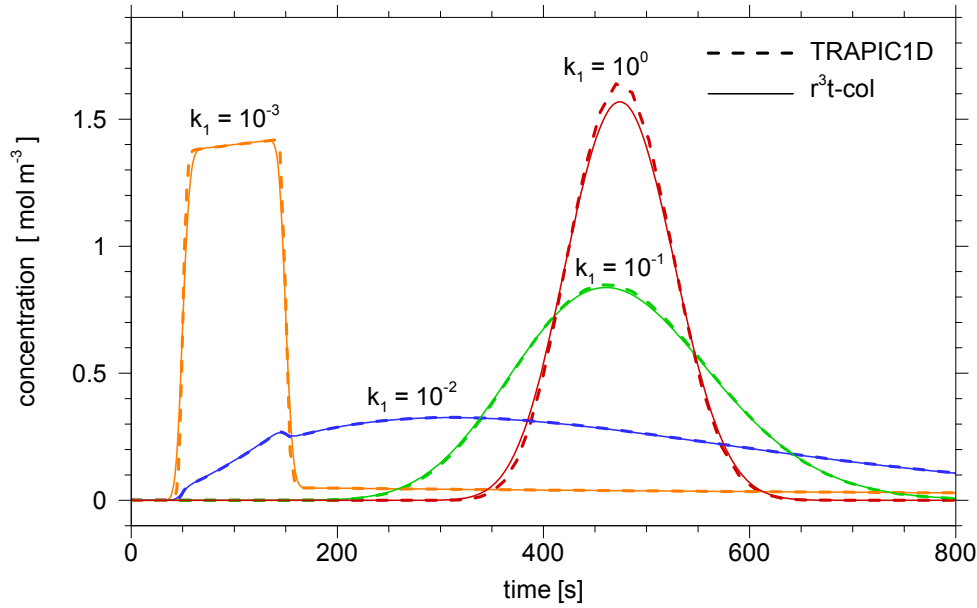


Figure 6-3: Breakthrough curves from calculations with TRAPIC1D and $r^3t\text{-col}$ for TC1

For small rates k_1 , i.e. *small* on the natural scale given by the inverse fluid transport time, the kinetics is so slow that the major part of the pollutant migrates without retardation through the system. On increasing k_1 a larger fraction of pollutants adsorbs to the matrix during the travel time resulting in a shift and a broadening of the arrival time distribution. When the transition rate has reached large enough values an instantaneous equilibrium is reached between the matrix-adsorbed and the free phase. This leads to a re-sharpening of the breakthrough curve. For these equilibrium conditions the arrival time of the peak maximum is retarded with respect to the fluid travel time by a retardation factor

$$R_F = 1 + \frac{(1 - \Theta)}{\Theta} \rho K_d \quad (8)$$

which computes to $R_F = 8.5$ for the chosen set of parameters.

6.2.4 TC2: Sorption process Q_1 and Q_3 :

This test case takes the transport-facilitating sorption paths into account, enabling the transition from the free and indirectly from the matrix-attached pollutant phase to the mobile colloid-bound state.

(1) Variation of the sorption rate k_3

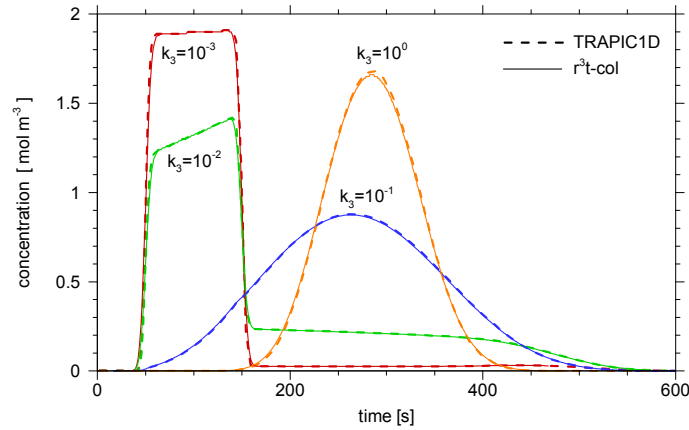


Figure 6-4: Breakthrough curves from calculations with TRAPIC1D and $r^3t\text{-col}$ for TC2 (1)

For small values of k_3 at high k_1 the transport dynamics of the pollutant, of which 99 % are initially bound to colloids, is dictated by the mobility of the colloids. With increasing exchange rate of the Q_3 -process, more nuclides detach from their carriers and adsorb to the matrix which leads to retardation and the shaping of the break-through curve as in TC1. Finally, for $k_3 = 0$, the transitions on the activated pathways can be considered instantaneous. Under these equilibrium conditions the mobile pollutant concentration is increased by colloid-attached pollutants and the overall K_d -value can be calculated for this case where colloids do not interact with the matrix by

$$K_{d,tot} = \frac{K_{d1}}{1 + c_C K_{d3}}, \quad (9)$$

resulting in $K_{d,tot} = 2 \cdot 10^{-3} \text{ m}^3 / \text{kg}$. According to the corresponding retardation factor $R_F = 6$ the migration velocity is increased in comparison with TC1 (equilibrium conditions).

(2) Variation of the sorption constant K_{d3}

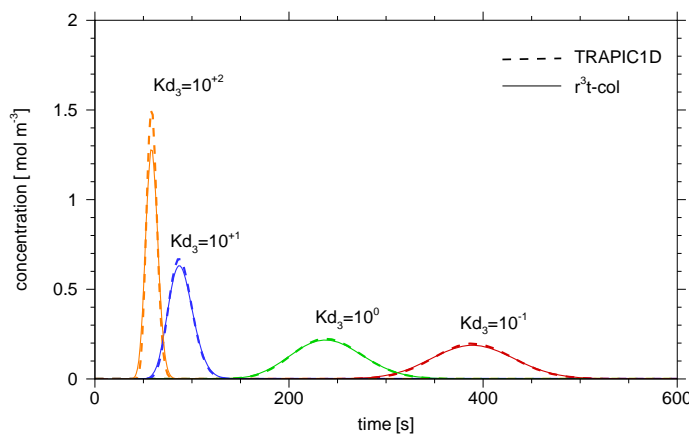


Figure 6-5: Breakthrough curves from calculations with TRAPIC1D and $r^3t\text{-col}$ for TC2 (2)

On variation of K_{d3} , defined as the equilibrium ratio between the concentrations of the pollutant bound to mobile colloids and the unbound pollutants, the affinity of the pollutant to sorb to the colloids is adjusted. Our calculations with $r^3t\text{-col}$ comply with the expectation that a larger fraction of colloid-bound particles, i.e. a high K_{d3} value, leads to a facilitation of the pollutant transport. Shifting the equilibrium in the other direction we observe an increased retardation and spreading of the breakthrough curve due to the interaction with the sediment.

6.2.5 TC3: All sorption processes. Variation of the sorption factor K_2

In the last test case all possible sorption processes are activated, although some pathways may be not accessible bi-directionally. The sorption factor K_2 determines the rate of transfer of dissolved colloids to the sediment-bound state.

(1) Simulating the irreversible filtration of colloids with $k_2 = 0$

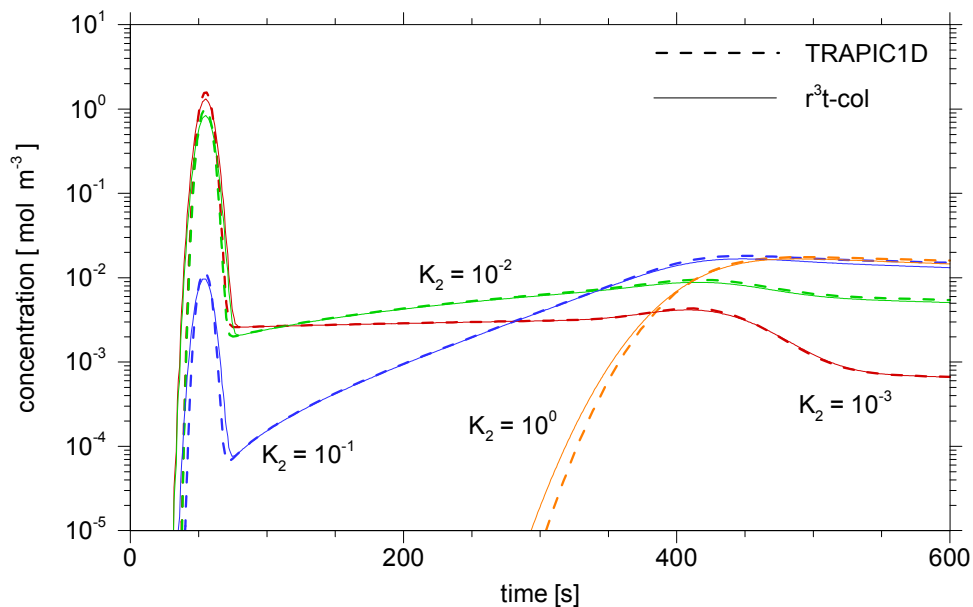


Figure 6-6: Breakthrough curves from calculations with TRAPIC1D and $r^3t\text{-col}$ for TC3 (1)

By setting $k_2 = 0$ the reaction process Q_2^C becomes unidirectional so that colloids which have adsorbed to the sediment with rate K_2 cannot escape anymore. This simulates the effect of mechanical filtration by the matrix. As a consequence the attached and collaterally trapped pollutant particles will have to desorb from their former carriers in order to reach the observation area. In the low K_2 regime only a small part of colloids and thereby pollutants get caught on the sediment surface. From these colloid-bound pollutants which are filtered only a low fraction of pollutants gets unstuck again because of the equally low k_4 constant chosen for this case. Therefore the arrival time distribution becomes very asymmetric decomposing into a nearly unaltered part with respect to shape which is colloid-facilitated and a long tail formed by “luckless” pollutants. The variation of K_2 tunes the contribution of these two characteristic curves fractions. For the highest K_2 values the first peak representing the colloid bound fraction vanishes, because nearly all colloids are filtered during transport.

(2) $k_2 > 0$, emphasis on Q_2

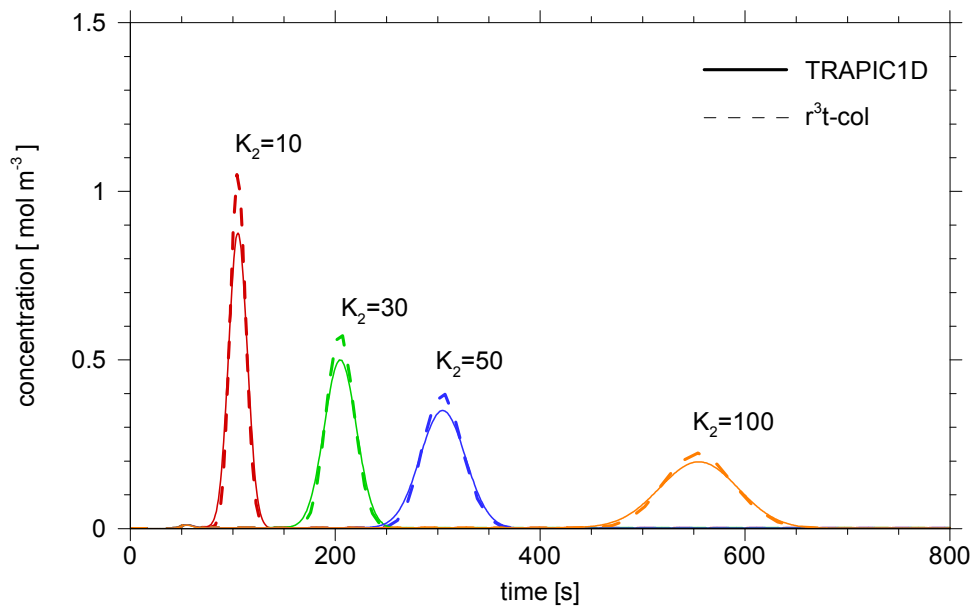


Figure 6-7: Breakthrough curves from calculations with TRAPIC1D and r³t-col for TC3 (2)

The choice of parameters for this sub-case causes the pollutant transport to be almost completely colloid-based with no direct pollutant-sediment interaction. Consequently the arrival time distribution depends exclusively on the kinetics of Q_2 . Due to the high rates of k_2 and K_2 the interaction of colloids with the sediment matrix can be regarded as an equilibrium process. In this case the K_d value for the colloids is given by the ratio $\frac{K_2}{k_2}$, and varies between one and ten, which is reflected in the arrival times of the breakthrough curves via the formula (8) in TC1.

6.3 Laboratory study on colloid stability and radionuclide – colloid interaction under Äspö groundwater conditions.

Abstract. The studies aim at the investigation of radionuclide behavior in a colloid-groundwater-fracture infill mineral system. Background of the experiments is the scenario of a potential release of clay colloids from the bentonite barrier in a repository and their subsequent transport with the groundwater flow in a water conducting fracture. Those colloids may sorb radionuclides and thus can act as carriers for the colloid-mediated radionuclide migration. First investigations reveal that the contact with oxygen (leading to the formation of Fe(III) oxy/hydroxide colloids) and the pressure release (leading to the precipitation of calcite) can significantly influence the colloid composition in Äspö groundwater (ÄGW). The stability of clay colloids prepared from MX80 bentonite and carboxylated polystyrene colloids in solutions of varying ionic strength and pH and in a groundwater sampled at the Äspö Hard Rock Laboratory (HRL) site (TRUE-1 site, Feature A, KXTT4) has been studied. Instantaneous agglomeration with subsequent sedimentation is observed indicating that the current Äspö groundwater chemistry represents a regime of solely diffusion controlled agglomeration. The destabilization of colloids is complete with however some indications for a possible mechanical remobilization. The colloids appear stable in media with salinity two orders of magnitude lower than found in the actual ÄGW. The presence of organic matter, simulated by addition of fulvic acid, does not lead to a finally increased colloid stability and reduces only slightly the coagulation and sedimentation process. The impact of MX80 bentonite colloids, fracture filling material and fulvic acid on the speciation of various radionuclides (Sr⁹⁰, Cs¹³⁷) including various actinides (Am²⁴¹, Np²³⁷, U²³³, Pu²⁴⁴) was observed in ÄGW over a period of 8-12 months. Sr(II) and U(VI) remain unaffected by the presence of colloids and do not sorb significantly to solid fracture minerals. Cs(I) is sorbed onto the fracture filling material. Am(III) and Pu(IV) form unstable colloidal species in presence and absence of bentonite colloids. Rapid sorption to fracture filling material occurs even in presence of fulvic acid which then only slightly delay the sorption. Without fracture filling material, both actinide ions remain mainly dissolved in presence of fulvic acid, shown to be stable in this medium. Np(V) appears to be slowly reduced to Np(IV) even after complexation by fulvic acids, leading either to colloid formation, sorption to mineral surfaces or wall containers. Geochemical calculations performed in order to specify prevailing radionuclide speciation under given experimental conditions confirm to a certain extent the conclusions.

6.3.1 Material & Methods

6.3.1.1 Äspö Ground Water (ÄGW)

ÄGW was collected on site in December 2004 from the so-called True-1 site, Feature A, borehole KXTT4 situated at –390 m depth in the Äspö-tunnel. The water was stored in a 50 L Ar flushed Teflon coated Al-barrel until use. The evolution of the physico-chemical parameters determined for the water **a**- remaining in the barrel, **b**-stored in a glove box under anoxic conditions (Ar/1%CO₂) and **c**- in contact with fracture filling mineral from Äspö site are summarized in Table 6-3 to Table 6-5, respectively.

Table 6-3: Evolution of ÄGW (TRUE-1 site, Feature A, KXTT4) element composition during storage in barrel.

	ÄGW ^{a)}	ÄGW ^{b)}	ÄGW ^{c)}		ÄGW ^{c)}
	April 1996	December 2004	August 2006		September- November 2007
pH	7.6	7.5 ± 0.1	7.5 ± 0.1		7.5 ± 0.1
E _h (SHE)		-50 ± 15 mV	~ 62 ± 20 mV		~ 62 ± 20 mV
				Particulate s+ colloids ^{d)}	
[Mg ²⁺]	81.5 mg.L ⁻¹ ₁	74.6 mg.L ⁻¹	70.9 mg.L ⁻¹	no	76.4 mg.L ⁻¹
[Ca ²⁺]	1.25 g.L ⁻¹	0.95 g.L ⁻¹	1.06 g.L ⁻¹	no	0.87 g.L ⁻¹
[Fe ^{2+,3+}]	717 µg.L ⁻¹	< D.L.	760 µg.L ⁻¹	min. 34 %	< D.L.
[Mn ²⁺]	489 µg.L ⁻¹	606 µg.L ⁻¹	565 µg.L ⁻¹	no	532 µg.L ⁻¹
[Sr ²⁺]	19.8 mg.L ⁻¹ ₁	15.8 mg.L ⁻¹	15.9 mg.L ⁻¹	no	15.4 mg.L ⁻¹
[Cs ⁺]	3.63 µg.L ⁻¹	n.d.	3.8 µg.L ⁻¹	no	3.5 µg.L ⁻¹
[La ³⁺]	0.34 µg.L ⁻¹	0.02 µg.L ⁻¹	0.2 µg.L ⁻¹	~ 85 %	0.03 µg.L ⁻¹
[U]	0.71 µg.L ⁻¹	n.d.	0.28 µg.L ⁻¹	no	0.35 µg.L ⁻¹
[Al ³⁺]	n.d.	n.d.	37.7 µg.L ⁻¹	~ 100 %	9.2 µg.L ⁻¹
[Na ⁺]	1.76 g.L ⁻¹	1.49 g.L ⁻¹	1.2 g.L ⁻¹	n.d.	1.2 g.L ⁻¹
[Cl ⁻]	5.01 g.L ⁻¹	4.2 g.L ⁻¹	3.9 g.L ⁻¹	n.d.	4.9 g.L ⁻¹
[Si]	5.2 mg.L ⁻¹	5.7 mg.L ⁻¹	6.3 mg.L ⁻¹	n.d.	4.9 mg.L ⁻¹
[SO ₄ ²⁻]	343 mg.L ⁻¹	276 mg.L ⁻¹	270 mg.L ⁻¹	n.d.	268 mg.L ⁻¹
[F ⁻]	n.d.	1.7 mg.L ⁻¹	n.d.	n.d.	1.3 mg.L ⁻¹
[Br ⁻]	25 mg.L ⁻¹	n.d.	20.4 mg.L ⁻¹	n.d.	n.d.
[NO ₃ ²⁻]	n.d.	< D.L.	< D.L.	n.d.	< D.L.
[HCO ₃ ⁻]	98 mg.L ⁻¹	135.8 mg.L ⁻¹ ₁	n.d.	n.d.	125.6 mg.L ⁻¹

a) Äspö Hard Rock Laboratory, SKB Technical Report TR-00-07, March 2000

b) KIT-INE, ICP-MS/AES analysis; water analysed after coming back from the sampling campaign

c) KIT-INE, ICP-MS/AES analysis; sampled from the barrel

d) Calculated from supernatant analysis after ultracentrifugation, 2h at ~ 500 000 g

n.d.: not determined, D.L.: detection limit

Table 6-4: Evolution of ÄGW (TRUE-1 site, Feature A, KXTT4) element composition during storage in glove box under anoxic conditions (Ar/1%CO₂)

	ÄGW ^{a)}	ÄGW ^{b)}	ÄGW ^{b)}	ÄGW ^{b)}	ÄGW ^{b)}	ÄGW S ^{d)}
	April 1996	August 2006 (%particulates+colloids ^{c)})	November 2006 (%particulates+colloids ^{c)})	June 2007 (%particulates+colloids ^{c)})	September 2007 (%particulates+colloids ^{c)})	September 2007 (%particulates+colloids ^{c)})
pH	7.6	7.5 ± 0.1	7.5 ± 0.1		7.0 ± 0.1	
E _h (SHE)		~ 62 ± 20mV			~ 62 ± 20 mV	
[Mg ²⁺]	81.5 mg.L ⁻¹	70.9 mg.L ⁻¹ (no)	69.6 mg.L ⁻¹ (no)	85.3 mg.L ⁻¹	85.4 mg.L ⁻¹ (no)	84.1 mg.L ⁻¹ (no)
[Ca ²⁺]	1.25 g.L ⁻¹	1.06 g.L ⁻¹ (no)	0.86 g.L ⁻¹ (no)	1.05 g.L ⁻¹	0.918 g.L ⁻¹ (no)	0.942 g.L ⁻¹ (no)
[Fe ^{2+,3+}]	717 µg.L ⁻¹	760 µg.L ⁻¹ (min. 34%)	< 100 µg.L ⁻¹	< 80 µg.L ⁻¹	< 40 µg.L ⁻¹	~ 70 µg.L ⁻¹
[Mn ²⁺]	489 µg.L ⁻¹	565 µg.L ⁻¹ (no)	455 µg.L ⁻¹ (no)	n.d.	292 µg.L ⁻¹ (no)	290 µg.L ⁻¹
[Sr ²⁺]	19.8 mg.L ⁻¹	15.9 mg.L ⁻¹ (no)	18.3 mg.L ⁻¹ (no)	n.d.	18.8 mg.L ⁻¹ (no)	18.9 mg.L ⁻¹ (no)
[Cs ⁺]	3.63 µg.L ⁻¹	3.8 µg.L ⁻¹ (no)	3.7 µg.L ⁻¹ (no)	n.d.	3.0 µg.L ⁻¹ (no)	2.8 µg.L ⁻¹ (no)
[La ³⁺]	0.34 µg.L ⁻¹	0.2 µg.L ⁻¹ (~ 85 %)	0.01 µg.L ⁻¹ (no)	n.d.	< D.L.	0.02 µg.L ⁻¹
[U]	0.71 µg.L ⁻¹	0.28 µg.L ⁻¹ (no)	0.4 µg.L ⁻¹ (no)	n.d.	0.35 µg.L ⁻¹ (no)	0.35 µg.L ⁻¹ (no)
[Al ³⁺]	n.d.	37.7 µg.L ⁻¹ (~ 100 %)	< D.L.	< 15 µg.L ⁻¹	< 15 µg.L ⁻¹	70 µg.L ⁻¹
[Na ⁺]	1.76 g.L ⁻¹	1.2 g.L ⁻¹	n.d.	n.d.	1.4 g.L ⁻¹ (no)	1.4 g.L ⁻¹ (no)
[Cl]	5.01 g.L ⁻¹	3.9 g.L ⁻¹	n.d.	n.d.	4.5 g.L ⁻¹	n.d.
[Si]	5.2 mg.L ⁻¹	6.3 mg.L ⁻¹	n.d.	n.d.	5.5 mg.L ⁻¹	5.3 mg.L ⁻¹
[SO ₄ ²⁻]	343 mg.L ⁻¹	270 mg.L ⁻¹	n.d.	n.d.	284 mg.L ⁻¹	n.d.
[F]	n.d.	n.d.	n.d.	n.d.	1.2 mg.L ⁻¹	n.d.
[Br]	25 mg.L ⁻¹	20.4 mg.L ⁻¹	n.d.	n.d.	22.3 mg.L ⁻¹	n.d.
[NO ₃ ²⁻]	n.d.	< D.L.	n.d.	n.d.	< D.L.	n.d.

a) Äspö Hard Rock Laboratory, SKB Technical Report TR-00-07, March 2000

b) KIT-INE, ICP-MS/AES analysis; the water is sampled from the barrel, stored in a 2L bottle in the glove box and analyzed regularly

c) Calculated from supernatant analysis after ultracentrifugation, 2h at ~ 500 000 g;

d) The 2L bottle is shaken in the glove box before sampling

n.d.: not determined, D.L.: detection limit

Table 6-5: Evolution of ÄGW (TRUE-1 site, Feature A, KXTT4) element composition during storage in glove box under anoxic conditions (Ar/1%CO₂) contacting with fracture filling material (FFM)^{a)}, CT:contact time.

	ÄGW ^{b)}	ÄGW ^{c)}	ÄGW	ÄGW	ÄGW	ÄGW S ^{e)}
	April 1996	August 2006 (% particulat es + colloids. ^{d)})	September 2006 CT: 2 weeks (%particulat es + colloids ^{d)})	November 2006 CT: 2 months (% particulat es + colloids ^{d)})	September 2007 CT: 1 year (%particulat es + colloids ^{d)})	September 2007 CT: 1 year (%particulat es + colloids ^{d)})
pH	7.6	7.5 ± 0.1		7.5 ± 0.1		
E _{n(SHE)}		~ 62 mV			~ 60 - 90 mV	
[Mg ²⁺]	81.5 mg.L ⁻¹	70.9 mg.L ⁻¹ (no)	n.d.	81.5 mg.L ⁻¹ (no)	98.5 mg.L ⁻¹ (~ 17 %)	142 mg.L ⁻¹ (~ 43 %)
[Ca ²⁺]	1.25 g.L ⁻¹	1.06 g.L ⁻¹ (no)	1.36 g.L ⁻¹ (~ 25 %)	0.971 g.L ⁻¹ (no)	1.05 g.L ⁻¹ (no)	1.1 g.L ⁻¹ (no)
[Fe ^{2+,3+}]	717 µg.L ⁻¹	760 µg.L ⁻¹ (min. 34%)	< 30 µg.L ⁻¹	1272 µg.L ⁻¹ (~ 100 %)	165 µg.L ⁻¹ (50 %)	9515 µg.L ⁻¹ (100 %)
[Mn ²⁺]	489 µg.L ⁻¹	565 µg.L ⁻¹ (no)	440 µg.L ⁻¹ (no)	447 µg.L ⁻¹ (~ 17 %)	220 µg.L ⁻¹ (~ 30 %)	745 µg.L ⁻¹ (~ 80 %)
[Sr ²⁺]	19.8 mg.L ⁻¹	15.9 mg.L ⁻¹ (no)	22.3 mg.L ⁻¹ (11 %)	19.5 mg.L ⁻¹ (14 %)	19.4 mg.L ⁻¹ (no)	19.8 mg.L ⁻¹ (no)
[Cs ⁺]	3.63 µg.L ⁻¹	3.8 µg.L ⁻¹ (no)	1.34 µg.L ⁻¹ (6 %)	1.29 µg.L ⁻¹ (27 %)	0.85µg.L ⁻¹ (15 %)	2.05 µg.L ⁻¹ (65 %)
[La ³⁺]	0.34 µg.L ⁻¹	0.2 µg.L ⁻¹ (~ 85 %)	0.08 µg.L ⁻¹ (~ 35 %)	3.11 µg.L ⁻¹ (~100 %)	3.19 µg.L ⁻¹ (~ 85 %)	41.22 µg.L ⁻¹ (~ 100%)
[U]	0.71 µg.L ⁻¹	0.28 µg.L ⁻¹ (no)	31.3 µg.L ⁻¹ (3 %)	53.9 µg.L ⁻¹ (18 %)	39.0 µg.L ⁻¹ (14 %)	43.5µg.L ⁻¹ (25 %)
[Al ³⁺]		37.7 µg.L ⁻¹ (~ 100 %)	135 µg.L ⁻¹ (100 %)	1355 µg.L ⁻¹ (100 %)	1415µg.L ⁻¹ (100 %)	1483 µg.L ⁻¹ (100 %)
[Na ⁺]	1.76 g.L ⁻¹	1.2 g.L ⁻¹	n.d.	n.d.	1.4 g.L ⁻¹ (no)	1.5 g.L ⁻¹ (no)
[Cl]	5.01 g.L ⁻¹	3.9 g.L ⁻¹	n.d.	n.d.	n.d.	n.d.
[Si]	5.2 mg.L ⁻¹	6.3 mg.L ⁻¹	n.d.	n.d.	8.7 mg.L ⁻¹ (32 %)	45.8 mg.L ⁻¹ (95 %)

a) Sieved fraction of raw FFM has been washed several times with ÄGW prior a final equilibration step in a ratio solid (g) to liquid (mL) 1:4 (see 2.c.), the element composition determination consists on the regular analysis of the ÄGW in contact with this FFM by ICP-MS

b) Natural ÄGW analysis from Äspö Hard Rock Laboratory, SKB Technical Report TR-00-07, March 2000

c) KIT-INE, ICP-MS/AES analysis; the water is sampled from the barrel and stored in the glove box

d) Calculated from supernatant analysis after ultracentrifugation, 2h at ~ 500 000 g; n.d.: not determined

e) the 2L bottle is shaken in the glove box before sampling

6.3.1.2 MX80-bentonite colloids

The raw material was provided in 2004 by SKB. It was crushed and the < 63 µm fraction was isolated after sieving. Delamination of the clay was achieved by washing the isolated fraction with 1M NaCl solution during 1 week. Smaller-sized colloids were collected after 4 centrifugation-collection-resuspension cycles in ultra pure water. The final pH of the colloidal stock solution was pH 8.5. The colloidal concentration was calculated from the Al concentration measured by ICP-MS (Perkin-Elmer 6000) using the Al mass fraction based on the structural formula of the MX80 bentonite ($\text{Na}_{0.3}(\text{Al}_{1.55}\text{Fe}_{0.21}\text{Mg}_{0.24})(\text{Si}_{3.96}\text{Al}_{0.04})\text{O}_{10}(\text{OH})_2$). The element concentrations of the colloid stock solution are presented in Table 6-6. Considering an Al content in the clay of 11.5 mass%, the final concentration of colloids is $(502 \pm 44) \text{ mg.L}^{-1}$.

Table 6-6: Al, Mg, Si, Fe, Ca contents of the MX80-colloid stock solution as determined from 15 ICP-MS measurements.

Element concentration (mg.L^{-1})	
Al	57.8 ± 5.1
Mg	9.5 ± 0.8
Si	174.2 ± 14.4
Fe	15.3 ± 1.2
Ca	3.0 ± 0.2

The colloid mineralogy was analysed by XRD. Samples were prepared by pipetting a slurry of the samples on a oriented silicon wafer and drying it at room temperature for a few hours to obtain an air-dried specimen. The oriented clay slides were exposed to ethylene glycol vapor at 60° C for 12 h and XRD scans were recorded on a Bruker D8 diffractometer (Cu radiation at 40 kV and 40 mA). The measuring range was from 2 to 50° θ with a step size of 0.04 and 6 s counting time. The divergence slit, the two Soller slits, the antiscatter slit, and the resolution slit were 0.5, 2.3, 2.3, 0.5, and 0.06, respectively. XRD characterization showed pure montmorillonite.

AFM is performed by a Veeco Dimension 3100 (Veeco Metrology, Santa Barbara, USA). Bentonite colloids are adsorbed on a freshly cleaved mica sheet, thoroughly washed with ultra pure water and dried at 40 °C in an oven. Samples are measured in tapping-mode using silicon probes (RTESP from Veeco; nominal radius of curvature < 10 nm; nominal spring constant 40 N/m; nominal resonance frequency 300 kHz). The Veeco AFM software is applied for image processing and particle diameters are calculated from particle areas assuming a round shape. AFM imaging (Figure 6-8) shows the presence of a size distribution with small colloids in the size range around ~30 nm and larger platelet-like particles ~180 nm which might be aggregates of the smallest ones.

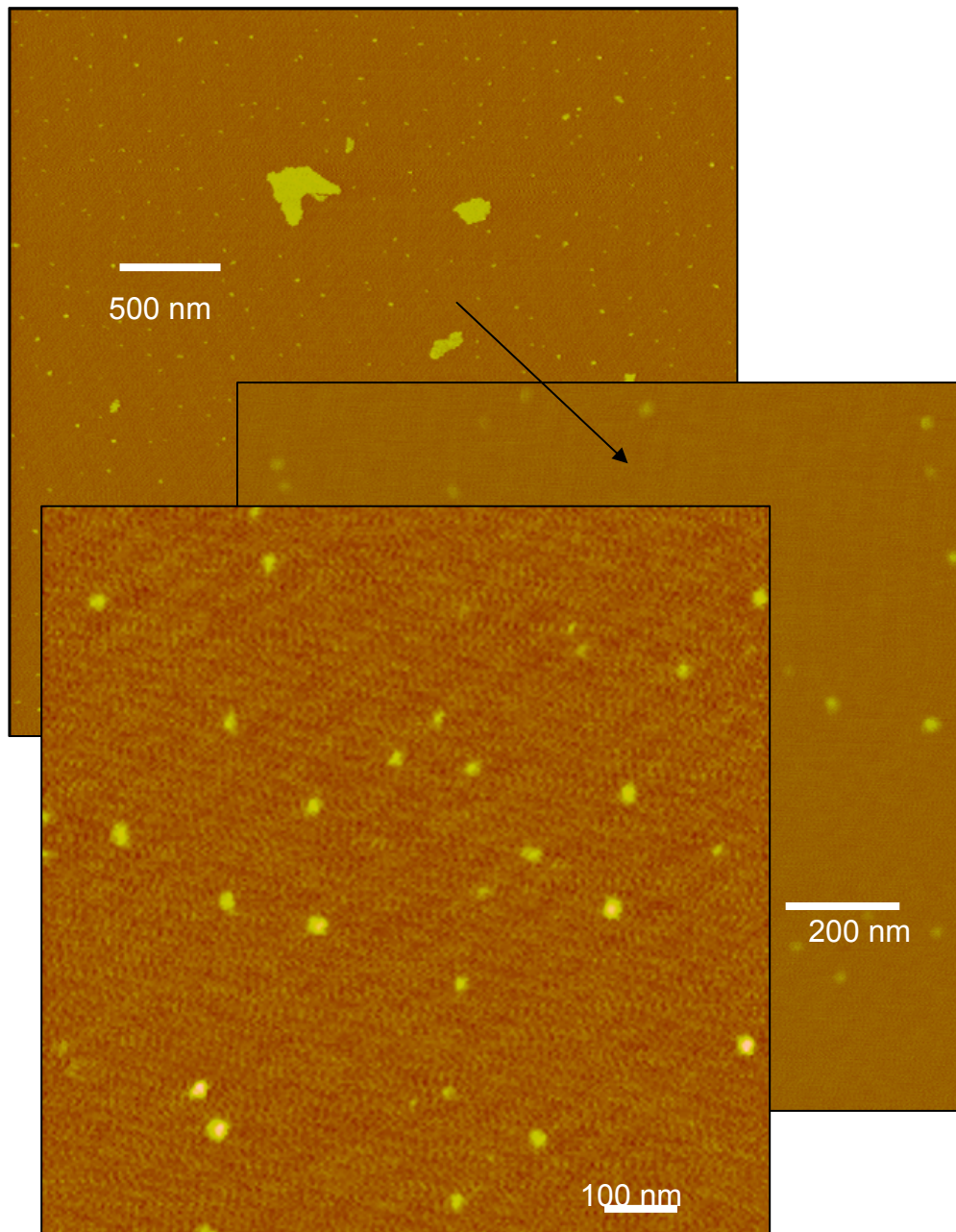


Figure 6-8: Tapping mode AFM of a dry MX80-bentonite colloidal solution sample

6.3.1.3 Fracture filling material (FFM)

This material was taken at the Äspö-HRL. The composition of this material is given in details in [175]. From X-rays diffraction diagram analysis, the main phases are identified as being quartz and microcline while albite and sepolite phases have been detected additionally. The material was crushed and sieved and a size fraction of 2 to 8 mm was isolated and washed several times with ÄGW under anaerobic conditions (Ar). For sorption experiments, the conditioned material was contacted with fresh ÄGW in a solid to liquid ratio 1:4 (g.mL⁻¹) in a

glove box (Ar/1%CO₂). The influence of the FFM on the initial ÄGW element concentrations is monitored by ICP-MS measurements (see Table 6-5).

6.3.1.4 Fulvic acid (FA)

The fulvic acid (FA) used is isolated from a natural deep groundwater (139 m depth) located at Gorleben in the Northern German Plain (Lower Saxony, GoHy-573) and purified (as described in [176]). A stock solution is obtained by dissolving a small amount of this product in NaOH 0.1 M (ultrapure, Merck) and is then subsequently diluted with ultrapure deionized water (MilliQ plus, Millipore). The final pH is (7.7 ± 0.1). The dissolved organic carbon content is measured with a TOC analyzer (TOC-5000, Shimadzu). The measured DOC = (832 ± 18) mg.L⁻¹ can be converted to a fulvic acid concentration by considering the carbon mass fraction of 54.1 ± 0.1 mass % as indicated in [176]. The stock solution containing a FA concentration of 1538 mg.L⁻¹ is then stored at 4°C in a fridge prior to use.

6.3.1.5 Stability measurements

According to the experimental protocol described in [26, 177, 178] the colloid stability ratios (W) were calculated from the coagulation rates of the bentonite MX80 colloids. The stability ratio is defined as the ratio of fast to slow aggregation rates (k_a), $W = k_{a,fast} / k_a$, and is inversely proportional to the collision efficiency in colloid interaction. It could then be defined as the ratio of the coagulation rates in the fast and slow aggregation regime, namely the slopes $d[\ln(d_h)]/dt$ obtained in both regimes, where d_h is the hydrodynamic particle diameter measured by light scattering. The colloid stability ratios (W) are measured as a function of the ionic strength and pH by Photon Correlation Spectroscopy (PCS) using a homodyne (single-beam) ZetaPlus system (Brookhaven Inc.) equipped with a 50mW solid-state laser ($\lambda_{em} = 632\text{nm}$). After vigorous shaking, an aliquot of the MX80-bentonite colloid stock solution is first diluted in ultra pure water in a disposable plastic cuvette (Plastic Brand) and the size is registered by PCS. The initial intensity-weighted mean colloid size was at (220 ± 30) nm. Size evolution is then recorded after the simultaneous addition of concentrated electrolyte aliquots (NaCl 2 M or CaCl₂ 2 M) and NaOH or HCl to adjust the desired final ionic strength (from 0.01 M up to 1 M) and pH varying in the range 4-10. The pH cannot be monitored directly in the PCS cell and thus is monitored continuously during an agglomeration measurement in a second suspension of identical composition placed in a second cuvette. Additional Laser-Induced Breakdown Detection (LIBD) measurements of suspensions after coagulation and sedimentation were performed after more than 5 months. LIBD is a very sensitive method for the direct detection of colloids at very low concentration level. The method is based on the focusing of a pulsed laser beam in a cuvette containing the suspension to be analyzed. At high power density a dielectric breakdown occurs and then a plasma is generated which is detected via the produced shock wave. As the power density necessary to initiate a plasma in a solid is lower than for a liquid, the plasma is generated almost exclusively in colloids, as long as the laser pulse power density does not exceed the breakdown threshold of the solvent. The number of breakdown events detected per number of laser shots results in a breakdown probability (BDP), which is dependent on both particle size and concentration. Detailed descriptions of the LIBD are available in the literature [50, 51, 179, 180]. The spatial distribution of the individual breakdown events within the focal area of the laser beam depends on the colloid diameter and is independent of the colloid concentration. The width of the breakdown volume along the laser beam axis (effective focal length, $L_z(P)$), therefore, can be taken as a measure for the mean colloid size. $L_z(P)$ is defined as the length in which 95% of the plasma events are found. The system is calibrated as seen in Figure 6-9 by analyzing polystyrene reference colloids of well-known mean diameters (Duke Scientific Corporation) for which the $L_z(P)$ is determined by recording

the light emission of single plasmas by a microscope charge-coupled device (CCD) camera system. More details on the calibration procedure can be found in [181].

Nevertheless, the value of the mean particle diameter ($d_{LZ(P)}$) determined via this calibration method has to be corrected taking into account the LIBD theory and in particular the fact that the critical laser power density (or breakdown threshold) required to induce a breakdown depends on the colloid material and shape [179, 181]. The relative breakdown thresholds $P_{A,crit.}$ for polystyrene lattices, thoriasol, alumina and silica are reported to be 1-1.1-1.7-1.8, respectively. This value is not yet determined for bentonite particles due to their nonavailability as monodisperse particles. The value is then assumed to be that of alumina and silica. Considering the eq 2 of reference [179]: $P_{A,crit.} \cdot A_T = \text{constant}$, where A_T corresponds to the maximum particle cross section, $A_T = \pi r^2$, then $A_{T(bentonite)} = 1.8 A_{T(polystyrene)}$. The mean particle diameter corrected is then $d_{corr} \sim 1.8^{1/2} d_{LZ(P)} \sim 1.34 d_{LZ(P)}$ [51].

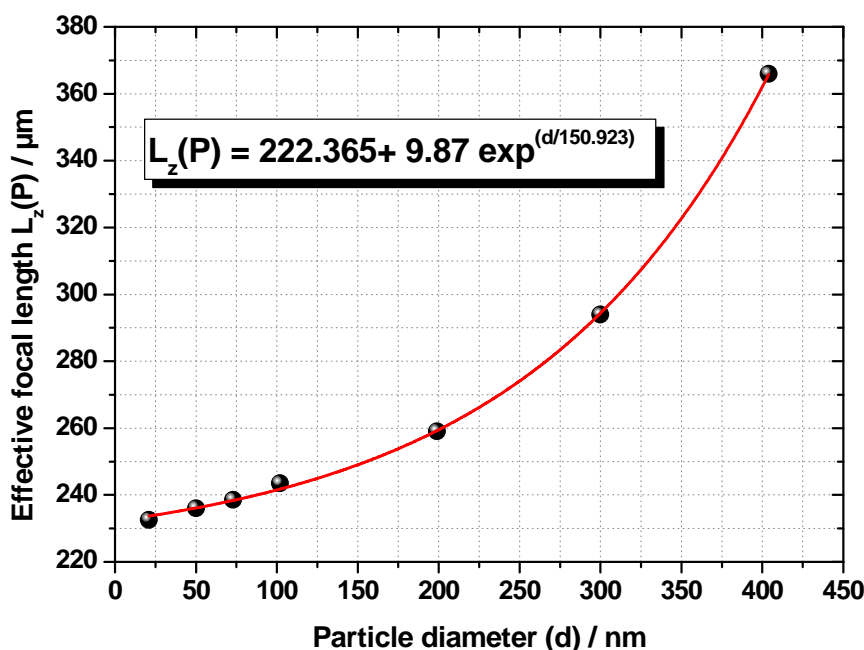


Figure 6-9: Effective focal length ($L_z(P)$) determined by analyzing the position of 5000 single plasma events in the laser beam axis using a microscope CCD camera. Commercial polystyrene reference colloid dispersions (DUKE Scientific) with different colloid diameters (21, 50, 73, 102, 199, 300, 404 nm) are diluted with ultrapure water to the required colloid concentration.

Solutions analysed by LIBD consist of mixtures of MX80-bentonite colloids (1.2 mg.L⁻¹ or 0.12 mg.L⁻¹ at pH=7.5) in CaCl₂ solution of the following ionic strengths: 1M, 0.5M, 0.2M, 0.1M, 0.01M, 0.001M and in presence or absence of fulvic acid. A summarizing list of all samples is given on Table 3. Measurements were performed on 2-3 mL aliquots of the uppermost part of the supernatants by transferring the sample in a quartz cuvette for LIBD analysis.

Table 6-7: Solutions preparation for LIBD analysis, a) IS: ionic strength , b) CT: contact time between MX80 bentonite colloids and FA.

Solution (Volume total: 30 mL, stored in the laboratory)	MX80- bentonite colloids (mg.L ⁻¹)	IS ^{a)} due to CaCl ₂ added (M)	FA-573 (DOC in mg.L ⁻¹)	MX80/FA CT ^{b)} prior to IS ^{a)} increase (Months)	Initial adjusted pH 7.5 ± 0.2
					pH before measurement
F	1.2	0.001	-	-	6.7 ± 0.3
A	1.2	0.01	-	-	6.7 ± 0.3
B	1.2	0.1	-	-	6.7 ± 0.2
E	1.2	0.2	-	-	6.5 ± 0.4
C	1.2	0.5	-	-	6.4 ± 0.1
D	1.2	1	-	-	6.7 ± 0.2
MX80-C1	1.2	0.2	-	-	6.3 ± 0.2
MX80-C2	0.12	0.2	-	-	6.6 ± 0.2
FAE1	1.2	0.2	416.1	-	6.2 ± 0.3
FAE2	1.2	0.2	41.61	-	6.5 ± 0.1
FAE3	1.2	0.2	4.16	-	6.3 ± 0.3
FAE4	1.2	0.2	0.42	-	6.4 ± 0.2
FAE5	0.12	0.2	41.61	-	6.4 ± 0.1
FAE6	0.12	0.2	4.16	-	6.4 ± 0.1
FAE7	0.12	0.2	0.42	-	6.6 ± 0.2
FA1	1.2	0.2	416.1	5	6.6 ± 0.2
FA2	1.2	0.2	41.61	5	6.6 ± 0.2
FA3	1.2	0.2	4.16	5	6.4 ± 0.2
FA4	1.2	0.2	0.42	5	6.3 ± 0.2
FA5	0.12	0.2	41.61	5	6.4 ± 0.2
FA6	0.12	0.2	4.16	5	6.2 ± 0.2
FA7	0.12	0.2	0.42	5	6.4 ± 0.2

6.3.1.6 Batch sorption experiments

Sorption of radionuclides to colloids and fracture filling material (FFM) and complexation by fulvic acids have been studied in five batch type experiments.

- **Set 1:** ÄGW (TRUE-1 site, Feature A, KXTT4) has been spiked with radionuclides: Sr⁹⁰(2.2 10⁻⁹ M), Cs¹³⁷(2.3 10⁻⁹ M), Am²⁴¹(1.10⁻¹⁰ M), Np²³⁷(1.06 10⁻⁸ M), U²³³(2.3 10⁻⁸ M) and Pu²⁴⁴(1.07 10⁻⁹ M). These concentrations have been chosen to remain below the solubility limits of the elements at the final pH of (7.5 ± 0.2) especially for Am(III) and Pu(IV) as given in [175].
- **Set 2:** This solution is prepared as in Set 1, but MX80 bentonite colloids (2.4 mg.L⁻¹) have been added.
- **Set 3:** Pre-conditioned fracture filling material contacted with fresh ÄGW (solid-liquid ratio 1:4 g.mL⁻¹). Radionuclides are added at concentrations as described in Set 1.

- **Set 4:** For this set of experiments a FFM suspension as prepared for Set 3 experiments has been spiked with MX80 bentonite colloids (2.4 mg.L⁻¹) and fulvic acid (DOC: ~ 5 mg.L⁻¹) prior to radionuclide addition.
- **Set 5:** ÄGW has been spiked in a first step with fulvic acid (DOC: ~ 5 mg.L⁻¹). In order to complete the **Set 4** of experiments, MX80 bentonite colloids (2.4 mg.L⁻¹), pre-conditioned fracture filling material (see § 1.f.) contacted with fresh ÄGW (solid-liquid ratio 1:4 g.mL⁻¹), Am²⁴¹(1.10⁻¹⁰ M), mixture of Np²³⁷(1.06 10⁻⁸ M), U²³³(2.3 10⁻⁸ M) and Pu²⁴⁴(1.07 10⁻⁹ M) are added separately or all together to this fulvic acid-spiked ÄGW.

After their preparation, the different samples are not shaken anymore and are let to sediment. Time dependent evolution of the radionuclide, bentonite colloid and groundwater element concentrations have been followed over 1 year by direct analysis of the supernatant and sample aliquots after ultracentrifugation (2 h at ~ 500 000 g, XL90 Beckmann). Sr⁹⁰, Cs¹³⁷, Am²⁴¹ concentrations were measured by LSC and data treated with the SPECWORK software, while Np²³⁷, U²³³ and Pu²⁴⁴ concentrations were determined by ICP-MS (Elan 6100, Perkin Elmer). Evolution of the fulvic acid concentration in ÄGW has been measured by UV-Vis spectrophotometry (Cary, Varian).

6.3.2 Results and discussion

6.3.2.1 Characterisation of ÄGW

6.3.2.1.1 Storage in barrel

ICP-MS/AES results. After the first sampling, the result of ICP-MS/AES analysis performed for the groundwater stored in the barrel for two years (Table 6-3, column 4) is not significantly different from the analysis given by SKB (Table 6-3, column 2). The water shows a high salinity with an ionic strength around 0.2 M dominated by CaCl₂. LIBD analysis reveals, surprisingly for the highly saline medium, the presence of colloidal species in the natural groundwater as indicated by a BDP of 0.8. Additional analysis after ultracentrifugation confirms this result showing that ~ 34 % of the Fe, ~ 100 % of the Al and ~ 85 % of the lanthanides are under colloidal form while naturally present Cs⁺, Sr²⁺ and U do not reveal colloidal behavior. One year later, the ICP-MS/AES analysis performed after a new sampling in the barrel shows that the Fe and La³⁺ concentrations reach their detection limit. The instability of the colloids detected by LIBD and ultracentrifugation points to their origin as a consequence of oxygen intrusion, during or after the sample transfer. The same conclusions could be drawn from the analysis of a groundwater sample collected in-situ during the barrel filling but measured only when the field team came back to the INE institute (See Table 6-3, column 3). In this case, the Fe and La³⁺ concentrations were at their detection limit, indicating a sedimentation of the Fe/La associated colloids or precipitates formed in contact with oxygen. In addition, the redox potential value measured in-situ is clearly lower than the one obtained after storage in the barrel two years later, indicating once more a possible intrusion of oxygen.

Geochemical modeling (Geochemist's Workbench 6.04). The original water was at 14 °C. The analysis of this water corresponds to RT and a redox potential of about -50 mV can be assumed for this water. A calculation in which the redox potential is changed to a value of about 60 mV, which is measured after several years, and which then apparently stays constant, does not indicate severe changes in the speciation. In all cases, solid Fe and Al

containing phases are oversaturated and this agrees with the fact that part of the iron and aluminium is found in colloidal form. Also the fact that lanthanides are found in colloidal form concurs with this finding, since they are known to strongly adsorb to iron and aluminium minerals. The nature of the minerals is not known. Also they may have already been present in the original sample. The original water is according to the calculations slightly oversaturated to such solids, which it is known to have been in contact with (albite, quartz, microcline). Another solid mentioned in this context, sepiolite, was strongly undersaturated according to the calculations. Since the temperature in the groundwater is different from that of the analysis (affecting pH, pe), this indicates that the geochemical calculations reproduce the observations fairly well.

6.3.2.1.2 Influence of oxygen contact

In order to evidence the influence of oxygen contact on groundwater chemistry, ~130 ml of the groundwater have been taken out from the barrel after the first sampling, placed in a PE-container with a magnetic stirrer and left in contact with air. After 3-4 days, the magnetic stirrer became colored and brown entities were appearing, sticking on the container walls. SEM analysis of these entities reveals iron associated calcite precipitates. Additional ICP-MS analysis performed before and after filtration (filter pore size: 100 nm), as seen on Table 4, leads to the conclusion that iron colloids with sizes > 100 nm are formed which scavenge trace elements such as lanthanides. Similar observations have already been reported in a previous report [182]. The same experiment repeated one year after does not lead to the same observation. This confirms the ICP-AES/MS results which lead to the conclusion of a precipitation of the iron due to oxygen intrusion in the barrel during the first sampling.

This observation points out the necessity of controlling the geochemical conditions when planning in-situ radionuclide migration experiments.

Table 6-8: Effect of air contact and pressure release on the element composition evolution of ÄGW (TRUE-1 site, Feature A, KXTT4). The supernatant is analyzed directly or after additional 100 nm filtration. Only iron and lanthanides concentration are significantly affected (La represents hereafter the lanthanides); n.d.: no more measurable/detectable.

Concentration in $\mu\text{g.L}^{-1}$	Initial	After 3 days No filtration	After 3 days 100 nm filtration	After 10 days No filtration	After 10 days 100 nm filtration
[Fe ^{2+,3+}]	760	4.03	n.d.	n.d.	n.d.
[La ³⁺]	0.2	0.02	0.009	0.008	0.01

6.3.2.1.3 Storage under anoxic conditions (glove box, Ar/1%CO₂)

ICP-MS/AES results. The evolution of ÄGW element composition during storage in glove box under anoxic conditions is quite similar to those observed in the barrel: Fe, La and Al concentrations tend to their detection limit (see Table 6-4, column 6). An additional decrease of the Mn concentration is observed. The formation of colloidal/precipitates phases is confirmed by sample analysis after vigorous shaking of the water container in the glove box (see Table 6-4, last column). In this case, much higher concentration of Fe and Al are recovered.

SEM-EDX pictures analysis. The visible “white” precipitates discovered in the water samples which were kept in the glove box were collected and SEM pictures recorded. The precipitates were identified by SEM to correspond to calcite, gibbsite, illite, chlorite as seen

respectively on Figure 3 a-b-c-d below even if the identifications of the last two phases is subject to uncertainties.

Geochemical modeling (Geochemist's Workbench 6.04). When the precited Äspö water is put into the glovebox, where an atmosphere of 1% carbon dioxide has a potential effect on the geochemistry of the water, a decrease of the pH is measured, whereas the redox-potential remains at about 60 mV. The decrease in pH can be followed in the calculation assuming that the carbon dioxide partial pressure is somewhere between zero and 1 %. A partial pressure of about 0.7% yields a pH of about 7. It is not clear what the actual partial pressure of carbon dioxide in the closed tubes is. Since they are opened for measurements and then closed again, it can only be assumed that equilibrium is achieved. It is also possible that a smaller partial pressure is active in the test tubes as the calculations suggest. The observed drop in pH can be explained by the increased partial pressure of carbon dioxide in the glove box. In these calculations calcite is allowed to precipitate. In the water samples which were kept in the glove box, white precipitates could be discovered in the test tubes. They developed with time. The precipitates were identified by SEM to correspond to calcite, gypsum, illite and chlorite. The geochemical calculations for these conditions show that illite is strongly oversaturated. Calcite is saturated, since it is allowed to precipitate, which the calculations actually show. Also some chlorite minerals are oversaturated according to the calculations whereas gypsum is slightly undersaturated. Again the calculations agree fairly well with the observations given the uncertainties in the boundary conditions. Even in these calculations Fe and Al containing phases are oversaturated, which agrees with the measurements for these elements. The Fe containing solid phases (among which ferrihydrite is the most probable to form) may adsorb or incorporate An(III). This is discussed later.

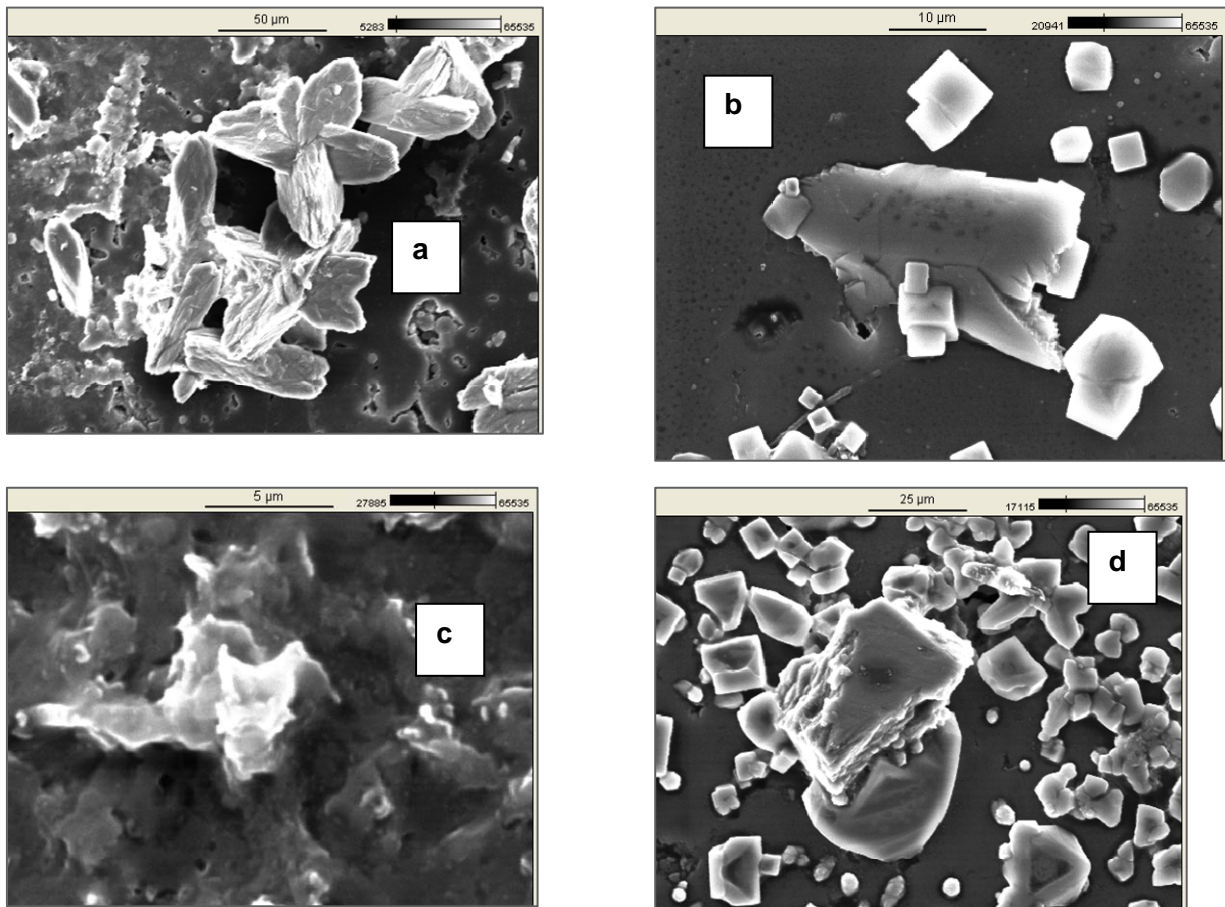


Figure 6-10: SEM pictures of “white” visible precipitates developing with time in the water samples kept in the glove box.

6.3.2.1.4 Storage in contact with fracture filling material (FFM) under anoxic conditions (glove box, Ar/1%CO₂)

Contact with FFM, as seen in Table 6-4, does not cause a major concentration change of the groundwater main components (Ca, Mg, Na, pH) indicating an overall equilibrium state of the solid/liquid system. However, the clear increase of Al, La and Fe concentrations, which can be removed by centrifugation indicates the existence of particulate and colloidal matter in the FFM, which can be mobilized after agitation of the sample. The water analysis after a vigorous shaking definitely confirms this assumption with a drastic increase of Fe, Al, La and even Mg concentrations, element present mainly under colloidal form. Cs concentration is clearly reduced by a factor of ~ 4 over one year by sorption to the solid, on fractions which can be mobilized as shown from the result obtained after shaking. The release of uranium from the rock agrees with recent observations [183] showing a mobilization of natural uranium. This has been explained by the presence of U(VI) in the solid due to air contact of the sample during sampling and storage.

6.3.2.2 MX80 bentonite colloid stability

6.3.2.2.1 Stability ratio as a function of ionic strength (IS) and pH

To test the feasibility of the protocol described in chapter 6.3.1, a first experiment using carboxylated latex particle (105 nm diameter, Magsphere, USA) has been conducted. The results are presented in Figure 6-11 showing clearly, as expected from [177], the coagulation of the 105 nm carboxylated latex colloids. The coagulation rate as shown in Figure 6-11 is a function of the initial colloid concentration with faster coagulation rates at higher colloid concentration as a result of the increased colloid collision frequency.

Colloid stability ratios (W) of the bentonite MX80 colloids, calculated from the coagulation rates measured by PCS as a function of the ionic strength varied from 0.01 M up to 1 M in NaCl or CaCl₂ solution in the pH range 4-10 are presented in

Figure 6-12. The results indicate clearly that at the high ionic strength of the Äspö groundwater (IS ~ 0.2 M), the stability ratio equals to 1 in all systems (NaCl, CaCl₂, and in MgCl₂ – data for the latter system are not presented here), which means that the colloids are instable and coagulation is purely diffusion controlled.

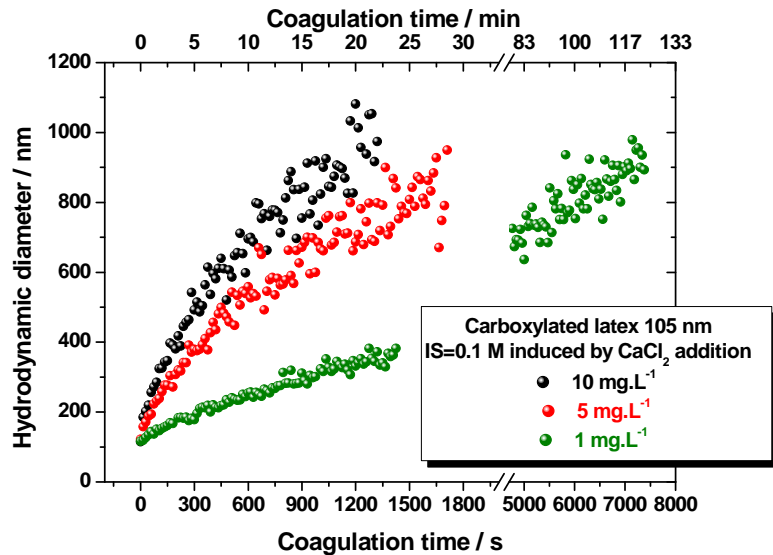


Figure 6-11: Variation of the hydrodynamic diameter as a function of time for standard carboxylated latex particles (105 nm diameter, Magsphere, USA) in 0.1 M ionic strength medium (CaCl_2) at $\text{pH} > \text{pH}_{\text{pzc}}$.

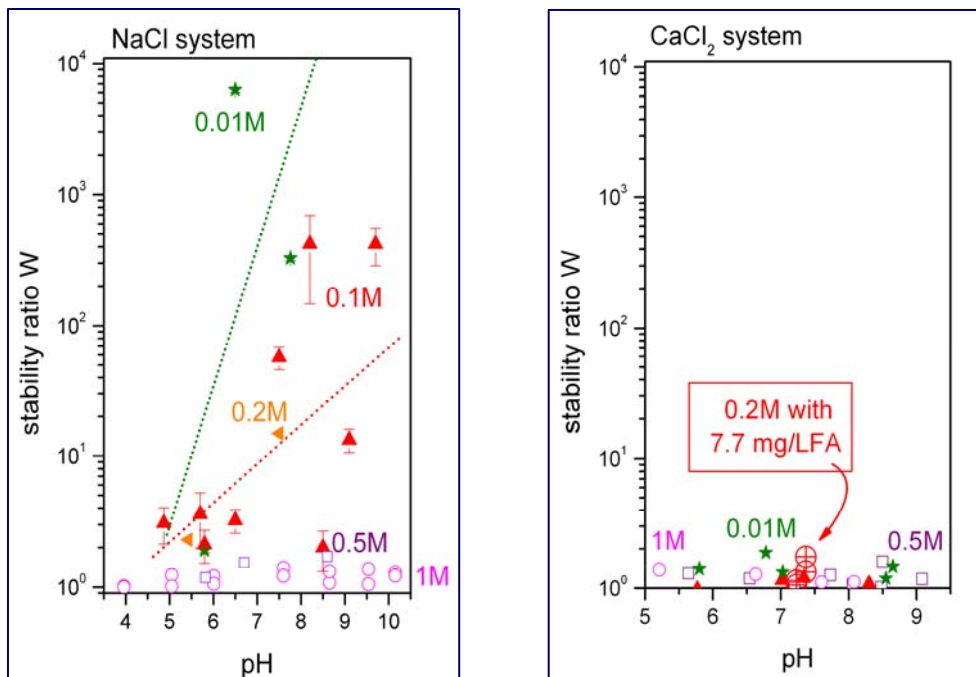


Figure 6-12: Stability ratio of the MX80-bentonite colloids ($1.2 \text{ mg}\cdot\text{L}^{-1}$) as a function of pH and ionic strength induced by addition of NaCl or CaCl_2 . The presence of natural dissolved organic matter is simulated by addition of FA.

LIBD measurements of supernatant were performed after 5 months agglomeration/sedimentation time. Dispersions contain $1.2 \text{ mg}\cdot\text{L}^{-1}$ MX80-bentonite colloids at a pH adjusted to (7.5 ± 0.2) . With time, the pH in all these solutions decreased down to 6.6 ± 0.3 . SEM analysis proves that the precipitate is, as expected, composed of bentonite colloid agglomerates (see Figure 6-13) partially also associated with carbonate phases probably

present as impurity in the clay (Figure 6-13e) or formed with time due to air contact. The BDP evolution as measured by LIBD for all the supernatants is reported in Figure 6-14.

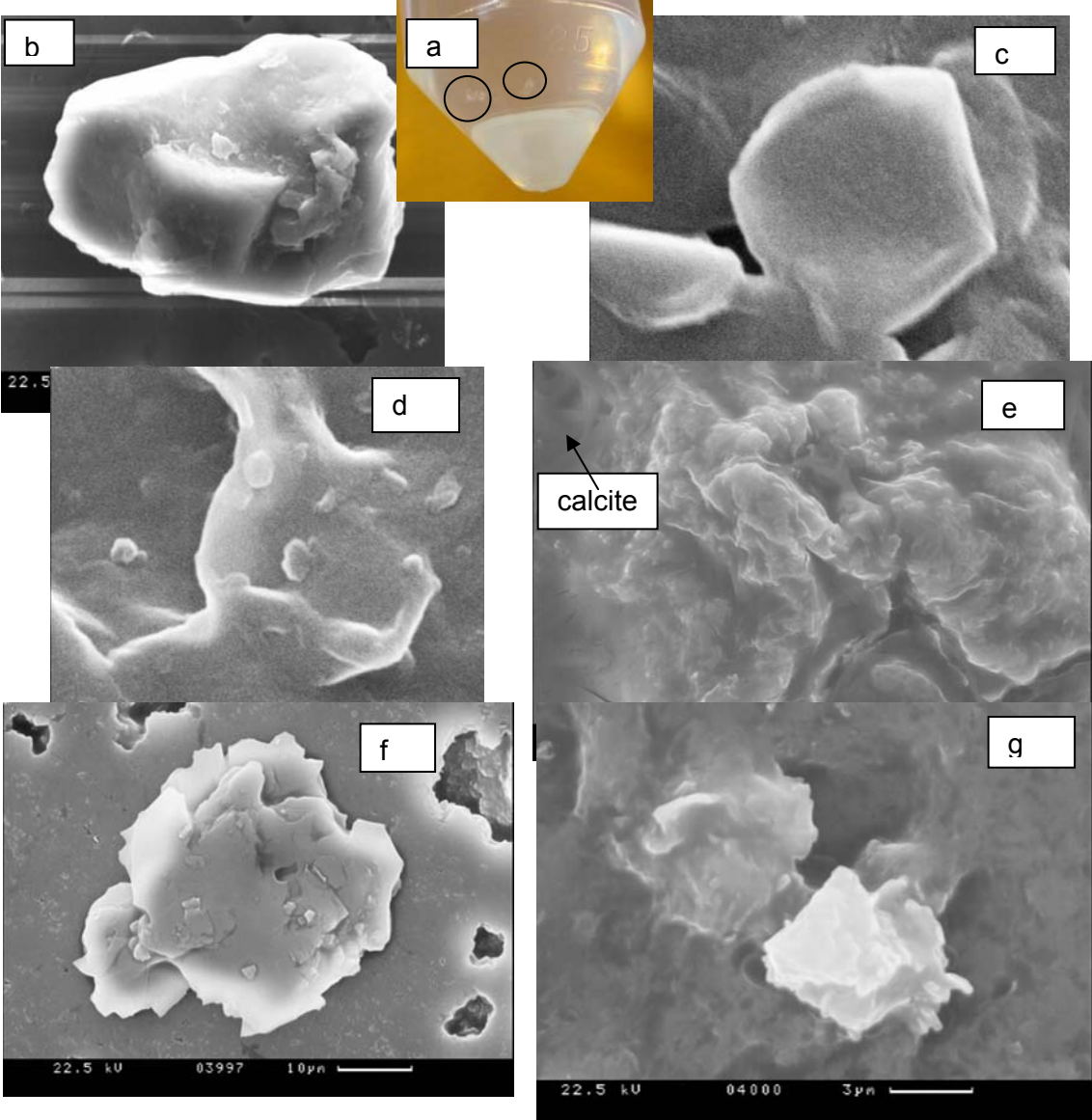


Figure 6-13: a) Example of colloidal flocculate present in all solutions; b-c-d) SEM pictures of the colloidal precipitates seen in solution A (IS=0.01M); e) and f) extracted from solution B (IS=0.1 M), g) extracted from solution E (IS=0.2 M)

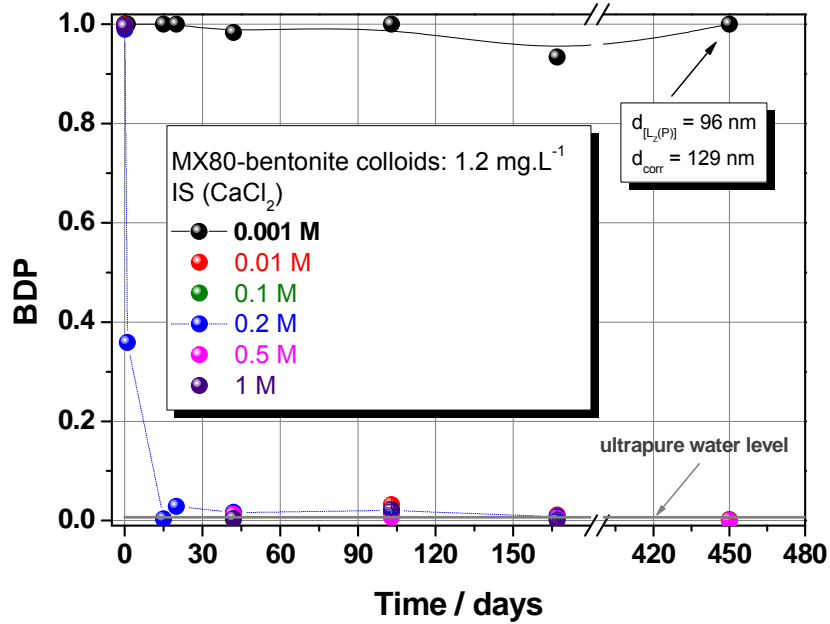


Figure 6-14: a) Supernatant BDP evolution for solution A, B, C, D, E, F (see Table 6-7 for details).

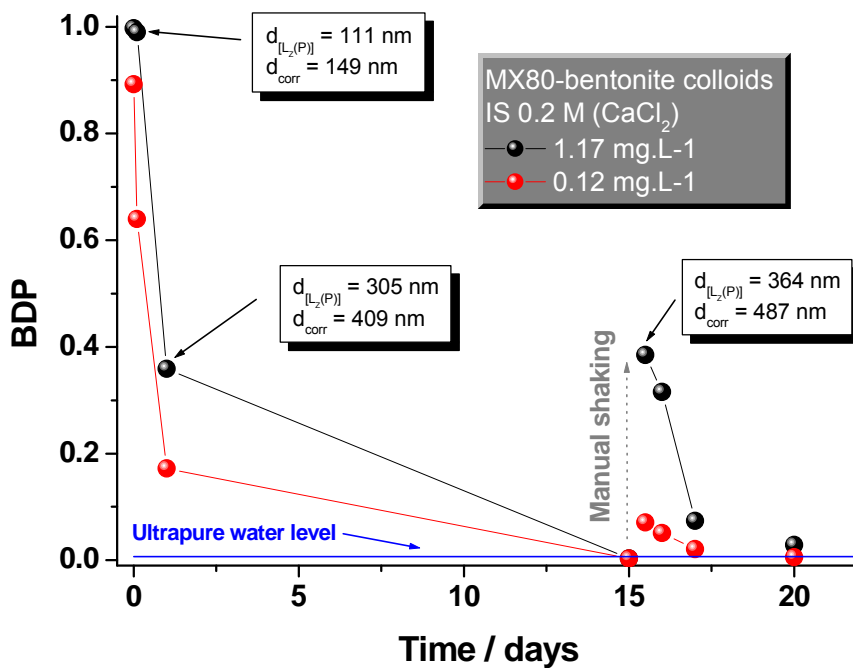


Figure 6-15: b) Effect of mechanical shaking after coagulation, $d_{Lz(P)}$ is the diameter value determined directly from the calibration (see Figure 6-9) when d_{corr} is the corrected diameter value obtained after taking into account the material dependence for LIBD measurement (see text and [51]).

The clear decrease of the BDP values starting from ~ 0.98 down to a BDP value obtained for the ultra pure water (~ 0.007 corresponding to a colloid concentration < 2 ppb) for solutions with ionic strengths $> 0.01M$ confirms the complete instability of the bentonite colloids. Even vigorous shaking of an agglomerated colloid suspension (1.2 and 0.12 $mg.L^{-1}$ MX80-bentonite colloids; ionic strength: 0.2 M) resuspends colloidal matter only for a short time

period (see Figure 6-15). BPD values increase from 0.003 up to 0.4 and 0.07, respectively, and then rapidly drop to the detection limit. LIBD measurements reveal that the colloids appear to be stable only at low ionic strength of 0.001 M for at least the observation period of 15 months in the CaCl₂ system. As indicated in Figure 6-15, the initial MX80 colloid diameter determined from LIBD ($d_{\text{corr}}=149$ nm) is smaller as the one determined by PCS (220 ± 30) nm. This is a consequence of the intrinsic sensitivity differences of both methods as already discussed in detail in [51]. With both methods, a consistent increase of the MX80 colloid size up to ~ 500 nm as a function of time is detected.

6.3.2.2.2 Is the stability enhanced by the presence of organic matter?

Various Äspö groundwaters contain significant DOC concentrations. Fulvic acid dominates the organic component of organic matter in deep granite groundwater and was already isolated from various Äspö groundwaters [184]. The impact of a purified natural fulvic acid (Gohy 573) on colloid stability was studied in a first set of experiments. The coagulation rate of bentonite colloids ($1.2 \text{ mg}\cdot\text{L}^{-1}$) was determined in presence of fulvic acid (FA) at two different concentrations (77 and $7.7 \text{ mg}\cdot\text{L}^{-1}$), at an ionic strength of 0.2 M (CaCl₂ solution) and at $\text{pH} = 7.5 \pm 0.2$. As illustrated in Figure 6-12 (see the additional points marked with a cross in an open circle), no significant change in the measured stability ratios could be observed as compared to the experiments in absence of organic matter.

Again, additional LIBD measurements of the supernatant were performed over 15 months agglomeration/settling time (see Table 6-7 for details). The pH values decreased as already observed for experiments in absence of organic matter. The presence of organic matter, even at the high concentrations not relevant for Äspö conditions, does not stabilize the MX80-bentonite colloids. Figure 6-16a and Figure 6-16b show MX80-bentonite colloid behavior in presence of various FA concentrations. For $[\text{FA}] = 769 \text{ mg}\cdot\text{L}^{-1}$, the $\text{BDP}_{t=0}$ equals already zero as a result of the strong absorption of the laser beam due to the dark brown color of this solution. In the other solutions, the BDP values again drop to the value of ultrapure water. In addition, contacting bentonite colloids with fulvic acid for 5 months prior to the ionic strength adjustment does not lead to a higher colloidal stability. However, the presence of fulvic acid influences the sedimentation kinetics as seen in Figure 6-16c and Figure 6-16d depending on the organic matter: inorganic colloid ratio.

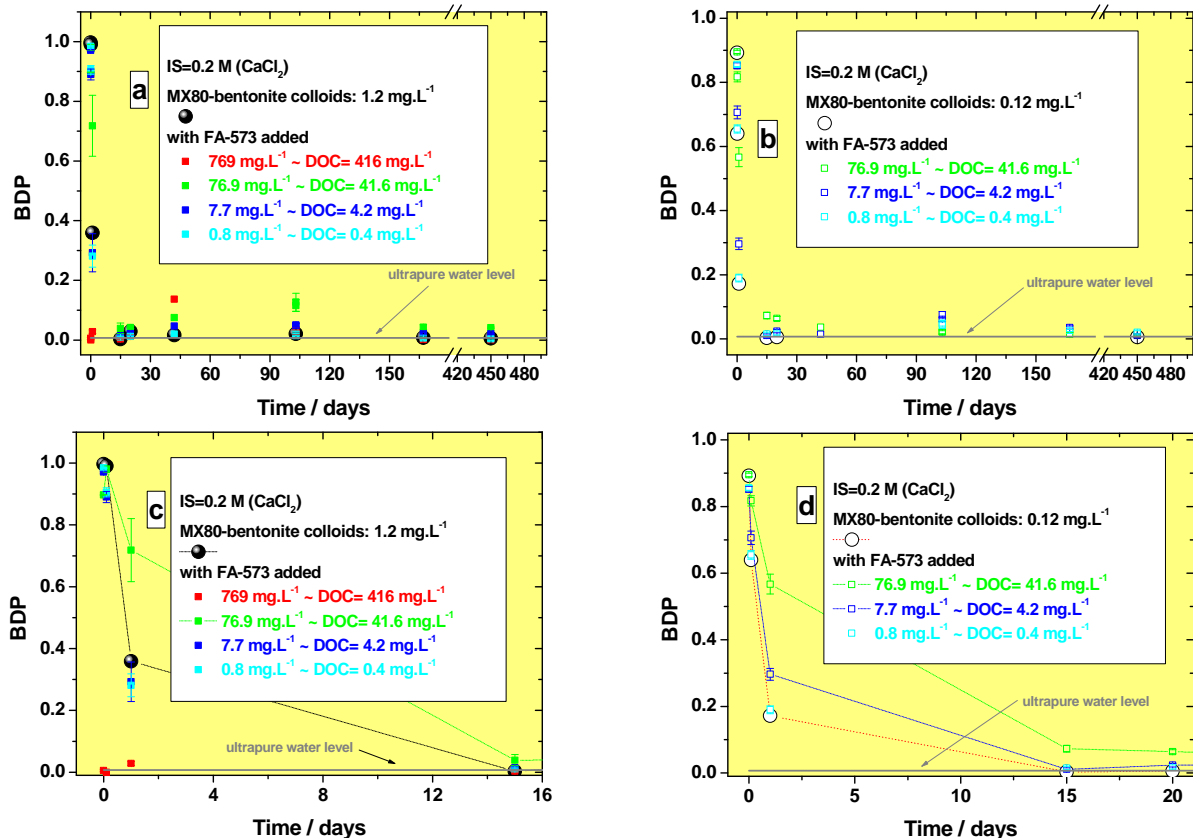


Figure 6-16: Influence of organic matter (FA-573) on the MX80-bentonite colloids stability and sedimentation kinetics. c) and d) zooms of a) and b) over the first days.

6.3.2.3 Radionuclide behavior in Äspö groundwater in presence of bentonite colloids, fracture filling material and fulvic acid.

In order to be complete, one has first to examine the behavior of the bentonite colloids and fulvic acid in ÄGW.

- **MX80-bentonite colloids behavior in ÄGW:** in agreement with the results of the colloid stability study (see chapter 6.3.2.2), the MX80 bentonite colloids are unstable under the KXTT4 groundwater conditions and sediment after 2 days. These conclusions are drawn from the analysis of the Al concentration evolution in the supernatants of the batch samples where bentonite colloids have been added, which are not explicitly plotted here. The concentration of Al as a main constituent of the aluminosilicate montmorillonite is taken as an indicator for the MX80 colloids. SEM analysis of the visible precipitates confirms this result as seen on Figure 6-17.

More surprisingly is the presence of bigger particles containing the montmorillonite main components (Si, Al, Mg...) formed under the conditions of the batches 2, 4 and 5 as observed by SEM and seen on Figure 6-18 in addition to white calcite precipitates.

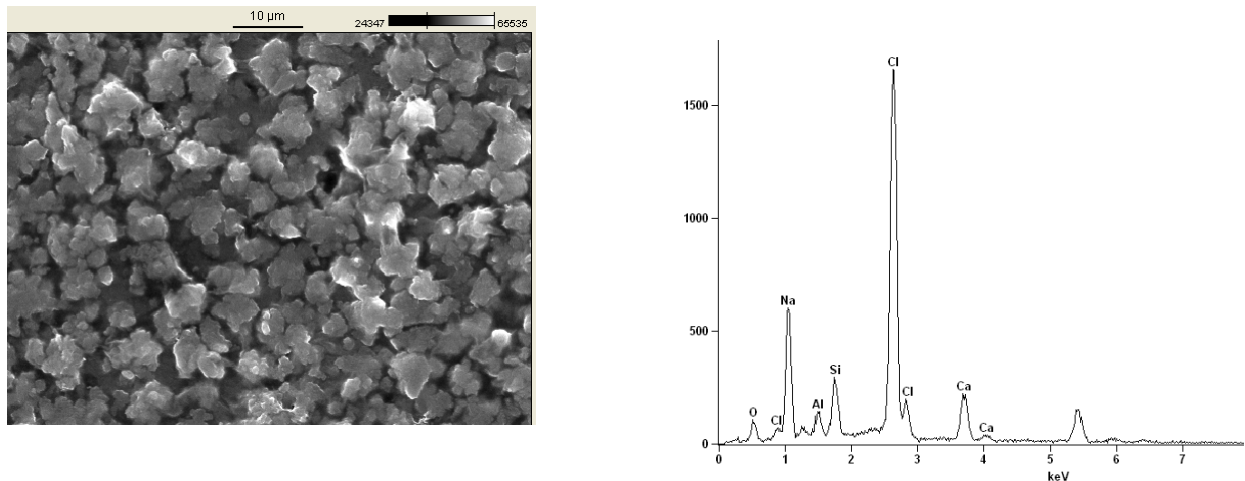


Figure 6-17: SEM-EDX analysis of the visible precipitates formed in batch 2 and 5, Al:Si ratio ~ 0.34

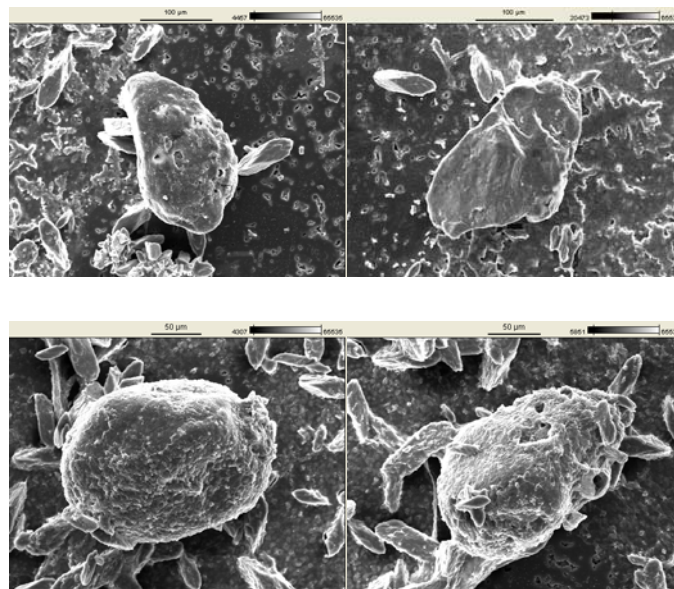


Figure 6-18: Additional SEM-EDX analysis on residual particles formed in batch 2, 4 and 5.

As well surprising is the observation of additional greyish precipitates formation which disappears very rapidly in contact with air, when a sample is taken outside from the glove box. The white and greyish precipitates were collected from a batch tube and after XRD-analysis clearly identified as calcite and probably green rust. This could explain the disappearance in contact with air, when the sample is taken outside from the glovebox. The question is still to know why the greyish precipitate appears only in batch samples where bentonite colloids have been added. This might result from the provision of iron present in the montmorillonite.

Geochemical modeling (Geochemist's Workbench 6.04). Here are detailed the modelling results of the batch samples where 2.4 mg/l of montmorillonite (Na) are added to the water in the glovebox. After addition the solution is clear. The addition causes a decrease of the pH to 6.5 and the appearance of an additional greyish solid to the white one, as said just before. Assuming a similar partial pressure as above the calculations yield a pH of about 6.6, the

redox potential always being fixed at the value of 62 mV (no experimental value is available). Again calcite is allowed to precipitate, which occurs (white precipitate seen by eye, confirmed by SEM and XRD analysis). Particles found by SEM (Figure 6-18) were estimated to correspond to montmorillonite, rather big particles containing Mg-Si and Mg-Ca-Na- Al-Si. Calculations show that a number of solids may correspond to such a composition. To further study this system from a geochemical point of view, calculations were carried out for ambient conditions in terms of carbon dioxide and redox potential, but no conclusive identification was possible. Additional experiments could be planned in the frame of a future project in order to identify in more details the different solids formed since it may be relevant to the system.

- FA-573 fulvic acids:** the evolution of the UV-Visible spectra has been followed by measuring over 8 months 3 mL of the supernatants of the batch samples from the Set 5. The results are presented on the Figure 6-19. The black curve corresponds to the KXTT4 ÄGW alone and does not show any variation with time. The other solutions could be classified in two groups: one which contains FFM and the other without. The group of solutions without FFM, namely FA-573 in ÄGW, FA-573+MX-80 in ÄGW, FA-573+Am²⁴¹ in ÄGW and FA-573+U²³³, Pu²⁴⁴, Np²³⁷ in ÄGW, does not show any variation in the UV-Visible spectra measured over the 8 months period analysis. On the opposite, the group of solutions containing some FFM, namely FA-573+FFM in ÄGW, FA-573+MX-80+FFM+Am²⁴¹ in ÄGW and FA-573+MX-80+FFM+U²³³, Pu²⁴⁴, Np²³⁷ in ÄGW shows a clear intensity signal decrease with time, interpreted as the sorption of a part of the fulvic acid on the FFM. The spectra recorded freshly after preparation with a higher intensity than for the FA-573 alone, are due to the turbidity induced by the FFM. A detailed analysis of the UV-Vis. spectra indicates the following percentages of sorption on FFM; after 11 days: (19 ± 1) %, 1 month: (29 ± 1) %, 4 months: (31 ± 1) %, 8 months: (42 ± 1) %. In conclusion, the FA-573 fulvic acids are stable in ÄGW, in presence of MX80-bentonite colloids or actinides but sorb up to 42 % to fracture filling material after 8 months. A last comment to precise that the fulvic acids do not present any colloidal behaviour (at least for the UV-Visible fulvic acid fraction if several are present) as no difference was observed on the UV-Visible spectra obtained after ultracentrifugation (2h at ~ 500 000 g).

The behavior of the radionuclides Sr⁹⁰(2.2·10⁻⁹ M), Cs¹³⁷(2.3·10⁻⁹ M), U²³³(2.3·10⁻⁸ M), Am²⁴¹(1·10⁻¹⁰ M), Pu²⁴⁴(1.07·10⁻⁹ M) and Np²³⁷(1.06·10⁻⁸ M) is illustrated in Figures 11a-f. The upper part of each figure shows the radionuclide portion remaining in solution while the lower part represents the colloidal fraction. The following conclusions can be drawn from the results.

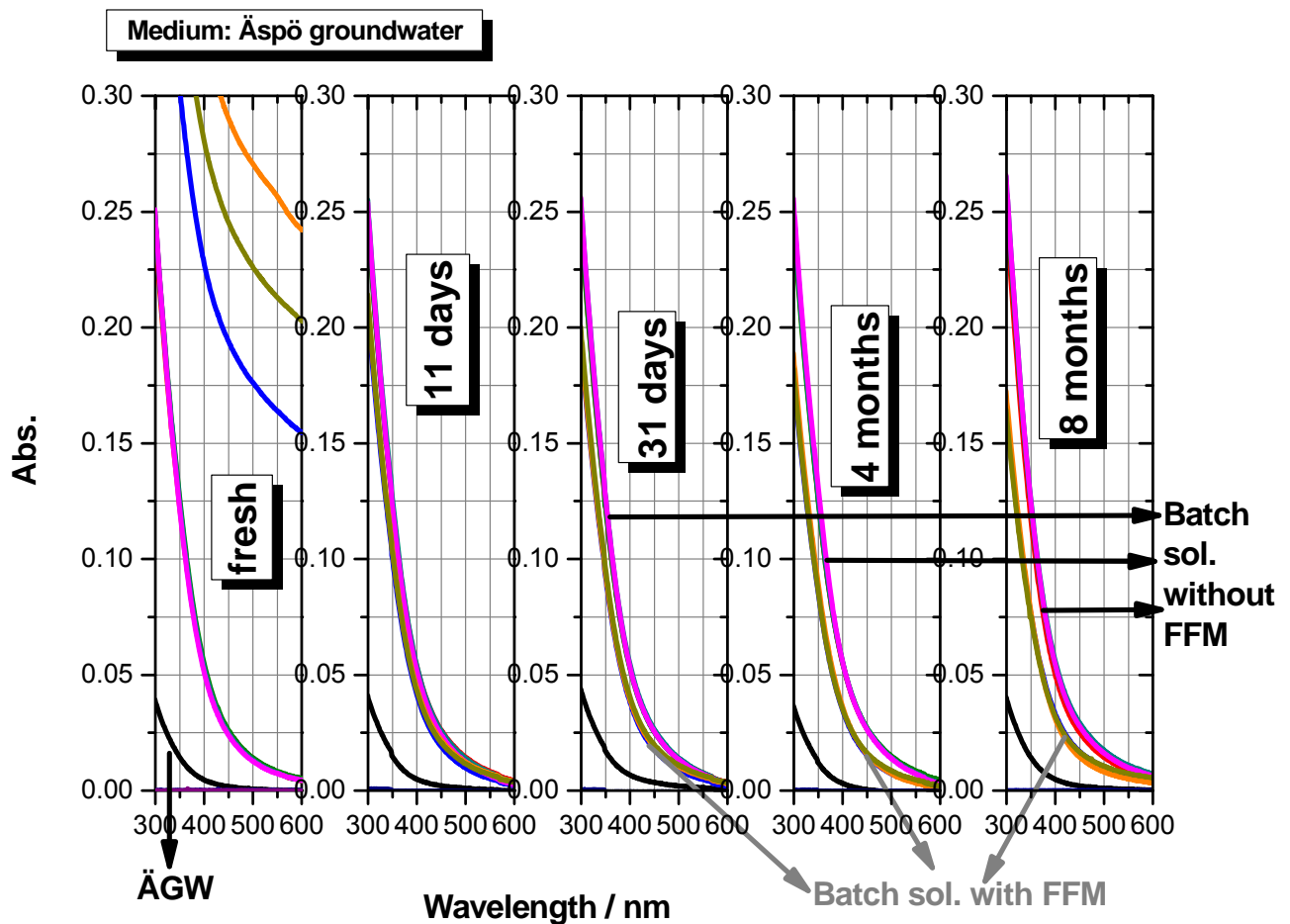


Figure 6-19: Evolution of the fulvic acid (FA-573, 10 mg.L⁻¹) UV-Visible spectra in Äspö groundwater in presence of MX-80 colloids, fracture filling material, radionuclides or mixture of both.

ICP-MS and LSC results

- **Sr(II):** Sr⁹⁰ does not show any significant attachment to neither MX80 bentonite colloids nor initially present groundwater colloids. Moreover, no sorption to fracture filling material or complexation to fulvic acid could be evidenced. This is in agreement with the behavior of Sr⁸⁸ occurring naturally in the groundwater (see Table 6-4).
- **Cs(I):** Cs¹³⁷ does not show as well any significant colloidal behavior in presence or absence of MX80 bentonite colloids and fulvic acid. This is consistent with the behavior of the naturally occurring Cs¹³³ (Table 6-4). In presence of fracture filling material (green and blue points), ~ 75 % of the Cs¹³⁷ sorbs on the fracture filling material after 3 weeks to reach 90 % after 9 months, which seems to be a plateau value. The same is true for the natural Cs¹³³ (see Table 6-5 and Figure 11b) which is sorbed as well: ~ 50 % after 3 weeks up to 85 % after 9 months.
- **U(VI):** U²³³ (full points on figure 11c) does not show any significant colloidal behavior in presence or absence of MX80 bentonite colloids, or fulvic acid, like the naturally abundant U²³⁸ (Table 6-4). In contact with fracture filling material the U²³⁸ concentration increases, from 0.3 µg.L⁻¹ up to 6 µg.L⁻¹ after 3 weeks to reach a plateau value after 6 months around 15 µg.L⁻¹. This fact (clearly seen as well in the water composition evolution in Table 6-5) has already been observed and mentioned in recent studies [183] and was explained by oxidation of U(IV) to U(VI) in the rock due to contact with air in the Äspö tunnel during sampling and transport. U(VI) is soluble under given conditions and is thus transferred to the groundwater.

- Am(III):** Am-241 forms colloids (black points on figure 11d) when spiked to the ÄGW similar to what is observed for La(III) (Table 6-4). These colloids consist most likely of artificially formed Fe(III)/Mn oxyhydroxide due to oxygen contact during groundwater sampling and storage, although performed under Ar atmosphere. They sorb trace metal ions such as La/Am(III), are instable and disappear from solution after 2 months. In presence of MX80-bentonite colloids (red points on figure 11d), Am exists as well in colloidal form and is certainly associated with the instable MX80-bentonite colloids as it disappears even faster from the supernatant (20 % remaining in solution after 2 days vs. 75 % in absence of added MX80 colloids). All types of colloidal Am are removed from solution after 2 months. In contact with fracture filling material (green points on figure 11d) Am sorbs strongly within 3 weeks and disappears from the solution. With fulvic acid added to the ÄGW (pink points on figure 11d), the spiked Am remains longer in solution: 75 % are still present in solution after 8 months. The slow percentage decrease could not be explained by an instability of fulvic acids (cf. the UV-Visible experiments) but rather by a competition between the fulvic acids and the artificially formed colloids pre-cited: the initial fast complexation by the fulvic acids would be followed by a slow dissociation-sorption to those colloids which, by disappearing from solution, reduce finally the amount of Am remaining in solution. The presence of colloidal Am at this point, when the FA acids do not present any colloidal behavior supports this assumption. Finally, in the common presence of MX-80 colloids, fulvic acid and fracture filling material, the Am sorbs and disappears from the solution after 3 months. In conclusion, the Am sorption to FFM is only slightly kinetically hindered by the addition of fulvic acid. Here once more, one can assume a fast complexation by the fulvic acids followed by a fast dissociation-sorption process in benefit of the mineral phases constituting the FFM like the quartz, one of its main constituents.
- Pu(IV):** Pu-244 forms as well colloids when spiked to the ÄGW in presence and absence of bentonite colloids similar to the behavior of Am. As found for Am, the Pu concentration is below the detection limit after 2 months. Pu is also removed from solution in presence of FFM. As for Am, in presence of fulvic acid added to the ÄGW~75 % of the spiked Pu remain in solution after 8 months, but in the common presence of MX-80 colloids, fulvic acid and fracture filling material, the Pu sorbs and disappears from the solution after 6 months. The same processes as those detailed for the Am could be involved to explain the Pu behavior.
- Np(V):** Np-237 spiked to the ÄGW does not form colloids but disappears nevertheless almost completely from solution after 6 months (~ 35 % remaining in solution after 2 months, only ~ 10 % after 3 months and less than 5 % after 6 months). This could be explained by a slow reduction of Np(V) under these conditions considering the redox potential (~ 60 mV) (see the Eh-pH diagram plotted in [185]). Np(IV) phases may either sorb to container walls or artificially formed colloids or coagulate and sediment. In presence of MX80-bentonite colloids, the Np is removed even faster and only ~5 % remain in solution after 2 months compared to ~35 % in absence of MX80-colloids. This indicates a possible Np sorption to sedimenting MX80-bentonite colloid agglomerates. Sorption to FFM is clearly visible and complete after 3 months when the simultaneous addition of fulvic acid slightly reduces the sorption kinetics. In presence of fulvic acids only, the behavior differs as those observed for Am or Pu. Actually, the Np is removed faster and only 10 % remain in solution after 8 months. This could be explained by referring to the weak complexation constants of Np(V) by fulvic acid [Marq98] in addition as already mentioned to a competition with the reduction process followed by a sorption to existing water colloids.

Geochemical modeling (Geochemist's Workbench 6.04). It was attempted to describe the interaction of Am with the different potential adsorbents present in the different sets of experiments. In all systems the aqueous speciation of Am was calculated according to the work by Bradbury and Bayens [186]. This is necessary to insure internal consistency with the bentonite adsorption model. The results are discussed in some details below.

Set 1: Am in ÄGW: One possibility of the decrease in Am in this case is retention on the iron minerals, which are usually accepted as strong scavengers for heavy metals and actinides. It would be expected that hydrous ferric oxide would be a potential solid forming. This has been confirmed in the speciation calculations on the water. Ferrihydrite (HFO, $\text{Fe}(\text{OH})_3$) was supersaturated in those calculations and Fe was found to be to a significant extent in colloidal form. A simple surface complexation model was developed based on published Eu-data (Music) in combination with the averaged acid-base properties given by Dzombak and Morel [187]. The calculations showed that Am could be completely removed from these particles, assuming that some kind of incorporation would occur. If a more complex model, which would involve all the potentially adsorbing solutes (like carbonate, sulphate etc.), was used, the available sites would be saturated by those solutes, which may have a lower affinity but are far more abundant compared to Am. However, a kind of incorporation mechanism might be justified based on literature data [188]. Thus it is known that trivalent solutes can be incorporated into goethite crystals. To elucidate the actual mechanism in the multi-component system, more experimental work is required. The model calculation retained for the subsequently discussed systems is based on incorporation data.

Set 2: Am + MX80 in ÄGW. The model of Bradbury and Bayens was applied. First calculations involved the full water composition and the available speciation according to the NEA data base (vol. 5). This means that complexation of Am with sulphate, fluoride, carbonate influences the results. The partial pressure of carbon dioxide was fixed at 10^{-2} (glove box). This resulted in such a strong dominance of Am carbonate complexes in solution and retention of Am on the clay was close to zero. Decreasing the carbon dioxide partial pressure resulted in some uptake, but it was not sufficient to explain the observations. The model would not even in the simple system predict the required uptake of Am. This was due to the low amount of solid. Since the iron discussed in set 1 is also present in set 2, it was then assumed that the bentonite is responsible for an additional removal of Am (i.e. assuming that the results from system 1 imply a decrease of Am total concentration by 30 percent). This gives a final concentration of Am of about 55 to 60 percent of the total concentration for the first measurement assuming a low partial pressure of carbon dioxide; so the bentonite would be responsible for an additional decrease in Am concentration by 10 to 15 percent. This is still too high compared to the observations (20 percent or 50 % additional decrease). Several factors influence the results: (i) the partial pressure chosen, (ii) ternary surface complexes are not included in the model, since their stabilities are not known. For longer time the Am concentration decreases also in the absence of bentonite to very low concentrations. The conclusion from this system is that the bentonite model prediction for the chosen partial pressure of carbon dioxide indeed predicts some additional uptake of Am, but it fails to predict it quantitatively.

Set 3: Am + FFM in ÄGW. Addition of 250 g/l fracture filling material was treated in the calculation by assuming that 65 percent of that material would correspond to quartz [175]. The specific surface area of the quartz was supposed to correspond to that of quartz particles studied at INE with a mean particle size of 1 mm. This was based on the observation that the amount of quartz in fraction below 1 mm mesh size and above is nearly the same. The specific surface of the Äspö fracture filling material was measured with 0.2 m^2/g [189]. This is a lower value measured for a couple of quartz samples as reported by Huber [108]. The model for quartz Am interaction was taken from Stumpf et al. [37]. Using this model without considering potential competition from any of the other cations present except sodium (no data for Ca, Mg, as well Fe and Al, if applicable) could be considered for

lack of consistent data. However, it is expected that Ca and Mg start adsorbing at higher pH. Fe and Al could dissolve from their colloidal form and adsorb to the quartz. But from the amount of quartz surface sites present (assuming the specific surface area specified above), this is not expected to affect the results too much. In agreement with the observation Am is nearly entirely bound to the quartz surface even if the carbon dioxide partial pressure is 0.01 atmospheres. Some calculations were carried out with lower specific surface area. The specific surface area could be decreased by a factor 1000 and still Am would be bound to the quartz to 98.5 percent. If the assumed specific surface area is decreased by a factor 10,000, the amount of Am sorbed to the quartz is decreased to about 10 percent.

Set 5: Am+ FA-573 in ÄGW. Addition of 10 mg·L⁻¹ fulvic acid to the system was also modelled. Here, the NICA Donnan model was used. The parameterisation was according to the equations given by Milne et al. [190]. The parameters were recalculated using the formula for fulvic acid and the log K_{OH} for Am according to the NEA TDB. Competition with Ca and Mg was considered first. A low partial pressure of carbon dioxide was fixed. In this case the Am is entirely bound to the fulvic acid. The results is the same if the colloidal iron phases formed in the ÄGW are considered as competing with the FA for the Am. In the next step Al and Fe (trivalent) were allowed for competition, but even this was not enough to saturate the fulvic substances within the model calculation to release some of the Am as observed. Finally one calculation was done with an increased partial pressure of carbon dioxide. The partial pressure corresponding to that in the glove box produced a significant effect above pH 8. Here the Am in solution increased. At pH 8.2 10 percent are retrieved in the solution, at pH 8.4 30 percent. The implication of this result is that given the uncertainties of the parameters, the total concentrations, the real partial pressure of carbon dioxide, the multiple models and the multi-component nature of the system the concomitant effect of competition for Am by carbonate and for adsorption sites on fulvic acid starts to have an effect on the calculate Am concentration quite close to the conditions where it is observed. It should be noted, however, that no consistent treatment in terms of the carbon dioxide partial pressure is possible, i.e. in the present system a high value is required, whereas in Set 2 a low value is required.

Set 4: Am+ MX80+ FFM+ FA-573 in ÄGW. For the multi-component system involving bentonite, fulvic acid and fracture filling material, the following calculations were done: CO₂ 0.01 atm, specific surface area of quartz 0.2 m²/g. Otherwise the same assumptions as specified already were made. This resulted in complete uptake of Am on the quartz according to the calculations, in agreement with the observations.

Summary. The modelling is complex in this multi-component system. In particular CO₂ partial pressure in the glove box was fixed to 0.01 atm, but this boundary condition does not necessarily apply for the test tubes. This disappearance of Am in the original water was attributed to interactions with iron. The iron originally present as Fe(II) was assumed to be converted to Fe(III) which results in precipitation of Fe(III) solids, with hydrous ferric oxide being the most probable phase forming. A model for adsorption of Am on HFO was only successful if no competition with the other components (in particular the anions and here again carbonate in an open system would be a strong competitor) was considered. The model in absence of competition could be seen as some incorporation of Am into HFO. For bentonite the model prediction was only showing retention of Am on bentonite if CO₂ < 0.01 atm. The possibility of ternary surface complexes was discussed in this case. For the fulvic acid system complexation of Am was starting to affect the Am solution composition only if a high partial pressure of carbon dioxide was assumed in contradiction to the previous case. The system containing FFM could be predicted using a model for Cm/Am adsorption to quartz. In this model the competition on quartz by other cations could not be taken into account for lack of self-consistent models and experimental data. But variation of the quartz surface area showed a buffer factor of 3 orders of magnitude. Finally for the system involving bentonite, fulvic acid and FFM (quartz) again complete adsorption to quartz was predicted.

Figure 6-20: a) Sr^{90} ($2.2 \cdot 10^{-9}$ M), b) Cs^{137} ($2.3 \cdot 10^{-9}$ M), and c) U^{233} ($2.3 \cdot 10^{-8}$ M) spiked to ÄGW (TRUE1-site, Feature A, KXTT4) in presence of added MX80-bentonite colloids (2.4 mg.L^{-1}), fracture filling material (FFM) ($1 \text{ g} : 4 \text{ mL water}$) and fulvic acid (FA-573, $10 \text{ mg.L}^{-1} \sim 5 \text{ mg.L}^{-1} \text{ DOC}$). The open symbols represent the behavior of the naturally occurring element measured in the batch supernatants, namely Cs^{133} and U^{238} . Error : $\pm 5 \%$.

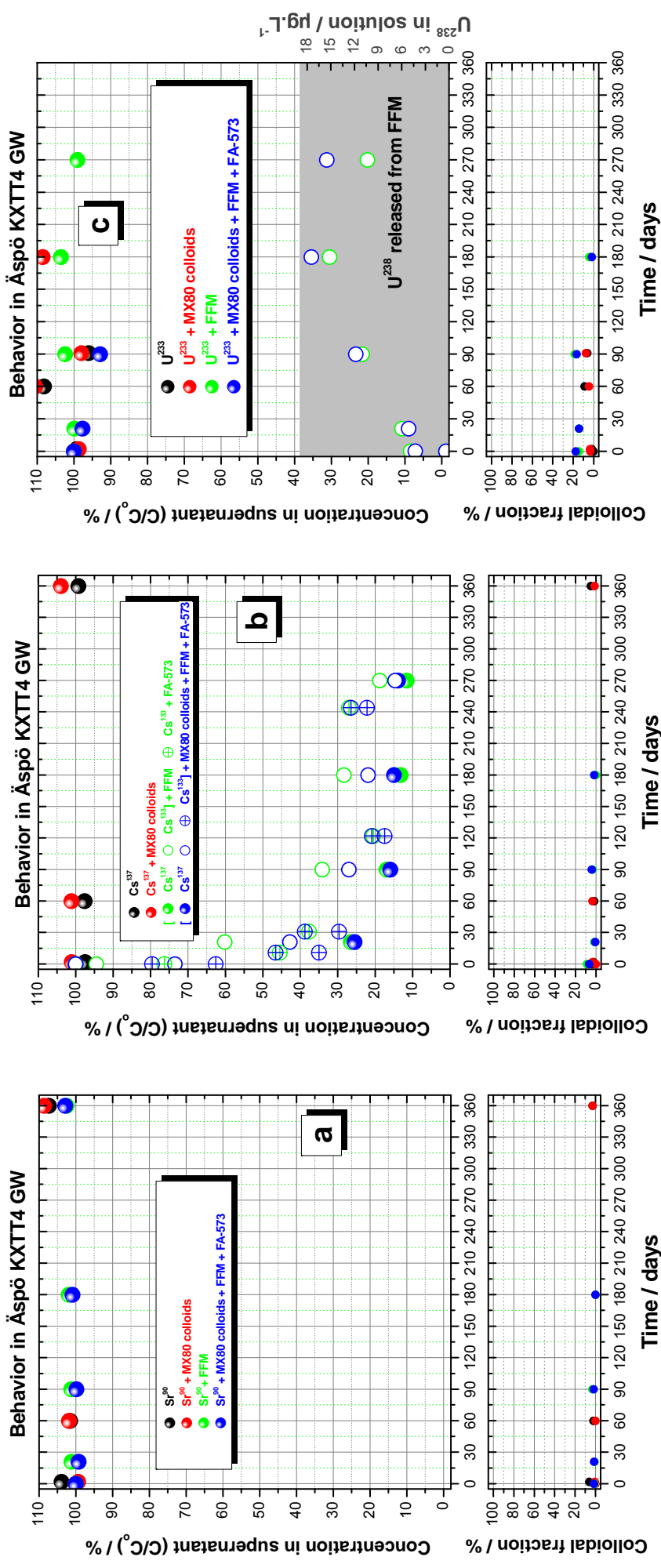
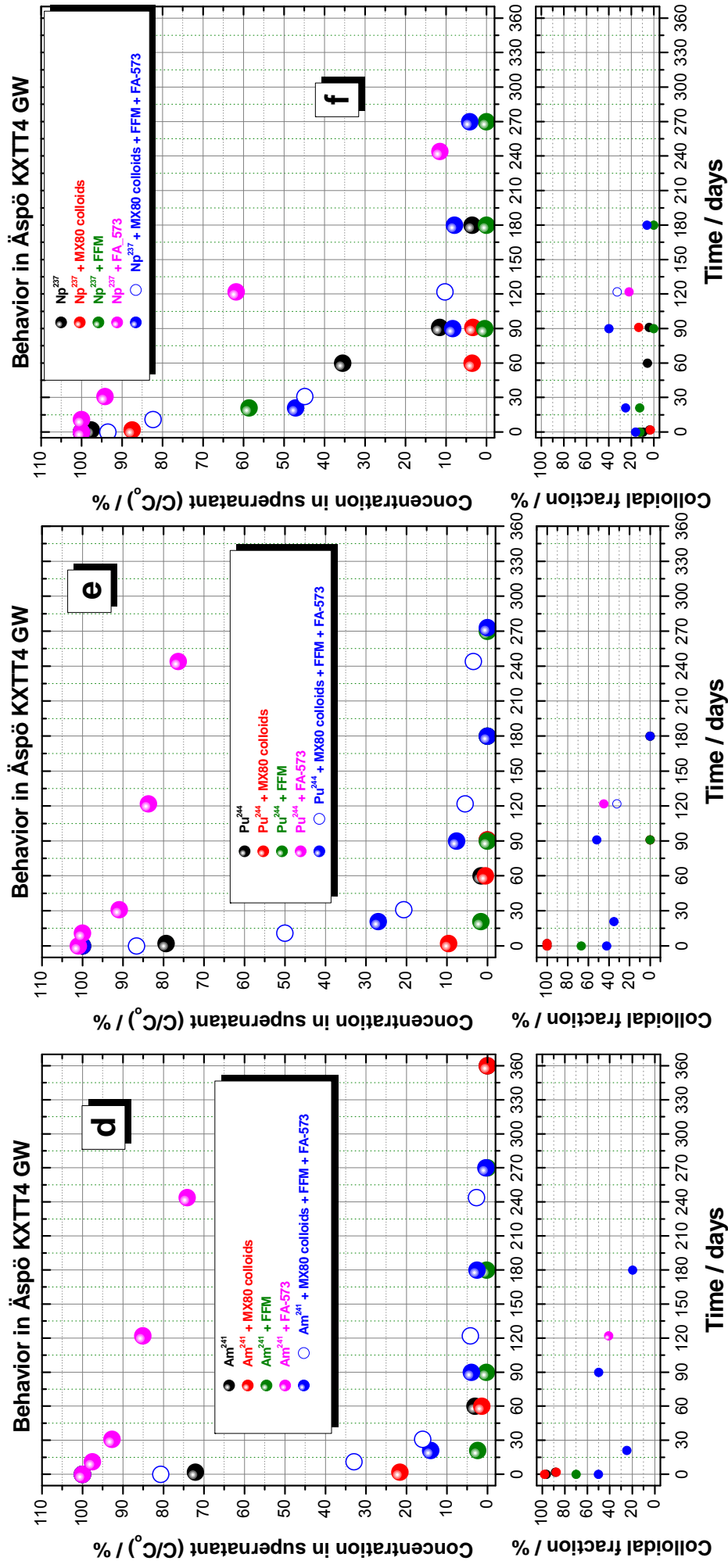


Figure 6-20: d) e) f) Behavior of d) Am^{241} ($1.10 \cdot 10^{-10}$ M), e) Pu^{244} ($1.07 \cdot 10^{-9}$ M) and f) Np^{237} ($1.06 \cdot 10^{-8}$ M) spiked to ÄGW (TRUE1-site, Feature A, KXTT4) in presence of added MX80-bentonite colloids (2.4 $\text{mg}\cdot\text{L}^{-1}$), fracture filling material (FFM) (1g : 4 mL water) and fulvic acid (FA-573, 10 $\text{mg}\cdot\text{L}^{-1}$ ~ 5 $\text{mg}\cdot\text{L}^{-1}$ DOC). Error : \pm 5 %.



Conclusions

- The colloid composition and concentration in Äspö groundwater are very sensitive to contact with oxygen trace concentration and partial pressure changes. **This has to be considered for planned in-situ experiments.**
- Montmorillonite colloids (as those supposed resulting from the bentonite barrier erosion) are shown to be instable in Äspö groundwater from the KXTT site, coagulate and sediment. Even after mechanical remobilization, they are rapidly removed from solution. Under given conditions, we have to conclude that **colloids eroding from bentonite backfill rather retain radionuclides such as actinides and do not act as mobilizing carriers.** Carboxylated polystyrene standards colloids are as well subject to agglomeration in ÄGW. However, agglomerates do not sediment due to their low density being close to that of water.
- The presence of organic matter does not enhance bentonite colloid stability in ÄGW but influences sedimentation kinetics and **acts as a complexing agent keeping tri- and tetravalent actinides in solution.** This effect could be even better evaluated by performing experiments where the “artificial” formation of colloids would be totally avoided.
- Geochemical calculations performed in order to specify prevailing radionuclide speciation under given experimental conditions confirm within the uncertainties the above made conclusions.